TAILORING SUPERCONDUCTOR AND SOFC

STRUCTURES FOR POWER APPLICATIONS

Thomas Mitchell-Williams

Queens' College

Department of Materials Science & Metallurgy

University of Cambridge

This dissertation is submitted for the degree of Doctor of Philosophy

May 2017

Declaration

This dissertation is the result of my own work and includes nothing, which is the outcome of work done in collaboration except where specifically indicated in the text.

It is not substantially the same as any that I have submitted, or, is being concurrently submitted for a degree or diploma or other qualification at the University of Cambridge or any other University or similar institution except as declared in the Preface and specified in the text. I further state that no substantial part of my dissertation has already been submitted, or, is being concurrently submitted for any such degree, diploma or other qualification at the University of Cambridge or any other University or similar institution except as declared in the Preface and specified in the text

This thesis does not exceed, 60,000 words, including summary/abstract, tables, footnotes and appendices, but excluding table of contents, photographs, diagrams, figure captions, list of figures/diagrams, list of abbreviations/acronyms, bibliography and acknowledgements.

Signed:_____

Date:_____

Thomas Mitchell-Williams

ABSTRACT

High temperature superconductors (HTS) and solid oxide fuel cells (SOFCs) both offer the possibility for dramatic improvements in efficiency in power applications such as generation, transmission and use of electrical energy. However, production costs and energy losses prohibit widespread adoption of these technologies. This thesis investigates low-cost methods to tailor the structures of HTS wires and SOFCs to reduce these energy losses.

Section I focusses on methods to produce filamentary HTS coated conductors that show reduced AC losses. This includes spark-discharge striation to pattern existing HTS tapes and inkjet printing of different filamentary architectures. The printed structures are directly deposited filaments and 'inverse' printed tracks where an initially deposited barrier material separates superconducting regions. Furthermore, the concept and first stages of a more complex 'Rutherford' cable architecture are presented. Additionally, Section I investigates how waste material produced during the manufacture of an alternative low-AC loss cable design, the Roebel cable, can be used to make trapped field magnets that produce a uniform magnetic field profile over a large area. This trapped field magnet work is extended to study self-supporting soldered stacks of HTS tape that demonstrate unprecedented magnetic field uniformity.

Section II looks at how nanostructuring porous SOFC electrodes via solution infiltration of precursors can improve long-term stability and low temperature performance. Inkjet printing is utilised as a scalable, low-cost technique to infiltrate lab-scale and commercial samples. Anode infiltration via inkjet printing is demonstrated and methods to increase nanoparticle loading beyond ~1 wt% are presented. Symmetric cells with infiltrated cathodes are shown to have improved performance and stability during high temperature aging. Additionally, the sequence of solution infiltration is found to be important for samples dual-infiltrated with two different nanoparticle precursors.

ACKNOWLEDGEMENTS

CONTENTS

LIST OF ABBREVIATIONS AND ACRONYMS

Abbreviation	Definition
2G	Second generation
2LUPS	Two level undercut profile substrate
8YSZ	$8mol\%\text{-}Y_2O_3$ doped ZrO_2
ABAD	Alternating beam assisted deposition
AC	Alternating current
acac	2,4-pentanedione
APU	Auxiliary power unit
ASR	Area specific resistance
B	Magnetic flux density
Bi-2223	$Bi_2Sr_2Ca_2Cu_3O_{10}$
BZO	Barium zirconate
CCA	Coated conductor applications (conference)
CGO	Gadolinium doped ceria
CHP	Combined heat and power
CIJ	Continuous inkjet
CoO	Cobalt oxide (Co_3O_4)
CORC	Cable on round core
CPE	Constant phase element
CTE	Coefficient of thermal expansion
CZO	Zirconium doped ceria
DC	Direct current
DoD	Drop on demand
EDX	Energy dispersive X-ray spectroscopy
EIS	Electrochemical impedance spectroscopy
EtOH	Ethanol
EUCAS	European conference on applied superconductivity
FC	Field cooled
FCL	Fault current limiter
FEM	Finite element method
GdBCO	Gadolinium barium copper oxide
H_2O	Water
H_c	Thermodynamic critical magnetic field
H_{c1}	Lower critical magnetic field for type II superconductors
H_{c2}	Upper critical magnetic field for type II superconductors
H_{irr}	Irreversibility magnetic field for type II superconductors
HTS	High temperature superconductor

Abbreviation	Definition
HVDC	High voltage direct current
IBAD	Ion beam assisted deposition
I_c	Critical current
ISD	Inclined substrate deposition
J	Current density
J_c	Critical current density
J_{cs}	Critical surface current density
LSC	Lanthanum strontium cobaltite
LSCF	Lanthanum strontium cobalt ferrite
LSF	Lanthanum strontium ferrite
LSM	Lanthanum strontium manganite
MeOH	Methanol
MOCVD	Metal-organic chemical vapour deposition
MOD	Metal-organic deposition
MRI	Magnetic resonance imaging
MSC	Metal supported cell
Ni/YSZ	Nickel YSZ composite
nL	Nanolitre
NMR	Nuclear magnetic resonance
OCV	Open cell voltage
Oh	Ohnesorge number
ORR	Oxygen reduction reaction
pL	Picolitre
PLD	Pulsed laser deposition
PPA	Propionic acid
PrBCO	Praseodymium barium copper oxide
PrYBCO	Praseodymium doped YBCO
Q	Energy loss
RABiTS	Rolling assisted biaxially textured substrate
RCE	Reactive co-evaporation
Re	Reynolds number
REBCO	(Rare-earth) barium copper oxide
R_p	Polarisation resistance
R_{rms}	Profile roughness
ScSZ	Scandium doped zirconia
SDC	Samarium doped ceria
SEM	Scanning electron microscopy
SFCL	Superconducting fault current limiter

Abbreviation	Definition
SOFC	Solid oxide fuel cell
SS	Stainless steel
T_c	Critical transition temperature
TEA	Triethanolamine
TFA	Trifluoroacetic acid
TFAA	Trifluoroacetic acid anhydride
TGA	Thermogravimetric analysis
TMIC	Total metal ion concentration
TPB	Triple phase boundary
We	Weber number
XPS	X-ray photoelectron spectroscopy
XRD	X-ray diffraction
YBCO	Yttrium barium copper oxide
YSZ	Yttria stabilised zirconia
ZFC	Zero field cooled

PREFACE

Improving efficiency and reducing greenhouse gas emissions in energy generation, conversion and transmission are particularly important topics of research. There is international agreement that greenhouse gas emissions must be sharply reduced to minimise the likelihood of even a 2 °C rise in average global temperature, Figure 1. Additionally, the increasing scarcity of fossil fuels motivates increasing renewable capacity and maximising energy efficiency.
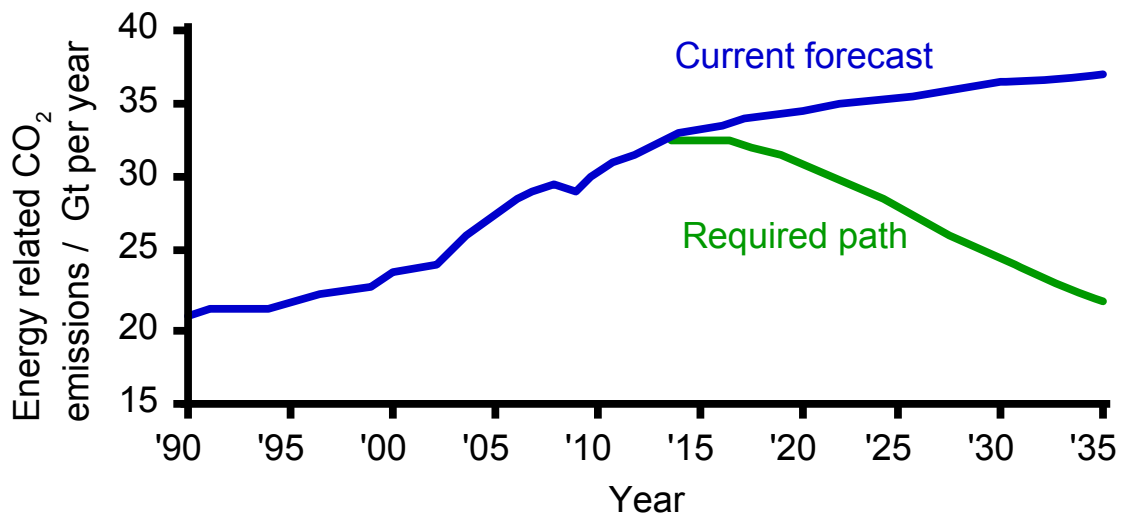
Figure 1. Current energy related CO_2 emissions forecast and the required reduction to avoid a 2 °C rise in average global temperature. Adapted from [1].

Current predictions about the required increase in renewable capacity and reduction in emissions rely on improvements in device efficiency and both lower unit and capital investment costs. Inkjet printing is a relatively new method for depositing functional materials for energy applications and crucially enables low capital and unit costs. This thesis will explore how scalable inkjet printing technology and structural modification can be used to enhance the properties of two important categories of energy materials systems: high temperature superconductors (HTS) and solid oxide fuel cells (SOFCs).

HTS COATED CONDUCTORS

Superconductors have zero DC electrical resistance when below their critical temperature. Therefore, HTS cables have the potential to significantly increase energy efficiency in power applications. The high current density achievable also allows for much more compact installations. However, the cost of HTS cables relative to traditional copper

conductors and the problem of AC loss both remain as significant barriers to widespread adoption in large scale power applications.

The effective cost of superconducting wire depends on performance, so the metric of dollars per kilo-amp per metre is used. Therefore, increasing current carrying capacity or reducing production costs will be beneficial for market uptake. The widely-agreed cost of $< \$10 \text{ kA}^{-1} \text{ m}^{-1}$ for operation at 77 K, self-field, that coated conductors need to achieve has still not been reached, despite forecasts, Figure 2. The cost of cuprate based, second generation (2G), coated conductors is not limited by the embedded materials cost in the way that first generation, silver sheathed conductors were. The raw materials cost $< \$1 \text{ kA}^{-1} \text{ m}^{-1}$ [2] so the manufacture and processing of superconducting wire is where reduction in cost should be focussed.
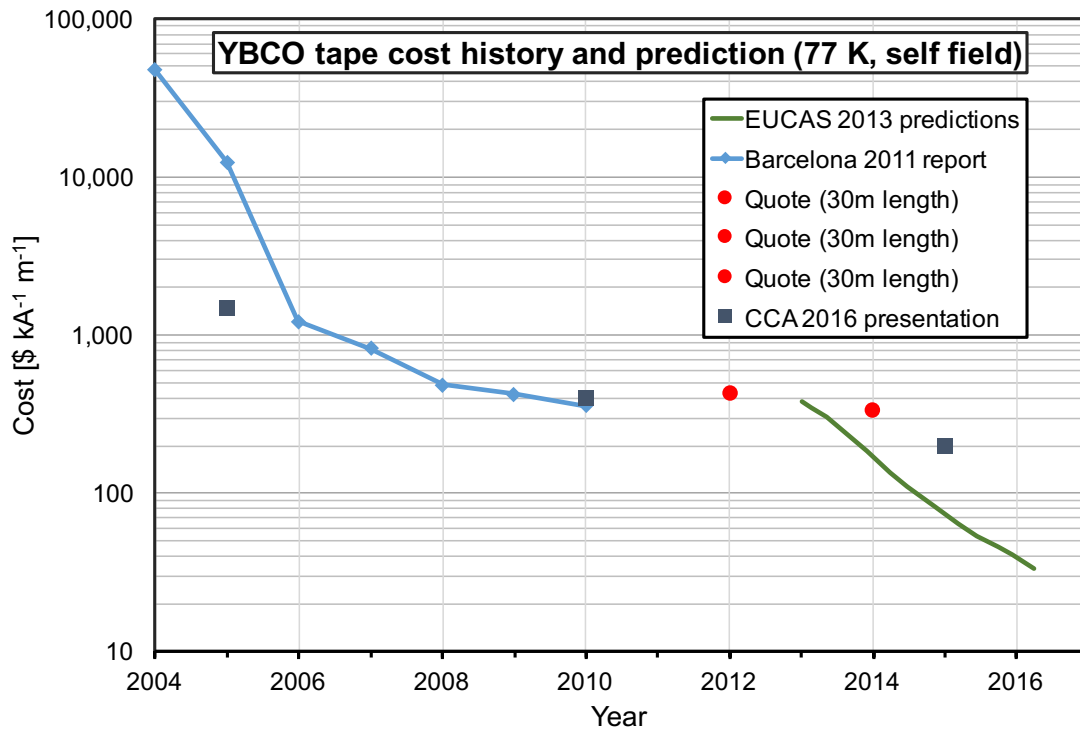
Figure 2. Historical and predicted HTS coated conductor tape costs. Despite predictions of substantial falls in price the costs have remained well above the $\$10 \text{ kA}^{-1} \text{ m}^{-1}$ level. Barcelona 2011 reference [3].

The energy losses present when superconductors operate in an alternating field or with alternating transport current complicate their use in large scale applications such as motors/generators, transformers and AC transmission. As well as the direct energy loss, there is an additional cryogenic load due to heat evolution, which can further complicate system design. The main source of AC loss is the hysteresis when the magnetisation of a

superconductor is cycled, Figure 3. Luckily, however, the losses can be significantly reduced through patterning and structuring the superconductor.
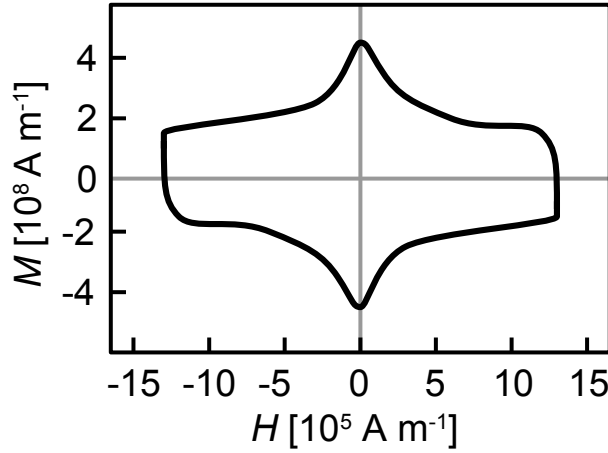
Figure 3. Magnetisation loop for an unstriated thin film of YBCO. The area enclosed within the loop represents the energy lost during a cycle. Adapted from [4].

The acceptable level of AC loss can be estimated from a comparison with traditional copper conductor without forced cooling [5]. Assuming the copper power loss is ~15 mW A^{-1} m^{-1} with no cooling requirement and that the cooling penalty for HTS wire at 77 K is ~15 times then the maximum acceptable power dissipation is 1 mW A^{-1} m^{-1}. However, if HTS wires are to be competitive with conventional technology, and justify the extra investment cost, then approximately half this value should be a suitable target.

Section I of this thesis will investigate how both the challenge of cable cost and AC loss can be tackled through different methods of producing and tailoring the wire structure, including the minimisation of waste material.

SOFCs

Solid oxide fuel cells (SOFCs) are highly efficient devices for converting chemical energy into electricity. The key target markets for SOFCs are utility scale generation, distributed generation and auxiliary power units (APU). The relatively high operating temperatures of SOFCs lend themselves well to providing distributed combined heat and power (CHP), which can increase total efficiency further.

However, for SOFCs to be competitive with incumbent technology there are a several technological challenges. The European Commission [6] and the US Department of Energy [7] have both identified cost and durability as the major issues for fuel cell development, see

Figure 4. Additionally, given that cost and durability are evaluated for a specific performance level, improvements to power output and efficiency will also benefit these goals.
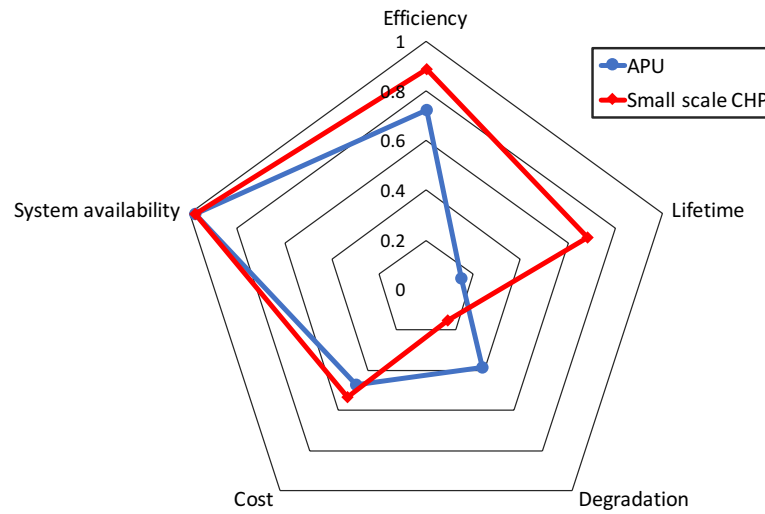
Figure 4. A star plot showing the current performance of SOFC systems relative to 2020 targets set by the US Department of Energy [7]. The target is to reach all outer corners by 2020. The main issues are durability/lifetime and cost.

There are different approaches to tackling the challenges of cost, durability and performance and the one focussed on in section II of this thesis is solution infiltration of the porous electrode structure. Specifically, the use of scalable inkjet printing technology to infiltrate precursor solutions that enable formation of oxide nanoparticles. This processing technique is inherently low cost and can improve the durability and performance of SOFCs without significantly increasing costs.

A diagram summarising the structure of this thesis addressing high temperature superconductors (HTS) and solid oxide fuel cells (SOFCs) is shown on the following page.

Tailoring superconductor and SOFC structures for power applications

I: Filamentary High Temperature Superconductors
1. Introduction to HTS

- 2. ROEBEL cables
  - Uniform trapped fields
- 3. Spark-plasma discharge striation
  - Bridged/non-bridged samples
- 4. Printed structures
  - Direct printed filaments
  - Inverse printed filaments
    - PrBCO leading to Rutherford

II: SOFCs
5. Introduction to SOFCs

- 6. Anode infiltration
  - Ni/Fe anodes → model system
- 7. Cathode infiltration

Inkjet printing
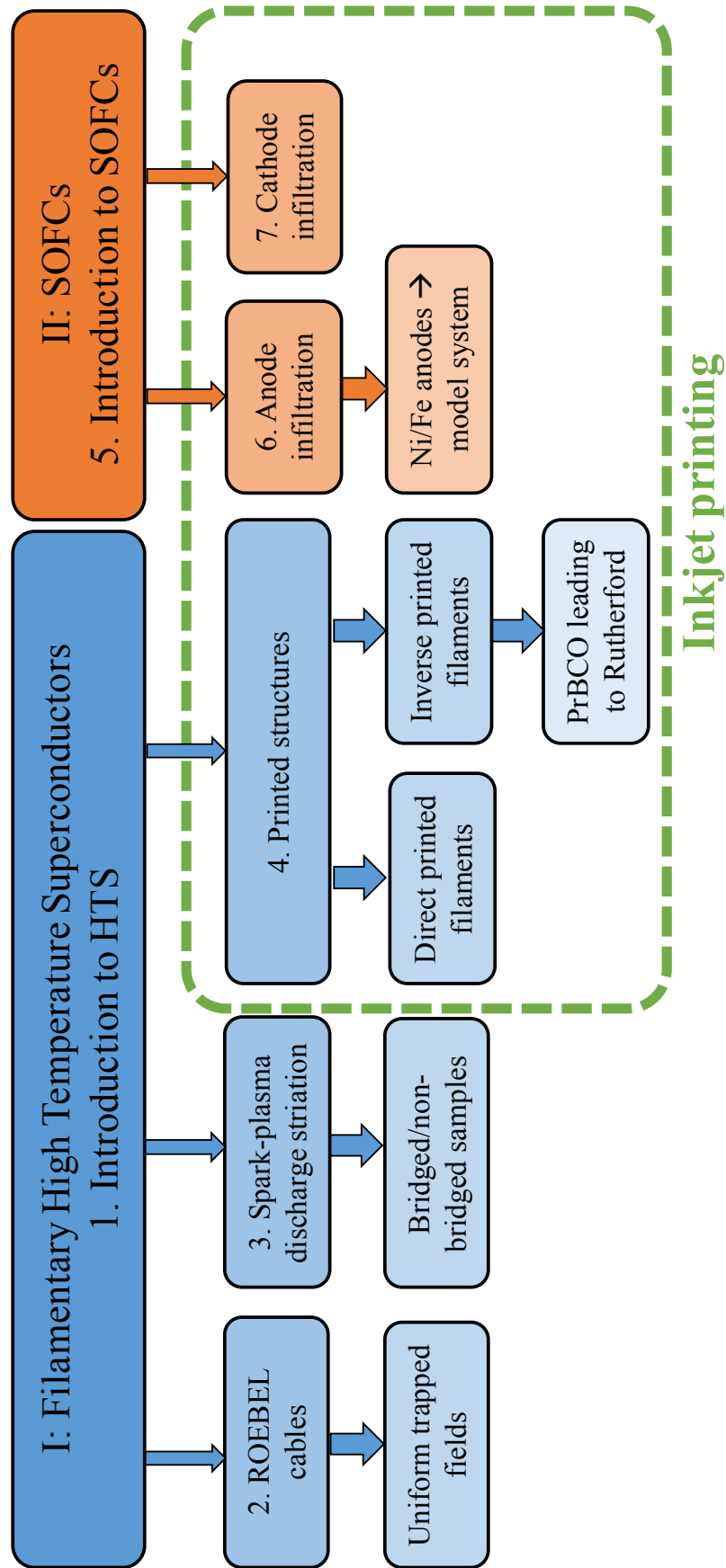
SECTION I: FILAMENTARY HIGH TEMPERATURE SUPERCONDUCTORS

1 INTRODUCTION: HTS

1.1 High temperature superconductors

1.1.1 Brief history

Superconductivity was discovered in 1911 when Onnes observed that the electrical resistance of mercury fell sharply to zero when cooled using liquid helium [8]. In the following years, other elements [9] and many compounds [10] were discovered to be superconductors including the Nb_3Sn intermetallic [11] and the widely-used niobium titanium alloys. A very significant development for superconducting materials was the discovery of superconductivity in La-Ba-Cu-O ceramics by Bednorz and Müller in 1986 [12]. In the following year, the first material to exhibit superconductivity above the boiling point of liquid nitrogen, 77 K, was discovered [13]. The cuprate, $YBa_2Cu_3O_{7-x}$, (YBCO), with a critical transition temperature (T_c) of ~93 K is now one of the most widely studied superconductors and this class of REBCO (RE = rare earth) materials will be the primary focus in this thesis.

Other cuprate materials with a T_c above 77 K, often collectively termed high temperature superconductors (HTS), include Bi-Sr-Ca-Cu-O discovered in 1988 and Hg-Ba-Ca-Cu-O in 1993 [14,15]. $Bi_2Sr_2Ca_2Cu_3O_{10}$ (Bi-2223) and $HgBa_2Ca_2Cu_3O_8$ have transition temperatures of ~110 K and ~134 K respectively, the latter being the current record at ambient pressure.

In 2001 magnesium diboride, MgB_2, was discovered to be superconducting with a T_c 39 K [16] and more recently a new class of superconductors, the iron oxypnictides, with transition temperatures up to ~56 K have been developed [17–19]. The current record for T_c is for the hydrogen sulphide system at high pressure with a value of 203 K at 155 GPa [20]. A timeline showing selected superconducting materials and their T_c is in Figure 5.
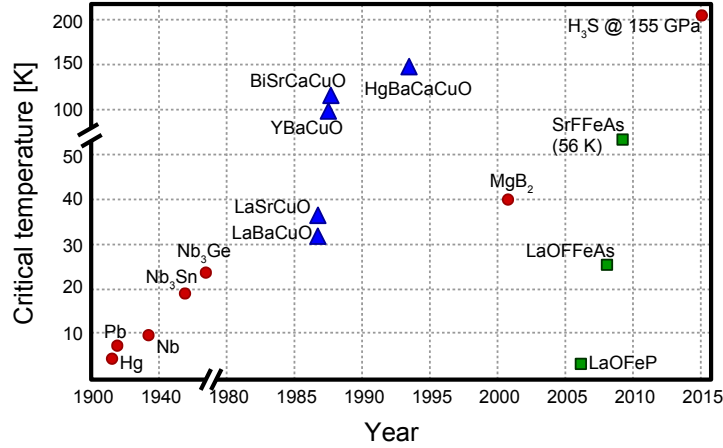
Figure 5. Critical transition temperatures (T_c) and year of discovery for several superconducting materials.

1.1.2 Superconducting properties

Superconductivity is the phenomenon where a material can display exactly zero DC resistance when cooled below a critical temperature, T_c. There are many excellent resources describing the physics [21] and materials science of superconductivity [22–24], so this thesis will not replicate those in great detail.

In addition to critical temperature the magnetic field and current density a material experiences also influences superconductivity. Plotting these critical properties against each other defines a surface, below which a material exhibits superconductivity, Figure 6.
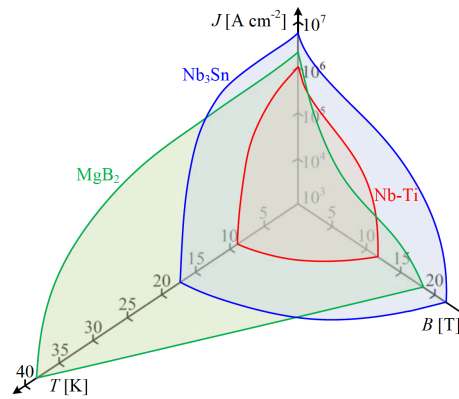
Figure 6. Critical surface for several type II superconductors showing the interdependence of temperature, magnetic flux density and current density on the superconducting state. A material will only be in the superconducting state when beneath this critical surface. From [24].

Before a microscopic theory of superconductivity was proposed by Bardeen, Cooper and Schrieffer in 1957 (BCS Theory) [25] phenomenological descriptions of superconductor

properties were given by the London brothers in 1935 [26] and Ginzburg and Landau in 1950 [27]. In the Ginzburg-Landau theory two characteristic length scales are introduced, the coherence length, ξ, and the penetration depth, λ. These can be related to the microscopic description given by BCS theory [28] as a characteristic size for Cooper pairs (in certain limiting cases) and the depth an external magnetic field will penetrate into a superconductor respectively. The coherence length is also a measure of the distance over which there is a transition between superconducting and normal states at the edge of a superconductor. The ratio between the penetration depth and coherence length, often termed the Ginzburg-Landau parameter, κ, equation (1) is important for classifying superconductors based on their response to an applied magnetic field.

$$\kappa = \frac{\lambda}{\xi} \tag{1}$$

The value κ takes determines whether the surface energy of the interface between normal and superconducting regions is positive or negative. For $\kappa < 2^{-1/2}$ the surface energy is positive and the superconductor is type I, for $\kappa > 2^{-1/2}$ the surface energy is negative and the superconductor is type II. The consequence of this is that in type II superconductors the formation of boundaries between normal and superconducting regions is favourable and flux can penetrate the material when the applied field gets above the lower critical field, H_{c1}. Conversely in a type I superconductor as soon as the thermodynamic critical field, H_c, is reached the material enters the normal state.

The critical field for type I superconductors is typically low (e.g. $\mu_0 H_c \sim 0.03$ T for tin) and because the field experienced by the material includes the self-field due to circulating supercurrents the maximum current density that it can support is correspondingly low. This is the reason all superconductors used or proposed for applications with high fields or current densities are type II. The response of a type II superconductor to an increasing applied field, at $T < T_c$, can be described in three main stages, illustrated schematically in Figure 7.
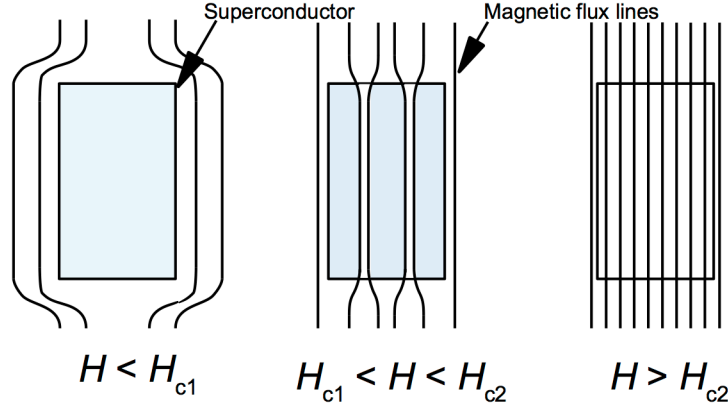
Figure 7. Schematic showing how magnetic flux penetrates a superconductor between critical values.

As shown in Figure 7 for applied fields less than H_{c1} the magnetic flux is completely excluded from the bulk of the material and it behaves in the same way as a type I superconductor below the thermodynamic magnetic field, H_c, Figure 8.
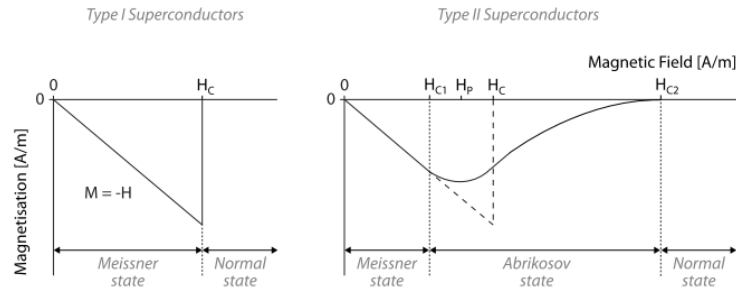
Figure 8. The magnetisation response for type I and type II superconductors to an applied external magnetic field. From [24] and [29].

When the field is between H_{c1} and H_{c2} it becomes favourable for magnetic flux to penetrate the bulk and the material is in the mixed state. It does this in discrete flux quanta, each with magnitude Φ_0 ($\approx 2\times10^{-15}$ Wb). Abrikosov predicted in 1957 that these flux lines would arrange themselves into a triangular lattice in the absence of defects [30], which was observed in 1967 [31], Figure 9.
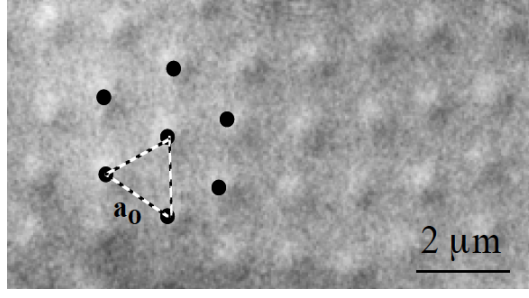
Figure 9. Electron holography image of the flux line lattice in a type II superconductor thin film. From [24].

The flux lines are non-superconducting cores (of radius $\sim\xi$) surrounded by shielding supercurrents. As the magnetic field is increased further the flux lines become more closely spaced until at H_{c2} the flux line cores begin to overlap and the material becomes normal.
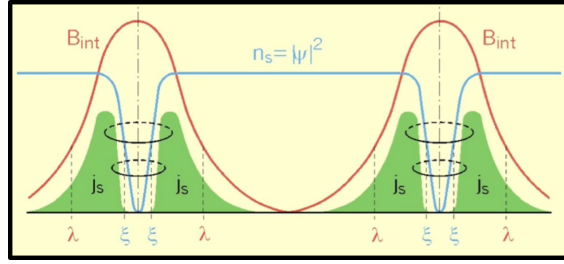
Figure 10. Schematic showing the characteristic length scales near flux cores in a type II superconductor. B_{int} is the magnetic flux density, n_s is the density of superconducting electrons, j_s is the shielding supercurrent density, ξ is the coherence length and λ is the penetration depth. From [24].

During use, most type II superconductors operate in the mixed state. When a current in a superconductor flows perpendicular to the field the flux lines will experience a Lorenz force. The force experienced by each flux line is given by equation (2). The total flux density, B, is the product of the flux quantum and the number density of flux lines. The total force density experienced by the flux line lattice, F_l, is given by equation (3).

$$f = J \times \Phi_0 \tag{2}$$

$$F_l = J \times B \tag{3}$$

If the flux lines move due to this force, then current flow will become dissipative. This is because the movement of the flux lines at a velocity, v, and perpendicular to B will create an electric field per equation (4). This will be parallel to the transport current density, J, and therefore result in resistive loss.

$$E = v \times B \tag{4}$$

To prevent this dissipation the flux lines need to be pinned effectively at defects in the material. The total pinning force density, F_p, can be equated with the force experienced by the lattice to define the maximum current density, J_c, as shown in equation (5).

$$|F_l| = |F_p| = |J_c||B| \qquad (5)$$

The pinning force is dependent on the applied magnetic field such that if it reaches a certain value, the irreversibility field, H_{irr}, at a given temperature the critical current density falls to zero. It is this limit, rather than H_{c2} that determines the operating limits of type II superconductors. The different phases are shown schematically in Figure 11.
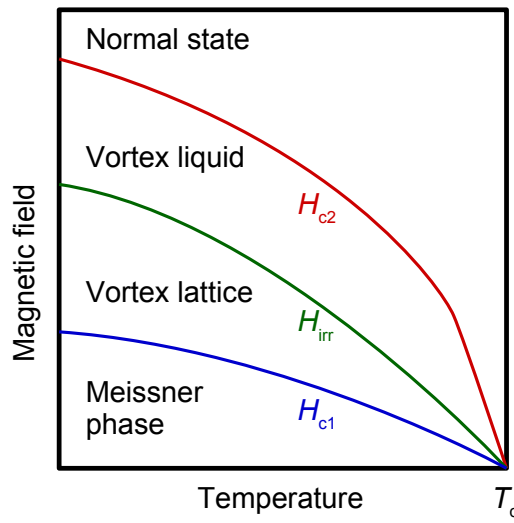
Figure 11. Schematic phase diagram showing how a type II superconductor responds to an applied magnetic field and temperature. In the vortex liquid phase the pinning force is zero and so the bulk critical current is zero despite it still being in the superconducting state. Adapted from [23].

Data for real superconducting materials are presented in Figure 12. The HTS materials Bi-2223 and YBCO have significantly lower H_{irr} than H_{c2} at 77 K, which limits their application in high fields at liquid nitrogen temperatures.
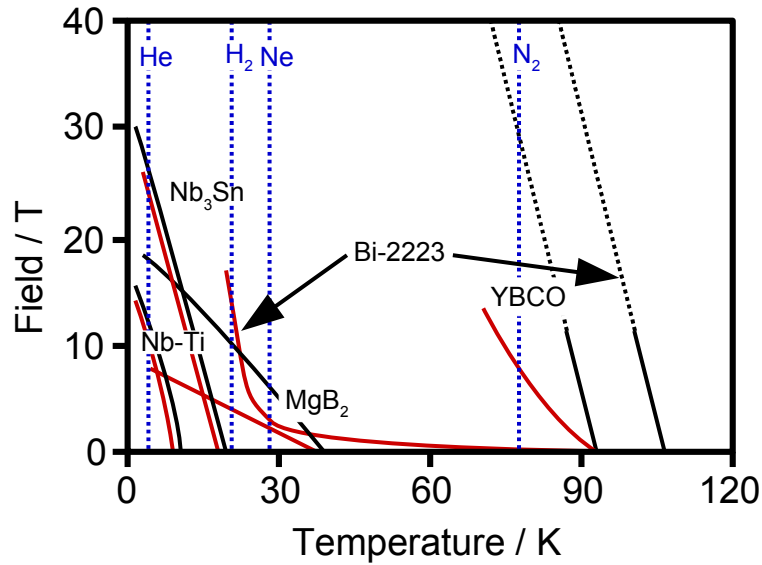
Figure 12. The temperature dependence of the critical field values for several superconducting materials. The irreversibility field, $\mu_0 H_{irr}$, is shown in red, upper critical field, $\mu_0 H_{c2}$, is in black and the vertical blue dotted lines are the boiling points of several cryogens. Redrawn from [32].

In contrast to the HTS materials both LTS materials Nb-Ti and Nb$_3$Sn have H_{irr} lines that are close to H_{c2}. This can be explained in part by comparing the anisotropy of the crystal structure. Both the niobium alloys are virtually isotropic, whilst MgB$_2$, Bi-2223 and YBCO are anisotropic. The anisotropy in REBCO materials is discussed further in section 1.1.3.1 but the key concept is that one of the crystallographic axes, conventionally labelled the c-axis, is significantly longer than the other two. Coupling along the c-axis across the CuO$_2$ planes through the Cu-O chains is not very effective due to the difference in coherence length and penetration depth parameters in the different crystallographic directions. The critical current density is much higher within the planes perpendicular to the c-axis and this significant anisotropy can lead to decoupling of the flux lines into pancake vortices. If these are not correlated effectively along the c-axis they experience weaker pinning forces and are more susceptible to thermally assisted motion and so the irreversibility field is significantly reduced [33].

Superconductors display a highly non-linear I–V characteristic when they pass through the critical transition, Figure 13.
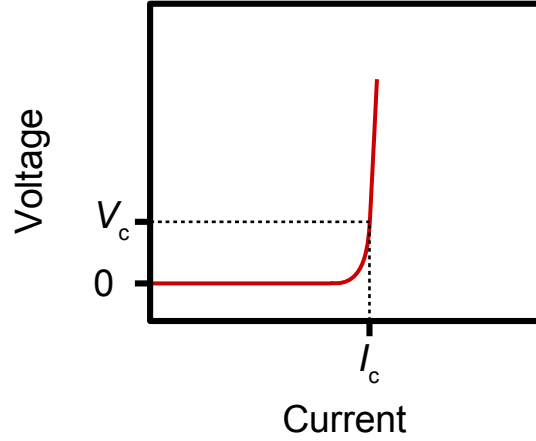
Figure 13. Schematic voltage-current characteristic of a superconductor as it passes through the critical current transition. The critical current, I_c, is typically defined by the current value when a voltage criterion, V_c, is reached.

The transition region can be described by a power law relationship, equation (6).

$$\frac{V}{V_c} = \left(\frac{I}{I_c}\right)^n \qquad (6)$$

Where I_c is the critical current and V_c is the critical voltage criterion. Commonly an electric field criterion of $E = 1$ μV cm^{-1} is used. The n-value provides a measure of the sharpness of the transition and typically REBCO coated conductors have n-values of 30–50 [34]. High n-values are generally desired because a conductor can operate closer to I_c without dissipative loss.

1.1.3 REBCO

(RE)Ba$_2$Cu$_3$O$_{7-x}$ (REBCO) materials where RE = Y, Nd, Pm, Sm, Eu, Gd, Dy, Ho, Er, Tm, Yb or Lu have some of the most impressive superconducting properties of all the HTS materials. The superconducting phase of these materials has an orthorhombic crystal structure as shown in Figure 14. The highest T_c and J_c are attained when the oxygen stoichiometry is just less than seven, i.e. 7-x, where x is typically 0.02-0.20 [35,36]. The superconducting properties are quite sensitive to the oxygen content and the transition temperature drops rapidly as x increases beyond ~0.2 and the material becomes non-superconducting when $x \gtrsim 0.7$.

The motivation for using REBCO in power applications becomes apparent when its critical properties are compared with other superconducting materials, Table 1. The primary benefit is the significantly higher T_c, which allows liquid nitrogen or even liquid hydrogen to be used as a cryogen rather than the much more expensive liquid helium. Also, if operating at

lower temperatures the critical current density and critical field are much greater than conventional low temperature superconductors. Additionally, compared with Bi-Sr-Ca-Cu-O compounds REBCO has a much greater H_{irr} at 77 K, see Figure 12 and Table 1.

Table 1. Superconducting properties for several materials. T_c and critical field data from [32]. Critical current references provided in table.

Material	T_c / K	$\mu_0 H_{c2}$ / T (4 K)	$\mu_0 H_{irr}$ / T	J_c / kA mm^{-2} (Temperature, Field) [Ref]
YBCO	92	>100	5–7 (77 K)	40 (4 K, 5 T ∥ c-axis) [37]
Nb-Ti 47wt%	9	12	10.5 (4 K)	2.3 (4 K, 6 T) [38]
Nb$_3$Sn	18	27	24 (4 K)	3 (4 K, 12 T) [39]
MgB$_2$	39	15	8 (4 K)	4.3 (4 K, 5 T) [40]
Bi-2223	108	>100	~0.2 (77 K)	4 (4 K, 5 T) [41]

Detailed HTS wire performance can be found at the public database compiled by Wimbush and Strickland [42,43]. Additionally, an up-to-date plot produced by Lee showing the in-field performance of the best wires constructed from different superconductors can be found at [44].

These impressive superconducting properties motivate the study of REBCO as a material for long length conductors for power applications. However, REBCO is an anisotropic, brittle ceramic where grain boundaries act as weak links. The origin of the difficulties and current progress in production of suitable conductors will be discussed in the following sections.

1.1.3.1 Anisotropy

As shown in Figure 14 the crystal structure of YBCO is anisotropic. The main consequence of this is the critical current density in the a-b planes, specifically the CuO$_2$ planes adjacent to yttrium, is much greater than along the c-axis. The intrinsic anisotropy in the coherence lengths, ξ^{ab}/ξ^c, is of the order 5–7 [45,46]. At low temperatures and fields the critical current anisotropy is of this order for single crystals but rises by an order of magnitude at higher temperatures [47].
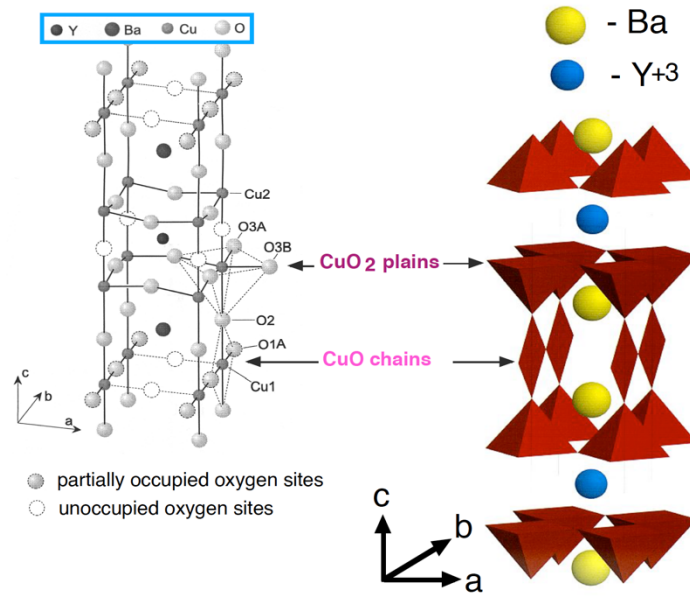
Figure 14. Crystal structure of orthorhombic YBCO showing the copper oxide planes and chains. From [24].

For the long length required for applications the use of single crystal REBCO is not feasible. The most successful method for producing long lengths of suitably textured REBCO is the coated conductor, which will be explained in more detail in section 1.2. Jia et al. [48,49] have found that in coated conductors the ratio of the critical current density in the a-b planes to the c-axis, J_c^{ab}/J_c^c, (77 K, self-field) ranges from 500-600 up to ~2000 in some cases. The higher degree of anisotropy compared to single crystals, and the difference between different coated conductors, are explained by the various microstructures and specifically the concentration of stacking faults present. Stacking faults act as pinning sites in YBCO and so can be deliberately encouraged to increase the in-plane critical current density. However, their geometry can then disrupt the current flow in the c-direction.

The critical current in the a-b planes is also affected by the angle of any external fields as shown in Figure 15. When the field is parallel to the a-b planes there is a significantly higher critical current than at other field orientations.
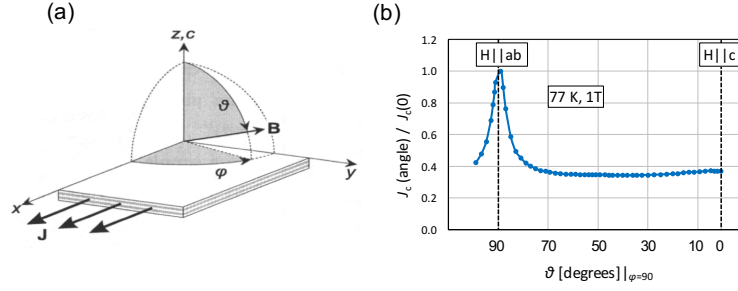
Figure 15. (a) Angular dependence of in-plane current density for a textured REBCO coated conductor. (b) Definition of the angle between external field and tape surface. There is a strong intrinsic peak when the external field is parallel to the a-b planes. Adapted from [37] and [24].

The anisotropy can be explained in terms of intrinsic pinning by weakly superconducting layers. As mentioned earlier, equation (5), the critical current is proportional to the pinning force on flux lines. When the applied field is an angle $\theta = 90°$, $\varphi = 90°$ and therefore parallel to the a-b planes the flux lines are pinned by the weakly superconducting layers between the strongly superconducting CuO_2 planes. Therefore, in crystals of REBCO the flux lines will be pinned along their entire length in this configuration and so the pinning force, and hence J_c, will be high [50]. In the absence of other, artificial, pinning additions the intrinsic peak dominates leading to a strongly anisotropic response to applied fields.

In general, however, the anisotropy is more complex and influenced by both angles θ and φ. When $\varphi = 0°$ and $\theta = 90°$ for example, Figure 16, the superconductor is in the "force-free" configuration and consequently the material can transport higher critical currents because the flux lines do not experience a force, if perfectly parallel to the external field [51–53].
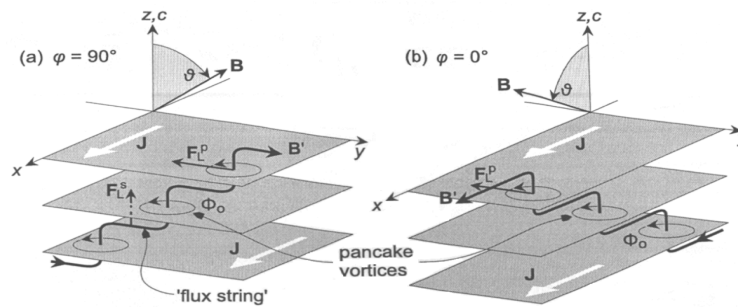
Figure 16. Diagrams showing the forces experienced by flux lines when (a) $\varphi = 90°$ and (b) $\varphi = 0$ in an anisotropic type II superconductor. From [24].

1.1.3.2 Pinning

The critical current density of REBCO is strongly dependent on the pinning of flux lines. Flux lines will be pinned by defects because the material in the flux core is normal rather

than superconducting and in a superconductor these regions will have a higher energy, part of which can be recovered if the region is defective [53–55]. Hence, defects represent local energy minima for flux lines. The size of the coherence length determines the length scale of effective pinning sites, Figure 10. In YBCO this is of the order 1.5 nm in the a-b planes but 0.3 nm in the c-axis.

As mentioned above the intrinsic pinning by the weakly superconducting layers can give acceptable critical currents for fields parallel to the a-b planes. However, in general the field will not necessarily be parallel to the a-b planes and for applications in high external magnetic fields increased J_c is required. Foltyn et al. [56] provide a comprehensive review of pinning in coated conductors.

1.1.3.3 Grain boundaries

The highly anisotropic nature of REBCO mean that grain boundaries behave as weak links. The current across a grain boundary drops exponentially with increasing misorientation angle for high angle boundaries and ~linearly for low angles (<2–5°) [57,58]. A plot of the critical current density for [001] tilt boundaries in YBCO is shown in Figure 17.
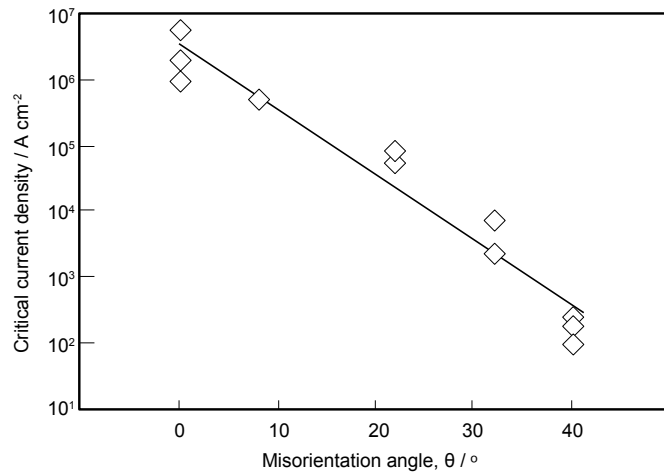
Figure 17. Exponential reduction in critical current density for large misorientation angles for [001] tilt boundaries in YBCO, measured at 77 K. Adapted from [59].

There are two predominant theories describing the cause of the exponential drop in current density: local strain [60] and charge carrier depletion [61]. The consequences of this are that any practical polycrystalline conductor must only contain low angle grain boundaries and therefore must exhibit a high degree of crystallographic texture.

1.2 Coated Conductors

To produce a highly textured REBCO conductor with sufficient strength and flexibility for cables is not trivial. The brittle nature of REBCO means traditional wire forming and drawing techniques are not suitable. To address the issues of texture, strength and flexibility the coated conductor architecture was developed [62,63], and quickly improved [64,65], and now critical current densities greater than 10^6 A cm^{-2} (77 K, self-field) are routinely reported [37,66,67].

The coated conductor concept is to grow a textured film of REBCO on multifunctional buffer layers that are supported by a metallic substrate, Figure 18. The superconductor typically makes up only ~1% of the wire thickness.

Silver cap layer ~2 µm

REBCO ~0.5-3 µm

Buffer layers ~0.2 µm

Metallic substrate ~30-100 µm
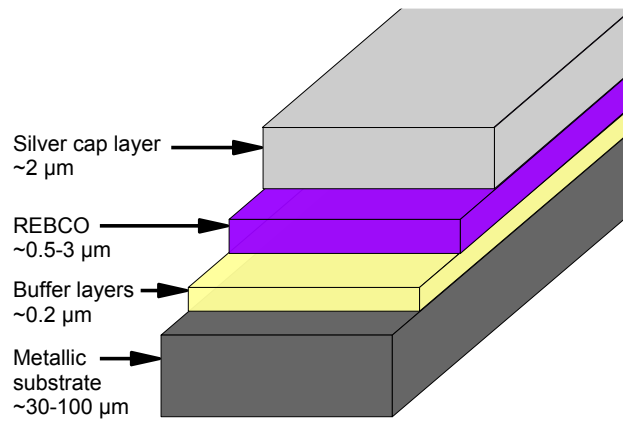
Figure 18. Schematic of coated conductor architecture. Typical widths are 4 – 12 mm. Dimensions not to scale.

The two dominate approaches to producing the textured buffered substrate that REBCO can be grown on are rolling assisted biaxially textured substrate (RABiTS) and ion beam assisted deposition (IBAD). In RABiTS texture is developed in the metallic NiW substrate through rolling and recrystallization. The addition of tungsten to nickel improves strength, oxidation resistance, percentage cube texture (up to ~5 at% W) and reduces the Curie temperature of the alloy, which is beneficial for AC applications.

In the IBAD approach a textured thin film of MgO is deposited on an untextured metal substrate, commonly Hastelloy (a Ni-Cr-Mo based non-magnetic corrosion resistant alloy) [68], using an ion beam to ensure the correct crystallographic texture. In both architectures, the metal substrates need to have low surface roughness. To achieve this, they can be electropolished prior to buffer layer deposition or, if the metal is untextured, the surface can be smoothed with "solution deposition planarisation". This is where repeated deposition

of an oxide precursor solution acts to smooth out asperities because the surface tension in the liquid leads to greater volumes of material in the 'valleys' rather than on 'peaks'. After several (~9 to 15) layers the surface roughness can be reduced by an order of magnitude [69].

The role of the buffer layers is to transfer the crystallographic texture to the growing REBCO film and prevent deleterious reactions between the metal substrate and HTS film. Multiple layers of buffer material are commonly used to achieve a graded lattice match with the REBCO and ensure epitaxial growth. For the REBCO deposition two main routes have been established: physical and chemical, which are discussed in the following sections.

1.2.1 Physical methods

The two most successful methods for physical deposition of the REBCO layer that are currently used by HTS tape manufacturers are pulsed laser deposition (PLD) and reactive co-evaporation (RCE).

1.2.1.1 Pulsed laser deposition

Pulsed laser deposition (PLD) is one of the most widely used methods for deposition of REBCO films, see Table 2. It allows the formation of complex oxides from stoichiometric targets. During deposition, a laser is focussed on a target (e.g. YBCO). This causes local heating and vaporisation and the ejected material forms a plume out from the target. The ejected material then deposits on the substrate, which is heated to help control film growth. There are several difficulties associated with PLD such as production of particles during ablation, high energy impacting species and complex atmospheric requirements. The presence of particles impacting the substrate, which may then cause defects in the film, can be minimised by careful control of the deposition geometry and the use of fully dense targets, whilst adjusting the pressure of the background gas in the chamber can reduce the high energy of depositing atoms that could otherwise cause defects [70]. However, the atmospheric requirements during deposition necessitate high capital cost equipment.

PLD also allows for the straightforward inclusion of nanoparticles that act as pinning centres. The relevant material can be included in the correct concentration in a single target, for example $BaZrO_3$ (BZO) and REBCO powders can be combined so that REBCO containing BZO nanoparticles grows [71].

1.2.1.2 Reactive co-evaporation

The principle in reactive co-evaporation (RCE) is for the material of interest to be heated, resistively or with an electron beam, such that atoms evaporate from the surface and deposit on the substrate. The low energy of depositing species requires vacuum conditions. An issue for the deposition of multicomponent oxides such as REBCO is that the vapour pressure of the components will not be equal from a single source. To avoid this several targets can be used and heated appropriately to give the correct ratios at the substrate. Metal targets are normally used, so an oxidant must be introduced to form the film and if the low partial pressure of oxygen is insufficient a different oxidant such as NO_2, O_3 or atomic oxygen can be used [70,72].

1.2.2 Chemical methods

The two main chemical methods for REBCO deposition are in-situ metal-organic chemical vapour deposition (MOCVD) and ex-situ metal-organic deposition (MOD). In-situ referring to case where the film grows as the species are deposited on the substrate whilst ex-situ involves deposition followed by a subsequent heat treatment to grow the textured REBCO.

1.2.2.1 Metal-organic chemical vapour deposition

Reactants are delivered to the substrate in the gas phase. The substrate is heated to control the film growth. An advantage compared with the physical deposition methods is that it does not require line of site and therefore does not suffer from shadowing. Additionally, the process does not require vacuum conditions and can be readily scaled up [73,74].

1.2.2.2 Metal-organic deposition

In MOD the deposition and film growth are separated into two separate processes: deposition and growth. The first stage involves a chemical precursor solution containing the required metal ions being deposited on the textured substrate before a controlled thermal treatment produces the REBCO film. There are several methods used for the deposition of the chemical solution including, spin, dip and slot die coating and inkjet printing. Spin coating is typically only used for research samples because the high angular speed that spreads the solution across the substrate surface is only suitable for short samples.

In dip coating the substrate is submerged then withdrawn from a bath of solution leading to a residual film on the surface. The thickness of the film is dependent on the withdrawal speed and solution rheology. The process is scalable but leads to material wastage

as both sides of the tape are coated. Additionally, the solution bath can become contaminated or suffer from solvent evaporation leading to variable rheology and subsequent film thickness. Slot die coating avoids these problem by enclosing the chemical solution reservoir and coating a single side only.

Inkjet printing is a scalable non-contact method for solution deposition that enables improved control and patterning during deposition. This flexibility to pattern the film during deposition is advantageous for reducing material waste and enables the possibility of more complex REBCO wire architectures than other methods. Inkjet printing technology and the its application in HTS coated conductor production will be discussed further in section 4.

1.2.3 Coated conductor manufacturers

There are, as of Autumn 2016, fifteen different manufacturers of REBCO coated conductor tape. The companies along with their location and preferred production route are given in Table 2.

Table 2. Location and preferred processing route for REBCO coated conductor manufacturers.

Manufacturer	Location	Substrate	Deposition method
AMSC	USA	RABiTS	MOD
SuperPower	USA/ Japan	IBAD	MOCVD
SuNAM Co. Ltd	Korea	IBAD	RCE
SuperOx	Russia/ Japan	IBAD	PLD
Fujikura	Japan	IBAD	PLD
Bruker HTS	Germany	IBAD	PLD
Theva	Germany	ISD*	RCE
STI	USA	IBAD	RCE
Shanghai Superconductor	China	IBAD	PLD
D-Nano (BASF)	Germany	RABiTS	MOD
Shanghai Creative Superconductor	China	IBAD	MOD
SAMRI/CAS	China	IBAD	MOCVD
Oxolutia	Spain	IBAD	MOD
Sumitomo	Japan	RABiTS	PLD
Metox	USA	RABiTS	MOCVD

*ISD = inclined substrate deposition. Similar to IBAD, except the angle of the substrate relative to depositing atoms is used to ensure textured film growth rather than a separate ion beam.

1.3 AC Applications

Superconductivity has numerous applications including: medical imaging, scientific analysis, transportation, devices and energy production, distribution and storage [24]. Power applications and machines are the primary focus of the current work, where AC losses complicate the use of HTS coated conductors [75].

The attraction of using HTS coated conductors is in the potential to save energy. Therefore, the total power losses, including the cooling factor, should be lower than in conventional conductors. Otherwise the HTS must offer an additional benefit that cannot be achieved with conventional materials, such as much higher power density in a motor or more compact dimensions that allow upgrade of underground distribution cables. The latter is particularly applicable in major cities where space is severely limited or large-scale

underground work would be prohibitively expensive and disruptive. AC loss is a concern for motors and generators due to the higher magnetic fields experienced than in the other power applications discussed, Figure 19.
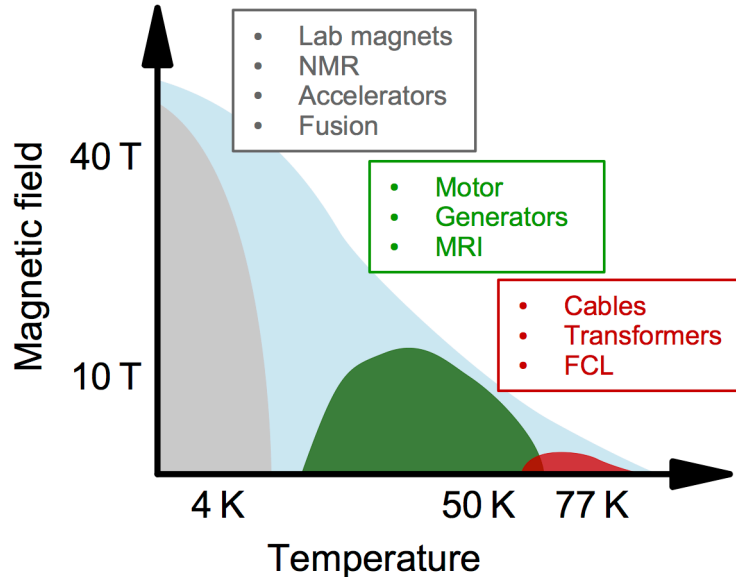
Figure 19. Schematic illustrating the magnetic field and temperature ranges for different large-scale applications for HTS. The green and red regions highlight the conditions of interest for the applications discussed below.

1.3.1 Cables

Power distribution cables need to carry high currents with minimal resistive losses. Superconductors have lower resistive losses than traditional materials meaning lower voltages can be used. HTS cables can be routed underground and can be isolated systems, with minimal thermal or electromagnetic influence on their surroundings. There are several demonstration installations of HTS cables being integrated with power grids [76–79], with a notable example being the "AmpaCity" project in Essen, Germany [80]. This is currently the longest grid level HTS cable installation worldwide and incorporates a HTS fault current limiter. Whilst most demonstration installations use Bi-2223 some of them are being upgraded to use REBCO coated conductors such as in Long Island, USA [81]. REBCO coated conductors have the advantage of reduced silver usage and lower AC losses [82], which are critical if HTS cables are to make a significant impact in power distribution.

HTS are also under consideration for use in high voltage direct current (HVDC) cables [83,84]. This would have the advantage of inherently lower losses and reduced cryogenic load. However, the power distribution network functions primarily with AC

generation and so integration with existing infrastructure is prioritised. In the future DC transmission may become more popular with the rise in decentralised energy generation that naturally generate DC power, such as solar cells and fuel cells.

1.3.2 Fault current limiters

Fault current limiters (FCLs) are required in grid systems to minimise damage to the grid in the case of fault [24]. This is particularly relevant for distributed generation and interconnected grids where faults need to be isolated from the rest of the grid without having to upgrade the entire system of circuit breakers every time a new connection is made. They limit the current without complete disconnection and are designed to respond very rapidly. A FCL needs to have a very low impedance during regular operation but a very high impedance during fault current conditions, Figure 20.
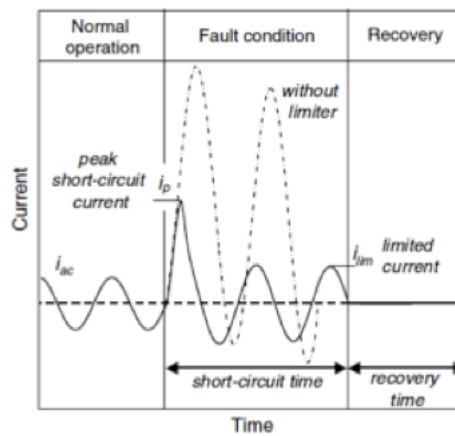
Figure 20. Schematic showing the current response with and without a FCL. The FCL experiences a rapid transition to high impedance during a fault situation, limiting the magnitude of the current. From [24].

There are two main types of superconducting FCL (SFCL), resistive and inductive [85]. Resistive SFCLs have a superconductor in parallel with a high impedance shunt. During normal operation, the impedance is very low, however, when a fault current occurs the superconductor quenches and the current is limited by the impedance of the shunt. Drawbacks of this design include heat leak from the current leads, AC loss in operation and recovery time required following HTS quench. However, their simplicity, compactness and fail-safe nature are significant advantages.

Inductive SFCLs work by either shielding or saturating iron cores. In the first type a superconducting cylinder shields a primary coil carrying the current of interest from an iron

core. When a fault current develops and the magnetic field exceeds that required to fully penetrate the HTS and the impedance increases sharply. This design still suffers from AC loss in the HTS cylinder but has a simpler cryogenic arrangement. However, the iron core leads to a much bulkier size than a resistive type. In the saturated core design a DC current in a superconducting winding saturates two iron cores that each have a copper winding around them. In regular operation, the copper windings have a low impedance but if a fault current occurs the iron cores are driven into the high permeability region of the magnetisation curve, significantly increasing the coil inductance. This design, in contrast to the others described, does not lead to a quench in the HTS material and therefore benefits from a very rapid recovery time. Additionally, the superconductor only experiences a DC current so experiences lower losses. The requirement of using superconducting material is simply to maintain acceptable losses whilst passing sufficient current to saturate the iron cores. As with the other inductive type limiter the cryogenic design is simpler but the size is much larger than comparable resistive devices [86].

1.3.3 Transformers

Like power cables, the windings of a transformer need to carry high current densities with minimal losses. However, due to the higher magnetic fields experienced by the material successful methods to reduce AC loss are even more important. Despite the high efficiency of conventional transformers, replacing copper with HTS can yield several advantages. Typically reducing the size of a transformer reduces its efficiency, however, with a superconducting transformer significant savings in mass and volume, by a factor of ~3 and ~2 respectively, can be achieved whilst improving on already high efficiencies. Additionally, the replacement of oil with liquid nitrogen as a coolant and dielectric is environmentally beneficial and much safer when considering fire risk. Furthermore, superconducting transformers can cope with overcurrent loads without insulation degradation and can display inherent resistive SFCL behaviour [87].

Due to the cryogenic load only HTS materials are economically suitable for transformer applications. Demonstrations of transformers using Bi-2223 [88] and more recently REBCO [89] have shown that the performance can improve on conventional technology. However, a significant challenge that remains is the cost of HTS wire.

1.3.4 Motors and generators

Motors and generators convert between mechanical and electrical energy. Their size is dependent on the torque, which is proportional to the product of current density in the armature and the magnetic flux density seen by the current. Increasing either of these properties by using superconductors will reduce the size or weight of a rotating machine. Superconductors can carry current densities several orders of magnitude higher than copper, 2 kA mm^{-2} c.f. 2–10 A mm^{-2}, and can generate magnetic flux densities much higher than permanent magnets [90]. The higher power density available from superconducting motors means they can act as an enabling technology for future electric aircraft [91].

Furthermore, lower resistive losses improve efficiency, though this is more important for very large machines. Machines based on low temperature superconductors have been demonstrated and perform well [92], however, at the low operating temperature AC losses become more problematic, due to lower heat capacity. It is the improved thermal stability, leading to greater reliability and simplified cryogenic design, that is the main advantage of using HTS in motors and generators. Several HTS demonstrators have been produced in various configurations including Bi-2223 windings and REBCO bulks and there is work to upgrade and design systems using REBCO coated conductors [93–95]. However, as with several of the other applications mentioned in this section, two of the key materials challenges for widespread adoption of HTS rotating machines are cost of the conductor and AC losses.

1.4 Reducing AC losses in coated conductors

As mentioned superconductors only have zero electrical resistance in DC operation. The hysteretic motion of magnetic flux during a cycled external or self-field leads to energy loss. Additionally, the energy loss increases the cryogenic demand of the system. This is more problematic when very low temperatures are used because the heat capacity of materials is much lower. The low heat capacity reduces the stability of the superconductor meaning it is more susceptible to small thermal fluctuations and more likely to quench. A recent review by Grilli and Kario [96] provides an excellent summary of methods to reduce AC losses in coated conductors.

1.4.1 Sources of loss

There are three main sources of AC loss in coated conductors: magnetisation, coupling and eddy current losses. The dominant mechanism will depend on the frequency, magnetic field and conductor properties.

1.4.1.1 Magnetisation loss

The motion of flux through the superconducting layer is a dissipative process. The magnitude of the hysteresis is proportional to the area of the magnetisation loop, Figure 21, which in turn is proportional to the size of the superconductor.
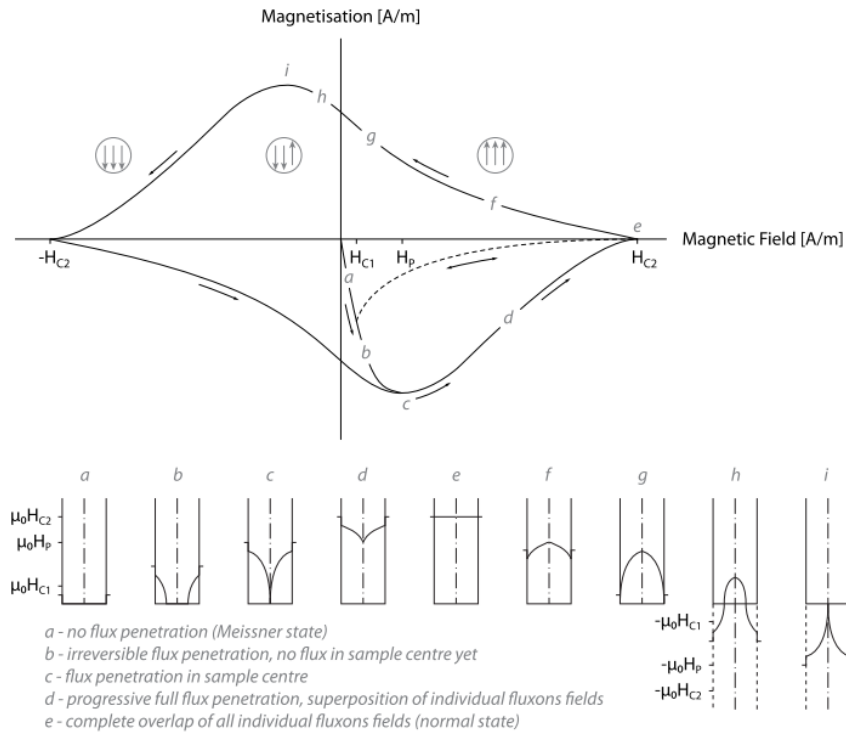
Figure 21. Schematic magnetisation loop for a type II conductor and corresponding magnetic flux profiles for a superconducting slab during a cycle of changing external magnetic field. From [24] and [29].

A simplified picture can illustrate the size dependence of the hysteresis. Consider the Bean model for a superconducting slab [97] where a changing magnetic field induces a current of $\pm J_c$. This model ignores the dependence of J_c on field but still illustrates the size dependence of the hysteresis loss for the situation where the field is perpendicular to the current in the superconductor, such as when the field is perpendicular to the flat face of a coated conductor. Consider two samples: a slab of width $2a$ and the same divided into two separate slabs each of width a, as in Figure 22.
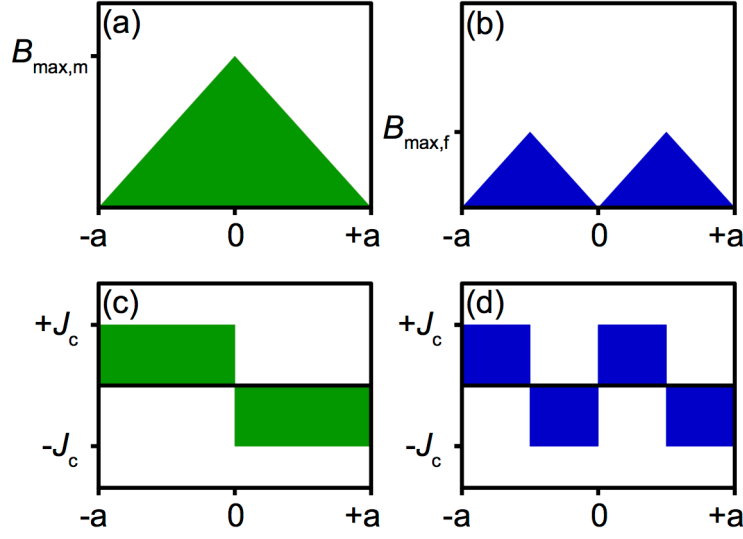
Figure 22. Schematic illustrating the Bean model for a superconducting slab. (a) and (b) show the trapped flux for a slab of width $2a$ and 2 slabs each of width a respectively following magnetisation with a field $> 2B_{max}$. (c) and (d) show the currents induced by the magnetisation.

The hysteresis loss is proportional to the change in magnetisation during a full cycle, which in this simplified model is proportional to the magnetic flux within the superconductor. This change in flux, and therefore loss, is proportional to the green and blue areas in Figure 22(a) and (b). Dividing the superconductor into two reduces the hysteretic loss by the same factor when external magnetic fields are high enough to fully penetrate the superconductor.

The thin film geometry of coated conductors means that relatively low magnetic fields can fully penetrate them when the field is perpendicular to the tape face, leading to high magnetisation losses. Brandt and Indenbom [98] derived analytical equations to describe the magnetisation of thin superconducting strips in a perpendicular field. The energy loss per unit length per cycle for a thin superconducting strip of width $2a$ subject to a sinusoidal external magnetic field is given by equation (7).

$$Q = 4\mu_0 a^2 J_{cs} H_a \left(\frac{2J_{cs}}{\pi H_a}\right)\left\{\ln\left[\cosh\left(\frac{\pi H_a}{J_{cs}}\right)\right] - \tanh\left(\frac{\pi H_a}{J_{cs}}\right)\right\} \tag{7}$$

Where μ_0 is the permeability of free space H_a is the amplitude of the applied field and J_{cs} is the critical sheet current density ($J_{cs} = I_c/2a$). The loss is proportional to the square of the width, therefore, dividing the superconductor into N filaments should reduce the total loss by

a factor of N. The validity of the expression and consequent reduction in AC loss, for fields that fully penetrate the conductor, has been well verified, for example Figure 23 [99].
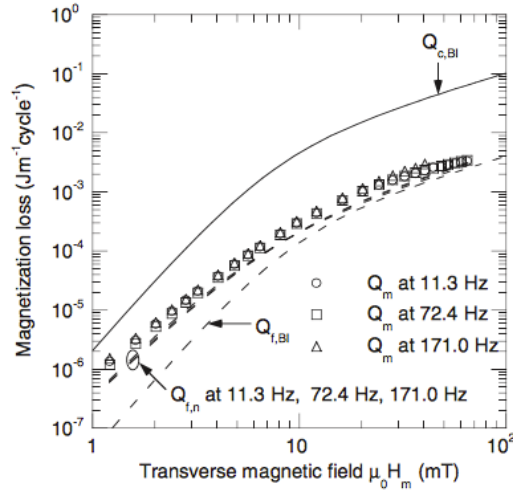
Figure 23. The measured magnetisation loss (Q_m) for a striated sample and comparison with the Brandt-Indenbom model for non-striated ($Q_{c,BI}$) and striated ($Q_{f,BI}$) cases and a numerical model ($Q_{f,n}$). The samples showed the expected reduction in magnetisation loss. There was good agreement between the experimental results, Brandt-Indenbom model and numerical model when the applied magnetic field was greater than the penetration field. From [99].

1.4.1.2 Coupling loss

The striation of a coated conductor into filaments is only effective at reducing the AC losses if the filaments are electromagnetically uncoupled. When filaments are coupled, electrical currents can be driven across the normal material between filaments leading to losses. These can be reduced by ensuring electrically resistive barriers between filaments and preventing coupling via the current lead contacts by twisting or transposing the filaments.

1.4.1.3 Eddy current loss

Eddy current losses occur in the normal metal components of the coated conductor and are inversely proportional to the resistivity of the material and proportional to the square of the width. Hence, it is advantageous to striate the stabilizer on the coated conductor due to its low resistivity. The substrate will also contribute to eddy losses but is usually insignificant due to the high resistivity of the alloy.

1.5 Filamentary conductors

Division of coated conductors into filaments to reduce AC loss was first proposed by Carr and Oberly [100]. Since then several techniques for dividing the superconductor into

separate filaments and reducing the coupling between them have been demonstrated and are summarised below.

1.5.1 Mechanical striation & punching

Using mechanical striation to divide the superconducting layer in to separate filaments has been successfully demonstrated by Kesgin et al. [101] using a diamond scribe. Mechanically removing the buffer layer before REBCO deposition and growth has also been demonstrated by Majkic et al. [102]. The removal of the buffer stack caused the REBCO layer to become contaminated and not textured above the striated regions leading to well separated filaments. Ashworth and Grilli [103] demonstrated the use of longitudinal and transverse 'cross cuts' to produce separated and decoupled filaments. The transverse cuts were bridged with normal metal and allowed magnetic flux to enter between the filaments. This technique introduces ohmic losses but this was compensated for by the reduction in hysteretic losses.

Another technique that mechanically divides the superconductor into separate filaments is the Roebel cable. This approach, first demonstrated by Goldacker et al. [104], has the added benefit of producing a conductor where the individual filaments undergo transposition. Additionally, cables that can carry larger currents than single tapes are required for power applications so an intrinsically low AC loss approach is beneficial. Goldacker et al. [105] also provides a recent review of Roebel cables fabricated from coated conductors and they will be further discussed in section 2.1. Briefly, the technique involves mechanically punching out trapezoid shaped sections of the HTS tape on alternating sides, as shown in Figure 24. The remaining meandering strands are then stacked together so that they interlock and the current along each strip follows a twisted path.
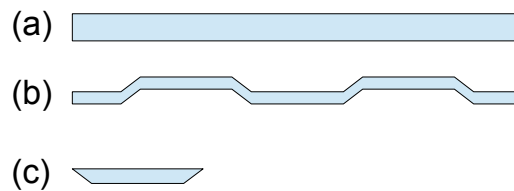
Figure 24. Schematic plan view of (a) a length of coated conductor tape, (b) tape following the punching process to give a meandering strand and (c) a waste offcut piece.

Despite the advantages of this approach for producing a low AC loss cable from coated conductor the significant disadvantage is the substantial loss of expensive

superconducting material. An approach to utilize this waste material is demonstrated and developed in section 2.

1.5.2 Chemical etching

Photolithography and etching of the tape has been demonstrated using dry [106] and wet chemical methods [107]. The method is effective at dividing the tape but leads to relatively large gaps, ~100–400 μm compared with <100 μm for alternative techniques. Additionally, when wet chemical etching is used the I_c degradation is more severe, possibly due to uncontrolled chemical attack of the REBCO layer.

A novel alternative method demonstrated by Wulff et al. [108] involves etching the substrate before functional layer deposition. The technique called "two level undercut-profile substrate" (2LUPS) involves selectively etching alternating tracks into the substrate. The resulting structure has 2 levels of flat surface on which to deposit the textured buffer and superconducting layers, see Figure 25 for a comparison between the 2LUPS and standard striation architecture. The curved surfaces between the filaments prevent successful deposition of superconducting REBCO in these regions whilst the undercut means the full width of the tape can be used in current transport.
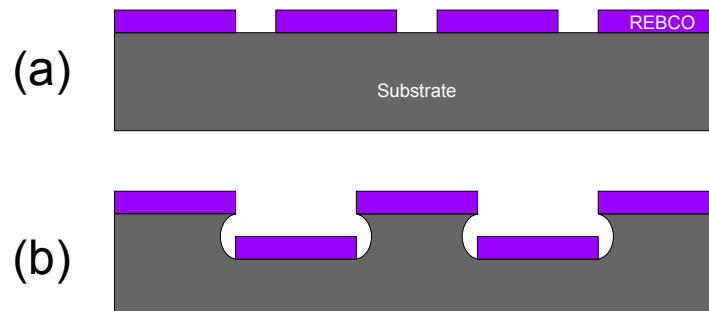
Figure 25. (a) Schematic cross-section for standard striated tape and (b) diagram of the "2LUPS" coated conductor design. Superconducting REBCO only grows successfully on the flat surfaces leading to separated filaments that use the full width of the substrate to transport current.

1.5.3 Laser scribing

One of the most popular methods for striating coated conductors is by using a laser to ablate material. The precision of the non-contact technique enables many fine filaments to be produced, with one hundred filaments per cm-width feasible [109]. However, when many fine filaments are produced the total current carrying capacity drops more rapidly than

expected due to defects preventing a percolative current path. Therefore, there is only a benefit in producing very fine filaments if there is some degree of current sharing via bridging, which will be discussed further in section 3.5.

Laser striated tapes often show higher than expected coupling losses due to re-deposition of the ablated material in the grooves [110,111]. The connection of filaments by low resistance paths leads to more substantial coupling losses. Levin et al. [112] demonstrated reduced coupling losses by performing an oxidation heat treatment on the striated tapes, which has since been scaled up to long lengths of coated conductor effectively [113]. Alternatively more substantial grooves can be cut [99] or a subsequent chemical etching performed [114] to achieve the desired reduction in coupling loss. The higher electrical resistance of the oxidised grooves also enable selective electroplating of copper stabilizer following striation [115].

Laser striated coated conductors have also been used as strands for cables that provide transposition such as Roebel [116] and conductor on round core (CORC$^{®}$) [117–119]. The Roebel cables constructed from striated strands, Figure 26, did show lower AC loss but not the full N-fold (for N filaments) reduction that might be expected. This is possibly due to the cabling not providing any further transposition than that for the strands themselves and hence some coupling between filaments occurred. CORC$^{®}$ type cables made with filamentary tapes did show the expected lower AC loss. However, it was noticed that outer filaments were coupled by the stabilizer that extended over the back surface of the tape and so to achieve the expected AC loss reduction this also had to be removed. Additionally, striation through the relatively thick copper stabilisation resulted in higher laser powers being required and the degradation of the total tape I_c.
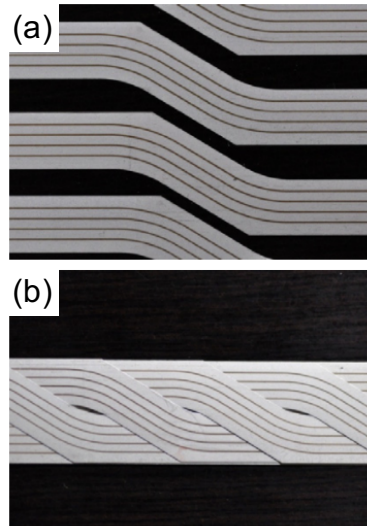
Figure 26. (a) Laser striated Roebel strands and (b) the same strands assembled into a cable. From [116].

1.5.4 Inkjet printing

Inkjet printing is a deposition technique that enables filaments to be formed directly during production rather than via a post-processing step. It has primarily been used in conjunction with the MOD processing route with the precursor solution deposited in a suitable pattern directly on the textured substrate. An overview of the types of inkjet printing technology that are suitable for filamentary HTS deposition will be given in section 4.1.

List et al. [120] produced directly printed filaments on RABiTS. However, it was found that the AC losses were not as low as anticipated [121] and this was ascribed to filament coupling. However, it may have also been due to inhomogeneous lateral current distribution. The analytical expressions for AC loss reduction scaling with filament width assume homogeneous current distribution and when this is not realised in practice losses can be higher than expected [122,123]. It was noticed by Duckworth and Rupich [124] that lateral thickness variations lead to non-uniform I_c across the filaments and due to the difficulty of optimising the heat treatment process for different thicknesses of film. Additionally, "undulations" in the width along the filament length were also found to contribute to the higher-than-expected losses. This was determined by fabricating two analogous laser striated samples with constant and undulating filament widths.

To minimise the issue of thickness variation across the width of directly printed samples an alternative method of "inverse printing" has been proposed [125]. The concept is to deposit a compatible, non-conductive barrier material that then prevents well textured

REBCO from forming in those regions and leads to separate superconducting filaments with a more uniform thickness. This process has been demonstrated in two ways, one using a fully printed superconductor structure [126] and also by just printing the barrier strips then growing the REBCO layer using MOCVD [127]. With both techniques, the total current capacity of the striated tapes was lower than the expected value considering the reduction in current carrying area alone. This was ascribed to non-optimum deposition and growth conditions. Further research on inkjet printing of REBCO coated conductors including discussion of more complex architectures will be presented in section 4.

1.6 Summary & section overview

In this chapter, a brief history and overview of superconductors has been given followed by a summary of the 'coated conductor' method for producing HTS conductor tapes that can carry high critical currents. The current variety of production routes has been described and relevant large scale applications discussed. The problem of AC losses was highlighted and the various methods to reduce the losses by producing filamentary structures were presented.

As mentioned in the preface, two of the most significant challenges to the widespread adoption of HTS coated conductors in large-scale applications are the relatively high production costs and the high AC losses inherent with the flat tape architecture. The chapters in section I will investigate three possible ways to address these problems:

- Chapter 2 will demonstrate how the waste, offcut material produced during the manufacture of Roebel cables can be used usefully to produce trapped field magnets. This should effectively reduce the cost penalty and the main disadvantage of the Roebel cable design.
- Chapter 3 will illustrate a cost-effective method for producing filamentary tape using a spark-discharge to create resistive striations for low AC loss tapes.
- Chapter 4 investigates the use of inkjet printing to produce patterned, filamentary coated conductors in a low cost, scalable way with potential to produce more sophisticated low-AC-loss architectures without significant increases in cost.

2 ROEBEL CABLES AND UNIFORM TRAPPED FIELDS

Parts of the work presented in this chapter also appear in the following publications:

[128] **T.B. Mitchell-Williams**, A. Patel, A. Baskys, S.C. Hopkins, A. Kario, W. Goldacker, B.A. Glowacki, Toward Uniform Trapped Field Magnets Using a Stack of Roebel Cable Offcuts, IEEE Trans. Appl. Supercond. 26 (2016) 6800404. doi:10.1109/TASC.2016.2518994.

and

[129] **T.B. Mitchell-Williams**, A. Baskys, S.C. Hopkins, V. Kalitka, A. Molodyk, B.A. Glowacki, A. Patel, Uniform trapped fields produced by stacks of HTS coated conductor tape, Supercond. Sci. Technol. 29 (2016) 85008. doi:10.1088/0953-2048/29/8/085008.

2.1 Roebel cable concept

The Roebel cable, named after its inventor Ludwig Roebel, has existed for over 100 years and is the standard design for low AC loss windings in large conventional motors and generators. Hussennether et al. [130] demonstrated the concept with a HTS Bi-2223 cable and Goldacker et al. [104] produced the first Roebel cable constructed using REBCO coated conductor tape. As mentioned in section 1.5.1 the concept for producing a Roebel cable using coated conductor tape is to mechanically punch out trapezoid segments leaving behind a meandering tape strand that can be stacked with others to produce a cable where the current paths will follow a twisted path, Figure 27.

(a)

(b)

(c)

(d)
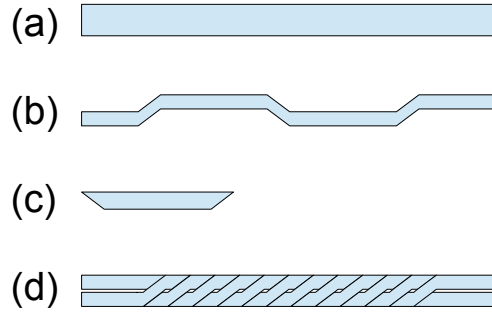
Figure 27. Schematic showing (a) original tape, (b) mechanically punched strand with a meandering current path, (c) the shape of the waste offcut pieces produced and (d) the resulting interlocking transposed cable produced by stacking several strands together appropriately.

2.2 Utilising waste material

It is apparent from Figure 27 that a significant portion of the superconducting tape, approximately 50%, is wasted when a Roebel cable is produced from a coated conductor. This increases the cost per kA·m by reducing the quantity of superconductor that can carry current in the final cable. If there is a use for the offcut material, however, then the drawback of materials waste and consequent cost increase will be mitigated to an extent. The following sections describe how these offcut pieces can be used to form trapped field magnets.

Superconductors can act as trapped field magnets when magnetised by applying and removing an external magnetic field. The changing magnetic field induces currents in the superconductor according to Faraday's law of induction, however, due to zero electrical resistance in the superconductor the current can circulate persistently and produces its own 'trapped' magnetic field. This effect has been demonstrated with both bulk pseudo-single crystal superconductors and with stacks of superconducting tape. The resulting current loops are shown schematically in Figure 28.
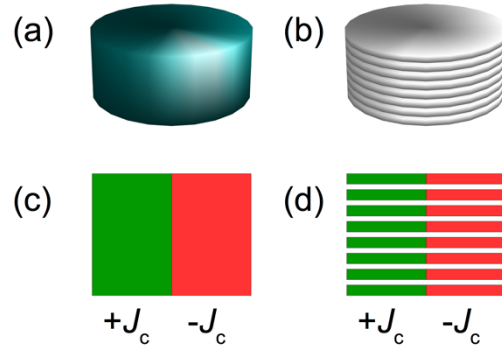
Figure 28. Schematic for (a) a bulk superconductor and (b) stack of tapes machined into a cylinder. Cross-sections illustrating the resulting current loops, assuming the critical state model, following magnetisation for (c) a bulk and (d) stack of tapes. Current flow is perpendicular to the plane of the page. The resulting trapped magnetic field will have a conical profile.

2.3 Uniform trapped field profiles

Spatially uniform trapped fields are required for a new generation of small-scale NMR/MRI devices. Large-grain bulk superconductors can trap high magnetic fields and the profile can be adjusted using soft ferromagnetic materials [131]. The conical trapped fields produced by bulk superconductors, or stacks of tape where there is no misalignment between tape layers, is highly non-uniform. This is due to the nature of macroscopic current loops circulating around the whole sample, throughout the sample cross-section, unlike the case of a permanent magnet, which can be described by an array of small current loops equivalent to only a *surface* current around the whole sample. Therefore, conventional bulk superconductors and conventional stacks of tape, although good at producing high fields, are fundamentally not suited to producing spatially uniform trapped fields. However, ring shaped bulks and stacks of tape samples have been used to generate uniform fields in a similar manner to a coil. Hahn et al. have investigated the use of stacks of 40 mm square tape annuli with a 25 mm bore for use in a compact NMR device [132,133] and similar experiments have also been done using bulk YBCO/GdBCO rings [134,135]. An alternative approach, presented here, seeks to replicate the properties of permanent magnets using trapped field stacks of tape to generate uniform fields. Selva et al. [136] have shown that stacked arrays of tape can yield more uniform trapped field profiles than previous stacks over a larger area but clear undulations in the fields would be a problem for an NMR device. The purpose of this work was to investigate new arrangements that are fundamentally better suited to producing more uniform trapped fields including a novel angled stack arrangement.

12 mm square stacks of superconducting tape have been established as efficient trapped field magnets with fields of up to 13.4 T recorded when field cooled due to the persistent currents set up in the tape layers [137]. They have also been shown to be advantageous compared to bulk superconductors when pulse magnetised at low temperature due to their higher thermal stability [138,139].

2.3.1 Roebel cable offcuts

2.3.1.1 Superconducting tape

Superconducting tape from SuperPower (12 mm wide, 0.096 mm thick, 325 A $I_{c,sf}$) was used to make a Roebel cable. The offcuts stamped out during manufacture were trimmed to enable easy handling as shown in Figure 29.
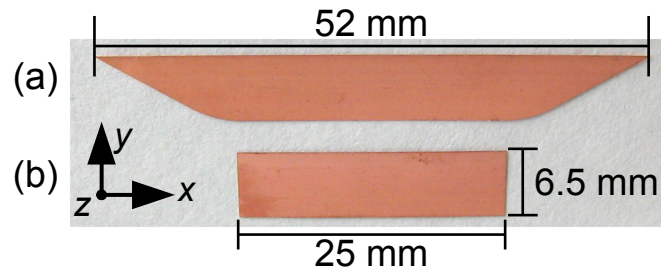
Figure 29. Top view of offcut piece from Roebel cable manufacture (a) before and (b) after trimming.

2.3.1.2 Stacking configurations

Initially several different stacking arrangements were tried to determine how the stacking influenced the trapped field profile. The offcut pieces were stacked in 5 different arrangements as shown schematically in Figure 30. with the new angled arrangement shown in Figure 30(e).

(a) 4A

(b) 4A1P

(c) 2LHO

(d) 4LHO

(e) AS
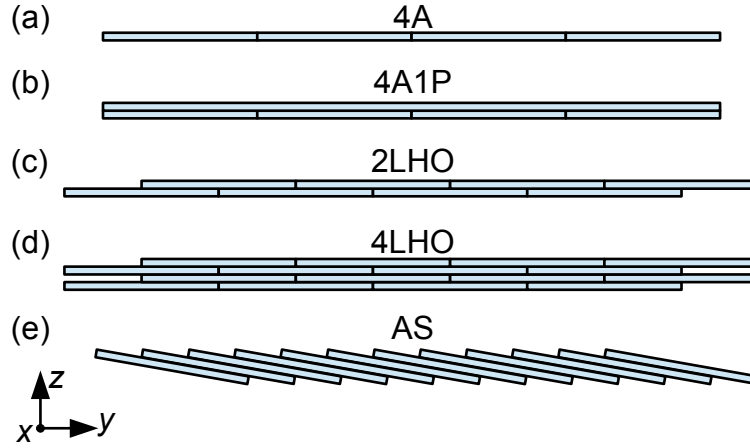
Figure 30. Schematic of tape stacks in cross section, not to scale. The majority of the tape pieces had their thickness parallel to z, their width parallel to y and length parallel to x. The primary Hall scan direction was parallel to y. (a) 4 adjacent pieces, (b) 4 pieces with 1 perpendicular, (c) 2 layers half offset, (d) 4 layers half offset, (e) angled stack. The angled stack was made of 27 tape pieces, each offset by 1 mm relative to adjacent pieces.

The trapped field profile for a rectangular piece of tape has a "rooftop" shape (approximately a triangular prism), with good uniformity parallel to the long axis [140]. Therefore, the interest was to find a stacking arrangement that extended the uniformity in the direction parallel to the tape width (in the y direction). Hence, configurations using overlapping tape pieces to smooth out the profile were investigated to replicate the array of magnetic dipoles responsible for permanent magnet fields.

The flats stacks, Figure 30(a)-(d), were held in place during cooling, magnetisation and measurement using Kapton® tape and vacuum grease. The angled stack, Figure 30(e), was made from 27 pieces of tape and constructed using a custom-built aluminium holder. The tape pieces were offset by 1 mm with respect to their neighbours and the pieces were at an angle of 5.7° to the horizontal.

2.3.1.3 Scanning Hall probe magnetometry

Scanning Hall probe magnetometry enabled the trapped magnetic field profile to be mapped as a function of position. The tape stacks were zero-field-cooled to 77 K in liquid nitrogen before being magnetised in an applied field of 0.20 T ramped at a rate of 6.25 mT s^{-1}. The Hall probe (Toshiba THS118) was scanned using a bespoke stage controlled by in-house software. The probe control current was nominally 5 mA and the sensitivity 1.18 V T^{-1}. The scan was started 300 s after magnetisation to ensure flux creep did not

significantly affect measurements. The trapped field was measured 2.15 mm above the sample surface. The scan step size was 0.25 mm in the y direction and 0.5 mm in the x direction.

2.3.1.4 Measured trapped field profiles

To quantify the uniformity of the trapped magnetic field a 'profile roughness' (R_{rms}) metric was developed. This was calculated in an analogous way to root-mean-square surface roughness for materials and gave a measure of the average variation away from the mean trapped field; the mathematical definition of this metric is given by equation (9), below. The ratio of the roughness to the mean trapped field was used to compare the relative roughness of stacks containing different numbers of tape pieces. The results for each of the stacking configurations are summarized in Table 3.

The profile roughness, R_{rms}, and mean trapped field, B^*, were calculated in the following way. The data were selected from a central region to avoid the end-effect peaks dominating the result. The regions of interest are shown in Figure 31. The mean trapped field and roughness were calculated using data between Y_s and Y_f in the region marked αL in Figure 31. In the current work $\alpha = 0.5$. The mean trapped field, B^*, for the n data points between Y_s and Y_f is given by equation (8).

$$B^* = \frac{\sum_i^n B_i}{n} \tag{8}$$

Where B_i is an individual data point in the sampled region. The profile roughness, R_{rms}, is given by equation (9).

$$R_{rms} = \sqrt{\frac{\sum_i^n (B_i - B^*)^2}{n}} \tag{9}$$
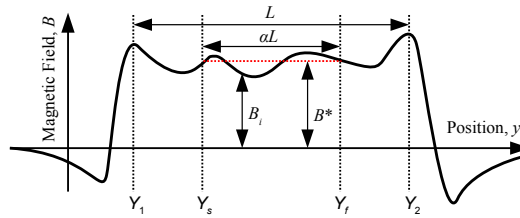
Figure 31. Schematic magnetic field profile showing the data range sampled. Y_1 and Y_2 correspond to the positions of the end-effect peaks. Data between Y_s and Y_f were used for analysis. The mean trapped field, B^*, is for the data sampled. In the current work $\alpha = 0.5$.

Table 3. Trapped field profile roughness data for stacks produced from Roebel offcuts.

Sample	Mean trapped field, B^* (mT)	Profile roughness, R_{rms} (mT)	Ratio, R_{rms}/B^* (%)
4A	1.73	1.00	57.7
4A1P	5.80	1.14	19.7
2LHO	3.73	0.39	15.8
4LHO	7.04	0.49	7.0
AS	8.52	0.31	3.7

With no overlap between adjacent pieces as for sample 4A, the trapped magnetic field profile had a pseudo-sinusoidal shape as can be seen in Figure 32. The peaks corresponded to the centre of the tape pieces and the troughs to the edges. When a tape piece was added with the long axis parallel to the scanning direction, as for sample 4A1P, the magnitude of the trapped field increased but the amplitude of the variation across the sample remained similar. In contrast when 2 layers of tape were offset by half a tape width, sample 2LHO, the mean trapped field was not increased as much but the profile was smoother. Adding an additional 2 layers to form configuration 4LHO resulted in a similar R_{rms} to 2LHO but an increased trapped field. The angled stack, AS, had the highest trapped field and smoothest profile.
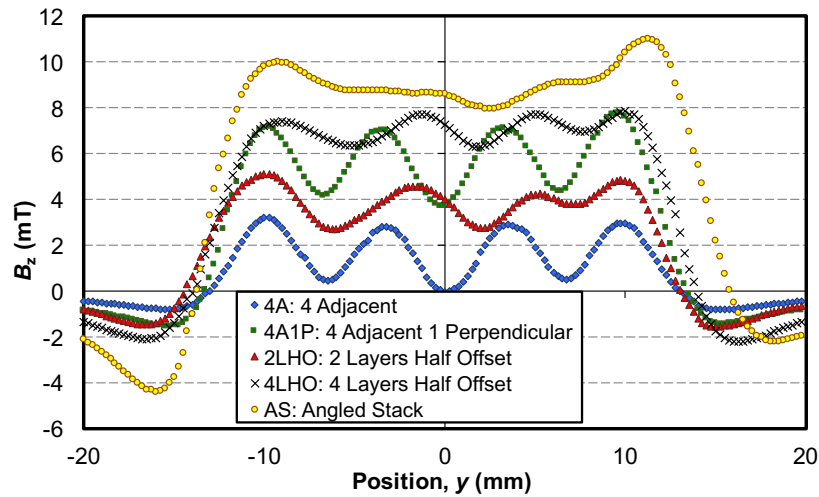
Figure 32. Trapped magnetic field profiles for each of the stacking configurations. The field was measured 2.15 mm above the top surface of the stacks. All measurements at 77 K.

The undulations seen in the 2LHO and 4LHO have 2 primary contributions; the relative height difference of the offset layers and small misalignments and non-uniformities in

the tapes. Although the latter contribution has the potential to be eliminated, the former, however, is a fundamental feature of the stacking arrangement and will always lead to some profile undulation as discussed through modelling in the next section.

The dip in the field profile at +3 mm in Figure 32 for AS was likely to be caused by a local defect in one of the tape pieces. It was found during preliminary tests that some of the individual offcut pieces had defects that reduced the field they could trap. It has been found in previous work that the effect of defects in individual layers tend to be averaged out when stacked simply [141]. However, for the stacks reported here, discrepancies between tapes were not as readily smoothed out due to the spatial offset each tape had relative to adjacent pieces.

The field profiles in the *x* direction (parallel to the tape axis) for a small central region of the stacks were also measured. The size of the scanned region in the *x* direction was limited to 5 mm. Nevertheless, the expected high uniformity of the field profile over the region scanned was seen with a profile roughness of < 0.14 mT for the angled stack, corresponding to a relative roughness of < 1.6%.

2.3.1.5 Comparison with modelling results

Simple finite element method (FEM) modelling was performed to investigate the parameters that affected the trapped field profiles. It also enabled the properties of the stacking configuration to be assessed without the complicating factors of misalignments and tape defects.

2.3.1.5.1 Modelling framework

A time independent model was constructed in COMSOL Multiphysics 5.0 using the AC/DC module and a stationary study [128]. The simple approximation of uniform surface currents was used to simulate the superconducting surfaces on domains of the same cross-sectional dimensions as the real tape pieces. The models were 2D, considering changes only in the *yz* plane shown in Figure 30, assuming no variation in the *x* direction, which is a good approximation for our region of interest. Although uniform surface currents may seem an oversimplification, it was an important first step for investigating the parameters that affected the trapped field profiles. More extensive time-dependent critical state modelling results for angled stacks are in section 2.3.6.3. However, the critical state models took a long time to solve and were often unstable due to the relatively high number of mesh elements and complex geometry.

2.3.1.5.2 Modelling results

It was found that the measurement height had a significant effect on the field profile and corresponding roughness as can be seen in Figure 33.
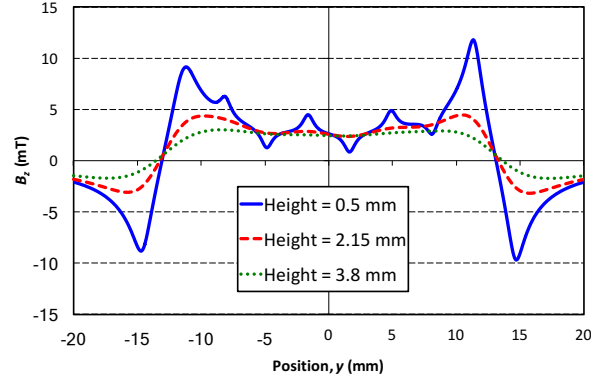
Figure 33. Simulated field profiles for 2LHO tape stack arrangement at different heights above the sample surface. The roughness is strongly dependent on the measurement height.

The modelling showed that the asymmetries and regular undulations present in the 2LHO and 4LHO configurations are inherent to the arrangements rather than purely due to non-uniformities and misalignments. For example, the asymmetry in the peak at +5 mm in sample 2LHO and 4LHO appear in the modelled profile too. The lower relative roughness for 4LHO compared to 2LHO suggested that yet more layers would lead to a smoother profile. This was confirmed by simulating an 8-layer stack (8LHO), which showed a lower relative roughness than either 4LHO or 2LHO, Figure 34.
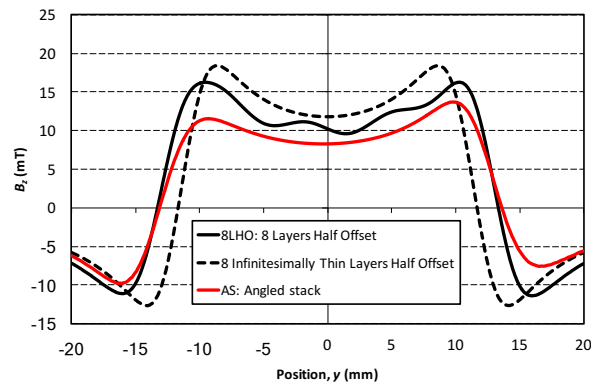
Figure 34. Simulated trapped field profiles for an 8-layer half offset stack (8LHO) and an angled stack equivalent to AS. Also, the profile for a half offset configuration with each of the layers infinitesimally thin. All profiles are for a measurement height of 2.15 mm.

However, the undulations are still present due to the difference in height each layer is away from the measurement plane. The undulations only disappear if the layers are

infinitesimally thin as can be seen in Figure 34. When the trapped field was measured above the top surface of the stack the layers closer to the measurement plane contributed more strongly than the layers further away. Hence each pair of layers did not fully cancel out each peak and trough. The advantage of the angled stack configuration is that it avoids this problem because in the central region each of the tapes contribute equally to the field profile. The angled stack arrangement has the advantage of a smoother field profile for a similar number of tapes.

The angled stack field profiles also displayed measurement height dependence, as can be seen in Figure 35, but the roughness dropped off much more rapidly away from the surface than for LHO stacks. The simulated magnetic field distributions for the angled stack and 8LHO arrangements are shown in Figure 36.
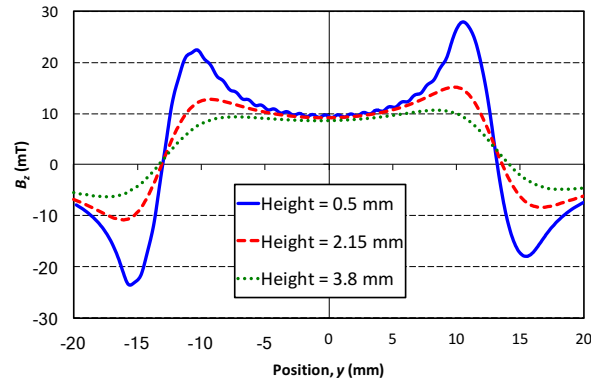
Figure 35. Simulated trapped field profiles at different measurement heights for an angled stack equivalent to AS.
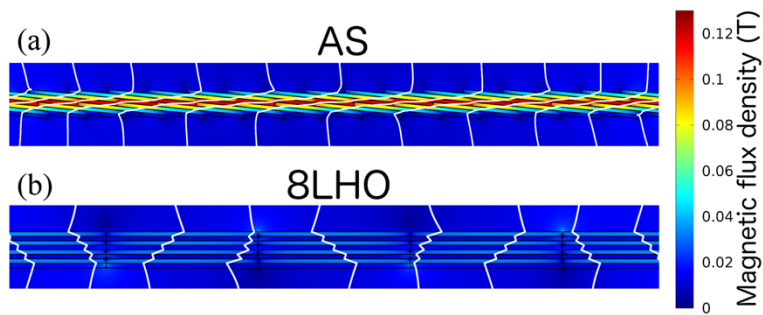
Figure 36. Simulated magnetic field distribution plots for (a) the angled stack and (b) 8 layers half offset configurations. Only the central region is shown for clarity. The field lines bend significantly within the stacks.

2.3.2 Improving field uniformity

To improve the field uniformity and magnitude further wider tape pieces were required because, unlike in a permanent magnet, the field produced by a superconducting trapped field magnet is size dependent. Therefore, multiple angled stacks were produced from 12 mm wide tape and more comprehensive modelling was performed to explore the limits of the angled stack geometry.

2.3.3 Multiple stack geometry, fabrication and measurement

2.3.3.1 HTS tape

Solder coated superconducting tape provided by SuperOx [142] was used to produce self-supporting angled stacks. The tape was 12 mm wide, 94 μm thick and had a minimum self-field I_c of 400 A at 77 K. The substrate was 60 μm thick non-magnetic Hastelloy C276, the buffer and $GdBa_2Cu_3O_{7-x}$ (REBCO) layers followed the conventional IBAD-PLD architecture with a ~1.5 μm thick HTS layer. The tape had a 1 μm thick silver layer, 5 μm thick copper layer and 10 μm thick lead–tin eutectic solder layer on either side of the tape.

2.3.3.2 Stack geometry and fabrication

Baskys et al. [143] demonstrated that self-supporting stacks could be produced from solder coated tape with minimal damage to the superconducting layers. For the angled stacks the solder coated superconducting tape was cut into 24 mm long pieces. To form a single angled stack, as in Figure 37, 26 of these were arranged so the relative offset between pieces was 1 mm in the tape width direction (y-axis in Figure 37 and Figure 38). There was no offset in the tape length direction (x-axis in Figure 37 and Figure 38). All tape pieces were oriented in the same way with the HTS layer closer to the top surface ($+z$ side) than the Hastelloy substrate. The tapes were held in place by a custom-made aluminium rig during assembly. The tape stacks were heated to 210 °C for 5 minutes to solder them together. Following this procedure, four self-supporting stacks were produced of the same geometry and specification; A, B, C and D.
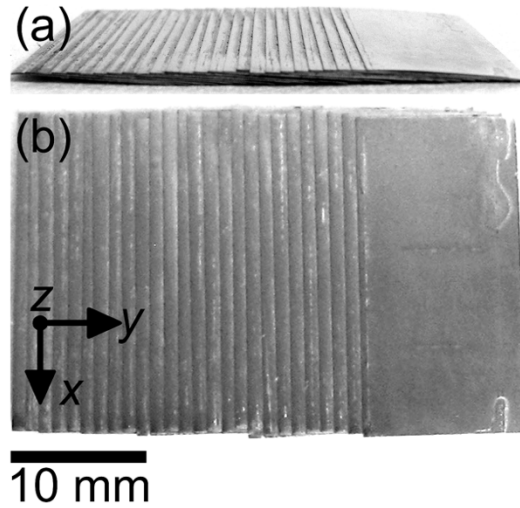
Figure 37. (a) Profile and (b) plan view of a single angled stack, stack A. The stack was constructed of 26 tape pieces each 12 mm × 24 mm in size, offset 1 mm laterally to adjacent pieces and at angle of 5.4° to the horizontal. The stack thickness was 1.2 mm.
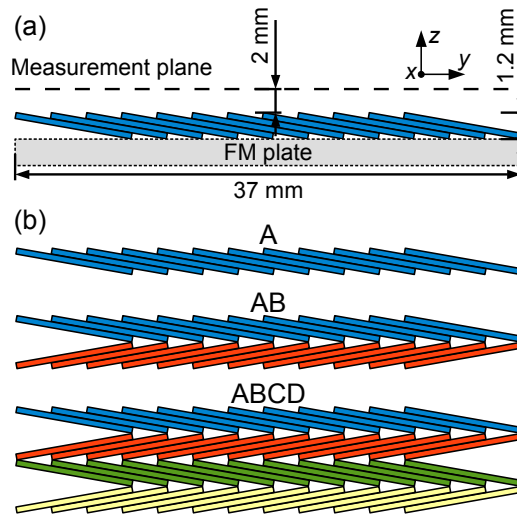
Figure 38. (a) Schematic showing measurement plane, axes and position of ferromagnetic (FM) plate, when used. (b) Schematic showing the different layers of stacks tested in the current work. The individual stacks A, B, C and D were all equivalent. Not to scale, individual stacks contained 26 tape pieces.

In addition to single stacks several layers of the stacks were investigated as shown schematically in Figure 38(b). These samples were referred to as A, AB and ABCD. Furthermore, it has been shown by Philippe et al. [131] that a plate of soft ferromagnetic (FM) material beneath a bulk REBCO superconductor can enhance the trapped field measured above it, so samples with a soft FM plate beneath were also characterised. The position of this plate relative to the stack, when used, is shown in Figure 38(a). The plate was 0.85 mm thick mild steel cut to the same area as the stacks, 37 mm × 24 mm.

2.3.3.3 Scanning Hall probe magnetometry

The samples were field cooled (FC) to 77 K in liquid nitrogen in an applied field of 0.20 T to ensure full penetration. The field was applied using an electromagnetic coil and was ramped down to zero at a rate of 6.7 mT s^{-1} once the sample had reached 77 K. The trapped magnetic field profile was characterized by scanning a Hall probe (Arepoc HHP-VA) 2 mm above the sample surface. The bespoke mechanical stage was controlled by software developed in-house. The probe control current was nominally 10 mA and the sensitivity was 0.0522 V T^{-1}. The lateral step size was 0.25 mm for trapped field profile measurements in the y direction. For full area field maps, the step size was 0.5 mm in the x and y directions. Scans were started 300 s after magnetisation.

Flux creep measurements were also performed using the Hall probe system. The trapped magnetic field at a height of 2 mm above the centre of the sample was measured for ~4 h at 10 s intervals following magnetisation.

2.3.3.4 Magnetic properties of the FM plate

The magnetic properties of the FM plate were measured using a sensitive vibrating sample magnetometer (PMC MicroMag 3900 Series VSM). A small sample, approximately 0.85 mm × 0.66 mm^2, was prepared from the same material as the FM mild steel plate. The sample was magnetically soft and displayed virtually no remanence. The relative permeability, μ_r, calculated from the initial gradient of the magnetisation curve was ~10.

2.3.4 Trapped field profile results

The trapped field profiles shown in Figure 39 have good uniformity. Having several layers of the stacks, as in samples AB and ABCD, led to a smoother trapped field profile than the single stack alone. Also, the asymmetry present in the trapped field profile for the single stack A was supressed when it was layered with additional stacks. The asymmetry in the field profile for a single stack is expected due to the nature of the stacking configuration and the property being measured; the z component of the magnetic field. As will be discussed below in section 2.3.4.1, the angled stack can be thought of like a coil with the edge segments contributing a net current.
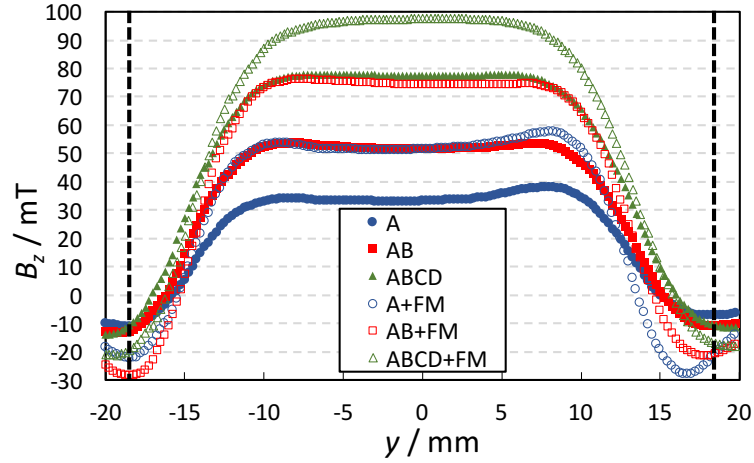
Figure 39. Trapped field profiles of the layered stacks with and without the ferromagnetic plate (FM). The stacks were field cooled to 77 K. The measurement height was 2 mm. Vertical dashed lines indicate sample dimensions.

To quantify and compare the uniformity of the field, the profile roughness metric, equation (9), was used again. The data from the central 10 mm of the field profiles were used to calculate the mean trapped field, B^* and the profile roughness, R_{rms}. The values for each of the samples are summarized in Table 4.

Table 4. Trapped field profile roughness data for self-supporting soldered angled stacks.

Sample	Mean trapped field, B^* (mT)	Profile roughness, R_{rms} (mT)	Ratio, R_{rms}/B^* (%)
A	33.6	0.67	2.0
AB	51.8	0.31	0.6
ABCD	77.6	0.13	0.2
A+FM	51.7	0.77	1.5
AB+FM	74.6	0.38	0.5
ABCD+FM	97.3	0.38	0.4

Layering stacks together increased the trapped field as did the addition of the FM plate beneath the samples. The magnitude of the increase resulting from doubling the number of stacks was approximately the same as that from the addition of the FM plate beneath the sample. The field enhancement due to the presence of the FM plate can be explained by considering the magnetic circuit around the sample when magnetised. The FM plate has a higher relative magnetic permeability, μ_r, than liquid nitrogen and so reduces the reluctance of

the circuit surrounding the sample, reducing the stray field and enhancing the field magnitude above the sample surface.

Figure 40 shows the full area trapped field maps for several of the samples. The uniformity in the *x* direction (parallel to the length of the tape pieces) is good, as expected. The trapped field maps show that layers of the angled stacks can be magnetised to produce uniform trapped fields over large areas, with uniformity good in both directions. Furthermore, the FM plate does not distort the shape of the trapped field above the sample.
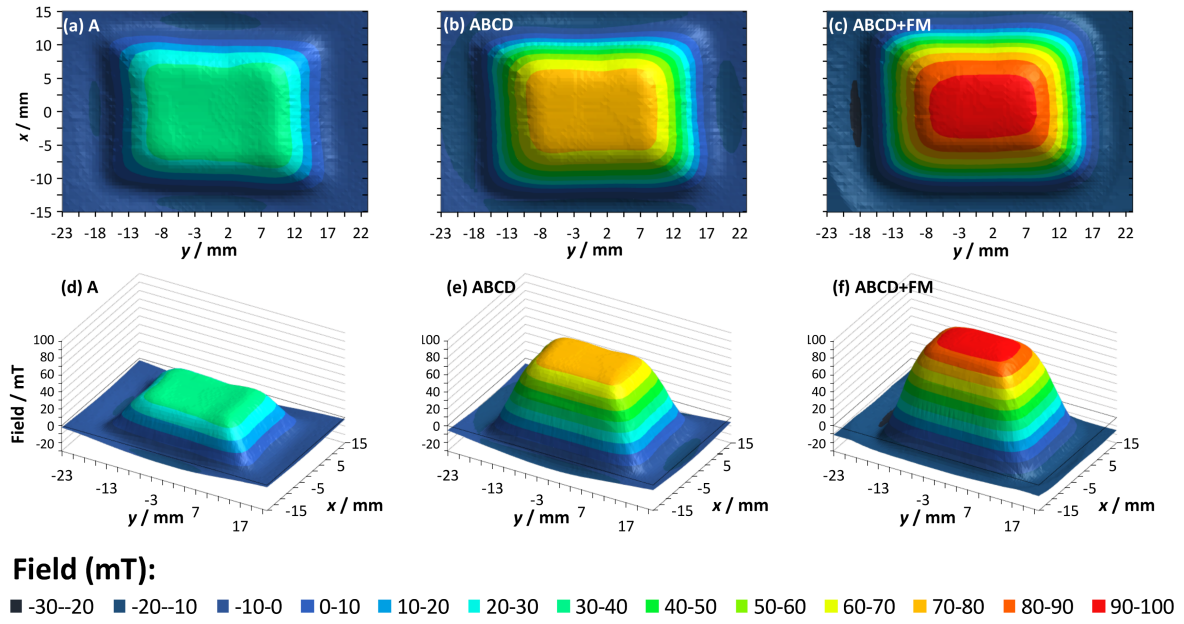
Figure 40. (a)–(c) Contour and (d)–(f) surface plots showing the trapped field profile for a single stack A, four-layer stack ABCD and four-layer stack with ferromagnetic plate beneath ABCD+FM. Measured at 77 K, 2 mm above the top surface.

The angled stacks show several advantages over alternative methods for producing uniform fields using trapped field magnets such as tape annuli, bulk rings, tape coils or unsaturated bulks or stacks. Unlike annuli made from either bulk rings [134] or stacks of tape [132], the size of the angled stacks is scalable and limited only by the method used for magnetisation and amount of coated conductor available. Furthermore, the technical difficulties encountered with producing long lengths of coated conductor that can be used to produce a persistent mode coil are avoided because only relatively short sections of tape are required and no superconducting joints need to be created. Also, the uniformity, magnitude and reproducibility of the field profile is much better for angled stacks than an unsaturated bulk or conventional tape stack.

2.3.4.1 Stack similarity to a coil

　　The angled stacks were found to have some similarities with a coil when considering the persistent current directions in the magnetised tape layers. Consider the current directions in a tape piece in a magnetised angled stack as in Figure 41, the two colours indicating current in opposite directions; the positive and negative *x* directions. The current in each tape piece can be approximated to a block rather than surface current, which, to a first approximation leads to the schematic in Figure 41(b) and (c). This can be further simplified to two current domains as shown in Figure 41(d). The relative contribution to the resultant field profile can be deduced by modelling the individual situations shown in Figure 41(e) and (f). The results for these models are shown in Figure 42. The magnitude of the trapped field measured above the centre is entirely due to the end segments, with the central region only contributing to the shape of the end peaks. Therefore, there is a similarity to a coil with an outer diameter the same as the sample dimensions.
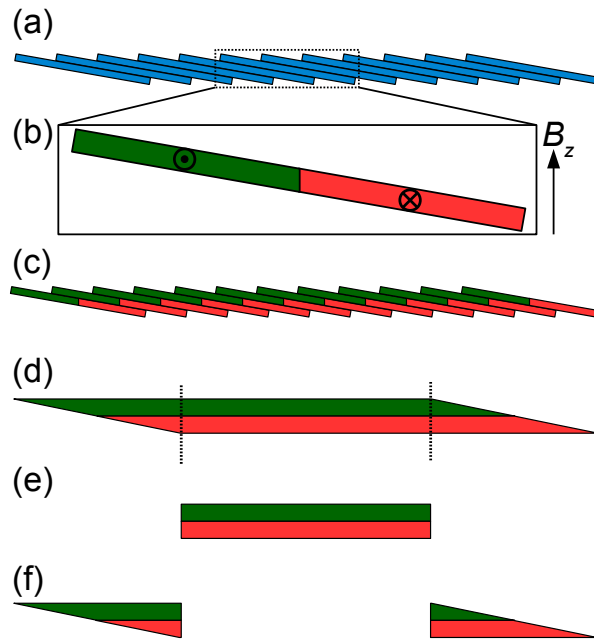
Figure 41. Schematic showing the equivalent block currents in the angled stack A. (a) The single angled stack. (b) A single piece of tape from the stack illustrating the current directions in two domains when magnetised. Block currents rather than surface currents are used for clarity. (c) The block currents in each tape piece are equivalent to a first approximation. (d) Simplification to two domains with opposite current directions, the dotted lines show the boundary between the central and end regions. (e) Central blocks only. (f) End segments only.
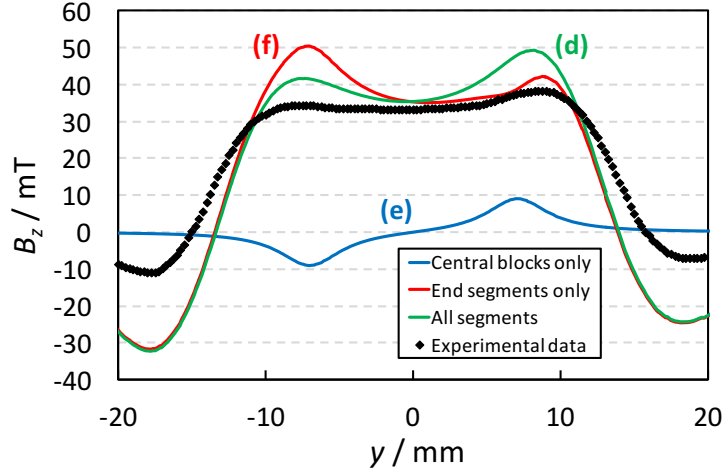
Figure 42. Field profiles from FEM block current models for the separate segments and the complete stack. The letters correspond to the sections of Figure 41. Experimental data shown for comparison. The modelled profile for block currents in all segments matched exactly with the surface current model used in section 2.3.6. The central blocks only contribute to the asymmetry of the end peaks; the end segments are responsible for the central field magnitude.

The end segments have an associated engineering current density, $J_{c,eng}$, when considering the net current over their effective area in the *y–z* plane. To maximize the magnitude of the trapped field the engineering critical current at the edge of the sample needs to be maximised, which leads to the stack design presented in section 2.3.7.

2.3.5 Magnetic flux creep results

The flux creep results for the single stack A are shown in Figure 43. The decay follows the expected logarithmic dependence given by equation (10). The decay constant, *a*, was found to be less than 5% per time decade, which is comparable to bulks [23] and conventional stacks of tape [140,144] at 77 K. The full area field profile remained unchanged in shape when measured after the flux creep experiment, the only perceptible change was the fall in magnitude predicted by logarithmic decay.

$$\frac{\Phi(t)}{\Phi_0} = 1 - a \log\left(\frac{t}{t_0}\right) = 1 + a \log t_0 - a \log t \tag{10}$$
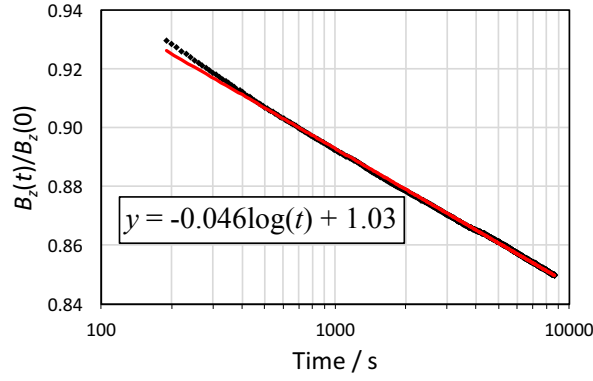
Figure 43. Flux creep for stack A. The rate of decay of flux, calculated from the gradient of the red trend line, is less than 5% per time decade.

2.3.6 Modelling trapped field profiles

The simple time-independent FEM model, see section 2.3.1.5.1 was adapted reflect the new angled stacks made with wider tape pieces. Additional, time-dependent, critical state modelling was performed and the framework used is outlined below [129]. This critical state model was only constructed for the single angled stack A because of the time and stability issues described earlier.

2.3.6.1 Critical state modelling framework

The H-formulation for magnetic fields was used in COMSOL Multiphysics 5.0. The framework used an *E*–*J* power law, equation (11), to simulate the critical state, where E_x and J_x are the electric field and current density respectively. A field dependant *n*-value was used as in [145] based on data in [34] giving typical *n*-values of around 27 for the model.

$$E_x = E_0 \left(\frac{J_x}{J_c(B)}\right)^{\left(\frac{n_0}{1 + B/B_{0n}}\right)} \tag{11}$$

The model used field cooling with a 0.1 T applied field, which was enough to saturate the sample, with the field ramp rate being the same as for the experiment. Flux creep was modelled for a further 300 s after magnetisation to match the time delay used for the experimental Hall scans. The field dependent *n*-value was most appropriate for the flux creep period as creep rates are sensitive to *n*-values. The Kim model [146] was used to describe the dependence of the critical current density, equivalent to the engineering critical current density, $J_{c,eng}$, for the experiment, on field at 77 K, equation (12).

$$J_c(B) = J_{c,eng} = \frac{I_{c0}}{wd\left[1+\dfrac{\sqrt{k^2|B_\parallel|^2+|B_\perp|^2}}{B_0}\right]} \tag{12}$$

Equation (12) includes the J_c anisotropy of the tape integrated into the Kim law as used previously in [147], where the parameter k varies between 0 and 1. Full descriptions of the parameters used are given in Table 5. The motivation behind equation (12) was to use a simple mathematical framework that can easily fit typical measured $J_{c,eng}$ values for commercial superconducting tape for fields of up to 4 T, which covers the field range in question at 77 K. The B_0 Kim law parameter was determined by fitting to data for typical SuperOx tape at 77 K. The anisotropy variation described by equation (12) does not give such a close fit to the available data because it describes a smooth variation in J_c with angle, rather than the sharper peak observed for real tape when the field is perpendicular to the c-axis. However, it was sufficient for a qualitative investigation, $k = 0.5$ was chosen as the closest fit. The thickness over which supercurrents could flow was varied between full tape thickness, d, and a quarter of the tape thickness, $0.25d$. The reported results were for superconducting domains with half tape thickness, $0.5d$.

Table 5. Descriptions and values of parameters used in critical state modelling.

Parameter	Description	Value
E_0	Electric field constant in equation (11)	10^{-4} V m^{-1}
$I_{c0} = I_c(77\ K, SF)$	Tape critical current at 77 K and self-field	400 A
w	Tape width	12 mm
d	Tape thickness	100 μm
k	Anisotropy constant in equation (12)	0.5
B_0	Flux density constant in equation (12)	0.192 T
n_0	n-value constant in equation (11)	30
B_{0n}	Flux density constant in equation (11)	0.75 T

It is worth mentioning what effects the critical state model can account for that the stationary study cannot. Although stationary studies can solve for the field-cooled state of a superconductor with $J_c(B)$, this is only possible for high symmetry cases such as a cylindrical bulk superconductor. The lack of symmetry in the angled stacks means that the distribution of

current density along the 12 mm width of a single tape piece can be asymmetric about the mid-point. This is because the two sides of the tape pieces can experience different field conditions leading to different J_c. Such asymmetries are not a problem for critical state models. The stationary study also only used surface current density. This is obviously a good approximation for the HTS layers but it gives rise to a discontinuity in flux lines causing them to bend at a point. This means that the angle of the flux density at the layer is not well defined making J_c anisotropy difficult to implement. Finally, the stationary model cannot simulate time dependent flux creep effects or the magnetisation process itself. These reasons motivated more complex critical state modelling to better approximate the real experiment.

2.3.6.2 Stationary study model results for angled stacks of tape

Figure 44 compares the simple modelling and experimental results for sample A and AB. There was generally good agreement in magnitude for the single stack A. However, for sample AB the experimental data had a lower magnitude than the simple model predicted. The difference can in part be explained by the lack of flux creep in the stationary study model. In both cases the experimental results are clearly more uniform than the model. In section 2.3.6.3 the critical state modelling shows some improved agreement with the experimental results.
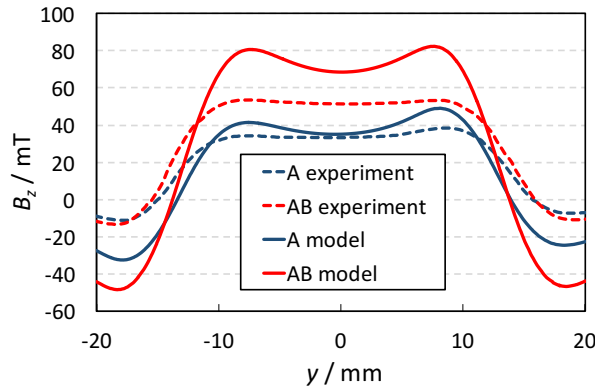
Figure 44. Comparison between modelled and experimental trapped field profiles for samples A and AB.

Figure 45 shows the simulated magnetic field distribution in a single stack, A, and double stack, AB. As mentioned above the tape pieces experience different field conditions, which is particularly apparent at the edges of the sample as can be seen in Figure 45(a). This difference could lead to differences in J_c between tapes, particularly as the field angle varies for each piece of tape. Figure 45(b) suggests that the flux lines undergo significant bending within the stacks and that the tape pieces will experience fields at a variety of angles, not just perpendicular to the superconducting layer. The effect of this $J_c(B,\theta)$ dependence was not

incorporated in to the simple stationary study but was investigated as part of the critical state modelling in section 2.3.6.3. However, despite the significant flux bending implied in the model the flux decay constant calculated from flux creep measurements, section 2.3.5, was similar to that for bulks and other stacks of tape.
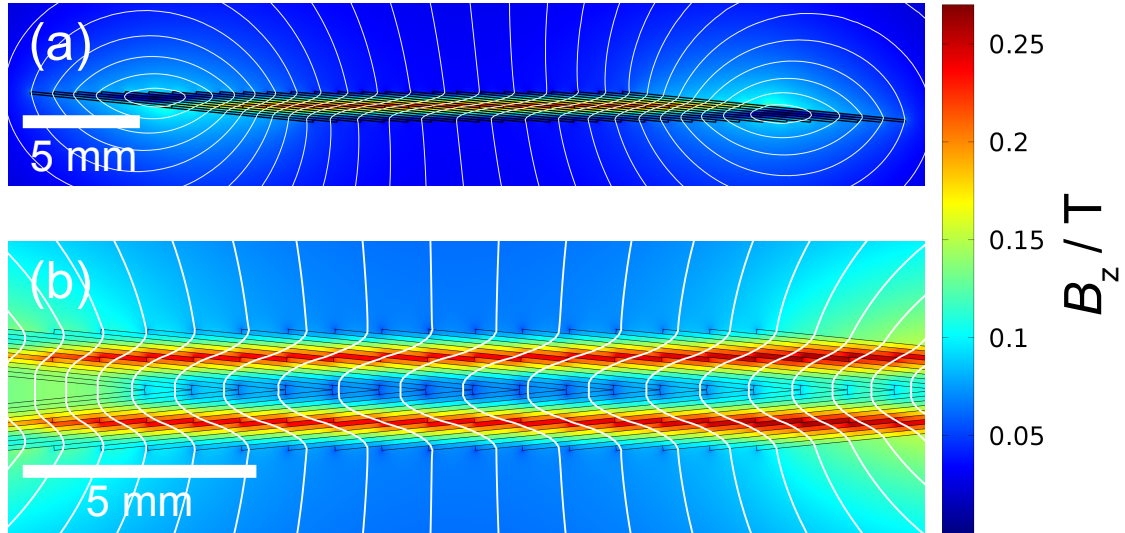
Figure 45. Simulated magnetic field distribution for (a) a single stack, A, and (b) the central region of a double stack, AB. The flux lines show significant bending within the stacks.

The increase in magnitude and symmetry of the field profiles seen experimentally for samples with the FM plate was reflected in the modelling results shown in Figure 46. However, as in the model without the FM plate, the experimental results were more uniform than the model. There was a much better match for the single stack A than the double stack AB. The larger difference for the AB+FM stack could be due to the lack of field dependent J_c, which is more important when the tapes are being exposed to higher field as is the case when adding a FM plate. The FM plate was modelled using a $B(H)$ dependence derived from its measured magnetisation curve.
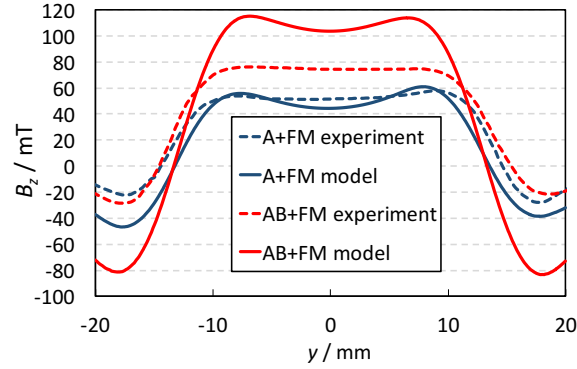
Figure 46. Comparison between modelled and experimental field profiles for samples A+FM and AB+FM.

The field enhancement due to the FM plate was expected to increase with increasing plate thickness and permeability [131]. Models with different values of permeability and variable thicknesses of FM plate were solved in the stationary study framework, Figure 47. The modelled data all show the FM plate enhancing the field magnitude up to a point where increasing the thickness further does not significantly increase the field magnitude. The results also suggest that the higher the permeability the thinner the plate required to achieve a given increase in trapped field, as expected. The larger discrepancy between modelled and experimental results when the FM plate was present may also be partly due to the challenges of measuring the permeability of the FM plate material precisely. Due to the sensitive nature of the magnetometer a very small sample had to be characterised because of the maximum magnetic moment measureable by the device. Hence, it is possible that the relative permeability of the small sample measured may not be fully representative of the entire FM plate used, contributing to the model discrepancy.
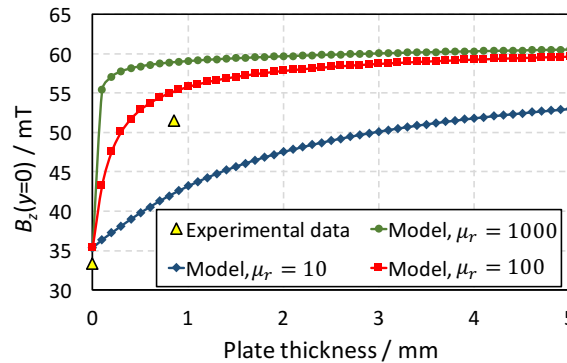
Figure 47. The central trapped field magnitude, B_z, with increasing ferromagnetic plate thickness for three different values of relative permeability, μ_r. Experimental data are included for comparison. The measurement height was 2 mm. The plate thickness used in experimental work was 0.85 mm.

2.3.6.3 Critical state model results

The trapped field profiles in Figure 48 show that the critical state model gave a closer match to experimental data in terms of both magnitude and shape than the stationary study. The time dependent flux creep in the critical state model appears to be a key feature that was not captured by the simpler stationary study and helps to explain the better match with experiment. However, there are still differences between the model and experimental data, most notably in the shape of the profile. As part of the critical state modelling, a sensitivity study was performed to determine if there were parameters that significantly affected the uniformity of the trapped field profile.
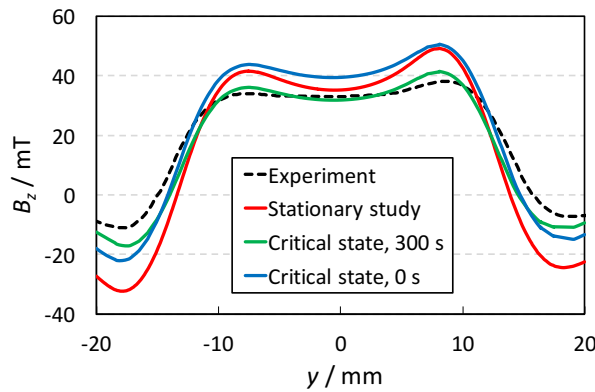
Figure 48. Trapped field profile results for a single angled stack, A. Comparing experimental data with the stationary study and critical state FEM data. The critical state model results 300 s after magnetisation showed good agreement with experimental data.

The thickness of the superconducting domains was adjusted from 100 μm down to 25 μm to better approximate the thin layer of superconductor in the tape pieces, below this thickness the computation time was too great. No discernible difference was detected in the shape or magnitude of the trapped field profile when the thickness was altered. The model data used in the figures above was for a domain thickness of 50 μm. Additionally, the $J_c(B)$ and anisotropic components of the model, k, were adjusted to extreme values to ascertain if they could help explain discrepancy between the model and experimental results. Only small differences in magnitude and negligible differences in shape were noticed. The field and angular dependence of J_c may have only had a very limited effect on the trapped field profiles predicted by the critical state modelling because of the relatively low fields in the angled stacks at 77 K and the expected symmetrical nature of the $J_c(B,\theta)$ curve due to spherical pinning centres. If superconducting tape with more complex $J_c(B,\theta)$ behaviour was used, such as that produced by SuperPower Inc. with columnar defects and vicinal substrate, then the effect of

the anisotropic fields experienced by the tape may have a greater effect. Baskys et al. [148] demonstrated that incorporating experimentally determined angular dependence of J_c in to finite element modelling gave better agreement with experiment for magnetised stacks of tape, particularly at higher fields.

The current densities within the tapes during and following magnetisation are shown in Figure 49. During the ramp down of the applied field the current density is highest at the edge of the tape pieces before reaching a state very similar to that modelled by the stationary study after magnetisation. This illustrates that the simple 'block current' model used in section 2.3.4.1 and the stack equivalence to a coil were suitable approximations.
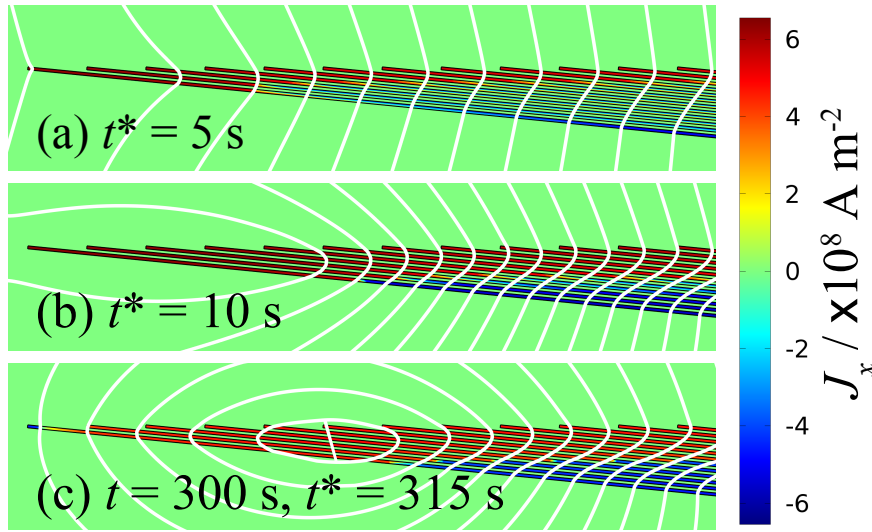
Figure 49. Evolution of current density (a) and (b) during and (c) after the magnetisation process. Time t* = 0 is defined as the start of the magnetisation ramp, where the external field is reduced. Time t = 0 is at the end of magnetisation.

The critical state modelling results do not fully explain the very high uniformity seen in the experimental trapped fields. There are likely two possible simplifications in the model which may be responsible. The real stacks are not infinitely long in the *x* direction. The tape pieces at the end of the stack along the *y*-axis may be experiencing magnetic flux conditions that vary along the x-axis. In other words, there may be complex end effects that alter the currents in the tapes and therefore the trapped field profile. The other possibility is that the FEM solution for the tape currents change when the superconducting layer becomes very thin (~microns) giving rise to an altered trapped field. Both these reasons are difficult to investigate numerically due to unmanageable numbers of mesh elements for 3D and thin layer models.

2.3.7 Optimising trapped field magnitude

2.3.7.1 Shallow angled stack experimental results

As discussed in section 2.3.4.1 the angled stack arrangement gives rise to a net current at the sample edges and an approximately zero net current in the centre and therefore behaves in a similar way to a coil. Alternative designs for maximising the trapped field magnitude whilst still retaining the field uniformity were considered. A shallower angled stack arrangement would give a larger engineering critical current density, $J_{c,eng}$, at the edges of the sample and therefore was predicted to give a higher trapped field magnitude.

The alternative 'shallow angled stack' had a similar cross-sectional area in the y–z plane to the angled stack A. The new stack was constructed and the field profile measured in the same way as the original angled stacks. Figure 50(a) shows the trapped field profile and Figure 50(b) the stacking schematic for the shallow angled stack. Although the average trapped field magnitude, B^*, was higher the uniformity was significantly poorer with a R_{rms} of 2.3 mT, corresponding to a relative ratio of > 5.4%. The reason for this was probably due to the shallow angled stack being much more sensitive to small offsets and non-uniformities between tape pieces. In the shallow angled stack, each piece of tape in the central region needs to exactly cancel out the contribution from its neighbours and hence a small offset or difference in I_c between tape pieces can lead to larger scale non-uniformities in the trapped field profile. The more robust stacking geometry of the angled stacks A, B, C and D accommodated for small discrepancies and misalignments more successfully. Therefore, the shallow angled stack remains an ideal case that would require more careful assembly to exploit its potential to achieve higher magnitude uniform fields.
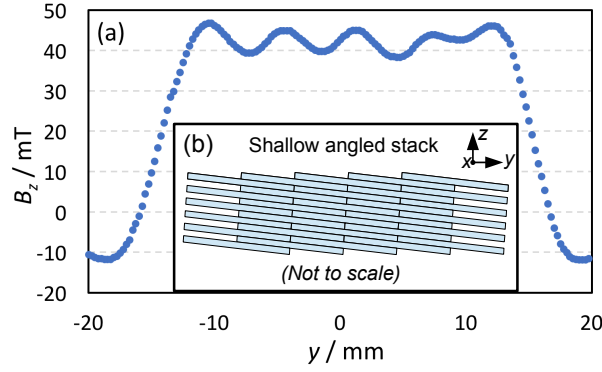
Figure 50. (a) Trapped field profile for the shallow angled stack. Inset, (b) shows the schematic structure of the stack. The stack was comprised of 30 pieces of tape each offset by 6 mm in the y direction with respect to adjacent pieces. The tape pieces were at an angle of 0.9° to the horizontal.

2.3.7.2 Model results for optimum magnetic field magnitude

To investigate the limitations for the maximum trapped field possible for an angled stack an explicit comparison with an equivalent coil was made and modelled in the simple stationary study framework. The shallow angled stack, discussed above and illustrated in Figure 51(a), has the potential for a high engineering current density at the sample edges. The edge regions that contribute to the field magnitude can be modelled by an equivalent coil, Figure 51(b), which allows for flexible estimates of the magnitude of the field the angled stacks can produce at different temperatures and sizes. The modelling in this section assumes 30 μm thick tape with 400 A I_c (77 K, self-field), which is now commercially available. The previous modelling considered stacks to be infinitely long in the x-axis, hence 2D infinite models. In this case, it is more helpful to assume cylindrical symmetry so that the equation for a 2D axisymmetric coil can be used, equation (13). Of course, the real experimental stacks have rectangular net currents flowing around the whole sample and so produce a central field somewhere between that resulting from the 2D infinite and 2D axisymmetric approximations.
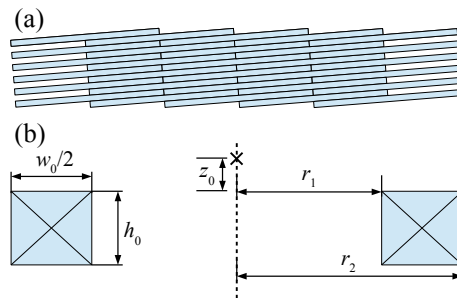
Figure 51. (a) Schematic diagram of the optimum shallow angled stack and (b) the equivalent coil dimensions.

Although the fields produced by the experimental angled stacks are very uniform, the magnitudes are much lower than the best rare-earth permanent magnets. Lower temperatures and greater stack thickness is needed to reach higher field values. The effect of the coil geometry on the magnetic flux density above the coil was calculated using equation (13), available from [149].

$$B = \frac{\mu_0 n I}{w_0}\left[(z_0 + h_0)\ln\left(\frac{r_2 + \sqrt{r_2{}^2 + (z_0 + h_0)^2}}{r_1 + \sqrt{r_1{}^2 + (z_0 + h_0)^2}}\right) - z_0\ln\left(\frac{r_2 + \sqrt{r_2{}^2 + z_0{}^2}}{r_1 + \sqrt{r_1{}^2 + z_0{}^2}}\right)\right] \tag{13}$$

Where μ_0 is the permeability of free space, n the number of turns per unit length, I the coil current, w_0 the width of the tape, r_1 the inner coil radius, r_2 the outer radius, h_0 the coil height and z_0 is the measurement height as shown in Figure 51. The collected term (nI/w_0) gives an equivalent engineering current density for the tape at the edges, considering the empty space in these regions.

Equation (13) was used to estimate the field 2 mm above an ideal stack that had a height of 20 mm. The results are shown in Figure 52 for two different critical currents corresponding to 77 and 20 K. For the chosen measurement height of 2 mm, there is an optimum inner radius, which gives the largest central field, however larger radii can be used but with reduced field magnitude, as expected for a coil. To calculate the current in the coil at the two different temperatures the same tape I_c fitting as described in [145] was used to give a field and temperature dependent $J_{c,eng}$. A factor of half was involved due to the 50% space present at the stack edges, Figure 51(a). A stationary study model was then used with $J_c(B)$ dependence to calculate the currents and hence field for the coil. The stationary study modelling framework could be used with $J_c(B)$ dependence in this case because of the simplification offered by using a 2D axis symmetric model. Unlike in a regular coil, there was no constraint to make the total current in each tape layer the same. This is because unlike a typical coil, the current can be different in each tape layer and hence there is no current constraint for the equivalent coil cross-section. The results of this FEM model are shown in Figure 52 and demonstrate large increases in trapped field possible at lower temperatures, where current densities can be much higher. The FEM model results are very similar to the analytic coil calculation, which uses uniform current density. The analytic curves were calculated using a current per half tape width that gave an appropriate match in magnitude with the FEM results, because the analytic equation had no method for considering the field dependence of J_c. The results show that trapped fields above 2.5 T could be expected with a

single stack and higher would be predicted between two stacks, thus showing the potential to produce greater fields than possible with rare earth magnets.
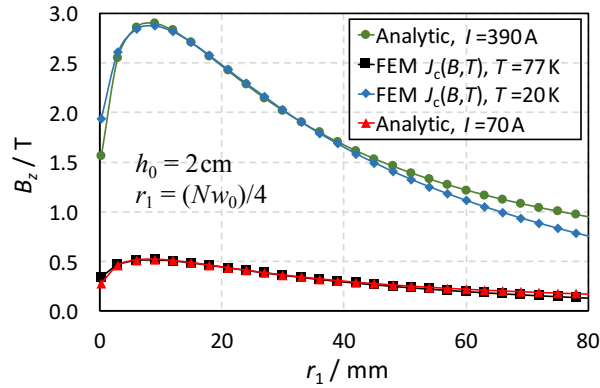
Figure 52. Field 2 mm above coil equivalent for different temperatures and current. Only discrete values of the inner radius, r_1, are allowed due to the way the equivalent stacks can be composed. ($N+1$) = number of tape pieces in a single layer.

2.4 Summary and outlook

In this chapter, the concept of using the wasted superconductor material from the manufacture of Roebel cables to produce trapped field magnets was presented. Roebel cable offcuts, 6.5 mm wide, were stacked in various arrangements to determine if a uniform magnetic field, that might be suitable for a small-scale NMR device, could be produced following magnetisation. A novel angled stack configuration was designed and tested and found to display promising properties compared with alternatives.

Further experiments with full width tape pieces were performed and several self-supporting angled stacks were produced from 12 mm wide solder coated tape. These stacks displayed much higher and more uniform trapped field profiles. Additionally, layering multiple stacks together and including a soft-ferromagnetic plate beneath them enhanced the field magnitude and uniformity even further. Both stationary and time-dependent modelling results from COMSOL Multiphysics were presented. There was found to be good agreement between experiment and model for the single stack case that improved further with time-dependent modelling. Limitations in the simple model framework were commented on, with experimental samples displaying lower magnitude but more uniform field profiles.

Estimates for the maximum trapped field magnitude were made by demonstrating the similarities between the magnetised angled stacks and a coil. The predictions indicated that by

using currently available, high performance, thin tape at 20 K a magnetised angled stack configuration has the potential to generate uniform fields much higher than rare-earth magnets. Therefore, angled stacks have the potential to be used as trapped field magnets for use in small-scale NMR/MRI devices.

Useful future work in this area could investigate how the angled stacks respond to pulse magnetisation, where a high magnetic field is applied in a short (~milliseconds) pulse rather than slowly ramped up and down. Additionally, experiments at temperatures below 77 K would help verify the model predictions and should enable larger fields to be trapped.

Finally, Goldacker et al. [150] have recently presented the concept of using wider tape to produce a 'double core' Roebel cable, where the central gap between strands made from wider tape is made large enough to accommodate a regular width Roebel cable. This cable design offers the possibility of increasing the current carrying capacity of Roebel cables but requires the use of wider tape and high fractions of material wastage. However, the ability to usefully utilise the offcut material may enable 'double core' Roebel designs to become feasible. Additionally, the magnitude of the trapped fields presented for the angled stacks made from 12 mm wide tape should be matched or exceeded if wider offcuts became available.

3 SPARK-DISCHARGE PLASMA STRIATION

Parts of the work presented in this chapter also appear in the following publication:

[151] **T.B. Mitchell-Williams**, A. Baskys, Y. Guo, S.C. Hopkins, U. Bangert, A. Molodyk, V. Petrykin, F. Gomory, L. Frolek, B.A. Glowacki, Spark-Discharge Plasma as a Method to Produce Low AC Loss Multifilamentary (RE)Ba2Cu3O7 Coated Conductors, IEEE Trans. Appl. Supercond. 27 (2017) 5900405. doi:10.1109/TASC.2017.2651584.

3.1 High voltage spark-discharge

As mentioned in section 1.4.1 the division of superconducting layers in coated conductor tapes into separate filaments is important for reducing hysteretic AC loss, particularly for applications where the external magnetic field is perpendicular to the flat face of the tape. Additionally, the separation of filaments by resistive barriers is required to prevent significant coupling between filaments, which may also result in substantial AC losses.

Approaches including laser striation, mechanical cutting, inkjet printing and substrate templating were discussed in section 1.5. This chapter proposes a new, non-contact, scalable, low-cost method to selectively degrade strips of superconductor tape. The concept was to damage the superconducting layer using the high temperature plasma that occurs during an electrical spark discharge between an electrode and the tape surface.

3.2 Experimental methods

3.2.1 Superconducting tape

The superconducting tape used was 12 mm wide and was produced by SuperOx. It had a nominal minimum I_c rating of 430 A at self-field and 77 K. The basic architecture of the tape was like that produced by several manufacturers and is shown in Figure 53. The tape is based on a 60 μm thick Hastelloy substrate, with the functional layers deposited by the IBAD-MgO/PLD-GdBCO route. The stabilizer consisted of a 2 μm silver layer, giving a total tape thickness of approximately 65 μm. Some samples had the Ag cap layer removed chemically using a 1:1:2 solution of H_2O_2:NH_3(aq):H_2O. The silver free samples were used to compare if

there was an advantage to striating without the Ag cap layer in terms of the resulting width of the striated region.

Ag	DC sputtering (2 µm)
GdBCO	PLD (1-2 µm)
CeO_2:RE	PLD (100-200 nm)
$LaMnO_3$	RF sputtering (30-50 nm)
IBAD-MgO	IBAD with RF sputtering (5-7 nm)
$LaMnO_3$	RF sputtering (30-50 nm)
Al_2O_3	RF sputtering (50 nm)
Hastelloy C276	Cold rolled & electropolished (60 µm)
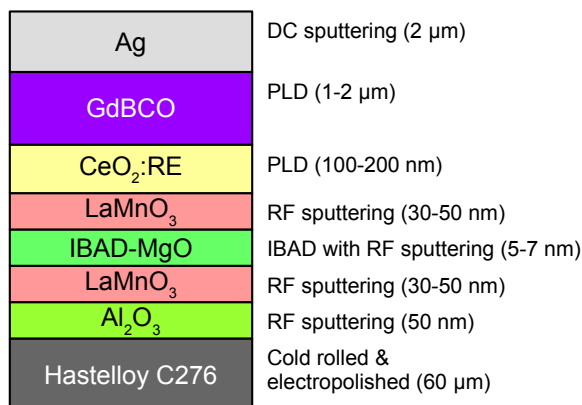
Figure 53. Schematic architecture for the SuperOx coated conductor tape used.

3.2.2 Spark-discharge generation and control

Spark-discharges were produced during the dielectric breakdown of air between electrodes held at high voltage. The voltage was generated using a voltage multiplier circuit (VMC) extracted from an electric fly-swatting device. This converted 4.2 V DC input voltage to a maximum of ~20 kV output across the electrodes, with ~450 V output used in practice. The input voltage and current were controlled using a regulated DC power supply (Kenwood PD 18-30). The lateral precision of the spark-discharge was improved by using a needle (radius of curvature 0.15 mm) as one of the electrodes. The motion of the tape with respect to the electrodes was controlled using a 3-axis mechanical stage (custom *xyz* stage, developed in-house). A schematic of the set-up is shown in Figure 54. The electrode-tape distance, relative speed and VMC input power were varied. Tests were performed with and without the silver stabilizer present. Spark-discharging was performed in ambient conditions at atmospheric pressure.
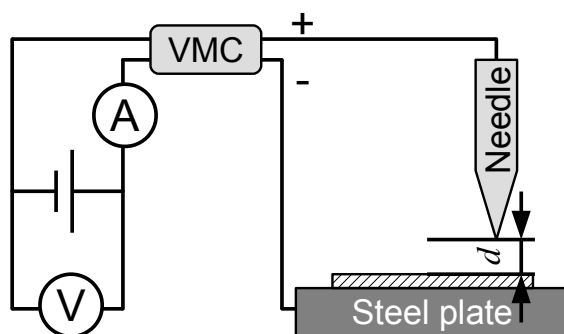
Figure 54. Schematic diagram of spark-discharge set up. The superconducting tape is represented by the hatched box. The steel plate was electrically isolated from ground. The details of the voltage multiplier circuit (VMC) are not included for simplicity. Not to scale.

3.2.3 Characterisation

Samples were characterised using scanning Hall probe magnetometry, scanning electron microscopy, interfilament resistance, critical current and AC loss measurement. Different sample sizes were required for different characterisation techniques, hence samples produced using nominally the same processing parameters but made from separate pieces of superconducting tape were given different prefixes. The prefix "M" was given for samples characterised using magnetic measurements (Hall probe), microscopy and interfilament resistance, "I" for samples used for critical current measurements and "AC" for samples that had their AC loss characterised.

3.2.3.1 Hall probe magnetometry

Samples 24 mm long were zero-field cooled to 77 K in liquid nitrogen and magnetised using an electromagnet with an applied field of 140 mT. The trapped magnetic field was measured by a Hall probe (HHP-VA, Arepoc) as it was scanned above the sample surface using a bespoke 3-axis stage controlled by in-house software. Measurements were started 300 s after magnetisation to avoid any significant effects due to flux creep. The scan height was 0.5 mm and lateral step size 0.25 mm.

3.2.3.2 Microscopy

Scanning electron microscopy (SEM) was performed using two different electron microscopes. For high resolution microanalysis a Hitachi SU-70 SEM with Schottky electron gun was used with a working distance of 15 mm and accelerating voltage of 15 kV. Energy dispersive X-ray spectroscopy (EDX) data were collected using INCA software (Oxford

Instruments). Morphology was assessed using secondary electron imaging (JSM-5500LV SEM, JEOL) with a working distance of 10 mm and accelerating voltage of 10 kV.

3.2.3.3 Interfilament resistance

Resistance measurements were performed using the 4-point method to determine the resistive barrier between filaments at 77 K. Current was supplied by a 1030 MicroCal Current Source (RS components) and measured using a Keithley 2000 multimeter. Voltage was measured using a Keithley 182 nanovoltmeter. Current was varied between -100 mA and +100 mA in 5 mA steps. Samples were cut down to 10 mm long from the original 24 mm and any silver at the sample edges was removed.

3.2.3.4 Critical current measurement

The critical currents of silver stabilised samples 40 mm in length were measured before and after striation. Only silver stabilised samples were tested due to the risk of sample burn out when the stabilizer was not present. Samples were tested at 77 K in liquid nitrogen and zero external magnetic field. Current was supplied (Hewlett Packard 6680A DC power supply) whilst the voltage was measured using a Keithley 182 nanovoltmeter. The current was ramped linearly at a rate of 8 A s^{-1}. Current contacts were 10 mm long at both ends of the sample. Voltage taps were soldered to the silver stabilizer of the tape surface and a criterion of 1 μV cm^{-1} was used to determine I_c. The entire system was controlled using software developed in-house.

3.2.3.5 AC loss measurement

The AC losses of 120 mm long samples were measured, by Lubomir Frolek, in an applied AC magnetic field by an established calibration free method [152]. Measurements were performed at 77 K at frequencies of 36, 72 and 144 Hz up to a maximum field of 100 mT (rms). The results were compared with calculations for full-width and multi-filamentary samples using the Brandt-Indenbom model for a superconducting strip in perpendicular AC field [98].

3.3 Striation morphology

3.3.1 Parameter selection

Single striations were made across the width of several 24 × 12 mm tape pieces and the trapped field profiles measured to determine the parameters required to separate the

superconducting regions. The needle height (*d* in Figure 54), relative linear speed and VMC input power were all varied. It was found that smaller distances, lower speeds and higher input power gave better separated filaments. Small distances, faster speeds and lower power gave narrower striations. Parameters were sought to achieve separated filaments with the minimum reduction in current carrying capacity.

The samples that were electrically characterised all had 4 filaments, were produced using a height, *d*, of 0.15 mm and VMC input power of 2 W. The frequency of discharge was ~20 Hz. The linear velocity of the needle for each of the 4 sample types presented are shown in Table 6.

Table 6. Parameters for the striated sample types reported.

Sample	Silver stabilizer	Linear velocity (mm s^{-1})
AgP01	Yes	0.5
AgP02	Yes	1.0
R01	No	1.0
R02	No	2.0

The large number of combinations available were not exhausted. Furthermore, other variables such as thickness of stabilizer, atmosphere composition and pressure, needle tip radius and multiple passes were not adjusted either, meaning there is still room for optimisation.

3.3.2 Single impact

Additionally, the morphology of an isolated single discharge impact was studied on a separate sample by using a high enough linear velocity to ensure the spark-impacts did not laterally overlap. The surface of the HTS layer following a single spark discharge impact is shown in Figure 55. There were 2 distinct regions within the impact zone. The EDX element maps, Figure 55(d) and (e), indicate that the central part was exposed Hastelloy whilst the surrounding area was severely degraded GdBCO. The GdBCO region appears to have melted then solidified during the sparking process, microcracks and pores are visible in Figure 55(b). The rapid melting and solidification ensured the damaged GdBCO did not carry a supercurrent

and acted as a resistive barrier between the superconducting filaments. This was confirmed by interfilament resistance measurements.
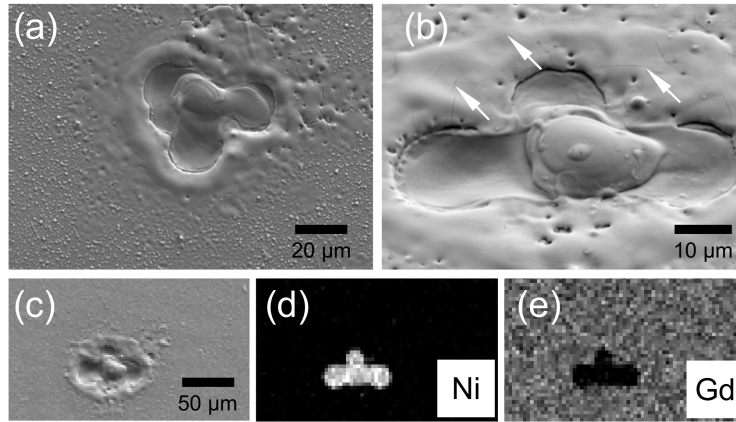
Figure 55. Tape surface of an un-stabilized sample after a single spark-discharge. (a) SEI at 0° tilt showing damaged region, (b) higher magnification SEI at 45° tilt. The white arrows highlight microcracks in the degraded GdBCO. (c) SEI and (d), (e) corresponding EDX element maps showing the distribution of Ni, a significant component in the Hastelloy substrate, and Gd a component of the HTS layer. Images courtesy of Dr Yina Guo.

3.3.3 Continuous striation

The filamentary samples were formed by using multiple, sequential, spark-discharges to produce continuous striations, as shown schematically in Figure 56. Figure 56 illustrates how a greater density of spark-discharges led to a wider striation width.
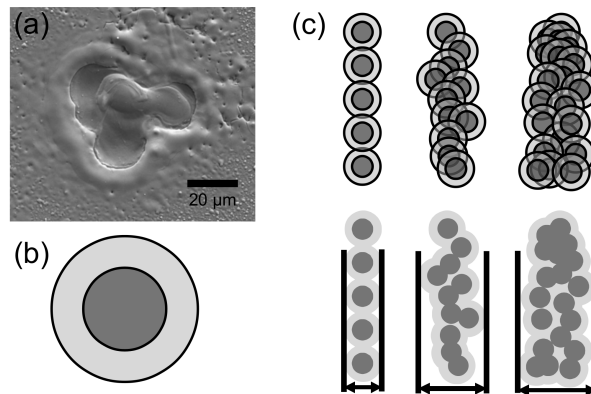
Figure 56. (a) SEI of single sparked region, (b) schematic equivalent with dark central disc representing the exposed Hastelloy and lighter region the degraded GdBCO surrounding it. (c) Schematics of ideal spark-discharge spacing (left), higher number of sparks per unit length (centre), even higher spark density (right), and the corresponding striation morphology and resulting width.

The ideal case, Figure 56(c, left) is feasible but requires greater spatial control of the sparking process. For example, using a sharper needle tip may enable more precise lateral

resolution because the electric field concentration is greater near a sharper point. A smaller tip would then allow the location of the plasma arc to be more accurately controlled. Figure 57 shows how the needle radius influences the magnitude and distribution of the electric field.
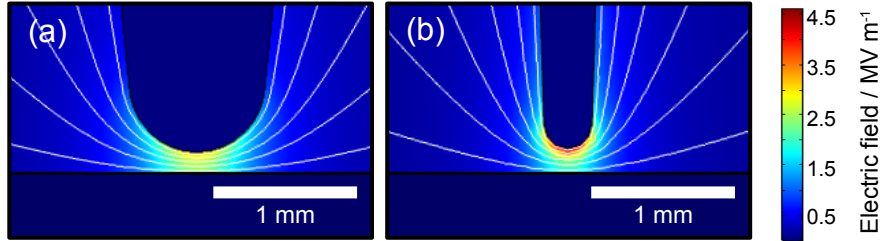
Figure 57. FEM simulation showing the electric field near the tip of a needle at 450 V with respect to ground with a tip radius of (a) 0.5 mm and (b) 0.15 mm. The sharper needle tip causes a greater electric field in a smaller region.

A surrounding atmosphere with a lower dielectric breakdown strength, such as argon [153], would require a lower voltage and the resulting spark would impart less energy, resulting in a smaller damaged region. Additionally, the use of reduced pressure may enhance the precision by extending the mean free path of charged species during the breakdown process and therefore result in a more stable arc. However, at very low pressures the small number of particles will limit the ionising avalanche process and lead to a very high breakdown voltage. Paschen's law is an experimental relationship between breakdown voltage and the product of electrode distance and gas pressure and shows a minimum for the breakdown voltage. Data from Beroual and Fofana [154] predicts the minimum voltage required for breakdown in air at a distance of 0.15 mm is 330 V and occurs at a pressure of 0.05 atm, whilst in argon it is 137 V and occurs at a pressure of 0.08 atm.

Qualitative testing was performed using different atmospheres. A collinear shroud of argon gas around the needle was tested but found to reduce the stability of the sparking process. This was attributed to the gas flow disrupting free motion of the ionic charge carriers. Stationary electrodes in an evacuated container (approximately -50 kPa gauge pressure) showed much more stable sparking and a more continuous arc between the electrodes than at atmospheric pressure. Further experiments in alternative atmospheres, including tape striation, were not performed due to the practical difficulty associated with enclosing the 3-axis stage in a sufficiently gas-tight housing. However, the principle of using a rough vacuum to improve spark-discharge stability was confirmed.

Photographs showing the surface of the four sample types are shown in Figure 58. The colour changes adjacent to the striations were due to partial oxidation of the surface due to the temperature of the spark plasma. The actual width of the damaged region was much narrower as was confirmed by SEM imaging, Figure 59, and I_c measurements, Table 8.
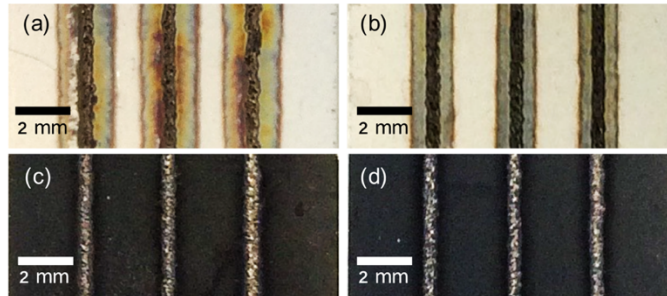
Figure 58. Photographs of the 4 sample types (a) AgP01, (b) AgP02, (c) R01, (d) R02. The striation width appears superficially larger than the damaged region due to colour changes from oxidation occurring during the high temperature spark-discharge.

Differences between the striations can be seen in Figure 59. The higher density of spark-discharges present in M_AgP01 and M_R01 led to more exposed Hastelloy regions and consequently a wider striation width than in M_AgP02 and M_R02 respectively.
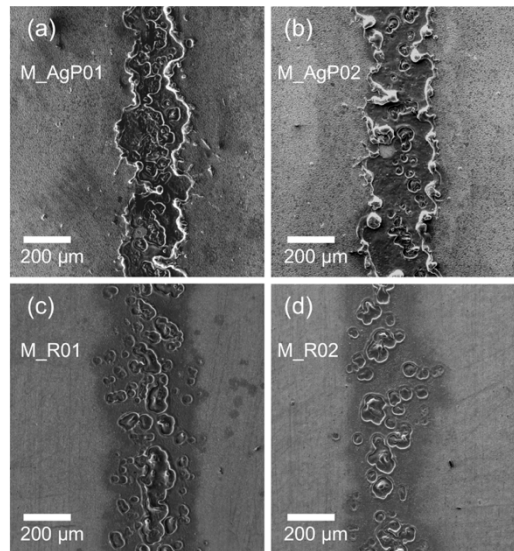
Figure 59. SEM micrographs (SEI) of the 4 sample types. The centres of the individual spark-discharge regions have not fully coalesced. The silver has been removed by the sparking process from the striated regions in the stabilised samples.

The width of the striations appeared similar for M_AgP01 and M_AgP02, however, the greater density of the exposed Hastelloy regions and proximity to the remaining silver in

M_AgP01 implied that the damaged GdBCO areas extended further. This was strengthened by the observation of a larger discoloured region visible in Figure 58.

3.4 Striated conductor properties

3.4.1 Trapped field profiles

The trapped field profiles for the 4 sample types are shown in Figure 60. Samples without silver stabilizer trap slightly lower fields than those with. This can be attributed to the slight damage caused by the etchant to the GdBCO surface during silver removal. All 4 samples showed 4 clear filaments visible, however, in sample M_R02 an indication of filament coupling can be seen between the far-right and centre-right filaments in Figure 60(d). The electrical connection between these filaments was confirmed by interfilament resistance measurements. These were the only filaments that were incompletely separated.
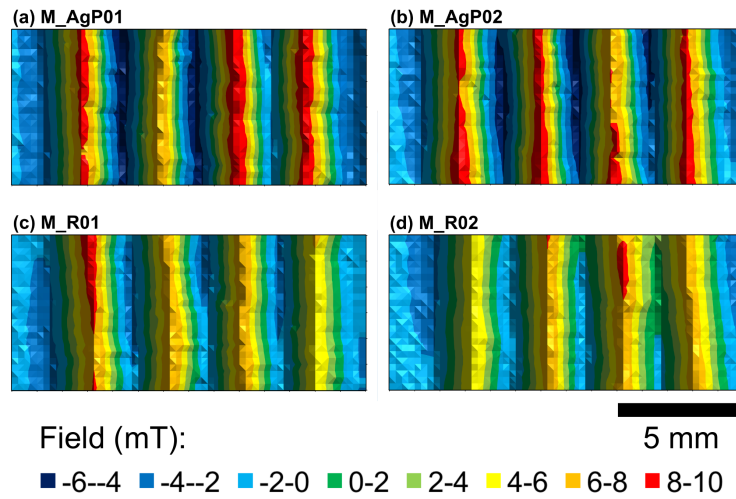
Figure 60. Surface plots showing the trapped field profiles for the 4 sample types. Samples were zero-field cooled to 77 K. The measurement height was 0.5 mm. Separated filaments can be seen in all samples, however the degree of separation is variable: M_R02 shows signs of slight filament coupling between the far-right and centre-right filaments.

3.4.2 Interfilament resistance

The average interfilament resistance for the 4 sample types is given in Table 7. Using the equivalent resistor model used in [99,111,155], Figure 61, and a resistivity of Hastelloy at 77 K of 1.24 $\mu W \cdot m$ [156] the barrier resistance, R_b, was calculated. The barrier resistance was much greater than the Hastelloy, suggesting good separation, which should prevent significant coupling losses. The barrier resistance was higher for the samples without the silver cap layer

because no re-deposition of Ag could occur to provide a lower resistance path. The samples striated using a lower linear velocity, and consequently a higher number of discharges per unit length, had a higher barrier resistance due to more extensively damaged interfilament material.
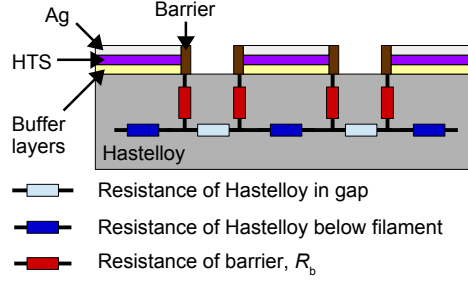
Figure 61. Equivalent resistor model used to determine the barrier resistance, R_b, when interfilament resistances were measured. Adapted from [111].

The barrier resistance values for the sparked samples are approximately 4 orders of magnitude higher than those reported by Demencik et al. [111] or Amemiya et al. [99], who reported interfilament resistance values for samples striated using laser ablation with groove widths of 20 μm and 100 μm respectively. However, they are approximately 1000 times lower than those reported by Machi et al. [157], who produced long lengths of filamentary tape using a two-step laser striation and chemical etching process leading to groove widths of 250 μm. However, the chemical etching led to additional loss of superconducting material and reduction in full tape I_c.

Table 7. Interfilament resistance for striated samples

Sample	Average interfilament resistance per metre / Ω·m	Calculated barrier resistance per metre / Ω·m
M_AgP01	0.80	0.40
M_AgP02	0.46	0.23
M_R01	1.76	0.88
M_R02	1.05	0.52

3.4.3 Critical current

The critical currents of the silver stabilized samples are given in Table 8. The effective width of the striations calculated from the reduction in current carrying capacity were

280 μm and 140 μm for I_AgP01 and I_AgP02 respectively. This was consistent with the SEM images in Figure 59(a) and (b) and suggested that the damaged HTS layer was slightly wider than visible full striation width for AgP01 and slightly narrower for AgP02. This meant that the spark-discharge process could produce striations that did not significantly damage the HTS layer beyond the impact region.

Table 8. Critical current for the silver stabilised striated samples.

Sample	I_c before striation / A	I_c after striation / A	Reduction in I_c / %
I_AgP01	443	413	6.8
I_AgP02	456	440	3.5

3.4.4 AC losses

The AC loss characteristics for each of the sample types are shown in Figure 62. All 4 have similar behaviour across the field range measured. The results were compared with the well verified Brandt-Indenbom model for a superconducting strip [98], using a full width of 12 mm and I_c of 450 A, equation (7), reproduced below.

$$Q = 4\mu_0 a^2 J_{cs} H_a \left(\frac{2J_{cs}}{\pi H_a}\right) \left\{ \ln \left[\cosh \left(\frac{\pi H_a}{J_{cs}} \right) \right] - \tanh \left(\frac{\pi H_a}{J_{cs}} \right) \right\} \tag{7}$$

Where Q is the energy loss per unit length per cycle, μ_0 is the permeability of free space, a is the half width of the superconductor, H_a is the applied external magnetic field and J_{cs} is the critical sheet current density (= $I_c/2a$).
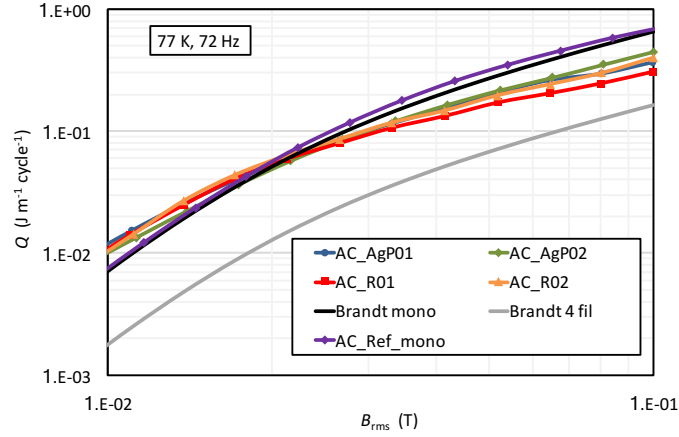
Figure 62. The magnetisation AC loss vs. AC external magnetic field (rms) for all 4 sample types and comparison with a reference monolithic sample and results from the Brandt-Indenbom model. The samples showed a reduction in the AC loss for higher applied fields of ~2 times, approximately half the expected 4-fold reduction. Samples measured at 77 K and 72 Hz. Data courtesy of Lubomir Frolek.

The samples all have a similar dependence with increasing applied field, with an approximate 2-fold reduction in AC loss at 100 mT (rms), relative to the monolithic case. To determine if the difference between measured and expected AC loss for the filamentary samples was due to filament coupling measurements at different frequencies were performed, Figure 63. Coupling losses have a frequency dependence, equation (14). Therefore, if significant coupling between filaments was present the loss measurements would show a strong frequency dependence.

$$p_C = \frac{(fLB_a)^2}{4\rho_\perp} \tag{14}$$

Where p_C is the power loss per unit volume, f is the frequency, L is the length of the tape (or length of twist pitch if twisted), B_a is the applied flux density magnitude and $\rho_\perp$ is the perpendicular resistivity across the tape width.
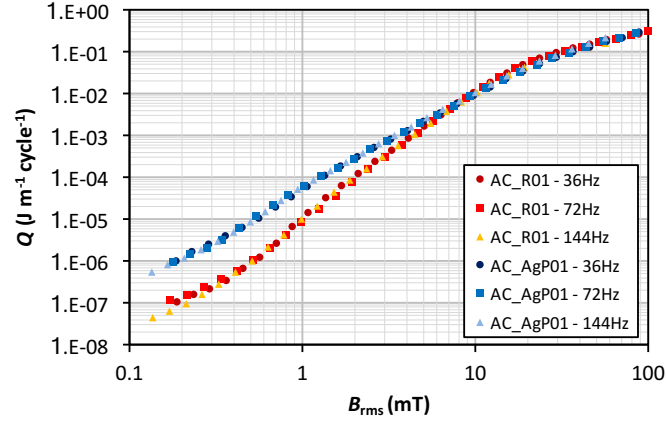
Figure 63. The measured AC loss at different frequencies as a function of applied field for two of the striated samples. The AC losses were independent of frequency. Data courtesy of Lubomir Frolek.

The AC loss of the striated samples, Figure 63, was virtually frequency independent. This agreed with the interfilament resistance measurements demonstrating that, on short samples, the barrier resistance between filaments was high. The slightly higher loss for the silver stabilised sample, AgP01, for field magnitudes below ~6 mT was ascribed to the presence of silver and was expected [111].

The higher-than-expected AC loss for filamentary samples and reference sample were attributed to two main contributions: I_c non-uniformities across the tape width [123,158] or, in the case of the filamentary samples, magnetic coupling of filaments [106]. The magnetic coupling of filaments was expected to be more significant at lower field magnitudes. The critical current non-uniformities can be inferred from trapped magnetic field measurements, Figure 64.
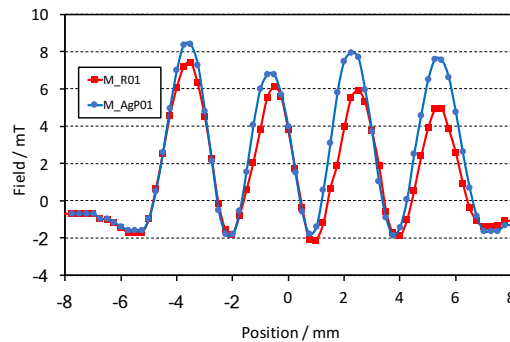
Figure 64. Trapped field profile across the width of two filamentary coated conductor samples. The inhomogeneity in I_c can be inferred from the slightly different trapped fields recorded for each separate filament. Measured at 77 K and at a height of 0.5 mm above the sample surface.

3.5 Partial striation and percolation

Whilst it has been stated, and demonstrated, that dividing a coated conductor into separate filaments is beneficial for reducing AC losses there is a danger of random defects blocking current percolation along the wire. Current blocking defects, such as high angle grain boundaries, are particularly problematic when many filaments with a small width are produced. The presence of defects has been used to explain the faster than anticipated drop in full tape I_c with increasing filament number for laser striated tapes [109,111].

To maintain reliability in long lengths Levin and Barnes [159] proposed the concept of multiply connected tapes. This concept involves deliberately introducing a sparse network of superconducting bridges between filaments to allow current redistribution. Different bridge designs such as "brick wall" and "fishnet" patterns, Figure 65, were demonstrated and found to result is acceptable AC loss reduction despite the filament connections [160,161]. Figure 65 also illustrates, in a simplified way, the benefit of multiple connections between filaments if there is a likelihood of defects blocking current flow in narrow filaments.
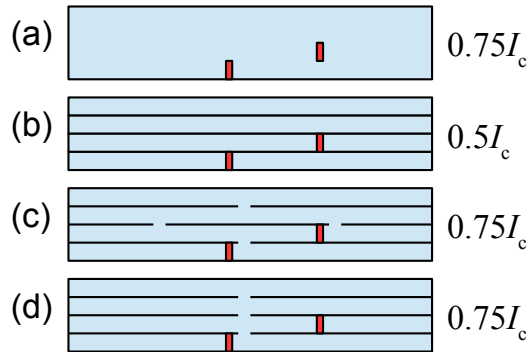
Figure 65. Plan view showing (a) an unstriated tape, (b) a fully striated tape, (c) a "brick wall" pattern bridged tape and (d) a "fishnet" pattern bridged tape. All examples also include two current blocking defects in red. The resulting fraction of the full width I_c is predicted for each example based on bridges allowing current redistribution. The benefit of a multiply connected structure is apparent when considering the current capacity after striation.

3.5.1 Continuous partial striation

The concept of bridging filaments can be extended to allow current redistribution along the entire length. If the striation does not completely prevent perpendicular current flow either by just suppressing J_c locally or by including many small bridges then current should be able to percolate around defects whilst the tape should have a lower total magnetic moment

and lower hysteretic AC loss than the unstriated case. The potential advantage of this concept is illustrated in Figure 66, when 2 defects are near each other.
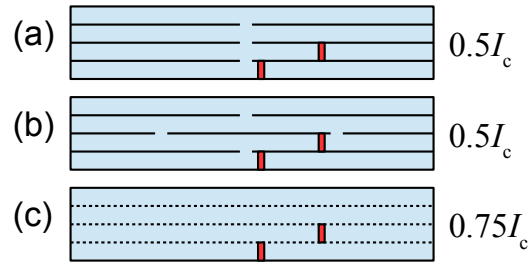
Figure 66. Schematic illustrating the expected current capacity for (a) the "fishnet" pattern, (b) the "brick wall" pattern and (c) the continuous partial striation concept when two defects (red blocks) are close to each other.

Clustering of defects is plausible if they are caused by transient changes in REBCO deposition or growth conditions. If too many defects occur between superconducting bridges the bridging will no longer provide the required reliability benefit. Having continuous partial striations should enable maximum reliability and current redistribution in the case of clustered defects.

The spark-discharge method for striating coated conductors described above has the potential to produce a partially bridged structure. The sparking frequency or linear speed of the needle can be varied to give a less dense pattern of spark impacts.

A silver-stabilised sample was striated using the same parameters as the fully striated samples reported above, except with a higher linear velocity of 2 mm s^{-1}. This led to incomplete separation of superconducting regions by leaving many small superconducting bridges between filaments. Figure 67 shows part of the trapped field profile, measured by Hall probe magnetometry, for two 24×12 mm tape pieces striated using different linear speeds.
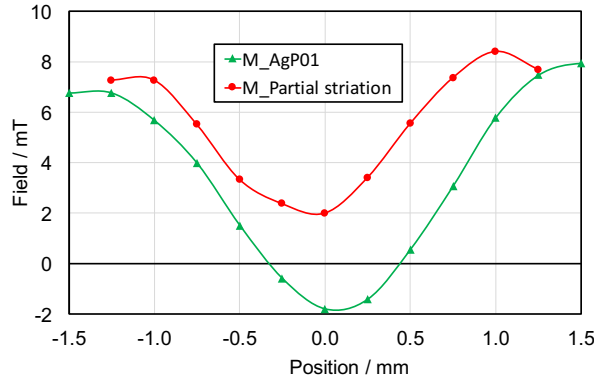
Figure 67. Partial trapped field profiles across sample pieces of tape when divided using different needle speeds. The partially divided tape was produced using a linear needle speed of 2 mm s⁻¹ and the fully striated tape used 0.5 mm s⁻¹. The positive trapped field value in the striated region (position 0 mm) indicates superconducting current circulating between filaments of the partially striated sample.

The greater trapped field in the damaged region for the partially striated sample indicates that whilst current flow across the striation is reduced there is still a superconducting bridge between separated parts.

3.5.2 AC losses

A 120 mm long piece of tape was divided into 4 partially bridged filaments and tested for AC loss relative to an unstriated reference sample, Figure 68.
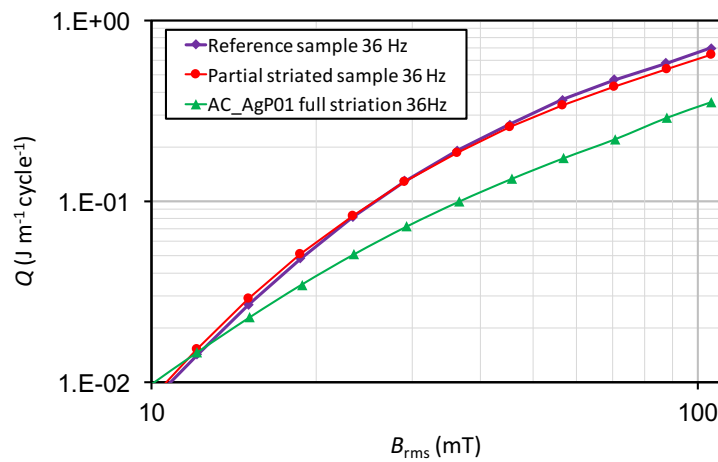
Figure 68. AC losses for a partially striated sample and comparison with fully and non-striated samples. The partially striated sample only shows a very small reduction in the measured AC loss relative to the unstriated sample. Samples measured at 77 K and 36 Hz. Data courtesy of Lubomir Frolek.

The partially striated sample only displayed ~7% lower losses at 100 mT (rms) than the non-striated reference sample compared with ~50% for the fully striated sample. The small

reduction in AC loss was ascribed to simply the loss of superconducting material and suppression of I_c in the striated regions.

It was expected that the hysteretic magnetisation losses should be lower for a sample with an anisotropic current capacity, where I_c was higher parallel to the striations than perpendicular, as discussed by Majoros et al. [161]. This was also expected from the Hall probe magnetometry measurements that indicated a reduced total magnetisation with suppressed trapped field in the striated regions. However, a lower AC loss was not observed for the partially striated sample. This was ascribed to the different behaviour occurring in the dynamic AC loss measurements compared with the trapped magnetic field behaviour.

The position of the bridging with respect to the sample geometry was thought to be important. The sample length can be considered equivalent to half the twist pitch for a longer conductor. The alternating magnetic field induces an electric field that depends on the proximity to the sample ends [162]. The alternating external magnetic field then induces currents to flow perpendicular to the filaments through the bridges. The further the bridge is from the sample centre-line the higher the electric field and therefore the higher the resulting power loss from current flow via the bridge. The network of closely spaced low current bridges present in the partially striated sample enable current transfer between filaments at all positions. Therefore, current flow perpendicular to the filaments causes sufficient dissipation to counteract any benefit from the striation. Due to the poor AC loss performance of the partially striated sample further characterisation was not performed.

3.6 Summary

In this chapter, a new method for producing filamentary coated conductors was presented. An electrical spark discharge was used to selectively degrade regions of superconducting tape. The robust, noncontact and scalable method was used to striate tapes into four filaments. The filamentary samples had lower AC losses than non-striated tapes with less than a 7% reduction in current carrying capacity. The high temperature plasma resulting from the spark impact at the tape surface resulted in exposed Hastelloy and severely degraded REBCO. This material in the striated regions provided an effective resistive barrier ($> 0.2 \ \Omega \cdot m$, several orders of magnitude higher than purely laser striated tapes) between adjacent filaments preventing excessive filament coupling.

The striated grooves were of the order of 200 μm wide and methods to reduce their size by improving the spark-discharge precision were discussed. The slightly higher than expected AC losses were discussed and ascribed to I_c non-uniformity with a contribution from magnetic coupling at low magnetic field amplitudes.

The use of spark-discharge plasma to produce robust, continuously bridged filamentary samples was discussed and demonstrated. The 'continuous partial striation' concept developed had the possibility to improve upon the reliability of fully striated and sparsely bridged tapes when considering clustered defects. However, the bridged samples showed a loss reduction of only 7% with respect to the non-striated reference. This was ascribed to the dissipative perpendicular current flow that could occur along the entire length of the sample, which counteracted the expected reduction in magnetisation expected by dividing the conductor into filaments. Only a sparse network of strategically placed superconducting bridges should be used when designing long lengths of filamentary coated conductor.

4 PRINTED STRUCTURES

Parts of the work presented in this chapter also appear in the following publications:

[126] S.C. Hopkins, D. Joseph, **T.B. Mitchell-Williams**, A. Calleja, V.R. Vlad, M. Vilardell, S. Ricart, X. Granados, T. Puig, X. Obradors, A. Usoskin, M. Falter, M. Bäcker, B.A. Glowacki, Inkjet printing of multifilamentary YBCO for low AC loss coated conductors, J. Phys. Conf. Ser. 507 (2014) 22010. doi:10.1088/1742-6596/507/2/022010.

and

[163] S.C. Hopkins, **T.B. Mitchell-Williams**, D.R. Vanden Bussche, A. Calleja, V.R. Vlad, M. Vilardell, X. Granados, T. Puig, X. Obradors, A. Usoskin, M. Soloviov, M. Vojenciak, F. Gomory, I.V. Driessche, M. Backer, B.A. Glowacki, Low AC Loss Inkjet-Printed Multifilamentary YBCO Coated Conductors, IEEE Trans. Appl. Supercond. 26 (2016). doi:10.1109/TASC.2016.2542001.

4.1 Inkjet printing HTS

Inkjet printing has been used as a chemical solution deposition method for the formation of HTS films since 2000 [164] and since then much work has been done improving the process, with the focus on filamentary structures [29,120,121,124,127,165–167]. Calvert [168] reviewed how inkjet printing began to be applied to functional materials and device fabrication. More recently Derby [169] provided an excellent review of inkjet printing of functional materials including technology, ink requirements, substrate-droplet interactions and pattern stability. The following sections will discuss the types of print head used in materials research, the rheological requirements for printable inks, and synthesis of solutions used to produce REBCO coated conductors.

4.1.1 Inkjet printing technology

Inkjet print heads can be categorised into two types: continuous inkjet (CIJ) and drop-on-demand (DoD). CIJ heads form a continuous stream of charged droplets that are selectively

electrostatically deflected to land on the substrate or into a gutter that recirculates the ink for re-use. DoD printing, on the other hand, only produces drops when a signal is received by the print head. CIJ is less commonly used in materials research due to the issues with solvent evaporation and contamination associated with recirculating the ink.

4.1.1.1 Drop-on-demand printheads

The three main types of DoD print head are thermal, piezoelectric and electromagnetic, Figure 69. A thermal inkjet print head uses a thin film heating element to locally vaporise fluid, causing a pressure wave to eject a droplet. In piezoelectric printing the pressure wave comes from a voltage waveform applied to a piezoelectric crystal in contact with the ink chamber. In both techniques, the ink is prevented from flowing out of the nozzle in the absence of an applied signal through surface tension at the orifice and an applied pressure to the fluid reservoir, with the magnitude and sense depending on relative positions of the nozzle and ink reservoir.

In electromagnetically actuated printheads a stopper blocks the nozzle orifice and a positive pressure is applied to the ink. When a signal is sent to a solenoid the stopper is raised and ink is released through the orifice. The length of time the orifice remains open (opening time) and the pressure on the fluid can be regulated to control drop formation.
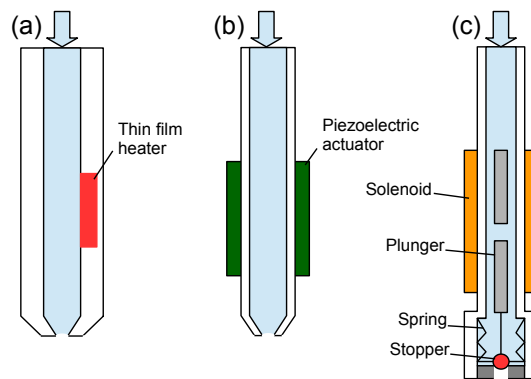
Figure 69. Schematic of (a) thermal, (b) piezoelectric and (c) electromagnetic inkjet nozzles. The arrow at the top indicates fluid flow direction. In electromagnetic printing the fluid is positively pressurised, whilst in thermal and piezoelectric the fluid is typically under slightly reduced pressure. Adapted from [169] and [170].

Although thermal printheads are commonly used in commercial and desktop printers it is less popular in functional materials deposition due to the restrictions on compatible materials. The bubble formation requires ink with sufficient volatility, plus there is the possibility that solvent loss during vaporisation could lead to destabilisation of the solution or

orifice blockage due to solid precipitation. The greater materials compatibility of piezoelectric and electromagnetic printheads enable a larger range of solvents and ink systems to be studied. Only a single nozzle for each type of printhead is shown in Figure 69, but multi-nozzle configurations are commercially available, e.g. Fujifilm [171], that have different geometries. For example, more compact designs and greater nozzle densities can be achieved by allowing adjacent nozzles to share actuators.

The key differences in jetting performance between piezoelectric and electromagnetic printheads are the maximum print frequency and minimum drop volume. The drop volume depends on the orifice diameter but typical values for piezoelectric and electromagnetic nozzles are 1–100 picolitres (pL) and 1–100 nanolitres (nL) respectively. Piezoelectric print heads can also operate at frequencies an order of magnitude greater than electromagnetic, ~10's kHz compared to ~1 kHz. However, electromagnetic print heads are typically more reliable due to the robust dispensing mechanism. An active piezoelectric nozzle is very sensitive to pressure fluctuations and, if a fine orifice is used, very susceptible to blockages from precipitates or other particles [172].

4.1.2 Ink requirements

The primary requirements for suitable solution inks for functional materials deposition are stability and printability. Stability is characterised by the absence of precipitation or rheological change during storage and use and is affected by metal ion concentration, the presence of particles and chelating ligands. Total metal ion concentrations can be adjusted; however, the resulting thickness of the oxide film will be affected. It has been suggested that REBCO films > 1 μm thick are the lower limit to producing coated conductors with industrially acceptable current capacities [173].

Particle contaminants in solution inks may act as nucleation sites for precipitation. Filtration using a suitably fine mesh can minimise their presence and is also important prior to inkjet printing to prevent nozzle blockage.

The choice of chelating ligand for the metal ions can affect the stability of precursor inks. Also, the presence of nanoparticles added to act as artificial pinning centres in YBCO films can affect the stability of solutions. For example, nanoparticles that are stably dispersed in standard trifluoroacetic acid (TFA) based REBCO precursor solutions may agglomerate in solutions with a lower fluorine content [174].

Printability of an ink is complex and depends on the viscosity, density and surface tension in addition to any shear rate dependent behaviour. Furthermore, the interaction with the substrate will determine the wetting behaviour and the ability to produce suitable films and patterns.

The density of inks is difficult to change significantly and will be around 1000 kg m^{-3} for alcoholic, organic acid or aqueous solutions. The viscosity and surface tension are more readily adjusted by, for example, polymeric additions or surfactants. Criteria for printability of a fluid can be expressed in terms of the dimensionless ratios used to analyse flows in fluid mechanics [169,175], specifically the Reynolds (*Re*), Weber (*We*), and Ohnesorge (*Oh*) numbers, equations (15), (16) and (17) respectively.

$$Re = \frac{v\rho a}{\eta} \tag{15}$$

$$We = \frac{v^2\rho a}{\gamma} \tag{16}$$

$$Oh = \frac{\sqrt{We}}{Re} = \frac{\eta}{\sqrt{\gamma\rho a}} \tag{17}$$

Where *v* is velocity, ρ density, *a* characteristic length, such as nozzle diameter, η is viscosity and γ is surface tension. It has been suggested by Reis and Derby [175], using experimental results for ceramic suspensions in paraffin wax, that stable drop formation occurs for 0.1 < *Oh* < 1, whilst Jang et al. [176] refined this to 0.07 < *Oh* < 0.25 for aqueous solutions containing ethylene glycol. It was observed that when values of *Oh* are too low many satellite drops form and if *Oh* is too high the fluid is too viscous. Further considerations of surface tension at the nozzle orifice and splashing on the substrate surface led to a regime of printability for a fluid in terms of the Reynolds and Weber numbers, Figure 70.
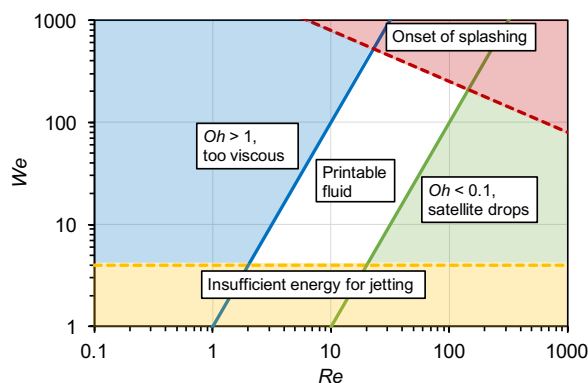
Figure 70. Printability of a fluid as a function of the Reynolds and Weber dimensionless parameters as determined by Reis and Derby. Adapted from [169].

4.2 Ink synthesis

4.2.1 REBCO

The majority of REBCO precursor solutions have been based on the trifluoroacetic acid–metal organic deposition route (TFA-MOD) [177]. This was first developed in 1988 by Gupta et al. [178,179]. As described earlier, the process of MOD is to deposit a solution containing the relevant metal ions on a suitable substrate and then subject the film to a pyrolysis step to remove the organics and leave inorganic oxides/fluorides well distributed in the correct stoichiometric ratio. These then go through subsequent growth and oxygenation heat treatments to form the REBCO structure and attain the correct oxygen stoichiometry. In practice the rare-earth and copper precursors are relatively easy to transform into REBCO but barium proves more problematic as it forms stable $BaCO_3$, which can be detrimental due to its relative stability. To avoid the formation of barium carbonates the fluoride route was developed, in which $Ba_{1-x}Y_xF_{2+x}$ forms during pyrolysis and is subsequently reacted with water vapour during the growth phase to form $Ba(O_xF_y)_2$, which then further reacts with the rare-earth and copper precursors to form REBCO [180].

However, despite its versatility and widespread use there are issues with the basic TFA-MOD route, including the liberation of hydrogen fluoride gas during heat treatment and environmental concerns about the use of fluorine. Furthermore, copper trifluoroacetate species are prone to sublimation during the pyrolysis stage and this can lead to film degradation [181]. The presence of water vapour suppresses the sublimation of copper fluoride species. To prevent film cracking and severe porosity developing during pyrolysis a slow heating rate can also be used. However, to enable a production rate that is suitable for reel-to-reel processing

higher heating rates need to be used. Several authors have reported using additives such as 2,4-pentanedione [66] and diethanolamine [182] that improve stress relaxation during organic removal and suppress copper trifluoroacetate species sublimation.

The environmental issue of fluorinated solvents is being addressed through the development of low fluorine and zero fluorine, aqueous, precursor solutions [183,184]. Good results have been reported for low fluorine methods, but aqueous solutions have yet to meet the performance of standard TFA-MOD films on technical coated conductor substrates.

In the work presented in this chapter both standard and reduced fluorine precursor solutions were used to grow REBCO films. Two different YBCO inks were used, one full-TFA YBCO ink synthesised using the method described below based on work done by Mariusz Mosiadz [29] and another received from a European collaborator (Oxolutia, Spain) as part of the EUROTAPES project. The synthesis of PrYBCO solutions was also performed, section 4.6.2.

4.2.1.1 Full-TFA YBCO synthesis

$YBa_2Cu_3O_{6.9}$ powder (99.90 %, SSC Inc.) was desiccated in a vacuum oven (150 °C, 22 h). The powder was added to acetone (99.8 %, Fisher Scientific) in the approximate ratio 3 g to 10 cm^3. Trifluoroacetic acid (TFA, 99 %, Sigma- Aldrich) was added drop-wise at room temperature with stirring. The TFA was added in the molar ratio 13:1, TFA:YBCO, with additional 10% molar excess acid to ensure complete reaction. The reaction mixture was refluxed with vigorous stirring (70 °C, 20 h) to yield a clear, blue solution. Trifluoroacetic anhydride (TFAA, 99%, Acros Organics) was added drop-wise at room temperature with stirring to remove water (approximately equal volume ratio TFAA:TFA). The solution was refluxed (70 °C, 1 h) to yield a clear, green solution. Excess solvent was removed in a rotary evaporator to yield a viscous dark green gel. This was diluted with anhydrous methanol (MeOH, 99.8 %, Sigma-Aldrich). A quantity of 2,4-pentanedione (acac) was added to give a molar ratio 0.64:1, acac:yttrium. The solution used had a 0.5 M total metal ion concentration. The solution was filtered (1 μm, glass fibre) and stored under argon.

4.2.1.2 Low fluorine YBCO ink

The YBCO precursor ink received from Oxolutia, referred to as "OxoYBCO" hereafter, was produced from yttrium trifluoroacetate, barium acetate and copper acetate. These were dissolved in propionic acid (PPA) before dilution with methanol (MeOH) and

addition of triethanolamine (TEA). This produced an ink with a fluorine content only 23% that of the standard full TFA-YBCO ink and was less sensitive to humidity and moisture. The ink had a total metal ion concentration of 0.5 M.

4.2.2 Cerium oxide

Oxide buffer and barrier layers require less complex precursor solutions than REBCO due to the relative simplicity of the final phase. For example, cerium oxide, CeO_2, requires only one metal ion in solution and can be formed from the decomposition of a stable solution of the ions in propionic acid [29].

A ceria precursor ink was synthesised to print barrier strips for the "inverse printed" samples, described earlier in section 1.5.4 and below in section 4.5.1, using the following method. Cerium (III) acetate hydrate (99.90%, Sigma-Aldrich) was desiccated in a vacuum oven (150 °C, 22 h). The powder was added to propionic acid (PPA, 99%, Sigma-Aldrich) in the approximate molar ratio 1:14 (cerium acetate : PPA) and heated under reflux until a clear yellow solution formed (120 °C, 3 h). This was diluted with PPA to form a solution of 0.5 M metal ion concentration. The solution was filtered (0.2 μm, PTFE membrane) and stored under argon.

4.3 Drop visualisation

Before deposition of patterns and coatings drop visualisation was carried out on inks to determine suitable parameters for stable jetting.

4.3.1 Visualisation system

The drop imaging system consisted of a collinear LED strobe and camera (F-125 Stingray, Allied Vision Technologies), Figure 71. The camera was fitted with a telephoto lens with adjustable zoom. Synchronised signals to the nozzle controllers and the strobe enabled images to be collected with an adjustable delay time. The maximum framerate of the camera was 30 frames per second. Using different delay times between nozzle actuation and image capture enabled the formation of droplets to be imaged in microsecond time steps. This meant that the sequence of images collected for a given ink, nozzle and parameter combination was for a series of different drops.
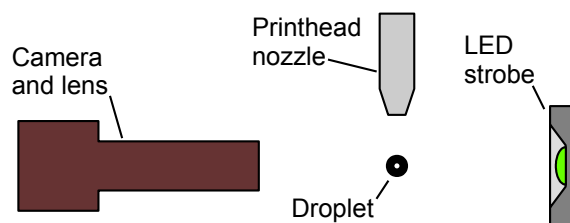
Figure 71. Relative positions of the components of the drop visualisation system.

Software processed and analysed image sequences generated by the visualisation system. The software automatically cleaned, cropped, thresholded and quantitatively analysed each image. The drop volume was calculated assuming cylindrical rotation symmetry and the centre of mass was used to determine the drop velocity. The number of droplets produced, their volume and their velocity were the primary statistics used to compare the influence of printing parameters on ink jetting. Whilst, qualitative observations on the stability and reproducibility of jetting were also used to decide on appropriate parameters.

4.3.2 Optimisation of jetting for different inks

Different ink and nozzle combinations were used depending on the desired pattern. Only single nozzle printheads were used in the current work to simplify the optimisation. Generally, an electromagnetic nozzle (SMLD 300 with 100 μm diameter orifice, Fritz Gyger AG) was used for depositing continuous coatings or when positional accuracy was less important. A piezoelectric nozzle (MJ-AT with 60 μm diameter orifice, MicroFab Technologies Inc.) was used for printing filamentary coatings, where the smaller droplet size enabled better spatial resolution.

4.3.2.1 Electromagnetic nozzle printing

The electromagnetic nozzle was used to deposit the full TFA-YBCO and the OxoYBCO ink. The nozzle opening time and pressure applied to the ink reservoir were varied in the range 80–500 μs and 90–400 mbar respectively. An example of good and poor jetting for the full TFA-YBCO ink is shown in Figure 72.
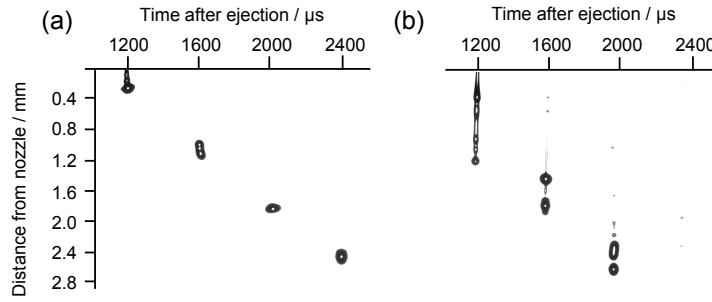
Figure 72. Image sequence demonstrating (a) good and (b) poor jetting and drop formation for the full TFA-YBCO ink. The parameters for (a) were 90 μs opening time and 100 mbar pressure whilst for (b) were 150 μs and 200 mbar. The good jetting formed a single droplet with a volume of 5.8 nL and velocity 1.8 m s^{-1}.

Good jetting was characterised by the reliable formation of a single well defined drop. Poor jetting resulted in a long ligament that fragmented into multiple satellite drops. The formation of large, or multiple, drops was avoided to ensure accurate and uniform deposition. Additionally, parameters that gave low drop velocities, below ~0.5 m s^{-1}, were not used, which ensured accurate placement by minimising lateral drift on route to the substrate. It was found that higher pressures and longer opening times both gave larger drops with higher velocity. An image sequence illustrating good and poor jetting for the OxoYBCO ink is shown in Figure 73. A summary of the jetting parameters used and the resulting drop volumes and velocities are given in Table 9.
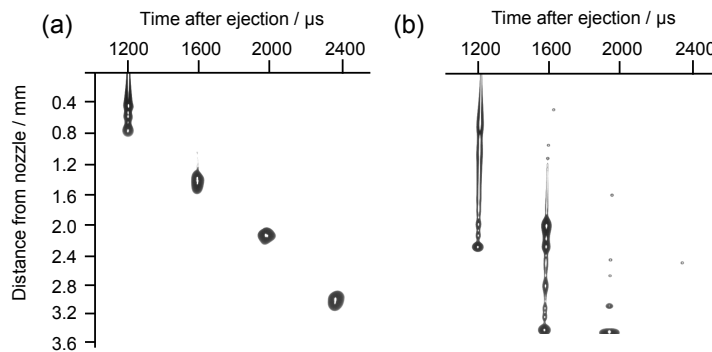
Figure 73. Image sequence demonstrating (a) good and (b) poor jetting and drop formation for the OxoYBCO ink. The parameters for (a) were 100 μs opening time and 100 mbar pressure whilst for (b) were 200 μs and 200 mbar. The good jetting formed a single droplet with a volume of 6.8 nL and velocity 1.9 m s^{-1}

4.3.2.2 Piezoelectric nozzle printing

The piezoelectric nozzle was used to deposit the ceria precursor and OxoYBCO inks when filamentary structures were required. The waveform driving the piezoelectric actuator

was more complex, Figure 74, with several adjustable parameters including peak voltage, ramp rate and dwell. The pressure applied to the ink reservoir was not adjusted to tune jetting but was carefully controlled using a regulator and pressure gauge to keep the fluid meniscus at the nozzle orifice.
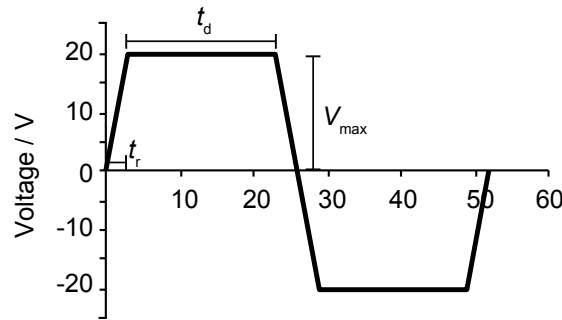
Figure 74. Schematic showing a characteristic waveform applied to the piezoelectric actuator during jetting. The waveform was symmetric and bipolar. Maximum voltage, V_{max}, dwell time, t_d, and ramp time, t_r, were adjusted to tune the jetting.

Whilst it was possible to fully specify the waveform a symmetric, bipolar type was chosen to reduce the number of variables and maintain a manageable parameter space. The number of combinations to test and analyse increases exponentially with the number of variables. Voltages were varied in the range 18–50 V, dwell times 10–35 μs and ramp times 1.5–7 μs. The range of ramp rates used was 2.9–26.7 V μs^{-1}.

Examples of good stable jetting and poor jetting resulting in satellite drops are shown in Figure 75. Drop volumes are approximately two orders of magnitude lower than those produced during stable jetting using the electromagnetic nozzle.
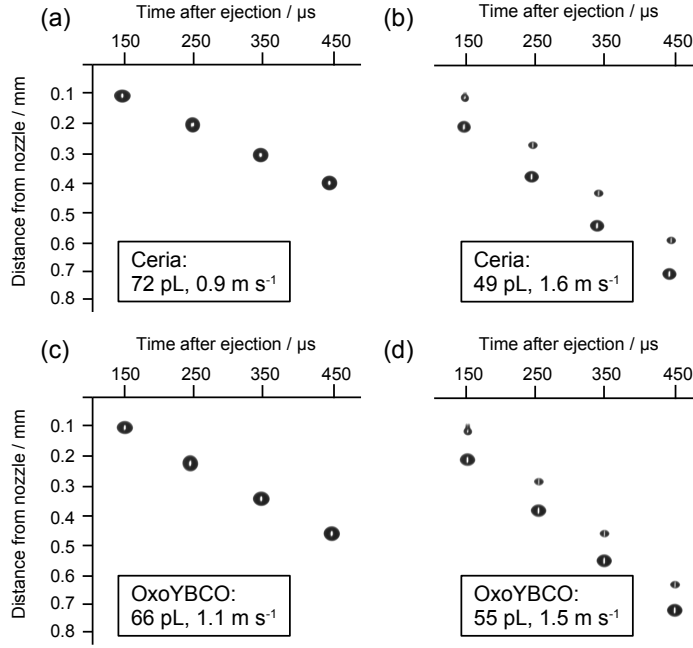
Figure 75. Image sequences showing stable jetting producing a single drop for (a) the ceria precursor ink and (c) the OxoYBCO ink. Also, image sequences showing jetting that results in satellite drop formation for (b) the ceria and (d) the OxoYBCO inks. All sequences shown are for the same V_{max} of 30 V and t_r of 3 µs, the differences are in the dwell time, t_d. (a) and (c) are for a dwell time of 30 µs whilst (b) is for 15 µs and (d) 20 µs.

The effects on drop volume and velocity with changing V_{max} and t_d for the ceria ink are displayed in Figure 76. A similar dependence was observed with the OxoYBCO ink.
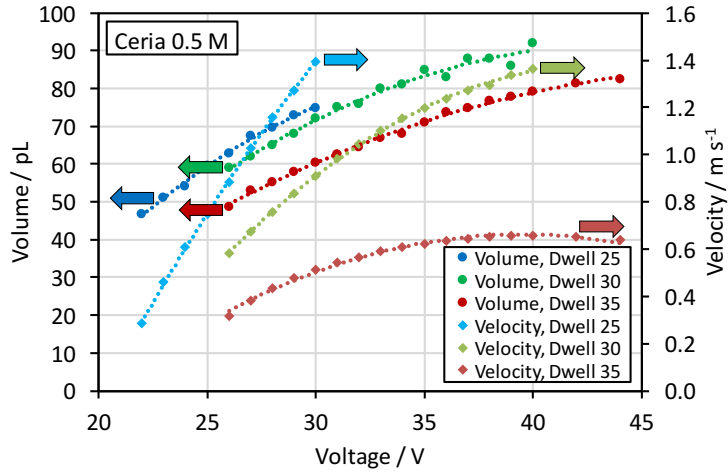
Figure 76. Drop volume and velocity dependence on V_{max} for three dwell times for the ceria ink. All data are for a constant ramp time of 3 µs. Drop volume and velocity both increase with higher voltages and shorter dwell times.

The data in Figure 76 are for a single ramp time, therefore, the change in voltage shows how the droplet properties depend on the ramp rate. Higher ramp rates led to larger

volumes and greater velocities. Furthermore, the shorter the dwell time the higher the velocity and volume. However, short dwell times also tended to be the least stable, with jetting at the lowest values becoming unreliable and the formation of secondary satellite droplets becoming more common. The parameters used for deposition of the various inks are summarised in Table 9.

Table 9. Printing parameters and drop properties for the nozzle and ink combinations used.

	Electromagentic		Piezoelectric	
Ink	Full TFA-YBCO	OxoYBCO	Ceria	OxoYBCO
Pressure; opening time	100 mbar; 90 μs	100 mbar; 100 μs	–	–
V_{max}; t_d; t_r	–	–	30 V; 30 μs; 3 μs	30 V; 30 μs; 3 μs
Drop volume (pL)	5800	6800	72	66
Drop velocity (m s^{-1})	1.8	1.9	0.9	1.1

4.4 Direct filament printing

Inkjet printing enables deposition of filamentary conductors without the need for subtractive post processing. Directly printing filaments has the advantage of simplifying the production route, when compared with other techniques such as inverse printing, section 4.5. A key challenge with directly-printed REBCO filaments is to increase the final filament thickness out-of-plane whilst retaining narrow tracks in-plane. The final film thickness depends on the concentration of metal ion concentration and the spreading of the ink. The REBCO thickness can be increased either by increasing the ink concentration, reducing the lateral spacing between drops or by performing repeated printing passes. More concentrated inks were challenging to jet using the piezoelectric nozzle and it was found that only a limited range of drop separations led to uniform tracks, e.g. [185], hence the number of printing passes was investigated.

4.4.1 Sample production

The substrate was stainless steel (SS) coated with a biaxially textured, alternating beam assisted deposition (ABAD) yttrium stabilised zirconia (YSZ) and zirconium doped ceria (CZO) layer. This substrate was ultrasonicated in ethanol prior to inkjet deposition.

The OxoYBCO ink was deposited using the piezoelectric nozzle with parameters given in Table 9. The printhead was scanned above the surface using a 3-axis stage (developed in-house) with a linear speed of 10 mm s^{-1}. The drop spacing was 0.08 mm and drops were deposited in a square array. The spacing was decided by studying drop replicas on the substrate and observing the resulting line widths using optical microscopy. Three filaments, each 2 mm wide, were printed. The filaments were formed using 1, 2 and 3 printing passes. Ink was left to dry at ambient temperature in air for 60 s between printing passes.

The sample was thermally processed in a 2-step heat treatment. First, the temperature was ramped slowly to 500 °C in a humid oxygen atmosphere. The second step was a growth and oxygenation process where the YBCO phase was grown in a low partial pressure of oxygen (200 ppm O_2 in argon) at 810 °C before oxygenating at 450 °C in pure oxygen for 3.5 hours, Figure 77. Temperature set point and gas switching were computer controlled and logged. The growth and oxygenation steps for the reported samples were performed by Dr Roxana Vlad at Oxolutia, Spain.
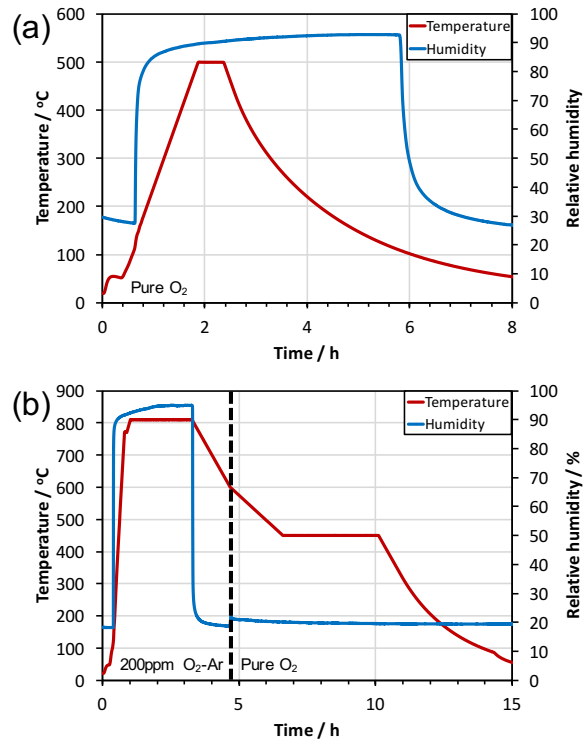
Figure 77. Temperature and humidity profiles for (a) the pyrolysis stage and (b) the growth and oxygenation of the thermal processing for YBCO films. The pyrolysis was conducted in flowing oxygen. The growth was in 200 ppm oxygen (balance argon) and oxygenation was in pure oxygen.

4.4.2 Sample properties

The superconducting properties of the sample were characterised using scanning Hall probe magnetometry as described earlier in section 2.3.1.3, except with a measurement height of 0.5 mm. However, the substrate received (as part of the EUROTAPES project) had a significant curvature and therefore had to be mounted for scanning without bending the sample, Figure 78.
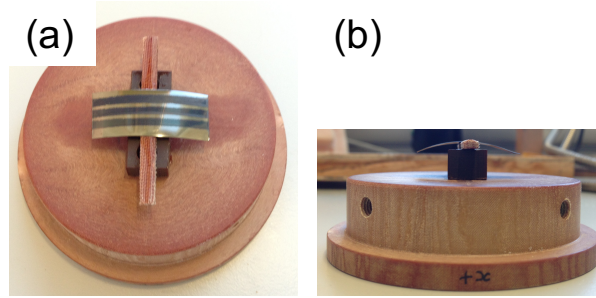
Figure 78. Photographs showing (a) plan view and (b) profile view of the directly printed sample mounted for Hall probe mapping. The significant curvature of the substrate made characterisation challenging.

The trapped field profile for the sample, Figure 79, indicated that the filament produced using 2 printing passes had the highest critical current. However, the value was not double the single pass filament implying the progression was not linear. Additionally, the strip formed with 3 passes showed the lowest critical current implying that continued increase in I_c was not possible simply by increasing the number of passes.
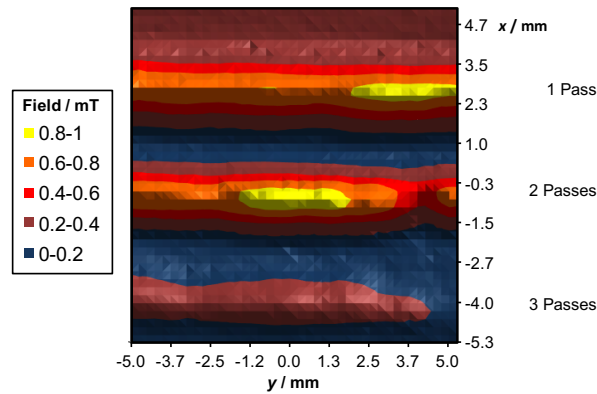
Figure 79. Trapped field distribution for the directly printed sample showing 3 superconducting filaments each formed using a different number of printing passes.

The non-linear increase in I_c with increasing film thickness has been reported for films grown by many different techniques [186] and Wang et al. [187] explained the phenomenon by measuring interfacial misfit dislocations near the substrate/film interface. The

misfit dislocations were thought to be effective pinning centres, increasing the critical current density. For thicker films the interfacial misfit dislocation density was lower. Multilayering with CeO_2 increased the misfit dislocation density again and enabled thicker films with high J_c to be produced [188].

The difference between the single and two print pass strips can be explained by the reduction in interfacial dislocation density and therefore reduction in the average J_c when growing a thicker film. However, the lower I_c of the 3-pass filament requires an explanation specific to the heat treatment of MOD derived REBCO films. When films are thermally treated the process liberates gases and the film shrinks in thickness. This can lead to film cracking and porosity during the pyrolysis stage. To reduce the impact of this and enable thicker films Holesinger et al. [189] have demonstrated multilayer, sequentially deposited and pyrolysed MOD REBCO films.

Thickness variation in the printed films may also impact the optimum growth conditions [124,190]. This is important for directly printed films due to the inherent film thickness variation across the width of a single filament, Figure 80. This film thickness variation makes it difficult to optimise the REBCO growth process for the full width of the filaments meaning some of the critical current capacity expected from the superconductor is lost. To avoid this fundamental difficulty associated with directly printed filaments the concept of "inverse" printing was investigated.
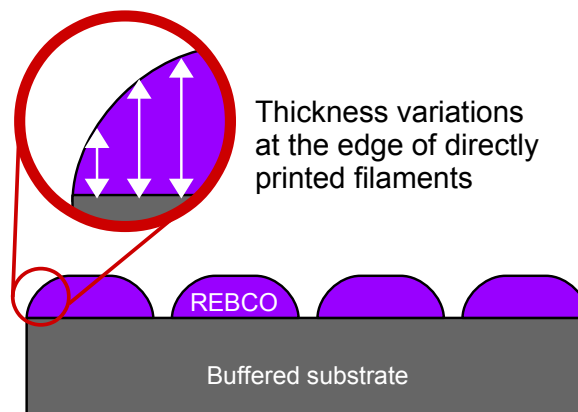
Figure 80. Schematic showing cross section of directly printed filaments and their resulting thickness variation at the edge. The aspect ratio of the filaments is of the order of 1000:1. Thickness variation makes it difficult to optimise REBCO growth across the full width.

4.5 Inverse filament patterning

4.5.1 Concept

As discussed above, the film thickness variations across the width of directly printed samples motivated the study of alternative methods to pattern the YBCO film into separate filaments. The patented "inverse" printing technique [125], Figure 81, involves depositing a compatible, insulating barrier material such as CeO_2 as fine filaments, then simply heat treating them before depositing REBCO precursor solution across the entire surface. The sample then goes through the standard thermal treatment and the barrier strips prevent correctly textured REBCO growing above them, leading to separated filaments.
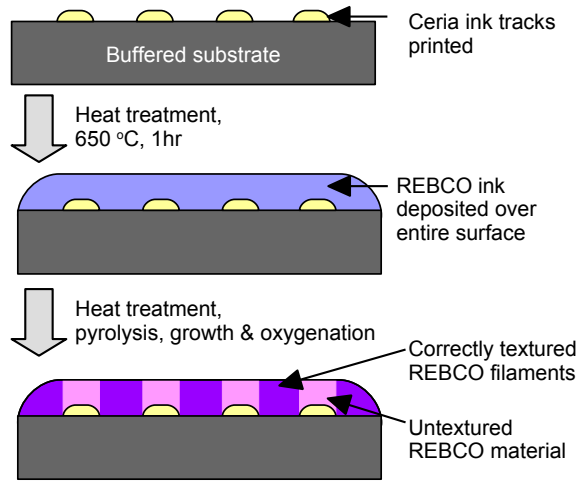
Figure 81. Schematic showing the inverse printing process. Untextured barrier material (e.g. ceria) prevents textured, superconducting REBCO from growing locally above, leading to separated filaments.

An advantage of this technique is that the precise deposition required for filament patterning is de-coupled from the REBCO precursor solution deposition and growth. This approach has been demonstrated for printed barriers and MOCVD grown REBCO [127] but the work reported here includes the only examples for fully printed conductors.

4.5.2 Sample production

Piezoelectric nozzle deposition was used for printing fine tracks of the ceria precursor ink, which acted as the insulating barrier material for both inverse printed samples, IP1 and IP2. The jetting parameters are given in Table 9. The velocity of the print head was 10 mm s^{-1}. The drop separations used are provided in Table 10. The substrate was the same as described in section 4.4.1; SS|ABAD-YSZ|CZO.

Table 10. Drop spacing used for producing the inverse printed samples.

Sample	Ceria ink	OxoYBCO ink
IP1	4 lines, 2.5 mm apart, 0.025 mm longitudinal drop spacing	0.7 mm spaced square array
IP2	4 lines, 2.5 mm apart, 0.040 mm longitudinal drop spacing	0.6 mm spaced square array

Following ceria ink deposition, the samples were subjected to a simple heat treatment where they were heated to 650 °C at a rate of 5 K min^{-1}, held for 1 hour before cooling back to room temperature. This resulted in the formation of non-textured CeO_2, confirmed by the presence of the $CeO_2(111)$ peak observed in X-ray diffraction (XRD) using the Bragg-Brentano geometry. The samples were then fully overprinted with the OxoYBCO ink using a square array of drops deposited with the electromagnetic nozzle. The samples then went through the same heat treatments as the directly printed sample described above, Figure 77, again with the growth and oxygenation stages performed by Dr Roxana Vlad at Oxolutia.

The OxoYBCO ink was chosen for producing the superconducting phase because it was more reliable for producing superconducting YBCO following heat treatment. Non-filamentary coated samples were produced using the full TFA-YBCO ink, however, despite the correctly textured phases being detected using x-ray diffraction (XRD) the samples did not display reliable superconducting properties, this is discussed further in section 4.6.4.3.

4.5.3 Conductor properties

Scanning Hall probe magnetometry was performed as described in section 2.3.1.3, with a lateral step size of 0.2 mm and measurement height of 0.35 mm. The trapped field profiles for both samples IP1 and IP2, Figure 82, show that separate superconducting filaments were formed.
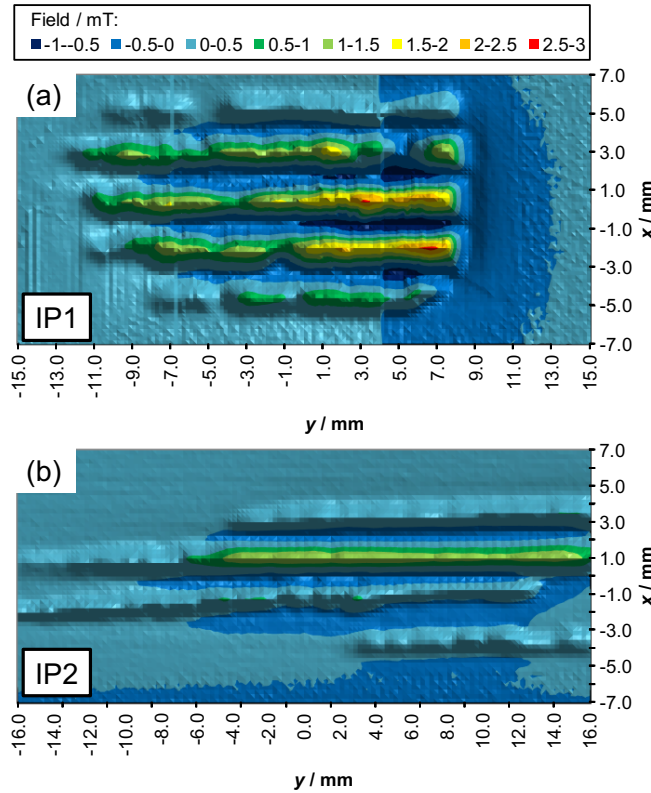
Figure 82. Trapped field profiles for samples (a) IP1 and (b) IP2. Distinct but non-uniform superconducting filaments can seen for both samples.

However, the uniformity and length of the superconducting filaments is not good. Photographs of both samples, Figure 83, illustrate some of the defects present that contributed to poor superconducting filaments.
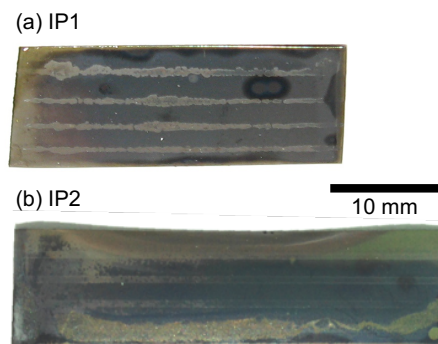
Figure 83. Photos showing the samples (a) IP1 and (b) IP2 after full processing. The ceria tracks are more uniform in IP2 but the YBCO at the sample edges is poorer. Cracked regions and incompletely converted phases are visible along the top and bottom edges of IP2.

Additionally, as experienced with the substrate used for direct filament printing, the excessive curvature of the substrate contributed to non-uniform properties across the tape

width and length. Figure 84 shows the curvature of several substrate pieces used for sample preparation. The curvature in the width direction of IP2 caused non-uniform wetting, leading to a build-up of ink along one edge, which then cracked during pyrolysis. The ends of the samples appeared to be affected by the flow of gas during thermal processing. The leading edge appeared to convert to superconducting YBCO more readily than the trailing edge suggesting that either HF gas evolution from the sample upstream or stagnant flow at the surface prevented full conversion of parts of the film.
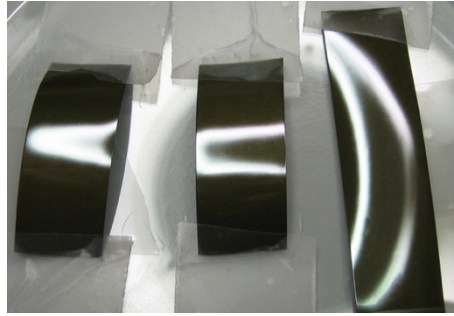
Figure 84. Photo showing as received pieces of buffered substrate. The reflected light illustrates the curvature of the tape pieces.

The sample IP1 was also tested for AC losses, by Dr Mykola Soloviov, using the procedure described in section 3.2.3.5. The AC loss data was compared with the Brandt-Indenbom model, equation (7), for an equivalent full-width sample using an equivalent surface current of 4100 A m^{-1}, Figure 85.
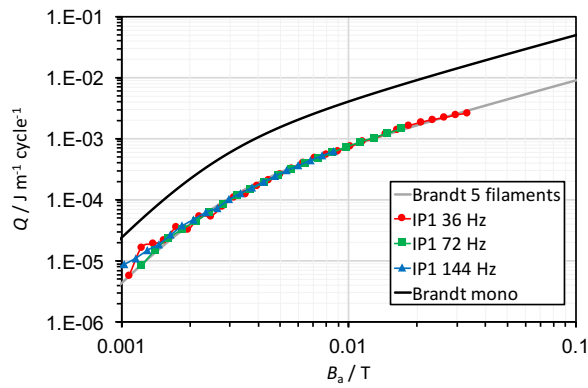
Figure 85. Measured and calculated AC losses for sample IP1. Calculated values used a sample length of 11 mm, filament width of 2.3 mm and surface current density of 4100 A m^{-1}. Sample tested at 77 K.

The I_c for the sample was calculated using equation (18), derived by Dr Anup Patel, which related the peak trapped field magnitude, B_0, above a thin rectangular film to the surface current density, J_s.

$$J_S = \frac{2\pi f B_0}{\mu_0 \ln\left[\left(\frac{a}{x}\right)^2 + 1\right]} \tag{18}$$

Where a is the half width of the rectangle, x is the measurement height, μ_0 is the permeability of free space and f is a correction factor to account for ferromagnetic substrates ($f = 1$ for non-magnetic substrate). Using a trapped field value of 2 mT gave an estimate of 4100 A m^{-1} for J_s, corresponding to a tape I_c of 49 A for the full 12 mm width. The AC loss measurements do indicate that, as expected, the filaments result in lower AC loss than an equivalent monolithic sample. However, the comparison has several limitations including sample length and uniformity. It is clear from the Hall scan data that the filaments are not uniform and so a single value of I_c required for the Brandt-Indenbom calculation results in significant error. Particularly as the real I_c is likely to be lower than the calculated value in several of the filaments, meaning the losses will naturally be lower than those predicted using the Brandt model. Furthermore, the short sample length also reduces precision in the measurement system.

The main performance limitations for the inverse printed samples were due to the lack of homogeneity in the substrate and uniformity of deposition and growth. Several of the causes, such as substrate curvature and gas flow over the edges of the sample, are related to using short samples. Preliminary results, reported by collaborators at Oxolutia, on longer samples using reel-to-reel type manufacturing, where the tape tension and perpendicular gas flow reduce those issues, were promising and 30 cm long samples have been produced.

4.6 Toward a Rutherford architecture

The inverse printing architecture aimed to solve some of the practical production problems with printing filamentary REBCO coated conductors. However, even with a fully optimised process the lack of filament transposition means the tape still needs to be twisted to reduce the effect of coupling loss.

Oberly et al. [191] proposed an approach for developing a low AC loss coated conductor design that mimics the Rutherford cable architecture. The twist pitch length can be made much smaller than achievable by simply twisting a striated tape, meaning coupling losses can be kept low even at high AC frequencies. The Rutherford cable architecture is shown in Figure 86.
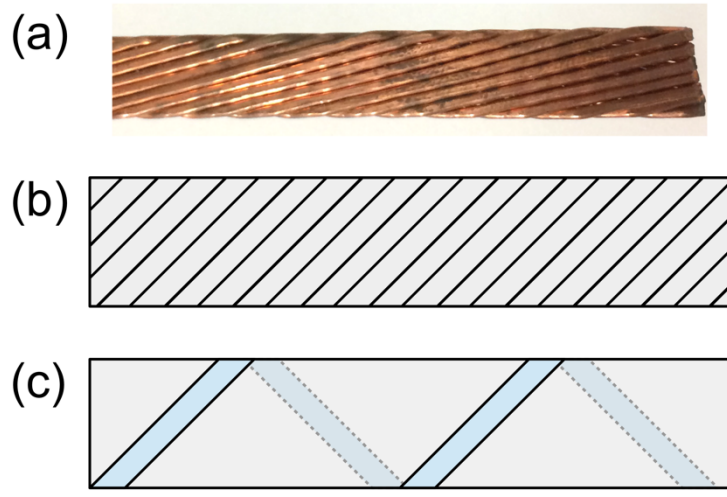
Figure 86. (a) Photograph of traditional metallic Rutherford cable. (b) Schematic diagram showing top surface and (c) winding path of a single filament.

Producing a coated conductor with the Rutherford cable architecture is much more complex than producing the same design using traditional metallic low temperature superconductors. The strains that would be induced by the tight curvature required in the tapes at the edges of the cable would supress superconductivity or damage the HTS layer. This leads to two feasible approaches; bonding multiple, patterned tapes together, or, producing the layered structure additively during manufacture. The first approach has been demonstrated by Abraimov et al. [192], where two patterned tapes were attached face-to-face with resistive joints, Figure 87. The sample demonstrated low AC losses over a wide range of frequencies confirming the benefit of the design in reducing coupling losses. However, the approach resulted in the loss of 50% of the superconducting layer through destructive chemical etching.
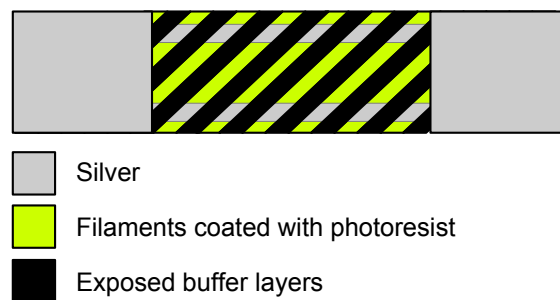
Figure 87. Diagram showing the pattern etched into coated conductor tape by Abraimov et al. [192]. Two tapes were then bonded face-to-face by diffusion bonding the exposed silver on the filaments. Current could then only follow the transposed path of connect filaments.

Ben Yahia et al. [193] have recently demonstrated a similar process with laser striated tapes and a different geometry to transpose filaments, Figure 88. This results in lower materials wastage but still requires complex processing and resistive joints between tapes.
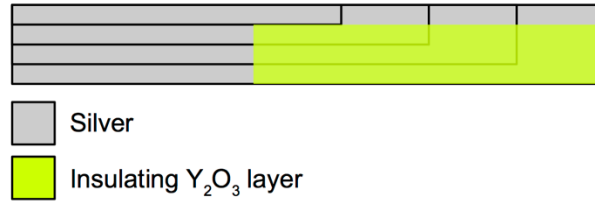
Figure 88. Diagram showing patterned tape structure used by Ben Yahia et al. [193]. A second tape patterned in the same way is then rotated by 180 degrees and bonded face-to-face with the first. The overlap area can be adjusted to ensure a low resistance contact. The contact area needs to be precisely aligned to prevent recoupling of filaments.

The concept presented in the current work is to use selective deposition possible via inkjet printing to additively manufacture a coated conductor that follows the Rutherford cable architecture. The processing steps are shown schematically in Figure 89.
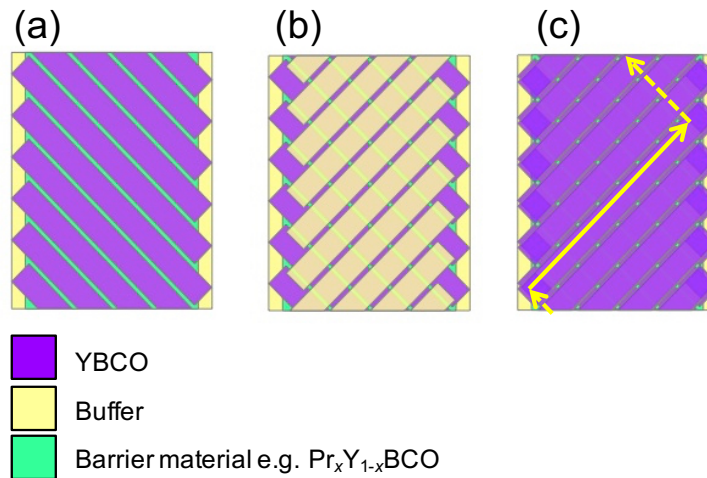
Figure 89. Schematic steps to produce a printed Rutherford architecture coated conductor. (a) Deposit and thermally process filaments of YBCO precursor simultaneously with an ink that will form an isostructural insulating material such that a flat layer forms. (b) Deposit and thermally process filaments/continuous layer of thin insulating layer such as ceria. (c) Connect exposed YBCO with filaments of YBCO. The current paths should then follow a route like the arrow in (c).

The 3 stages are as follows: printing diagonal partial filaments and barrier spacers in a single pass, then covering the central regions with a thin insulating barrier before finally connecting filaments across the top. Each stage has specific challenges associated with it. In the first layer the barrier material must be compatible with the REBCO, insulating and must

effectively transfer texture to the layers above whilst the entire surface must be flat and smooth enough for further chemical deposition. The second layer buffer material needs to be similar to the barrier material of the first layer except thin enough to not cause significant grain misorientation at the step between via and filament. The final layer must be able to grow effectively over the top of the insulating layer whilst retaining good current characteristics. The "vias" at the edge of the conductor should have an area ~3 orders of magnitude greater than the cross section of individual filaments to compensate for the lower c-axis critical current. This should be feasible because the typical filament thickness is of the order of 1–3 μm so the via needs to be approximately 1–3 mm long and could be extended to maximise the full width of the substrate [191].

Crossover and ramp structures with superconducting REBCO strips grown over CeO_2 insulating layers have been demonstrated on small (< 1 mm^2) single crystals by van Wijck et al. [194]. The purpose of their work was device fabrication but demonstrated that REBCO tracks could successfully be grown over thin (80 nm) steps of textured CeO_2. This indicated that it would be theoretically possible to have a Rutherford type coated conductor with superconducting filaments passing over thin insulating barriers. The purpose of the current work was to develop a suitable material and deposition method for the barrier material present in the first layer.

4.6.1 PrYBCO as a barrier layer

Cerium oxide was initially considered as a barrier material because it is electrically insulating, compatible with REBCO and can be used to transfer crystallographic texture to REBCO layers; for example, it is commonly used as the final layer in buffer stacks of coated conductors. However, the main issue envisaged was the difficulty of growing a strip of the precisely the required thickness simultaneously with the first layer REBCO. Ceria inks typically produce thin films, 20–40 nm, when grown using solution deposition and if good crystallographic texture is required.

The thickness of REBCO films grow from inkjet printed solutions is typically of the order of 1 μm. Therefore, using YBCO doped with praseodymium, $Pr_xY_{1-x}Ba_2Cu_3O_{7-d}$ (0 < x < 1), was decided upon. PrBCO is isostructural to other superconducting REBCO materials, with only a small lattice mismatch (< 3%) to YBCO. However, unlike other REBCO

HTS materials PrBCO does not typically display superconducting properties and when YBCO is doped with praseodymium the critical temperature, T_c, is reduced as shown in Figure 90.
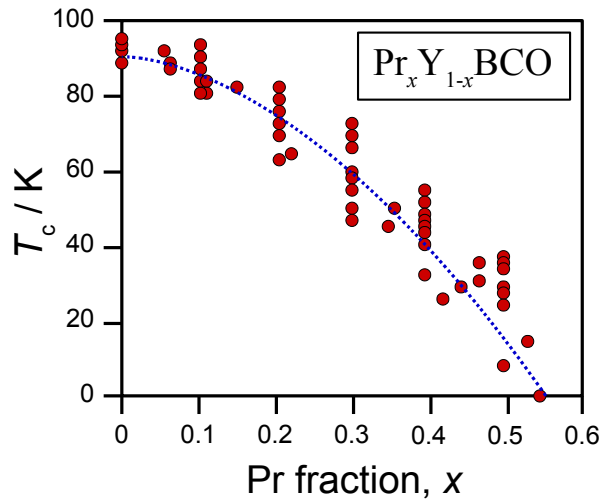
Figure 90. Critical transition temperature, T_c, dependence on praseodymium content for the $Pr_xY_{1-x}BCO$ system. Redrawn from [195].

Different mechanisms have been described to explain the lack of superconductivity in PrBCO [195], including mixed valence of the praseodymium, where the Pr^{4+} contributes an additional electron filling a hole in the Cu-O planes. However, experimental evidence suggests Pr is in the III valence state. Therefore, an alternative explanation that assumes that a Pr(4f)-O(2p) hybridisation takes place is plausible. This prevents superconductivity by magnetic interactions with Cooper pairs or by localising charge carries. Some authors suggest mixed models with both hole filling and magnetic pair breaking. Several authors have also reported superconductivity in PrBCO [196–199], but only detectable with magnetic or microwave measurement because the superconductivity is highly localised and so the material still exhibits high DC resistivity. Blackstead et al. [196] ascribed lack of bulk superconductivity in PrBCO to Ba site substitution by Pr.

Multilayers of YBCO and PrBCO have been studied to determine fundamental properties of HTS materials [200], develop epitaxial insulating layers for devices [201] and determine pinning mechanisms in coated conductors [202]. This confirmed that it would be feasible to produce superconducting REBCO on top of insulating PrBCO layers.

4.6.2 PrYBCO ink development

It was assumed that the similarity in reactivity of the rare-earth elements and the fact that PrBCO is isostructural to YBCO would allow PrBCO to be synthesised using an analogous route to TFA-MOD production of YBCO. Additionally, inks with reduced fluorine content were developed because of their lower sensitivity to atmospheric moisture and ability to produce thicker coatings in a single step.

Separate metal ion solutions were prepared to enable easy synthesis of different fluorine content solutions. Six different stock solutions were synthesised and are summarised in Table 11. The synthesis procedure was similar for all except the precise reagents.

Table 11. Chemical reagents used to synthesise stock solutions used to make PrYBCO inks

Stock solution	Solid reagent	Organic acid
Y(TFA)$_3$	Y$_2$O$_3$ (99.999%, Sigma-Aldrich)	
Pr(TFA)$_3$	Pr$_6$O$_{11}$ (99.9%, Sigma-Aldrich)	Trifluoacetic acid (99%, Alfa Aesar)
Cu(TFA)$_2$	CuO (>99.0%, Alfa Aesar)	
Ba(TFA)$_2$	BaCO$_3$ (99.999%, Sigma-Aldrich)	
Cu(PPA)$_2$	CuO (>99.0%, Alfa Aesar)	Propionic acid (99% Sigma-Aldrich)
Ba(PPA)$_2$	BaCO$_3$ (99.999%, Sigma-Aldrich)	

The starting powder (oxide or carbonate) was dissolved in an excess of organic acid reagent (propionic acid, PPA, or trifluoroacetic acid, TFA) in an aqueous (50 vol%) solution with de-ionised water. The reaction mixture was heated under reflux until a clear solution was obtained. Excess solvent was removed on a rotary evaporator to leave a viscous gel. The corresponding acid anhydride (propionic acid anhydride or trifluoroacetic acid anhydride) was added and solvent evaporation repeated. The product was diluted with anhydrous methanol before a final solvent removal stage. The viscous gel was then diluted to the required concentration with anhydrous methanol. To form the REBCO precursor inks, Table 12, stoichiometric quantities of each individual metal ion solution were mixed.

Table 12. Composition of PrYBCO inks with different fluorine contents. RE = Y or Pr.

Ink	Components
Full F	RE(TFA)$_3$, Ba(TFA)$_2$, Cu(TFA)$_2$
Low F-1	RE(TFA)$_3$, Ba(PPA)$_2$, Cu(TFA)$_2$
Low F-2	RE(TFA)$_3$, Ba(TFA)$_2$, Cu(PPA)$_2$
Low F-3	RE(TFA)$_3$, Ba(PPA)$_2$, Cu(PPA)$_2$

4.6.3 Thermal analysis

4.6.3.1 Experimental methods

Thermal decomposition of pure PrBCO solutions were analysed using thermogravimetric analysis (TGA). Samples were heated in flowing (60 cm^{-3} min^{-1}) wet oxygen at a rate of 10 K min^{-1} from room temperature to 1000 °C.

Samples were formed by drying the precursor solution in the platinum crucible used for testing to allow stable calibration of the initial mass prior to heating. Thin films on glass substrates were also produced because research by Eloussifi et al. [203] had suggested that the decomposition behaviour of thin films was different to that for bulk powder samples due to the differences in gas and thermal transport, with thin films displaying lower decomposition onset temperatures. However, the masses recorded for these films were too low to be analysed reliably.

4.6.3.2 Results

The thermogravimetric data is shown in Figure 91. The different ink types had different decomposition profiles, with the decomposition temperature range varying for different fluorine contents.
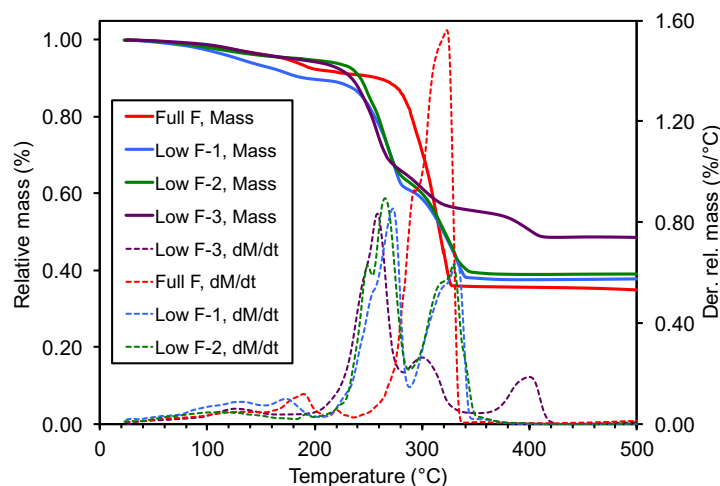
Figure 91. Thermogravimetry data showing the relative mass loss and derivative as the pure PrBCO precursor solutions were heated. Samples were approximately 10 mg and were heated at 10 K min^{-1} in wet oxygen. The inks with a lower fluorine content had a wider decomposition temperature range.

The Full F PrBCO ink showed a sharp mass loss. The shoulder to the Full F derivative curve at 290 °C indicated that multiple decomposition processes were occurring simultaneously in the same range of temperatures. The lower fluorine content inks decomposed over a larger temperature range. The Low-F1 and F2 inks had lower initial onset temperatures and higher final decomposition temperatures than the Full F. The Low-F3 ink had the largest temperature range of all the inks tested with an onset of 250 °C and final peak occurring at 395 °C.

The distinct peaks visible at ~250 °C and ~320 °C for Low F-1 and F-2 were ascribed to the decomposition of the propionate and trifluoroacetate components respectively, based on the analysis of low fluorine YBCO solutions by Palmer et al. [204]. This explained why the Full F ink decomposed over a narrower range with onset at a higher temperature. From thermal analysis of separate metal trifluoacetates performed by Mosiadz et al. [205–207] the onset of the decomposition peak for the Full F solution was ascribed primarily to copper species with the RE and barium decomposition reaching their maximum reaction rate at a slightly higher temperature.

The more gradual thermal decomposition was thought to be beneficial for film formation because it reduces the chance of thermal runaway, sudden thickness change or rapid gas release. Chen et al. [208] reported that low fluorine precursor solutions for YBCO could cope with higher temperature ramp rates partly because less hydrogen fluoride (HF) gas was

released during pyrolysis. The lower HF generation was ascribed to BaF_2 and $(RE)F_3$ still forming despite only one halogenated precursor.

The difference in the final relative mass loss between the samples followed the expected trend assuming a similar product phase; the propionate precursors had a lower mass than the trifluoacetates so with a similar final product the relative mass loss will be lower. Other differences in the final masses may be in part due to how hygroscopic each solution was [204]. The Full F and Low F-1 solutions both exhibited a slightly greater solvent loss before the main decomposition peaks, implying that they had retained more solvent or absorbed more water from the atmosphere.

Based on the thermal analysis results it was decided to use the low-F3 type ink for thin film production. The broader range for decomposition was likely to result in less extreme stress generation in the film during pyrolysis. Also, the composition matched more closely with the successfully used OxoYBCO ink that had previously been used for depositing filamentary conductors.

4.6.4 Thin films

4.6.4.1 Thin film preparation

To determine the if c-axis textured PrBCO could be grown from solution precursors an initial sample was produced by spin coating the Low F-3 PrBCO ink onto a 1 cm^2 lanthanum aluminate (LAO) single crystal substrate followed by pyrolysis, growth and oxygenation as described in section 4.4.1. An angular speed of 6000 rpm for 2 min was used to distribute the 1 M ink across the surface of the substrate.

Samples were also prepared on buffered metal substrate (SuperOx, buffer architecture as in Figure 53 but without the GdBCO and silver layers). Squares, 12 mm × 12 mm, of buffered substrate were spin coated with the different inks before thermal treatment. In addition to the pure PrBCO precursor solutions three doped solutions were also formulated and deposited. The doped solutions had $x = 0.1$, 0.2 and 0.3 respectively, where x was the relative fraction of praseodymium, $Pr_xY_{1-x}Ba_2Cu_3O_{7-d}$. They were all formed using the low-F3 formulation.

4.6.4.2 Phase identification

Following thermal treatment x-ray diffraction (XRD) was performed in the Bragg-Brentano geometry and data were collected 20–50° degrees 2θ. The peak positions were compared with International Centre for Diffraction Data (ICDD) reference patterns to identify the expected phases (YBCO: 00-038-1433, PrBCO: 00-050-0429, $BaCeO_3$: 00-035-1318).

The sample deposited on the LAO single crystal, Figure 92, showed that correctly textured pure PrBCO could be grown using the MOD approach, which had not been demonstrated before. The next stage was to determine if the process was repeatable for buffered metallic tapes.
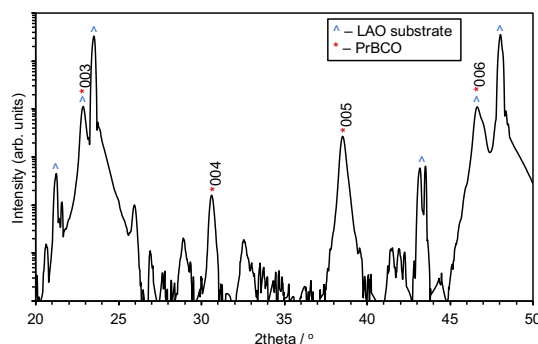
Figure 92. XRD pattern for pure PrBCO film grown on top of single crystal LAO substrate. The solution was 1 M PrBCO Low F-3. Several of the film peaks overlap with the substrate.

The 00l type peaks were less pronounced when PrBCO films were grown on buffered polycrystalline substrate, Figure 93. The fluorine content appeared to have a small effect on the phase evolution, with $BaCeO_3$ detected in the sample grown from the Full F solution.
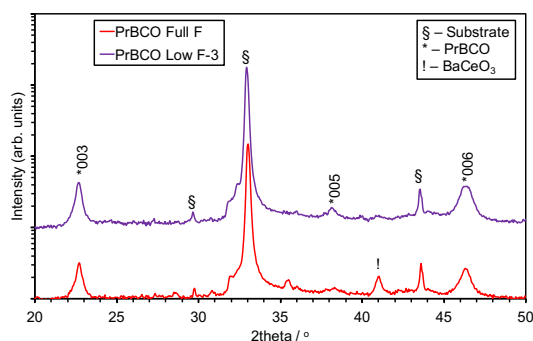
Figure 93. XRD patterns for pure PrBCO grown on buffered metal tape using full and low fluorine precursor solutions. The 00l peaks were more pronounced and there was less barium cerate detectable for the film grown from the Low F-3 solution.

The praseodymium in the PrYBCO barrier material needs to remain localised during heat treatment to avoid doping the surrounding filaments and supressing their critical properties. To reduce the diffusion gradient present during thermal processing a lower Pr content can be used. This would be important for simultaneously depositing and growing the first filamentary layer. A relative mole fraction of just 0.3 should be sufficient to supress the T_c of PrYBCO below 77 K. The films produced with a lower praseodymium content films showed better phase formation, Figure 94, however they also appeared to grow $BaCeO_3$, an impurity phase, more readily.
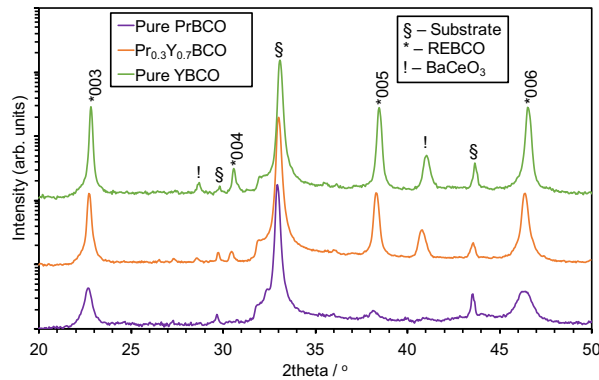
Figure 94. XRD patterns for films with different praseodymium contents but all from Low F-3 type solutions. Correctly textured REBCO was detectable in all cases.

The presence of $BaCeO_3$, formed by the reaction of Ba with the ceria buffer layer, is generally thought to be detrimental for formation of high quality superconducting films [209]. The barium cerate still transmits the correct crystallographic texture but the surrounding REBCO may become Ba deficient. Other authors have reported that pure PrBCO is very sensitive to synthesis conditions [197–199] and this may partly explain the apparent difference in phase formation between the films with different Pr contents.

4.6.4.3 Critical temperature of PrYBCO films

Critical temperature testing of films to confirm the expected T_c dependence was not successful due to lack of reliable superconducting films when pure YBCO was deposited and grown. The unreliability of successful superconductor growth prevented the subsequent stages of development required for producing a Rutherford architecture, including demonstrating that superconducting YBCO could be grown on PrYBCO using solution methods.

The growth of superconducting REBCO from solution precursors is a complex process with numerous variables to control, including temperature and gas atmosphere.

Several key challenges were identified that prevented reliable superconductor growth. Firstly, substrate uniformity for the majority of the project was poor. As was shown in Figure 84 the substrate was not flat, which caused problems for ink deposition and conversion. Alternative, more uniform substrate was sought following the conclusion of our groups involvement in the EUROTAPES project. The new buffered substrate from SuperOx was much more uniform, however, samples that were produced using the tape only showed measurable transition temperatures when tested inductively and did not give macroscopically connected superconducting films. This may have been caused by the second principle challenge; solution aging. Recently, Pinto et al. [210] reported a study on the aging of REBCO precursor solutions, where a time period of < 50 days was enough to degrade the T_c of YBCO grown from low fluorine precursor solutions. This is despite the solutions appearing visibly stable, i.e. without precipitation, for many months. The aging was linked to changes in the solutions detectable via NMR, with the formation of methyl propionate correlating with poorer solution performance. They found that aged solutions showed greater traces of impurities and a-axis oriented grains. This aging effect complicated the optimisation of the heat treatment process, adding an additional variable to control and invalidating earlier conclusions about unsuccessful combinations of growth temperatures and atmospheres.

4.7 Summary

In this chapter, a brief overview of drop-on-demand inkjet printing technology that can be used for functional materials deposition and patterning was given. The requirements of inks and jetting parameters were discussed.

Directly printed filamentary coated conductor samples were produced using piezoelectric nozzle printing. Different numbers of printing passes were investigated to increase the thickness of YBCO filaments and increase I_c. However, when more than 2 passes were deposited before thermal treatment the superconducting properties were poorer.

A patented "inverse" printed filamentary coated conductor architecture was described and fully printed samples using ceria as a barrier material were produced. The superconducting properties of samples were characterised using Hall probe magnetometry and AC loss measurements. Challenges and limitations with substrate and processing uniformity were discussed.

A more complex printed Rutherford architecture concept was described. Inkjet printing is the only scalable method that could deliver an additively produced conductor with transposed filaments. The concept required a suitable insulating material to act as an isostructural barrier material. Praseodymium doped YBCO, $Pr_xY_{1-x}Ba_2Cu_3O_{7-d}$, (PrYBCO) was identified as a suitable candidate. Pure PrBCO precursor solutions were synthesised with a range of fluorine contents. The thermal decomposition for the different inks was characterised with reduced fluorine content inks showing preferable characteristics. Thin films of pure PrBCO were grown on single crystal and buffered metallic substrates. Additionally, PrYBCO films with different Pr contents were grown on technical substrates. Lower Pr contents appeared to give the best films.

Further development of the complex Rutherford type architecture was limited by the reliability of superconducting film production. However, as mentioned inkjet printing enables patterning during manufacture, further increasing materials efficiency and reducing costs whilst reducing post-production subtractive processing. Therefore, this motivates further research into optimising the REBCO growth processing. Furthermore, the ability for an inkjet processing route to produce complex filamentary coated conductor structures in a single production line is unique. To capitalise on the benefits available for printed structures the reliability of thermal processing, substrate and compatible precursor inks need to be improved systematically for the specific laboratory conducting research.

SECTION II: SOLID OXIDE FUEL CELLS

5 INTRODUCTION: SOFCS

5.1 Solid oxide fuel cells

Solid oxide fuel cells (SOFCs) are electrochemical cells that directly convert chemical energy into electrical energy. They are inherently more efficient than conventional power generation systems such as internal combustion engines. SOFCs typically operate at high temperatures 500–1000 °C, which enable further efficiency gains by combining with gas turbines or producing combined heat and power (CHP). The high operating temperature also allows for internal reforming of hydrocarbon fuels and fast reaction kinetics with non-precious metal catalysts.

SOFCs have a solid, gas tight, electronically insulating oxide electrolyte that separates two porous electrodes, Figure 95. The fuel is oxidized at the anode and oxygen is reduced at the cathode. Cells also include electrically conducting interconnects required to attach an external load or for connecting several cells in series or parallel into a stack to increase voltage or current output. Gas seals are also used to prevent mixing of the fuel and oxidant gases.
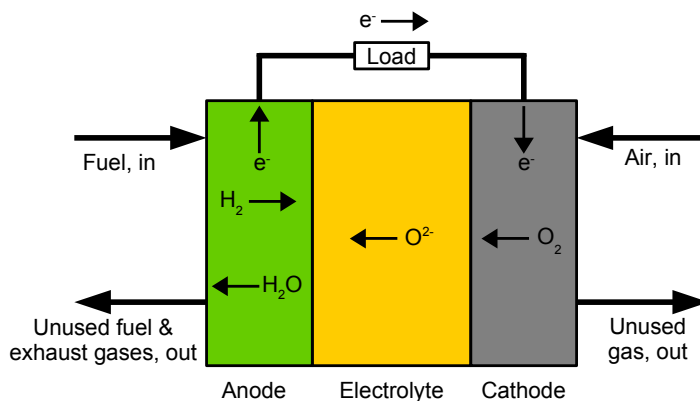
Figure 95. Schematic illustrating the operating principle of a SOFC. The electrodes are porous and conductive whilst the electrolyte is dense and electronically insulating.

5.1.1 Sources of loss

The voltage of a fuel cell is predicted by the Nernst equation, (19), which gives the theoretical potential based on the free energy change for the chemical reaction occurring.

$$E = E^0 - \frac{RT}{zF} \ln K \qquad (19)$$

Where E is the potential, E^0 is the standard electrode potential, R is the gas constant, T is the temperature, z the number of electrons transferred, F the Faraday constant and K the equilibrium constant for the reaction, which depends on reactant and product concentrations.

However, the actual cell voltage will be lower than this even at open circuit conditions due to current and gas leakage. The operating voltage is then further reduced below the open circuit voltage (OCV) due to overpotentials associated with the finite rates of reaction occurring in different cell components, Figure 96. Cell OCV is typically ~1 V but they usually operate at 0.5–0.7 V under load. The main sources of loss are due to limitations in the charge transfer processes occurring at the electrodes, ohmic resistance of the electrolyte and mass transfer of gas phase reactants in the porous electrodes. These losses can be minimised by a combination of cell design, materials choice and structural modification.
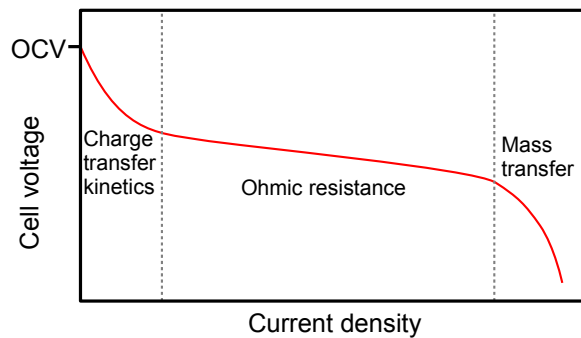
Figure 96. The main contributions to cell overpotentials under cell loading as the current load increases. Adapted from [211].

5.1.2 SOFC design

The two main types of fuel cell design are planar and tubular geometries, Figure 97. Tubular designs benefit from simpler gas sealing and handling. Planar designs have the advantage of cheaper conventional fabrication routes but the sealing is more complex due to differential thermal expansion, which can be problematic for thermal cycling.
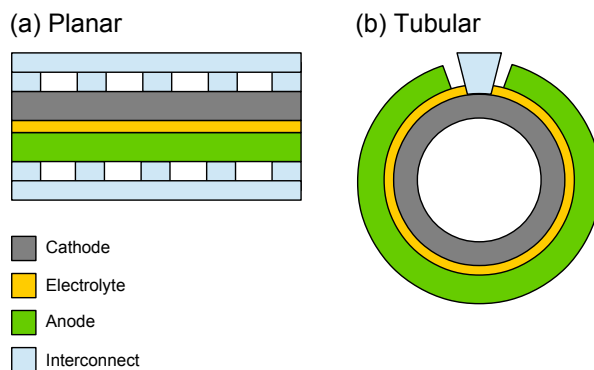
Figure 97. Schematic of two alternative SOFC geometries. Planar cells are generally easier to manufacture, whilst tubular designs simplify gas handling.

This thesis will look at planar cells due to their simpler manufacture and potential for modification by using scalable inkjet printing techniques. Within planar cells there are different designs, with differences based on the component that acts at the primary support, Figure 98.
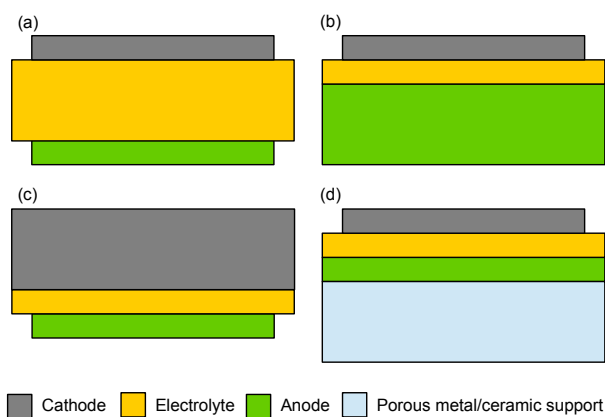
Figure 98. The main different planar cell designs. (a) Electrolyte supported (b) anode supported (c) cathode supported and (d) metal or ceramic supported. Adapted from [212].

Ohmic and mass transport losses can be addressed through cell design, typically by reducing the thickness of components. However, cost and mechanical integrity also play a part. In the various designs the thick component is typically of the order of 0.5–5 mm whilst the remaining layers are thin, ~5–50 μm. The thin layers improve performance by reducing ohmic and mass transport losses and improve mechanical integrity by reducing the number of critical flaws and lowering mechanical stresses during heating and cooling [212].

Each of the alternative cell designs have their own advantages and disadvantages. In electrolyte supported cells the electrolyte can be sintered and densified at high temperature

(~1400 °C) without danger of any deleterious reaction with other cell components, which can be particularly problematic with cathode materials [213,214]. The strength of electrolyte supported cells is usually good, because the primary support is fully densified. The main drawback for electrolyte supported cells is the relatively thick electrolyte required, which increases ohmic losses. Results from electrolyte supported symmetric cells will be presented in chapter 6 and 7.

Cathode supported cells benefit from a thinner electrolyte. However, cathode materials tend to be relatively high cost, high density and low strength. They have been used successfully by Siemens/Westinghouse [215] in a capped tubular design, which allows for simpler gas distribution and cheaper metal interconnects that are in a reducing atmosphere during operation.

Anode supported cells, commonly based on a nickel-yttria stabilised zirconia cermet (Ni/YSZ), are popular for enabling thin electrolyte and cathode layers [216,217]. Anode materials are typically stronger and cheaper than cathodes. The design is susceptible to thermal shock and electrolyte cracking due to volume changes during cell reduction. However, careful control of the microstructure and proportions of the phases present can reduce their fragility and several companies manufacture anode supported cells [218–220]. Anode supported cells will be studied further in chapter 6.

An alternative approach that allows all electrochemically active components to be thin is to use a metal or ceramic support with little or no chemical activity. This can substantially reduce the cost of the cell whilst improving the mechanical integrity. Ceramic supports are more chemically inert, which is beneficial for sintering of the other components and in the case of heating in a non-reducing atmosphere. Furthermore, the coefficient of thermal expansion (CTE) is more closely matched to the other components. However, the higher stiffness and lower toughness compared to metal supports is a drawback for rapid or frequent thermal cycling. Metal supports offer very good thermal shock resistance and the inherent electrical conductivity of the support is an advantage [221].

5.2 Material choice

5.2.1 Electrolyte

The electrolyte needs to be ionically conductive, electronically insulating and gas tight at the operating temperature. Additionally, it must be chemically stable over a wide range of temperatures and oxygen partial pressures (pO_2). The four main classes of material that have been utilised as SOFC electrolytes are stabilised zirconia, doped ceria, doped Bi_2O_3 and doped $LaGaO_3$. Of these yttria stabilised zirconia (YSZ) has been the most widely used. The doping level is commonly 3–10 mol% and the 8 mol% variant (8YSZ) has the highest ionic conductivity, Table 13. YSZ has good mechanical integrity and a wide range of stability but must be very thin to avoid substantial ohmic losses at intermediate temperatures (< 800 °C). Scandia doped zirconia (ScSZ) has better ionic conductivity than YSZ but the scarcity and relative cost of scandium makes it less attractive for large-scale SOFC implementation [222–226].

Doped ceria e.g. gadolinium doped ceria, $Ce_{0.9}Gd_{0.1}O_{2-x}$ (CGO), has a significantly higher ionic conductivity at intermediate temperatures than YSZ. However, at higher temperatures, above 600 °C, the material becomes a mixed ionic electronic conductor (MIEC), which results in electronic leakage across the electrolyte [226]. Hence, if doped ceria electrolytes are to be used they need to be operated at lower temperatures and with suitably active electrodes. Lower operating temperatures are beneficial for reducing degradation rates and allows cheaper metal interconnects and simpler gas sealing materials to be used [224]. Doped bismuth oxide has similar conductivity to doped ceria but also suffers from the same disadvantage of electronic conductivity at high temperatures [222].

Doping $LaGaO_3$ with strontium and manganese to form a lanthanum strontium magnesium gallate (LSGM) perovskite leads to a material with a similar ionic conductivity to CGO but with a wider temperature range for ionic conductivity. The disadvantage lies in the difficulty to produce the desired single phase. Moreover, the preferred phase is not as stable across the entire temperature range experienced during temperature cycling. All the non-zirconia based electrolyte materials also have poorer mechanical properties meaning they are only suitable in practical applications if they are supported by a different cell component [222,227].

Table 13. Ionic conductivity of electrolyte materials. Adapted from [222].

Material	Conductivity / S cm^{-1} at (temperature, °C)
3 mol% Y_2O_3-ZrO_2	0.058 (1000), 0.018 (800)
8 mol% Y_2O_3-ZrO_2	0.178 (1000), 0.052 (800)
10 mol% Y_2O_3-ZrO_2	0.136 (1000), 0.037 (800)
8 mol% Sc_2O_3-ZrO_2	0.31 (1000), 0.12 (800)
9 mol% Sc_2O_3-ZrO_2	0.34 (1000), 0.109 (800)
$(Ce_{0.7}Gd_{0.3})O_{1.85}$	0.25 (1000), 0.093 (800)
$(Ce_{0.8}Sm_{0.2})O_{1.9}$	0.25 (1000), 0.096 (800)
$(La_{0.9}Sr_{0.1})Ga_{0.8}Mg_{0.2}O_{3-\partial}$	0.316 (1000), 0.121 (800)
$(La_{0.8}Sr_{0.2})Ga_{0.83}Mg_{0.17}O_{3-\partial}$	0.17 (800)
25 mol% Er_2O_3-Bi_2O_3	0.37 (700)

5.2.2 Anodes

Anode materials need to have good electronic conductivity, oxygen diffusivity and reactivity for oxidation reactions. The dominant anode material in SOFCs is Ni/YSZ cermet. This is commonly constructed from a mixture of NiO and YSZ powders then the NiO is reduced to Ni in-situ. Nickel has the dual benefits of good electrical conductivity and excellent catalytic activity for the oxidation of hydrogen [216]. However, pure nickel coarsens at typical SOFC operating temperatures and the pure metal has a significant CTE mismatch with standard electrolytes. Spacil addressed these two shortcomings with a mixed Ni/YSZ composite structure [228]. The YSZ then prevents significant nickel coarsening by preventing substantial diffusion between nickel particles and the composite structure has a much more closely matched CTE with the ceramic electrolyte. The conductivity is reduced but if the nickel forms a percolative network the conductivity remains sufficient. Another advantage is the increase in the triple phase boundary (TPB) if the YSZ also form a continuous phase, Figure 99. The TPB is the location where gas phase, ionic and electronic conductors meet and the electrochemical reactions can occur.

The main disadvantages for Ni/YSZ anodes arise when hydrocarbon fuel is used. Sulphur is commonly present in commercial hydrocarbon fuels and poisoning occurs when

the H_2S concentration exceeds a few ppm [229]. Nickel also catalyses the formation of carbon filaments under reducing conditions [230,231]. This leads to "coking" of the anode and a severe reduction in performance. The carbon can be removed if sufficient steam is present, however, this requires dilution of the fuel and due to the catalytic activity of nickel is not effective for higher hydrocarbons. Adding small quantities of noble metals (Au, Rh or Ru) can suppress coking as can the addition of an oxidation catalyst such as ceria [232].

To avoid the fundamental challenges of Ni/YSZ anodes alternative oxide materials have been developed that show good redox stability and resistance to fuel impurities and coking. Perovskite materials such as lanthanum chromites and strontium titanates have been investigated. For example, doped lanthanum chromite ($La_{0.75}Sr_{0.25}Cr_{0.5}Mn_{0.5}O_3$) has been demonstrated to be redox stable and sufficiently chemically active in pure H_2 [233]. Also, $La_{0.4}Sr_{0.6}TiO_3$ was shown to be redox stable, sulphur tolerant and resistant to coking [234].

Alternative anodes also include composites of ceria with a relatively inert metal such as copper [235,236]. The copper does not suffer from carbon deposition and provides the required electrical conductivity, whilst the ceria behaves as an oxidation catalyst and provides an ionically conducting path to the electrolyte. Further discussion of anode enhancement is discussed in section 6.1.1.

5.2.3 Cathodes

The requirements for the cathode are similar to the anode in terms of stability and conductivity, however, the reactivity needs to be optimised for catalysing the oxygen reduction reaction (ORR). The polarisation losses associated with the ORR at the cathode are commonly the dominant sources of loss in SOFCs, particularly at intermediate temperatures [237]. Lanthanum manganite doped with strontium, $La_{1-x}Sr_xMnO_3$ (LSM), is a popular cathode choice because of the stability and good activity for the ORR at temperatures > 800 °C and decent electronic conductivity (> 200 S cm^{-1}) [238–240]. However, the material has poor oxygen ion conductivity [241] and therefore very thin cathodes are required to minimise the distance to the electrolyte and graded electrolyte/cathode interfaces can be used to maximise the TPBs and thereby reduce polarisation losses [242,243].

Cathode materials with better ionic conductivity include strontium doped lanthanum ferrites, lanthanum cobaltites and mixed perovskites: $La_{1-x}Sr_xFeO_3$ (LSF), $La_{1-x}Sr_xCoO_3$ (LSC), and $La_{1-x}Sr_xFe_{1-y}Co_yO_3$ (LSCF) [244,245]. These all have much better ionic

conductivities than LSM and generally have higher activity for the ORR at lower temperatures too. However, they tend to react readily with YSZ at standard electrode sintering temperatures [246–248]. The detrimental effects of this can be reduced by using a doped ceria interlayer [249,250]. Nanostructuring the cathode can improve the performance of the cathode in several ways, including by maximising the TPB length and by reducing the required sintering temperature to avoid deleterious reaction with the electrolyte, this will be further discussed in sections 5.3.1 and 7.2.

5.2.4 Interconnects

Interconnects provide electrical connection between cells in a stack and separate the fuel and oxidising gases from each other. They need to be electrically conductive, impervious to gases, stable in oxidising and reducing atmospheres during thermal cycling and mechanically robust. Both ceramic and metal materials have been used. Ceramic materials such as lanthanum chromite ($LaCrO_3$) can be doped with elements such as Sr and Ca to achieve the required electrical conductivity and stability [251]. Other ceramic materials that have shown good sinterability in air and compatibility with YSZ are calcium and nickel doped yttrium chromites [252]. Ceramic interconnects, whilst good in terms of oxidation resistance, tend to be expensive to fabricate, relatively fragile and with poorer electrical conductivity than metals.

Metal interconnects are preferred for their lower cost, higher conductivity and better mechanical properties, particularly at lower operating temperatures. The motivation to reduce cell operating temperatures is in part to enable the use of cheaper and more robust interconnects. Plansee Ducralloy ($94Cr-5Fe-1Y_2O_3$) [253] has excellent properties in terms of corrosion resistance, CTE and mechanical strength but the powder metallurgy required to form components results in a very high cost. Stainless steels are a natural choice but suffer from poor oxidation characteristics at high temperatures [254]. Additionally, cathode materials are poisoned by chromium that becomes mobile at elevated temperatures, resulting in degradation in cell performance [255]. Stainless steel interconnects can be protectively coated and materials such as chromium free $(Mn, Co)_3O_4$ spinels have been shown to be effective [256].

5.2.5 Sealing

Sealing is required to prevent mixing between fuel and oxidant gases and materials must match the CTE of cell components closely whilst remaining stable and inert at the

operating temperature. Rigid glass ceramic seals, e.g. $BaO\text{-}CaO\text{-}SiO_2$ and $BaO\text{-}Al_2O_3\text{-}SiO_2$, are relatively cheap and provide a gas tight seal [257]. However, they are susceptible to thermal shock and damage to one seal can result in failure of an entire stack [258]. Compressive metal or mica seals are much more resistant to thermal shock but require compressive stresses to be applied throughout usage. Metal seals can cause short circuiting and mica seals require high compressive loads to maintain gas tightness.

5.3 Minimising electrode losses

Lowering the operating temperature is beneficial for several of the auxiliary components of fuel cell stacks and will reduce the cost of manufacture and improve cell lifetime [224]. The higher electrode polarisation losses at intermediate temperatures, 500–800 °C, are one of the biggest impediments to lowering SOFC operating temperatures. This section will look at how the general approach of nanostructuring the electrodes can enhance performance, particularly at intermediate temperatures.

5.3.1 Nanostructuring electrodes

The rate limiting chemical reactions occurring at the electrodes are thermally activated and so there is an exponential decrease in rate when lowering temperatures, leading to higher electrode overpotentials. These reactions occur at regions in the electrodes where ionic and electronic conductors meet the gas phase: the triple phase boundary (TPB), shown schematically for an anode in Figure 99. Therefore, one way the overall rate of reaction can be increased is by increasing the total length of this boundary within the porous electrode structure. The longer the boundary the more reaction sites and therefore the lower the polarisation resistance. This can be achieved effectively by decorating the electrode surface with electronically or ionically conducting nanoparticles, Figure 100.
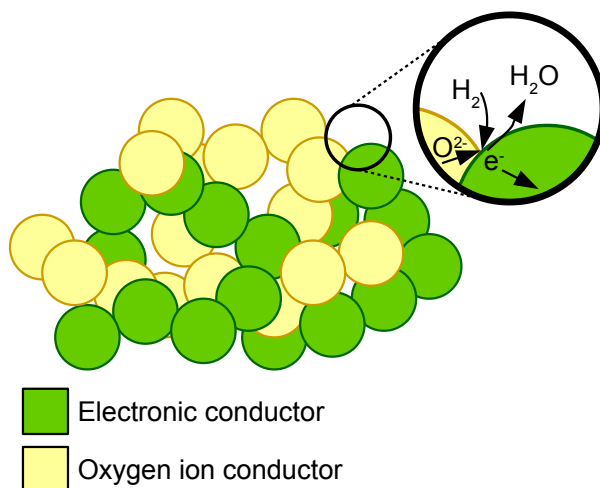
Figure 99. Schematic anode structure showing the triple phase boundaries (TPBs) where ionic and electronic conductors meet the gas phase.

If the nanoparticles are to extend the TPB then they need to form a continuous connected path. For example, ionically conducting nanoparticles on the surface of an electronically conducting scaffold need to form a continuous network to the ionic conductor phase of the electrode or the electrolyte. The grains that make up the electrode are typically 2 to 3 orders of magnitude larger than nanoparticles and so nanostructuring can increase the TPB length by at least an order or magnitude [259,260].
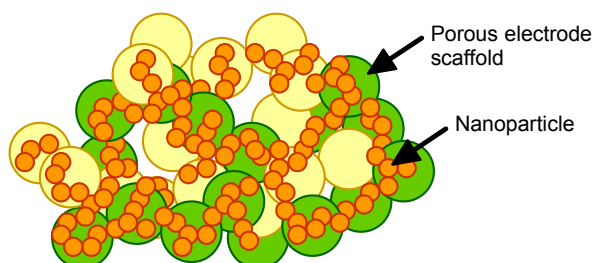
Figure 100. Schematic porous electrode with nanoparticles decorating the surface. The nanoparticles can be continuous or discrete.

However, the nanoparticles do not necessarily have to form a continuous network to reduce electrode polarisation resistance. If they catalyse the electrochemical reactions that occur at the surface then they can improve performance when discretely covering the surface. For example, ceria can catalyse the oxidation of hydrocarbons in the anode [216] and cobalt oxide can catalyse the ORR in the cathode [261].

5.3.2 Solution infiltration

Due to the high temperatures required for electrolyte sintering nanostructuring of SOFC electrodes is usually performed by infiltrating a solution precursor into porous electrodes after cell fabrication. A simple thermal treatment is used to grow well distributed particles. Solution infiltration separates the high temperature processing required to sinter the electrolyte and electrodes from the nanoscale development of the catalytic phases. The relatively low growth temperature prevents excessive particle coarsening.

Jiang provides a recent review of the advances and challenges of nanostructuring SOFC electrodes via infiltration [244]. Specific examples of solution infiltration of anodes and cathodes are in chapter 6 and 7 respectively.

Often vacuum impregnation, multiple infiltration steps and intermediate heat treatments are used to increase loading of the infiltrate into the porous electrode. Also, the infiltration is often performed by manual pipetting, immersion or flooding the sample. The use of many steps and waste of rare-earth or noble metal precursors is inherently expensive. Furthermore, the requirement of achieving high mass loading leads to more concentrated precursor solutions, which then results in poorer ink distribution.

Chapters 6 and 7 report work using drop-on-demand (DoD) inkjet printing to infiltrate solution precursor inks into anodes and cathodes respectively. Inkjet printing is a simple, scalable and cost-effective non-contact technique. It can be used to deposit solutions or suspensions on a variety of surfaces including very thin, fragile or non-planar porous electrode supports. It can reproducibly dispense droplets in the range of pL to nL volumes at high rates (kHz). Inkjet printing allows excellent uniformity control and introduces the possibility of printing 2D and 3D patterns as well as delivering precursors into porous scaffolds with high levels of reproducibility and accuracy. The precision of deposition is beneficial for experimental platforms and for large-scale production where waste minimisation of raw materials is important. DoD inkjet printing has been demonstrated by our group to be an effective technique for construction and infiltration of fuel cells utilising both suspension and solution precursor inks [262–268].

5.4 Impedance spectroscopy

To quantify the effects of tailoring the structure of fuel cell electrodes it is useful to test symmetric cells using electrochemical impedance spectroscopy (EIS). Symmetric cells, Figure 101, enable the response of a single electrode to be isolated from the other electrode.

Figure 101. Schematic of a symmetric cell with two identical electrodes.

EIS determines the complex impedance of the electrode as a function of frequency. This allows the different contributions to cell resistance to be identified. To measure the impedance a sinusoidal voltage with a small amplitude (e.g. 10 mV) is applied to the cell and the current response measured, Figure 102.
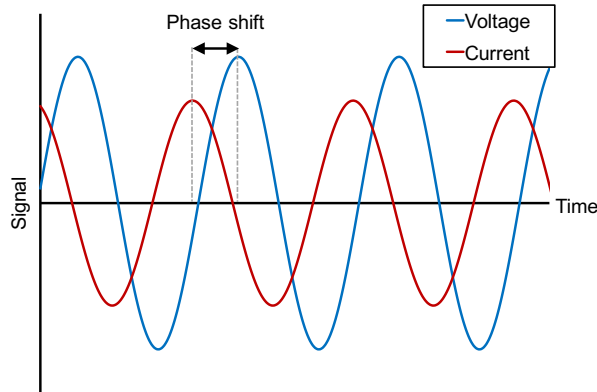
Figure 102. Schematic current response to an applied sinusoidal voltage.

The voltage can be considered as the real component of the general complex voltage given by equation (20):

$$V = V_0 e^{i\omega t} \tag{20}$$

Where V_0 is the amplitude of the voltage, i is $\sqrt{(-1)}$, ω is the angular frequency and t is time. The current response, equation (21), is measured and in general may have a phase offset:

$$I = I_0 e^{i(\omega t + \theta)} \tag{21}$$

Where I_0 is the amplitude and θ is the phase shift. The impedance is then calculated as the ratio of the complex voltage to the current, equation (22):

$$Z = \frac{V}{I} = \frac{V_0}{I_0} e^{-i\theta} = |Z| e^{-i\theta} = Z' + iZ'' \tag{22}$$

Where real and imaginary components are Z' and Z'' respectively. The impedance is calculated for a range of frequencies, typically spanning several orders of magnitude (e.g. 0.1 Hz to 1 MHz). The negative of the imaginary component, $-Z''$, can then be plotted against the real component, Z', to produce a Nyquist plot.

Equivalent circuits can be constructed to model the processes occurring at the electrodes and the expected impedance response can be fitted to experimental data to find values for the resistance of each process. Typically, equivalent circuits are constructed of resistors, capacitors and, where appropriate more complex components such as Warburg or Gerischer elements, which describe behaviour when diffusion and mass transport are limiting [269]. Some examples of equivalent circuits and their Nyquist plots are shown in Figure 103.
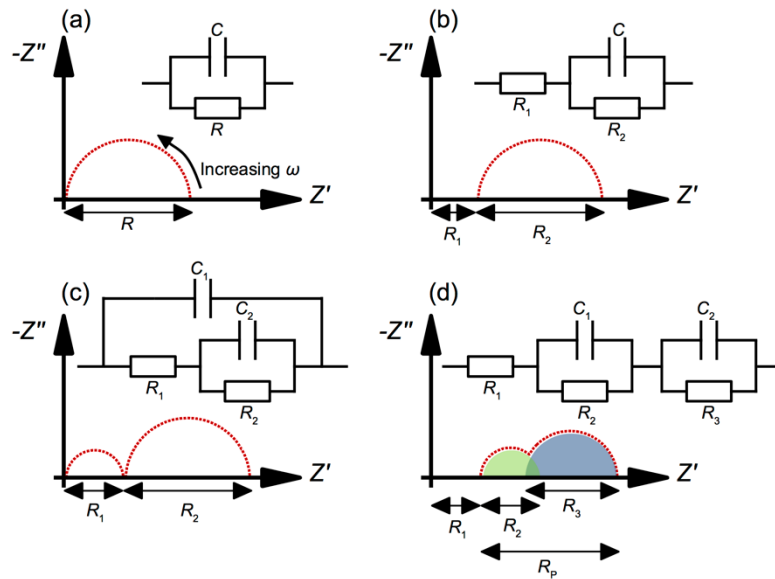
Figure 103. Impedance spectra for different RC circuits. The real axis intercepts can be used to determine the resistance of different loss components. The offset from the origin is a measure of the ohmic series resistance. The diameter of semi-circular arcs gives the contribution from polarisation losses. The frequency at the peak of the arcs are related to the capacitance and resistance of the component they arise from, i.e. $\omega = 1/(RC)$. The red dotted line shows the total measured impedance, the coloured shading in (d) shows the contributions from each separate element, which may overlap with each other, complicating deconvolution.

Equivalent circuits can be useful for determining the relative contribution from different cell processes. However, care must be taken that data are not over-fitted and that the circuit components correspond to realistic physical processes. In equivalent RC circuits the resistors generally model a conductive path, such as bulk conductivity, whilst the capacitors are usually associated with space-charge polarisation. The simple parallel element in Figure 103(a) is a common feature in electrochemical systems and is often used to represent the impedance of electrode interfaces or an electric double layer that occurs at the surface of electrodes. A constant phase element (CPE) is sometimes used instead of a capacitor to model imperfect capacitance [269].

Many authors have used EIS and equivalent circuit models to assign arcs occurring at different frequencies to specific electrochemical processes, e.g. [237]. The specific values for peak frequency are material and temperature dependent but in general the lowest frequency arcs are assigned to diffusion processes in the anode, low-medium frequency arcs to oxygen adsorption and dissociation and higher frequency arcs to charge transfer processes at solid interfaces. This will be discussed further in section 7.3.2.1.

5.5 Summary

This chapter has introduced the operating principle and advantages of SOFCs. The primary materials used for the components of SOFCs were briefly discussed and the main cell designs were described. The principal sources of loss that reduce SOFC power during operation were examined and electrode polarisation losses were identified as the key barrier to increasing power outputs at lower operating temperatures. Lower operating temperatures offer the opportunity to significantly reduce SOFC production costs and improve longevity.

Nanostructuring electrodes via solution infiltration was introduced as a method to reduce polarisation losses and improve stability. The benefits of using inkjet printing to infiltrate porous electrodes were presented. Finally, a brief overview of impedance spectroscopy and the interpretation of spectra in terms of equivalent circuits was given.

In the following chapters results of both anode and cathode infiltration using inkjet printing will be presented.

- In chapter 6 the infiltration of thick (~500 μm) anodes with doped ceria precursor solutions is investigated. With the aim of improving performance

using DoD inkjet printing; a simple, scalable technique. Methods to increase anode porosity and infiltrated Ni-Fe anodes will also be presented.

- In chapter 7 will study dual infiltration of cathodes with doped ceria and cobalt oxide nanoparticles. The sequence of the infiltration process will be investigated and tested in model symmetric cathode cells.

6 ANODE INFILTRATION

Parts of the work presented in this chapter also appear in the following publication:

[270] **T.B. Mitchell-Williams**, R.I. Tomov, S.A. Saadabadi, M. Krauz, P. V. Aravind, B.A. Glowacki, R.V. Kumar, Infiltration of commercially available, anode supported SOFC's via inkjet printing, Mater. Renew. Sustain. Energy. 6 (2017) 12. doi:10.1007/s40243-017-0096-2.

6.1 Anode supported cells

As mentioned in chapter 5 the state-of-the-art commercial SOFCs are based on a combination of cermet anodes (e.g. Ni/8YSZ) and ion-conducting ceramic electrolyte, most often yttria-stabilized zirconia (8YSZ). They operate at temperatures within the region of 800–1000 °C, which allows utilisation of the waste heat leading to higher fuel efficiency. Such operating temperatures require use of expensive corrosive resistant interconnects and are detrimental to the durability of the cell due to functional materials degradation. Consequently, the main barriers for the commercialisation of SOFCs have been the high cost of production and their operational durability. Thus, the success of SOFC commercialisation is critically dependent on the reduction of the operating temperature. However, lower operating temperatures leads to increased polarisation losses in the electrodes and decreased ionic conductivity of the electrolyte. The strategies used to compensate for this effect, apart from lowering the electrolyte resistance by using thinner electrolytes, include a reduction of the polarisation losses via electrode nanoengineering [244]. Wet infiltration has been shown to be one of the most effective approaches in enhancing of the electrochemical activity of the anodes and cathodes. Nanodecoration of the electrode surface with particles of a mixed conducting oxide and metal catalysts (e.g. gadolinium doped ceria, Ni, Pt, Pd, Cu) has been shown to be a successful method for lowering the operating temperatures and improving the long-term stability of SOFCs [271–273]. The concept, introduced in section 5.3.2, is based on the infiltration of precursor solutions into the porous electrode scaffold after the high temperature electrolyte sintering step. The formation of the nanoparticles is performed at relatively low temperatures with a simple heat treatment in air. The nanoparticles effectively increase the

triple phase boundary (TPB) length and catalyse the electrochemical reactions. Furthermore, the presence of oxide nanoparticles has been shown to prevent scaffold particles coarsening and increase the resistance to poisoning from non-pure fuel gases.

6.1.1 Solution infiltrated cells

Solution infiltration of both cathode and anodes has been demonstrated by various groups [274,275] in laboratory conditions. The infiltration is usually performed with micropipette drop delivery or sample immersion. The procedure often involves several loading steps with intermediate vacuum treatments to increase the mass load of the infiltrate. An appropriate heat treatment is performed after each step to form either a nanodecoration composed of discrete nanoparticles or interconnected nanoparticle coverage on the electrode scaffold. The process is cumbersome and slow resulting in non-uniform ink distribution (both lateral and in-depth) and waste of expensive ink. Liu et al. [276] infiltrated 1 M (metal ion concentration) water based inks of Sm doped ceria ($Sm_{0.2}Ce_{0.8}O_{1.9}$, SDC) into laboratory produced anode-supported button cells, $Ni/SDC|SDC|Sm_{0.5}Sr_{0.5}CoO_3$ (vertical lines separate cell components, slashes represent composites). The ink was manually dropped onto the porous anode under vacuum and the infiltration was driven by capillary action. After drying, the pellets were fired at 800 °C for 2 hours to decompose the nitrate salts and form corresponding metal oxides. Different loading levels were achieved by repeating the infiltration cycle. It was demonstrated that the cell performances at 600 °C in humidified H_2 changes with SDC loading. Loadings of $0.96 \, mmol \, cm^{-3}$ (two infiltration cycles) and $1.41 \, mmol \, cm^{-3}$ (three sequential infiltration cycles) led to an increase of the maximum power output by 8 and 22% respectively. Timurkutluk et al. [277] infiltrated gadolinium doped ceria (CGO) precursor ink into the anode and cathode of $Ni/ScSZ|ScSZ|LSF/ScSZ$ button cells. After five infiltration passes it was found that at 700 °C the cell impregnated with 1.5 M solution provides peak power density of $1.34 \, W \, cm^{-2}$ compared to the cell without impregnation producing only $0.78 \, W \, cm^{-2}$. They also noticed that infiltration with more concentrated precursor solutions reduced power output due to a reduction in open porosity. Sholklapper et al. [278] reported that infiltration of SDC into a composite Ni/ScSZ anode led not only to an increase in fuel electrode performance (from 348 to $403 \, mW \, cm^{-2}$) but more importantly to a significant increase in sulphur tolerance. Single step infiltration of the cathode of commercially available cells has been reported by Dowd et al. [279]. They could load ~8–10 wt% $La_{0.6}Sr_{0.4}CoO_{3-x}$ (LSC) into a composite LSCF/SDC cathode that had a thickness of

~50–60 μm in a single step using an ultrasonic spray nozzle. The samples showed improved power performance and increased durability after 200 hours of operation compared to a reference. The improved performances of the anodes infiltrated with mixed conducting oxides could be attributed to the extension of TPB as well as enhanced catalytic activities of the anodes.

6.2 Enhancing performance of commercial cells

For the infiltration to be incorporated industrially the process needs to be commercially viable. Inkjet printing is an inherently scalable, low-cost and controllable technique delivering nano- to pico-litre drops with kHz frequency over large areas with micrometre positioning precision. Our research group has shown it to be an effective technique for fabrication and infiltration of SOFCs [263,265,266]. The efficient use of potentially expensive precursor materials and reproducibility of the inkjet infiltration process are significant advantages for both research and scale-up. Additionally, the non-contact nature allows more delicate electrolyte supported cells to be infiltrated safely whilst the drop impact velocity, in the range or 1–2 m s^{-1} [280] can improve infiltration without having to employ vacuum processing.

The current chapter studies the feasibility of inkjet printing infiltration of anode supported SOFC produced via commercial fabrication technology. The aim of the research was to reduce the number of infiltration processing steps. The goal was to achieve deep penetration of the ink into the thick anode supports avoiding vacuum infiltration treatments and to ensure uniform lateral delivery of the ink with nanolitre precision.

The performance of two inks, one propionic acid based and another water based were investigated. Many research groups report results from water based solution infiltration, whilst our previous work showed how propionic acid based inks can be used to form doped ceria [264]. Propionic acid based solutions spread well on metal and oxide surfaces [281] and so, unlike aqueous solutions, do not require additional surfactants to achieve a high degree of wetting. Hence, there was interest in comparing the performance enhancement for alternative precursor solutions, particularly where the rheological properties for each ink may be different. In addition to fuel cell infiltration, symmetric anode cells were produced and infiltrated to demonstrate the suitability of propionic acid ink precursor. Finally, an alternative method for producing robust, infiltrated anodes was investigated.

6.2.1 Solution inks

6.2.1.1 Solution ink preparation

Two gadolinium doped ceria (CGO) precursor inks were prepared based on different solvents: water (H_2O) and propionic acid (PPA). Both were produced using cerium nitrate hexahydrate (99.999%, Alfa-Aesar) and gadolinium nitrate hexahydrate (99.9%, Alfa-Aesar). A stoichiometric quantity of the salts ($Ce_{0.9}$, $Gd_{0.1}$) were dissolved in the solvent to produce a stock solution with a total metal ion concentration (TMIC) of 1.5 M. The water based ink had a surfactant (Triton$^©$ X-100, Sigma Aldrich) added (3 wt% of nitrates used) to improve printability and wetting characteristics. The inks were then diluted to lower TMIC concentrations to achieve optimised rheology for inkjet deposition. The ink details and properties are summarised in Table 14.

Viscosity was measured using a programmable viscometer (LVDV-II+, Brookfield) fitted with a small sample adaptor and spindle (SC4-18, suitable for viscosities 1.5–30000 cP). Rotation speeds were scanned from 20 to 160 RPM, corresponding to shear rates of 26 and 211 s^{-1} respectively. No shear thickening or thinning behaviour was observed for either ink.

Table 14. Anode infiltration CGO ink details and properties

Primary solvent	Concentration / M	Additives	Viscosity / cP
Water	1.0	Triton$^©$ X-100, 3wt% of nitrates	1.8
Propionic acid	0.5	None	2.2

6.2.1.2 Jetting

A single inkjet printing nozzle (100 μm diameter ruby orifice, electromagnetically driven Domino Macrojet printhead) was used to produce symmetric anode cells and infiltrate the anode supports of the fuel cells. The pressure applied to the fluid reservoir and the opening time of the nozzle orifice were optimised to dispense well defined drops.

To ensure accurate and precise jetting and to fully characterise the jetting process drop visualisation and optimisation was performed. The system for visualisation was the same as described in section 4.3.1. This enabled optimisation of the jetting parameters to produce desired drop formation and ensure equivalent quantities of ink were uniformly distributed on the surface of each anode support.

6.2.1.3 Contact angles

A micropipette was used to dispense a single 10 µL drop of each ink onto flat, dense, polycrystalline substrates representative of the anode components: yttria-8mol% zirconia (8YSZ) and nickel oxide (NiO). The drop visualisation system was used to image the sessile drop and the drop spreading after deposition. Contact angles were measured by analysing images using ImageJ [282].

6.2.2 Fuel cell preparation

The cells used were commercially available anode supported solid oxide fuel cells (CEREL, Poland). They had a composite nickel oxide/yttria-8mol% zirconia (NiO/8YSZ) anode, 8YSZ electrolyte and lanthanum strontium cobalt ferrite (LSCF) cathode. The anode thickness was approximately 500 µm with an electrolyte and cathode total thickness < 25 µm. The anode diameter was 20 mm and the cathode was 17 mm, giving an effective area of 2.26 cm^2.

Two samples were infiltrated: one with the water based ink and the other with the PPA based solution. A third cell was left unaltered to act as a reference. The choice of optimum jetting parameters for each ink was also driven by the condition to have similar drop volumes and drop velocities for both inks. Thus, the difference in the performance could be attributed only to the difference in the inks rheological parameters or decomposition behaviour. Inks were deposited on to the anode surface at room temperature using jetting parameters that gave drop volumes of approximately ~19 nL and velocities of ~1.5 m s^{-1}. Drops were deposited across the entire anode in a square array pattern with a spacing of 1 mm. For the PPA based ink passes were repeated until the ink was no longer absorbed quickly into the porous anode (4 passes). Two passes were used for the H_2O ink to reflect the higher metal ion concentration. No vacuum treatment was employed at any stage of the infiltration procedure. Following the first ink deposition step the cells went through a brief thermal treatment to remove organic components in the anodes. The cells were heated to 500 °C in air with heating and cooling rates of 5 °C min^{-1}. The room temperature ink deposition was then repeated with the same number of passes. The final stage was a higher temperature calcination, where the cells were heated to 800 °C in air and held for 30 mins. Heating and cooling rates were 5 °C min^{-1}.

The cells were weighed (SI-234 Analytic Balance, Denver Instrument) before and after the infiltration process to determine the mass loading of CGO. In both cases the infiltrated cells had approximately 1 wt% CGO in the anode following infiltration and calcination.

6.2.3 Symmetric anode cell preparation

Symmetric cells were produced and tested in collaboration with Dr Chingfu Wang using the following procedures.

6.2.3.1 Suspension ink

A suspension ink of NiO:CGO (60:40 wt%) was formed by milling 10 mol% gadolinium doped cerium oxide powder (99.9%, Sigma-Aldrich) and NiO (99%, Sigma-Aldrich) powders for 8 hours. The powders were dispersed in a mixed solvent mixture of methanol and terpineol (50:50 vol%) and ethyl cellulose (99.9%, Sigma-Aldrich) was added as a polymeric dispersant.

6.2.3.2 CGO electrolytes

CGO pellets were formed from 10 mol% gadolinium doped cerium oxide powder (99.9%, Sigma Aldrich) milled with 3 wt% hydroxypropyl cellulose (Sigma-Aldrich, average molecular weight: 10,000) for 4 hours. Pellets were pressed using 0.350 g of powder in a 12.5 mm diameter die under 3 tonnes before sintering at 900 °C in air. CGO pellets were used due to their higher ionic conductivity relative to 8YSZ at intermediate temperatures, therefore allowing thicker, more robust symmetric cells to be produced.

6.2.3.3 Symmetric anode deposition

Symmetric button cells were fabricated by depositing the NiO/CGO suspension ink on to the surface of the CGO pellets. Drops were deposited in a square array pattern with 0.6 mm spacing and 0.2 mm offset between printing passes to avoid drop replica stacking. The deposition was performed on a hot stage at 90 °C. Six printing passes were performed on each side to give anodes with thicknesses of ~10 μm. The anodes were sintered in air at 1100 °C.

6.2.3.4 Symmetric anode infiltration

Cells were infiltrated on both sides with the propionic acid based ink. Infiltration was performed using a 1 mm square array pattern across the entire surface with the substrate at room temperature. Following every 2 print cycles an intermediate heat treatment was performed where the sample was heated to 350 °C before cooling back to room temperature.

This was to burn out organic residues and increase the loading fraction possible. A maximum of 20 printing passes was performed on each side leading to a maximum mass loading of ~30 wt%.

Following infiltration both the infiltrated and reference samples were heated to 1400 °C in air to simulate the conditions used during typical electrolyte sintering. Following sintering the anode area was 1 cm^2.

6.2.4 Characterisation

6.2.4.1 Fuel cell electrochemical characterisation

Electrochemical performance was characterised using an Open Flange test set-up (Fiaxell SOFC Technologies) with polarisation curves measured using a potentiostat (Gamry Instruments) controlled using proprietary software (Gamry Instruments Framework).

Cells were reduced in pure hydrogen at 800 °C for 2 hours then tested in pure humidified hydrogen. The humidity was controlled by bubbling the fuel gas through a water bath held at 30 °C, corresponding to an equilibrium humidity of ~4%. The flow rate was 100 cm^{-3} min^{-1}. Nickel and gold mesh acted as the current and voltage taps for the anode and cathode respectively. Sealing was achieved compressively against alumina felt on the cathode and against mica sheet at the anode. With the size of fuel cell used and the compressive sealing there was a small, consistent, leak during all cell tests. These measurements were performed in collaboration with Ali Saadabadi at TU Delft.

6.2.4.2 Symmetric cell electrochemical characterisation

Cells were reduced at 800 °C for 2 hours prior to measurement. AC impedance measurements were performed using a Solartron impedance analyser system (SI1260+SI1287) using a two-electrode configuration. The EIS scans from 0.1 Hz to 1 MHz, with an applied voltage of 10 mV and no bias, were conducted at a temperature of 600 °C under 4% humidified hydrogen (balance argon) with a gas flow rate of 30 cm^{-3} min^{-1}. Z view software (Solartron) was used to obtain Nyquist plots. Stability testing was also performed on an infiltrated sample for 50 hrs at 600 °C.

6.2.4.3 Microstructural characterisation

Microstructural characterisation was carried out after electrochemical performance testing. For full fuel cells using high resolution scanning electron microscopy (FEI Nova

NanoSEM). Samples were fractured and mounted with the exposed surface visible to determine the size and distribution of the nanoparticles in the anode. Image analysis for nanoparticle size was performed using ImageJ [282]. Symmetric cells were imaged using a JEOL JSM 6430 SEM in plan view.

6.2.5 Jetting parameters

The drops jetted towards the surface of the anode support had a defined kinetic energy prior to their contact with the porous medium, as discussed in [280]. Hence, while the axial momentum of the impact was transformed to radial spreading, the pressure of the impact facilitated the ink penetration into the substrate. Next, capillary effects have drawn the ink into the porous support. Reis et al. [283] presented a numerical model studying the dynamics of the impact/absorption of a liquid drop on a porous medium. Spreading and penetration of the drop into a porous medium was found to be governed by several parameters amongst which several have practical importance to our experimental scenario – Reynolds number (Re), Weber number (We), porosity (ε) and contact angle (θ). Equations (15) and (16) for Re and We are reproduced below.

$$Re = \frac{v \rho a}{\eta} \tag{15}$$

$$We = \frac{v^2 \rho a}{\gamma} \tag{16}$$

In this case v is the drop impingement velocity, a the drop radius at impact, ρ the density of the ink, η is the viscosity and γ the surface tension. Re can be thought of as the ratio of inertial to viscous forces whilst We gives a measure of the relative importance of the inertia to the surface tension. The model results of Reis et al., e.g. Figure 104, indicated that Re is more related to the amount of momentum dissipation, while We, ε and θ can be mainly related to capillary pressure. Consequently, the penetration depth and spreading of the ink in the infiltration procedure performed in our experiments were found to be a complex function of fixed parameters (ε), parameters with limited variability (ρ, η, γ and θ) restricted by the rheological window of stable jetting for the print-head in use and sufficiently variable parameters (v, a). Hence effort was directed towards achieving high impingement velocity (v) simultaneously preserving stable jetting without formation of satellite drops or splashing. Generally smaller drop volumes (a) were considered desirable to ensure more uniform delivery of the ink over the anode support surface. Additionally, the uniformity of the ink

distribution was controlled by the optimum choice of the printer lateral step size and the overlap between the drop replicas on the surface.
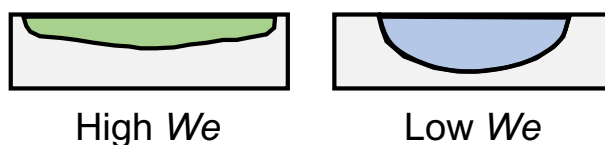
Figure 104. Example results redrawn from Reis et al. [283] illustrating the effect of Weber number on the infiltration of liquid droplets into a porous substrate.

Drop visualisation enabled both ink jetting parameters to be tailored in such a way that each triggering event resulted in a single drop, without satellite drops, before reaching the substrate. Figure 105 shows images of optimised jetting of the drops in flight for both the water and propionic acid based CGO inks. For both inks the initial drop forms an elongated tail after it detaches from nozzle, but the tail part catches up to form a single drop. Hence at optimised jetting parameters no satellite drop formation is achieved.
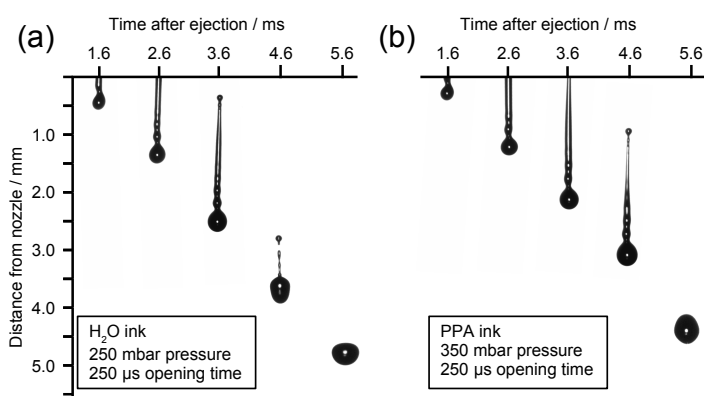
Figure 105. Time sequence illustrating drop formation for the (a) water based ink and (b) the propionic acid based CGO ink. The images shown are for the printing parameters used during infiltration. The formation of a single drop with a known volume and velocity was achieved by adjusting the ink reservoir pressure and nozzle opening time.

Figure 106 shows how the parameters of applied ink reservoir pressure and nozzle opening time influenced the drop volume and drop velocities. Higher pressures and longer opening times both led to larger drop volumes and greater velocities. The extreme values for both volume and velocity were constrained by the ability to reproducibly deposit well-formed droplets. When very low pressures or opening times were used, jetting was inconsistent and drop velocities were very low leading to poor accuracy at the substrate. When very large values

for opening time and pressure were used, very long ligaments formed and broke up in to many satellite drops resulting in poor control of placement and volume.
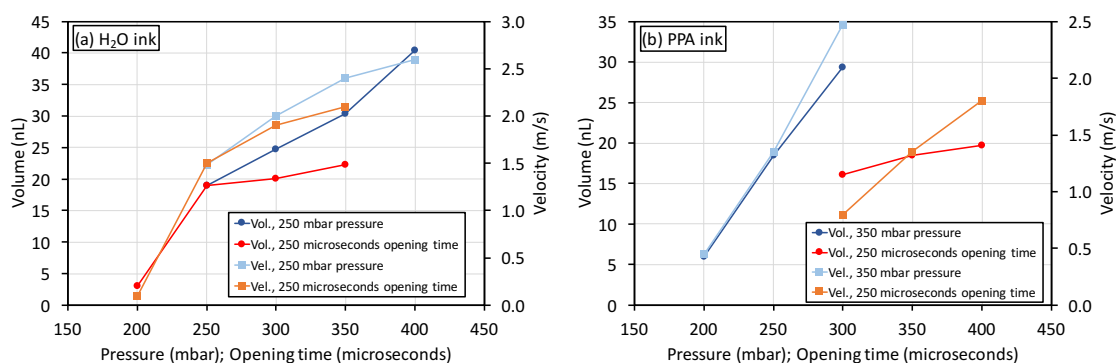
Figure 106. Plots illustrating how the adjustable printing parameters affected the drop volume and velocity for (a) the water based ink and (b) the propionic acid based CGO ink. Series are plotted showing how both drop volume and velocity vary with opening time for a fixed pressure and vice versa. Higher pressures and longer opening times both gave higher velocities and larger drop volumes.

6.2.6 Contact angles

The contact angle on relevant substrates was found to be lower for the propionic acid ink than the water based ink, Figure 107. The static contact angle was 24° for the water based CGO ink and 6° for the propionic acid based ink on 8YSZ. Both inks wetted the NiO surface better than the 8YSZ such that it was not possible to measure a static contact angle on the NiO substrate. In Figure 108 a time-series of photographs illustrates how drops of both CGO inks wet the NiO surface. These results indicate that the PPA ink is likely to have spread over the surface of the anode more uniformly and therefore should lead to a better distribution of the CGO nanoparticles.
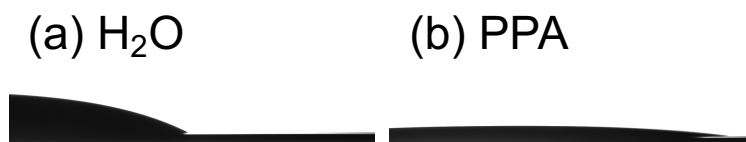
Figure 107. Photographs illustrating the difference in contact angle on polycrystalline, dense 8YSZ between (a) the water based ink and (b) the propionic acid based ink. The PPA ink showed better wetting and a lower static contact angle.

(a) H$_2$O

(b) PPA

Initial surface   Time: 70 ms   Time: >10s
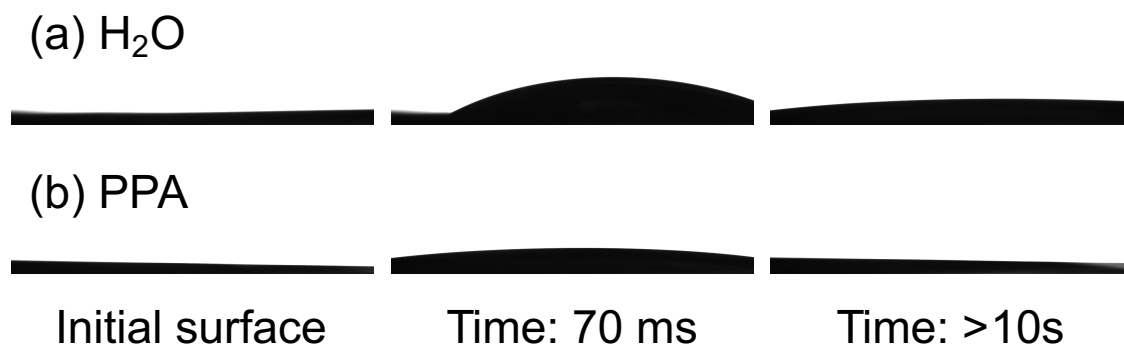
Figure 108. Time-series of photographs illustrating the wetting behaviour on NiO for (a) the water based and (b) the propionic acid based ink. Whilst both inks wet the surface well the PPA based ink spread further.

6.2.7 Full cell results

6.2.7.1 Microstructure

The presence and distribution of CGO nanoparticles was studied by high resolution SEM. It can be seen in Figure 109 that the CGO nanoparticles had a similar size in both infiltrated samples. The size of the nanoparticles varied from approximately 40 nm to 100 nm. An average of 120 particles gave a mean of 56 nm and standard deviation 16 nm.
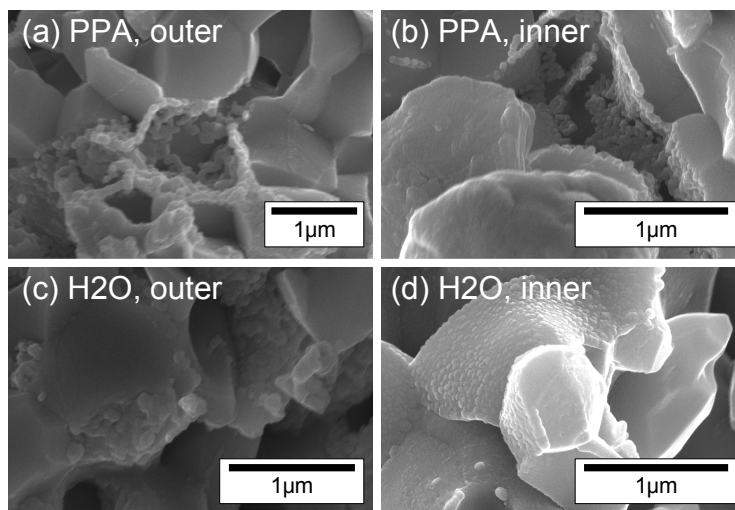
Figure 109. Secondary electron images showing the fractured cross-section of the fuel cell anodes. CGO nanoparticles decorate the anode surface for (a), (b) the PPA and (c), (d) the H$_2$O infiltrated cell. Both at the outer surface, (a), (c) and near the electrolyte interface, (b), (d).

Both also showed an approximately constant distribution of nanoparticles throughout the thickness of the anode from the outer surface to the electrolyte interface. The formation of CGO nanoparticles near the anode/electrolyte interface was the main target of the infiltration

experiment, as modelling studies have shown that the electrochemical reaction processes occur within ~20 μm of the interface [284].

6.2.7.2 Full cell electrochemical performance

The polarisation curve and power density for each of the cells is shown in Figure 110(a). The samples infiltrated with the CGO precursor solution show a small improvement in the maximum power measured. The power density was approximately 7% and 12% higher for the H_2O and PPA samples respectively, relative to the reference cell, but only at low voltages. The measured open circuit voltages (OCV) were lower than the theoretical expected value and indicated a small, but consistent, leak in the testing system. However, despite the leak all three samples show approximately the same OCV (950–980 mV). With the best performing cell, the PPA infiltrated sample, showing the lowest.

The results suggested that the presence of 1 wt% CGO in the anode only affected the power output of commercially available fuel cells at low cell voltages. The power output, for the PPA infiltrated cell, at 750 °C measured at different H_2/N_2 volume ratios is presented in Figure 110(b). The sharp rather than gradual decline in the power density with the reduction of H_2 vol% suggested the presence of substantial concentration losses, most likely due to the low porosity of the anode support.
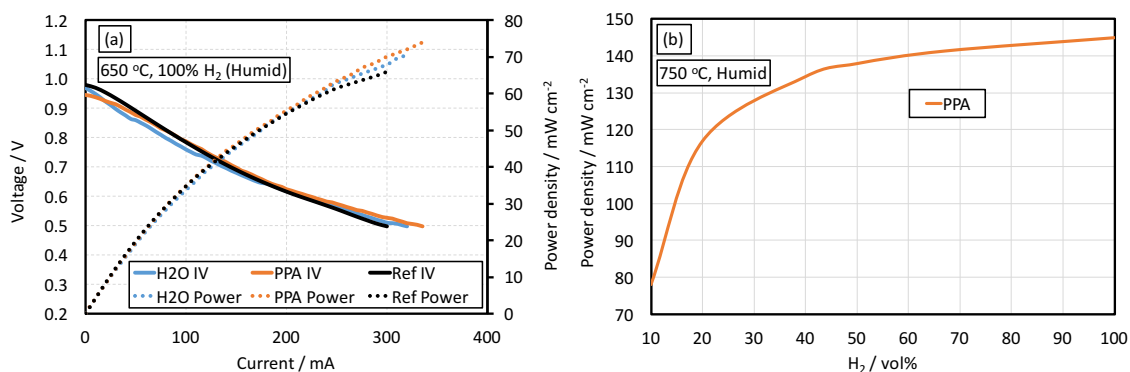
Figure 110. (a) I-V characteristics and resulting power curve for both infiltrated and reference fuel cells. The infiltrated cells only show a small improvement in the maximum power output relative to the reference cell at impractically low voltages. (b) The power density shows a sharp decrease when the fuel concentration is reduced indicating high concentration losses due to low open porosity in the cells.

The lack of substantial performance improvement for the infiltrated samples at suitable cell voltages was attributed to two factors: the relatively low nanoparticle loading and the relatively small contribution to total loss from the anode polarisation resistance. In symmetric cells when a large CGO particle loading fraction is achieved the polarisation

resistance of the anode is decreased significantly. However, in the real fuel cells there will also be loss contributions from the cathode polarisation resistance and concentration losses. Therefore, the small reduction in anode polarisation resistance may be dwarfed by the other loss mechanisms in this case.

The small difference between the performance of the H_2O and PPA infiltrated samples at higher current densities may be in part explained by the connectivity of the CGO nanoparticles. Although the particles are of similar sizes and shapes, the CGO in the PPA sample display better connectivity than in the H_2O, Figure 109(b) and (d), providing a more continuous percolative path through the anode scaffold. The small difference in the CGO particle morphology was ascribed to the higher surface tension of water compared to propionic acid, which was reflected by the contact angle measurements presented in section 6.2.6. This may have led to more isolated precursor residue replicas during the drying process and therefore less connected CGO nanoparticles.

To improve the performance more significantly the cathode should also be infiltrated to reduce the polarisation resistance of both electrodes. Kiebach et al. [285] infiltrated cells assembled into a stack by flooding the electrodes using the gas manifolds to deliver the aqueous CGO and CGO/Ni precursor solutions. They found an improvement in stack performance following cathode infiltration but no significant further improvement after subsequent anode infiltration. In fact, the flooding method led to poor electrical contact with one of the cells due to accumulation of CGO at the bottom of the stack and therefore a reduction in the total power output. The precise deposition achievable with an inkjet printing approach reported here avoids those inherent materials wastage and accumulation problems. However, our results broadly agree; anode infiltration alone did not significantly enhance the electrochemical performance of commercial cells at intermediate temperatures, due to the dominance of cathode losses [237]. The benefit of anode infiltration in commercial cells may be more pronounced for long term stability and fuel impurity tolerance [273,286,287].

Furthermore, using a more porous anode structure would benefit the cell in two ways: it would reduce the concentration losses occurring due to limited gas diffusion and increase the fraction of nanoparticle loading achievable. To determine the effectiveness of the infiltration procedure on enhancing the anode performance, symmetric anode cells were produced and tested. This enabled the anode losses to be separated from the more dominant

cathode and concentration losses. Therefore, verifying that the propionic acid ink precursor route was suitable for solution infiltration.

A CGO electrolyte was used due to the higher ionic conductivity at intermediate temperatures [288]. This meant a thicker electrolyte could be used, which facilitated easy production and handling. A composite NiO/CGO anode was used to ensure a compatible thermal expansion coefficient with the electrolyte. Thin anodes, ~10 μm, prevented significant concentration losses.

6.2.8 Symmetric cells

6.2.8.1 Symmetric cell microstructure

Following infiltration, the symmetric anodes were found to have a high density of CGO nanoparticles decorating the surface, Figure 111, even after 8 printing cycles. This indicated that the PPA ink could effectively deliver precursors for forming well distributed nanoparticles.
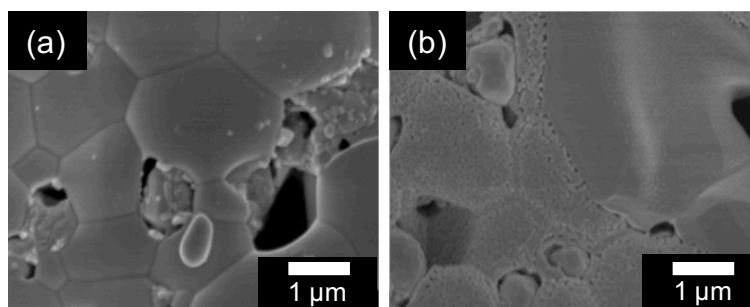
Figure 111. Secondary electron image showing the symmetric anode structure in plan view (a) before and (b) after 8 infiltration printing passes. The infiltrated sample had a high density of CGO nanoparticles decorating the surface. Images courtesy of Dr Chingfu Wang.

6.2.8.2 Symmetric cell impedance

The symmetric cell infiltrated with CGO using 20 printing cycles of the propionic acid ink demonstrated a lower polarisation resistance, Figure 112, than the reference cell. The smaller polarisation resistance arc for the infiltrated sample indicates that the infiltrated CGO nanoparticles effectively extend the triple phase boundary (TPD) and therefore geometrically enhance the electrode performance.
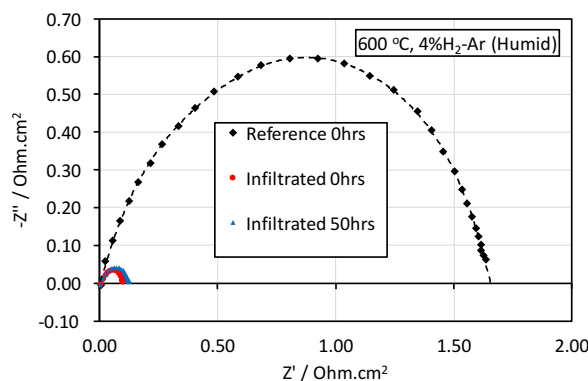
Figure 112. Nyquist plots for symmetric anode cells tested at 600 °C. The size of the arc indicates the magnitude of the polarisation losses. The infiltrated cell showed much lower polarisation losses than the reference both before and after 50 hours aging. Data courtesy of Dr Chingfu Wang.

The Nyquist plots were shifted to subtract the ohmic component, which depends on electrode contact and electrolyte thickness, for clarity. The area specific resistance (ASR) values were estimated using the real axis intercepts and are summarised in Table 15. The infiltrated cell had an ASR that was more than 10 times lower than the reference cell before and after aging. The lack of significant performance degradation after 50 hours was promising and demonstrated that at 600 °C the nanostructured anode was stable.

Table 15. Area specific resistances of the symmetric cells at 600 °C.

Sample	Area specific resistance (ASR) / $m\Omega \cdot cm^2$
Reference	830
Infiltrated: 0 hours	50
Infiltrated: 50 hours	60

6.3 Improving porosity

As mentioned above improving porosity should improve the effect of anode infiltration in two ways: increasing the mass loading achievable using solution infiltration and by lowering concentration losses that occur due to gas diffusion becoming limited. Two methods to increase anode porosity are demonstrated in the following sections.

6.3.1 Reduced anodes

When the NiO component of a typical SOFC anode is electrochemically reduced to nickel metal a solid volume reduction occurs with a corresponding increase in porosity. Kiebach et al. [285] used this approach to infiltrate a stack after sealing and anode reduction. They flooded the electrodes via the gas manifolds before heating to 350 °C and the process was repeated ~3 times to achieve sufficient loading, however, a figure for the loading was not provided. The advantage of infiltrating after cell production and reduction is that a subsequent high temperature stage, for example to sinter the electrolyte or cathode, is not required. Therefore, lower temperatures can be used to form the nanoparticles, which should lead to smaller sizes.

6.3.1.1 Porosity differences

The porosity of samples was measured using the Archimedes principle, equation (23), and using mercury porosimetry (AutoPore IV, Micromeritics Instrument Corporation). There was a close agreement, < 2% difference, between measurement techniques. The Archimedes method was performed by thoroughly drying the samples before weighing then vacuum impregnating the porous structure with de-ionised water for several hours. Then the samples were weighed suspended from a basket in de-ionised water before measuring the weight after removal from the water and patting dry to remove surface water.

$$open\ porosity = \frac{w_w - w_d}{w_w - w_s} \tag{23}$$

Where w_w is the weight of the sample with water filling the pores but not on the surface, w_d is the weight of the dry sample weighed in air and w_s is the weight of the sample measured whilst suspended in water.

Samples were reduced in flowing 4% H_2-Ar at 500 °C for 5 hours. Ramp rates were 5 K min^{-1}. The porosity of nickel-iron anodes, described in more detail below in section 6.3.2, was measured before and after reduction, Table 16. The pre-sintering temperature and reduction of oxide both make a significant difference to the open porosity of the anode, with reduction having a greater influence for initially less porous anodes.

Table 16. Porosity of nickel-iron anodes before and after reduction

Pre-sintering temperature / °C	Open porosity / %		
	Non-reduced	Reduced	Difference
1000	50	54	4
1400	21	30	9

6.3.1.2 Anode infiltration

To explore if greater loadings could be achieved with cell reduction 2 identical 'dummy' cells were infiltrated with the water based CGO ink described earlier, section 6.2.1.1. The dummy cells were nominally the same as the commercial fuel cells described above, section 6.2.2, except without a cathode, i.e. a NiO/8YSZ 500 μm anode with a dense 8YSZ electrolyte. Both cells were infiltrated using the procedure described earlier, section 6.2.2, with a single intermediate burn out stage between solution infiltrations via inkjet printing.

SEM micrographs of the fractured surface near the electrolyte interfaces are shown for both reduced and non-reduced samples in Figure 113. The reduced sample had a greater CGO loading, approximately 1.3 times larger, based on the mass differences before and after infiltration. The microstructure supports this observation with a denser network of CGO particles decorating the structure of the reduced anode sample, Figure 113(b).
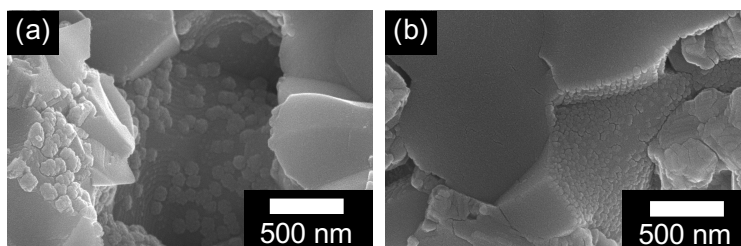
Figure 113. Secondary electron images showing the fractured surface of (a) the non-reduced and (b) the reduced dummy cells after infiltration. A greater density of CGO particles was observed in the anode that had been reduced prior to infiltration.

6.3.1.3 Cathode stability

Two symmetric non-infiltrated cathode cells were produced to determine whether complete button cells could survive the reduction procedure before anode infiltration. Full details of the cells are in section 7.3.1. They cells were formed from composite LSCF/CGO

cathodes approximately 20 μm thick supported by a CGO electrolyte. Both were tested using the EIS equipment described in section 6.2.4.2 but in air and with a frequency range of 0.01 Hz to 100 kHz. Both cells were characterised at temperatures 500, 550, 600, 650 and 700 °C before and after heat treatment. One of the cells was heat treated in 4%H$_2$-Ar at 500 °C for 5 hours to simulate the reduction process whilst the other went through an identical thermal cycle but in air.

The Nyquist plots for both cells are shown in Figure 114. As with other impedance data for symmetric cells the ohmic component has been subtracted for clarity. The heat treatment in a reducing atmosphere appeared not to significantly degrade the cathode performance. Both samples had similar impedance arcs regardless of the atmosphere they had been heated in.
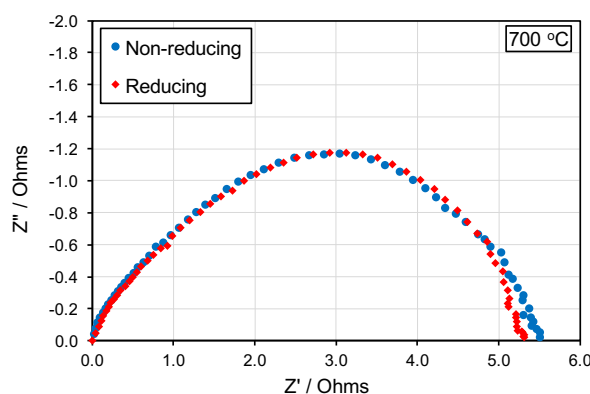
Figure 114. Nyquist plots for two symmetric cathode cells after reducing and non-reducing heat treatments. Both cells behaved similarly despite different heat treatment atmospheres.

A commercial button cell with LSCF cathode, identical to those in section 6.2.2, was reduced using the heat treatment described above. The cathode cracked and spalled off from the electrolyte surface. The difference compared to the symmetric cells may have been due to the cathode being pure LSCF rather than LSCF/CGO composite. A new cell with a composite cathode was fabricated. The anode was reduced prior to infiltration and the cathode remained intact and adherent. This sample also had the cathode infiltrated with CGO and was compared with a cell that did not have the anode reduced prior to infiltration and a separate reference cell that only had the cathode infiltrated. These three button cells were sent to collaborators at the University of St. Andrews for testing, but the reduced anode cell fractured during testing so the results were not comparable. Further testing using these 20 mm commercial button cells was not performed.

6.3.2 Pre-sintered anode infiltration

The difference in porosity between anodes pre-sintered at different temperatures was more significant, Table 16, than the difference when reducing the oxide to metal. This suggested that an alternative production route, Figure 115, could be used to utilise the higher porosity after an initial, lower temperature, sintering stage to maximise CGO particle loading.
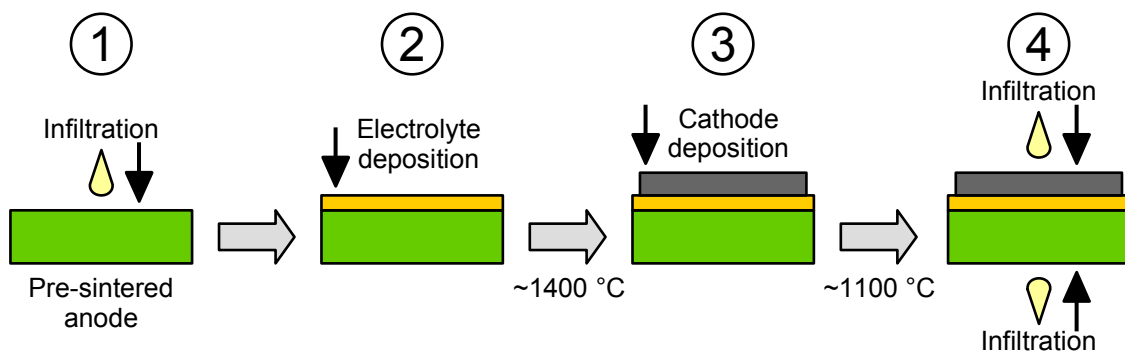
Figure 115. Alternative infiltration procedure. The additional infiltration of the pre-sintered anode in step 1 should enable high particle loading and good coverage near the electrolyte.

6.3.2.1 Nickel-iron anodes as a model system

To investigate the approach outlined above nickel-iron supported cells were chosen. Whilst Ni/YSZ has remained the primary material of choice for anode supported SOFCs, the brittle nature of the cermet causes cell failure due to cracking and the cells typically do not cope well with thermal shock or cycling, meaning they cannot be started at short notice. One solution is to use metal supported cells (MSCs). Metal supported cells either use the porous metal support as an anode directly or it can support a very thin electrochemically active layer adjacent to the electrolyte. MSCs are low cost, can be manufactured straightforwardly and can survive thermal and mechanical stresses well [221]. Furthermore, using a metallic anode ensures a percolative current path through the electrode, even when porosity is high.

Nickel has excellent catalytic activity for the oxidation of hydrogen [216] but the coefficient of thermal expansion (CTE) mismatch to common electrolyte materials, e.g. 8YSZ or CGO, and cost mean it is not entirely suitable. Alloying with iron lowers the CTE to a value much closer to the ceramics use for electrolytes whilst simultaneously reducing the cost substantially [221]. Ishihara first demonstrated the performance of Ni-Fe metal supports [289] and the process has been developed including the use of thin Ni-CGO anode layers [290–293].

Infiltration of stainless steel supported cells has been demonstrated [267,274] and the infiltration of CGO into Fe-Cr anodes was reported to improve oxidation resistance [294], however, infiltration of Ni-Fe supports has not been reported and is the subject of the current work. The feasibility of the alternative infiltration route shown in Figure 115 was investigated using nickel-iron porous anodes.

6.3.2.2 Pellet production

Nickel (II) oxide powder, NiO, (6–10 μm size, Hart Materials) was mixed with iron (III) oxide powder, Fe_2O_3, (99%, Fisher Scientific) in a molar ratio 4:1 (i.e. Ni:Fe 2:1 atomic ratio). Carbon (10 wt% of metal oxide powders) and hydroxypropyl cellulose (M_w~80000, 20 mesh, 99%, 10 wt% of metal oxide powders) powders were added as fugitives and binders. The mixture was milled for ~6 hours in a planetary ball mill. Pellets were uniaxially pressed using 2 g of powder in a 25 mm diameter cylindrical die with 5 tonnes applied for 1 minute (100 MPa). The pellets were then pre-sintered at 1000 °C for 2 hours, with an intermediate dwell at 500 °C during the heating ramp for 1 hour. Heating and cooling rates were 1 K min^{-1} and 5 K min^{-1} respectively. The pellets showed very little shrinkage after pre-sintering with diameters of 24.7 mm. The open porosity of the pre-sintered pellets was ~50%, Table 16.

6.3.2.3 Ink infiltration

6.3.2.3.1 Ethanol based CGO ink synthesis

A stoichiometric quantity of cerium nitrate hexahydrate (99.999%, Alfa Aesar) and gadolinium nitrate hexahydrate (99.9% Alfa Aesar) were added to absolute ethanol (Ce:Gd, 9:1 molar ratio). Urea (>99.5%, Fisher Scientific) was added as a complexing agent (1:1.5 molar ratio Metals:Urea). The powders were dissolved with stirring and gentle heating (40 °C). The solution was cooled to room temperature before being made up to 0.75 M total metal ion concentration with absolute ethanol and filtered (3 μm glass fibre) before storage. The solution remained stable and printable for a period of several months. The viscosity was 4.7 cP.

6.3.2.3.2 CGO infiltration and electrolyte printing

The ethanol based GCO precursor ink was infiltrated into a porous nickel-iron-oxide pellet using the same electromagnetic nozzle described earlier, section 6.2.1.2. The printing parameters were 225 mbar pressure and 240 μs opening time, giving drops of ~60 nL volume and 2.3 m s^{-1} velocity. Drops were deposited in a square array pattern with 1 mm separations

and drop stacking was avoided with 0.5 mm offsets in *x* and *y* directions between print passes. Eight printing passes were performed with no substrate flooding or intermediate heating. The total mass loading of CGO was ~2 wt% of the oxide pellet.

A 10 mol% scandium 1 mol% cerium doped zirconia (10Sc1CeSZ) electrolyte was deposited across the surface of the infiltrated and a non-infiltrated pellet in collaboration with Dr Rumen Tomov. The full ink details and jetting characterisation can be found in [268]. Briefly; the ink was a suspension of milled oxide powder and hydroxypropyl cellulose dispersed in a mixed solvent of terpineol and methanol. Drops (~22 nL) were deposited in a square array pattern (0.8 mm) whilst the substrate was heated (120 °C). The pellet was rotated and offset between each of the 3 printing passes. Both pellets were then sintered at 1300 °C in air for 4 hours. The electrolyte layer was ~10 µm thick after sintering.

6.3.2.4 Anode structure

Following electrolyte sintering both the pellets displayed significant shrinkage. However, the difference between the two was appreciable, Figure 116. The infiltrated sample had shrunk by ~8% compared with ~14% for the non-infiltrated sample, meaning the infiltrated sample will have retained greater open porosity. This difference in shrinkage was ascribed to the difference in diffusion mediated sintering of the nickel-iron oxide particles. The CGO nanoparticles will have supressed surface diffusion and grain necking during the high temperature sintering.
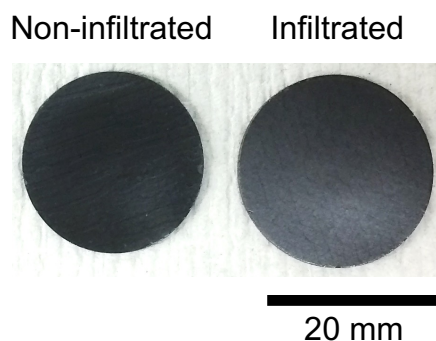
Figure 116. Photograph showing the difference in shrinkage during electrolyte sintering for the non-infiltrated and infiltrated Ni-Fe-O pellets. The infiltrated sample shows a lower degree of shrinkage.

The infiltrated anode was then broken into two halves; one was reduced (5 hours, 500 °C, 4%H_2-Ar) and the other was left oxidised. These were then infiltrated using the ethanol CGO ink again before going through a brief thermal treatment (700 °C, 1 hour). This

was to investigate the combination of both processes, lower temperature pre-sintering and reduction, on the ability to increase CGO nanoparticle loading. The microstructures are shown in Figure 117 for both halves and show that following the electrolyte sintering stage the non-reduced anode still retains sufficient porosity for effective CGO ink infiltration.
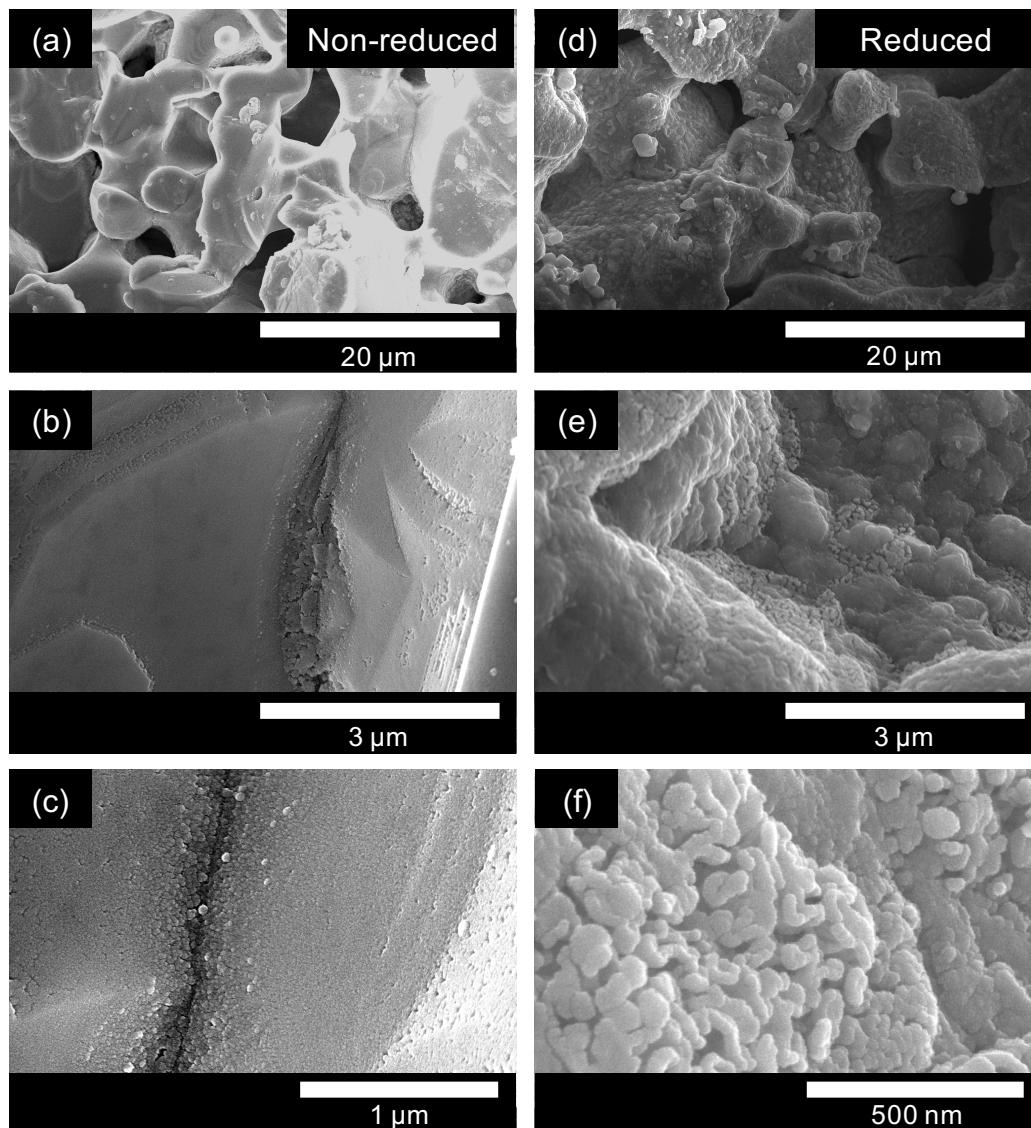
Figure 117. Secondary electron micrographs of the (a)–(c) non-reduced and (d)–(f) reduced halves of the infiltrated Ni-Fe pellet after the 2nd infiltration and heat treatment. Images from near the electrolyte interface showing that the CGO precursor ink penetrates the anode structure effectively, resulting in CGO particles distributed throughout the thickness.

In both halves of the infiltrated pellet there appeared to be some larger (600–900 nm) and many smaller (30–90 nm) particles covering the surface. The presence of this bi-modal distribution was more noticeable in the reduced half of the pellet. The larger particles of CGO were assumed to be from the first infiltration stage before electrolyte sintering, which then

coarsened and agglomerated during the high temperature processing of the electrolyte. The bi-modal distribution of particle sizes may be advantageous for maximising the triple phase boundaries (TPB), particularly if an additional infiltration of, for example, metal nanoparticle precursors is performed. Lee et al. [295] showed that a bi-modally sized Ni/CGO anode functional layer (AFL) dramatically improved the performance of a low-temperature solid oxide fuel cell, with power densities ~70% higher than cells with conventionally sized AFLs. The performance enhancement was attributed to the higher TPB density present when a bi-modal particle distribution was used.

Both electrochemical reduction of the anode before infiltration and reducing the pre-sintering temperature were found to improve the open porosity, which then enabled higher mass loading of CGO nanoparticles into the electrode scaffold. The double infiltration technique in combination with the lower pre-sinter temperature was more promising because it increased final anode porosity and did not lead to cathode delamination.

6.4 Summary and outlook

Commercially available anode supported solid oxide fuel cells (Ni/8YSZ|8YSZ|LSCF- 20 mm in diameter) were anode infiltrated with gadolinium doped ceria (CGO) using a scalable drop-on-demand inkjet printing process. Cells were infiltrated with two different precursor solutions; water based or propionic acid based. The saturation limit of the 0.5 mm thick anode supports sintered at 1400 °C was found to be approximately 1 wt%. No significant enhancement in power output was recorded at practical voltage levels. Microstructural characterisation was carried out after electrochemical performance testing using high resolution scanning electron microscopy showing that well distributed CGO nanoparticles decorated the anode surface. This work demonstrated that despite the feasibility of achieving CGO nanoparticle infiltration into thick, commercial SOFC anodes with a simple, low-cost and industrially scalable procedure other loss mechanisms were dominant. Comparison with infiltration of model symmetric anode cells with the propionic acid based ink demonstrated that significant reductions in polarisation resistance were possible.

Increasing the anode porosity was identified as an objective to both reduce concentration losses and improve CGO nanoparticle loading. Different approaches to improving porosity were investigated including electrochemically reducing the anode prior to

solution infiltration and infiltration at an earlier processing stage, when porosity was naturally higher.

Chemical reduction of conventional NiO/YSZ anodes before infiltration did enable a greater mass loading. Also, the reduction procedure was found to not deleteriously affect composite cathodes when tested in a symmetric cells configuration. However, when full button cells were reduced the cathode delaminated and spalled from the surface. Replacing the pure LSCF cathode with a composite LSCF/CGO electrode improved integrity but the cell later fractured during testing. This prevented a complete comparison with cells that had non-reduced infiltrated anodes.

Lowering the pre-sintering temperature of nickel-iron anodes from 1400 °C to 1000 °C significantly increased the open porosity and motivated the investigation of an alternative processing route. Infiltrating the anode before the electrolyte deposition and sintering reduced shrinkage. This was a promising processing route because it enabled a higher loading of CGO into the anode structure by including an additional infiltration step and by retaining a higher porosity for subsequent infiltrations after high temperature sintering steps. Furthermore, the bi-modal distribution in CGO particle sizes in doubly infiltrated Ni-Fe anodes may improve TPB density and enhance performance.

Future work will continue study of the alternative processing route for Ni-Fe anodes, including producing complete cells for electrochemical testing. Furthermore, functional grading of the infiltrated species will be investigated by adapting the rheological properties of precursor solutions and controlling the deposition conditions. The printing parameters and substrate temperature along with solution viscosity and substrate wetting will be the primary factors explored. Preliminary results suggest that solution additives such as citric acid facilitate rapid gelling of deposited infiltrate solutions, particularly at elevated substrate temperatures. This, in combination with a systematic study on the effect of drop volume and velocity, may enable controlled depth distribution of functional nanoparticles into the anode scaffold.

7 CATHODE INFILTRATION

Parts of the work presented in this chapter also appear in the following publication:

[296] R.I. Tomov, **T.B. Mitchell-Williams**, C. Gao, R. V. Kumar, B.A. Glowacki, Performance optimization of LSCF/Gd:CeO2 composite cathodes via single-step inkjet printing infiltration, J. Appl. Electrochem. 47 (2017) 641–651. doi:10.1007/s10800-017-1066-1.

7.1 Cathode materials

As discussed in the previous chapters lower operating temperatures result in the reduction of the overall electrochemical performance due to increased ohmic losses as well as electrode polarisation losses. The polarisation losses in the cathode are particularly high at intermediate temperatures. Hence, increasing the cathode electrochemical activity through surface nano-engineering of the porous electrode is particularly important.

The performance of state-of-the-art commercial cathodes based on $La_{1-x}Sr_xMnO_{3-\delta}$ (LSM) is hindered by insufficient ORR activity and low oxygen ion conductivity at intermediate temperatures. Therefore, $La_{1-x}Sr_xCo_{1-y}Fe_yO_{3-\delta}$ (LSCF) is preferred as a material for working temperatures below 700 °C, having high electronic and ionic conductivity as well as good catalytic activity for the oxygen reduction reaction [297–299]. LSCF is a mixed ionic-electronic conductor (MIEC) belonging to the perovskite family, ABO_3-type, in which both A and B sites can be partially or fully substituted. Partial substitution of La^{3+} by Sr^{2+} in $LaCoO_{3-\delta}$ was found to be accompanied by an increase in mean oxidation state of the cobalt and an increase in oxygen deficiency due to charge compensation [297]. Substituting Fe on the B site gradually decreases the degree of ionic conductivity at lower temperatures [299] but also leads to a reduced CTE and hence better thermo-mechanical compatibility with CGO electrolytes [298]. $La_{0.6}Sr_{0.4}Co_{0.2}Fe_{0.8}O_{3-\delta}$ (LSCF6428) is often chosen as a compromise offering high electronic conductivity (~340 S cm^{-1} at 550 °C), high ionic conductivity (~1 × 10^{-1} S cm^{-1} at 800 °C in air) and a lower CTE value (~15.3 × 10^{-6} K^{-1} at 373–873 K). Esquirol et al. [300] reported that LSCF/CGO composite cathodes offer further improvement at temperatures below 650 °C. However, the structural stability of LSCF-based cathodes limits their

widespread application. LSCF-based cathodes have been found to suffer from substantial long-term degradation, typically at a rate of 0.05% per hour [301]. Strontium surface segregation and the coarsening of the cathode microstructure are often reported as possible degradation mechanisms for LSCF-based cathodes. The combined effects of lower surface stress and surface charge results in SrO-terminated surfaces having lower energy than LaO-terminated surfaces thus promoting Sr segregation [301]. The enrichment of Sr at the cathode surface leads to an increase in the cathode polarisation losses through deactivation of ORR sites and decrease in surface activity [302].

7.2 Improving cathode stability and performance

Increasing the TPB density and including ORR catalysts on the surface of the cathode are critical to maintain acceptable levels of performance whilst reducing the operating temperature. Solution infiltration for electrodes has already been discussed in sections 5.3.2 and 6.1.1. CGO has been demonstrated as particularly effective for infiltrating cathodes [303] due to its high ionic conductivity, high surface exchange coefficient and good chemical compatibility with LSCF. Nie et al. [304] infiltrated LSCF6428 cathodes with aqueous solutions of $Sm_{0.2}Ce_{0.8}O_{1.95}$ (SDC) precursors and glycine as a complexing agent. Impedance analysis of LSCF/SDC|8YSZ|SDC/LSCF symmetric cells indicated substantially lower polarisation losses, relative to a non-infiltrated cathode. The area specific resistance (ASR), of the infiltrated cells was 0.074 $\Omega \cdot cm^2$ compared to 0.150 $\Omega \cdot cm^2$ for the reference at 750 °C. Yun et al. [305] impregnated LSCF6428 with $Ce_{0.8}Gd_{0.2}O_{1.9}$ sol ink. Symmetrical LSCF6428|8YSZ|LSCF6428 cells showed a reduction in polarisation resistance from 5.0 to 2.2 $\Omega \cdot cm^2$ at 700 °C. Liu et al. [306] used a 0.25 M $La_{0.4875}Ca_{0.0125}Ce_{0.5}O_{2-\delta}$ (LCC) precursor solution to produce a thin coating over the surface of LSCF cathodes. The polarisation resistance was reduced to 0.076 $\Omega \cdot cm^2$ from 0.130 $\Omega \cdot cm^2$ at 750 °C.

Burye et al. [271] used an alternative approach; a porous CGO scaffold was infiltrated with CGO followed by the electronic conductor LSCF. This led to a polarisation resistance of only 0.1 $\Omega \cdot cm^2$ at 540 °C. The low R_p at that temperature was due to the nanosized LSCF particles, which then did not substantially coarsen during aging due to the CGO nanoparticles decorating the scaffold surface.

7.3 Dual infiltration

Cobalt oxide has previously been shown to catalytically enhance the ORR occurring in the cathode, particularly at lower operating temperatures [261,307–309]. The infiltration of doped ceria into cathodes has also been demonstrated to reduce polarisation resistance and improve long term stability [271,285,304]. Imanishi et al. [310] demonstrated that dual infiltration of cobalt oxide (CoO = Co_3O_4) and gadolinium doped ceria (CGO) precursors into LSM/YSZ cathodes improved the low temperature performance of anode supported cells. The improvement was attributed to a combination of enhanced ORR from the nanoparticles combined with the low sintering rate of the CGO suppressing CoO particle coarsening and agglomeration. Cells with only CoO infiltrated showed poor stability and CoO particles aggregated substantially within 100 hours at 600 °C. Imanishi et al. performed the dual infiltration using a single, mixed metal ion precursor and assumed both separate nanoparticles formed.

Both CoO and CGO separately infiltrated improve cathode performance and as discussed, simultaneous dual infiltration also shows enhancement. However, the current work investigates if, when the infiltration is performed sequentially, there any advantage to one sequence over the other.

Symmetric LSCF/CGO composite cathode cells were produced to investigate the relevance of infiltration sequence. Symmetric cells allowed the performance of the cathode to be analysed separately from anode effects.

7.3.1 Symmetric cell production

7.3.1.1 CGO electrolyte pellet

CGO pellets were formed from 10 mol% gadolinium doped cerium oxide powder (99.9%, Sigma Aldrich) milled with 3 wt% hydroxypropyl cellulose (Sigma-Aldrich, average molecular weight: 10,000) for 4 hours. Pellets were uniaxially pressed in a 12.5 mm diameter die under 3 tonnes before sintering at 1400 °C in air. Furnace ramp rates were 5 K min^{-1}. The sintered pellet had a diameter of 11.6 mm and thickness 0.6 mm.

7.3.1.2 Cathode suspension ink

Suspension inks was formed from commercial $La_{0.6}Sr_{0.4}Co_{0.2}Fe_{0.8}O_3$ (LSCF, Fuel Cell Materials), $Ce_{0.9}Gd_{0.1}O_{1.95}$ (CGO, Sigma-Aldrich), denoted further as CGO, and

hydroxypropyl cellulose (Sigma-Aldrich) powders. Two stable primary inks, containing LSCF and CGO, respectively, were made from commercial ceramic powders in a mixture with alpha-terpineol as a carrier and dispersant. The inks were produced by wet milling with 3YSZ milling balls in a planetary ball mill for various several hours. Hydroxypropyl cellulose was used as a polymeric dispersant for ink stabilisation. It not only provided steric stabilisation of the suspension but also acted as a binder and a fugitive, promoting the formation of a porous scaffold. The rheology of the inks was adjusted to the viscosity range required for printing by varying the amounts of the diluting solvent. Methanol (reagent grade, Sigma-Aldrich) was chosen as a diluting solvent due to its high volatility allowing fast drying of the droplets. Terpineol (Sigma-Aldrich) was selected as a low vapour pressure carrier, inducing Marangoni flows counteracting the formation of coffee-ring stains. It also played the role of a natural dispersant of the oxide particles and had excellent miscibility with the dispersant and the diluting solvent.

The composite cathode suspension ink was produced by mixing equal volumes of the individual LSCF and CGO suspension inks. The ink was filtered (3 μm glass fibre) before deposition to prevent clogging of the printhead. The cathodes were deposited with optimised printing parameters [296] using the electromagnetic nozzle described earlier, section 6.2.1.2. Six printing passes were used to deposit the ink and the pellet was heated to ~120 °C between each pass. The cells were sintered in air at 1000 °C for 2 hours with heating and cooling rates of 5 K min^{-1}. The final cathode thickness was ~20 μm.

7.3.1.3 Cathode infiltration

The ethanol based CGO ink described earlier, section 6.3.2.3.1, was used along with a cobalt oxide precursor solution. The cobalt ink was synthesised using the same method as the CGO solution ink but with cobalt nitrate hexahydrate (99%, VWR International) as the metal ion source. The ink properties and printing parameters for both inks used are summarised in Table 17. Parameters were selected to give equivalent drop volume and velocities to achieve similar molar loading of both materials.

Table 17. Infiltration ink compositions and jetting parameters. Both inks were synthesised from metal nitrates and had ethanol as the primary solvent. Both inks had a urea concentration of 1.125 M.

Ink	Metal ratio; cation concentration	Viscosity / cP	Opening time / µs	Pressure / mbar	Drop volume / nL	Drop velocity / m s^{-1}
CGO	$Ce_{0.9}Gd_{0.1}$; 0.75 M	4.7	240	225	58	2.3
CoO	Co; 0.75 M	4.3	230	225	62	1.6

The infiltration was performed at room temperature with intermediate heating to 150 °C between print passes. Five infiltration passes of one ink (CGO or CoO) were performed on each side before the samples were heated to 700 °C for 1 hour in air. Then the second ink was infiltrated using the same process. Sample C_CGO_Co was infiltrated with the CGO solution ink first then the CoO solution ink. Sample C_Co_CGO was infiltrated using the opposite sequence. The total nanoparticle loading was ~20 wt% for both infiltrated samples. A non-infiltrated reference cell, C_Ref, was also tested.

7.3.1.4 Symmetric cell characterisation

Cells had gold coatings sputtered over the surface to provide a good electrical contact to gold wire electrodes. Two electrode impedance spectroscopy was performed at temperatures of 500, 550, 600, 650 and 700 °C in air with a frequency range of 0.1 Hz to 1 MHz using an applied voltage of 10 mV and no bias (Autolab PGSTAT302N, Metrohm Autolab B.V.). Samples were tested in their as-prepared state, after 24 hours aging at 650 °C and after a total of 72 hours aging at 650 °C. The aging was conducted in a separate furnace in air so each aging procedure incorporated an additional 2 thermal cycles. The total hours aging was described using the total time spent during the dwell phase of the aging heat treatment. Therefore, this does not include the time at intermediate temperatures in the ramp phases or the time it took to perform the measurements.

The microstructure was characterised using high resolution SEM (Nova NanoSEM) with an acceleration voltage of 15 kV. The cells were fractured and the cross-section sputter coated with palladium to prevent charging.

XRD diffraction patterns were collected for the symmetric cells, blank CGO pellets and the starting LSCF powder. Scans were performed (D8 Bruker) using Bragg-Brentano geometry with a position sensitive detector (LynxEye) from 20–80° degrees 2θ with a 0.02° step size and 0.7 sec/step.

7.3.2 Symmetric cell results

7.3.2.1 Electrochemical performance

Nyquist plots showing the impedance data at 500 and 550 °C for the 3 cells as-prepared and after 72 hours aging are shown in Figure 118. The ohmic contribution (high frequency real axis intercept) has been subtracted for clarity. The frequency response of the complex impedance is shown in Figure 119. The impedance data show that all the samples display a low frequency peak between 5 Hz and 30 Hz, which corresponds to the right-hand arc visible in the Nyquist plot. Most samples also display a high frequency peak near 100 kHz, corresponding to the left-hand arc in the Nyquist plot. For the reference and C_Co_CGO samples the high frequency losses were the dominant component of the polarisation resistance whilst the low frequency losses were more significant for the C_CGO_Co sample. There was generally an increase in the high frequency losses following aging.
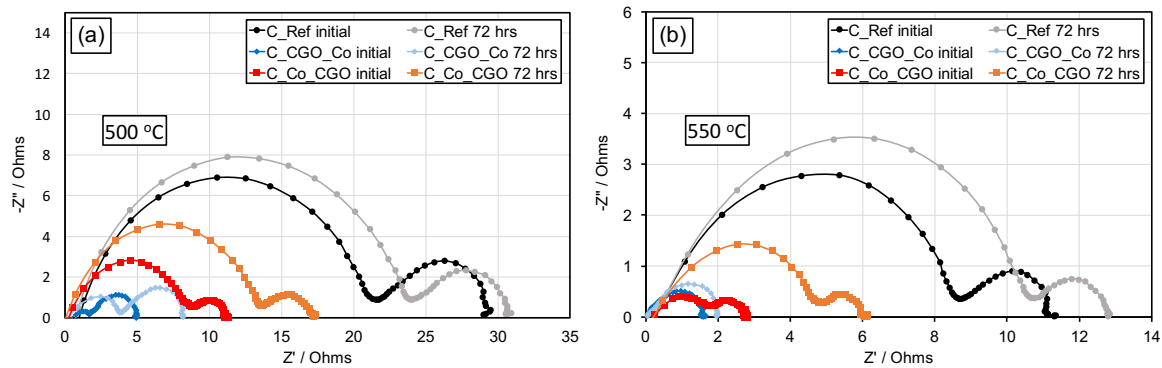
Figure 118. Nyquist plots showing the impedance of the symmetric cathode cells at (a) 500 °C and (b) 550 °C. The ohmic component has been subtracted. The infiltrated cells both show substantially lower polarisation resistances than the reference cell both before and after aging. The sample infiltrated with CGO before CoO has the lowest resistance before and after aging.
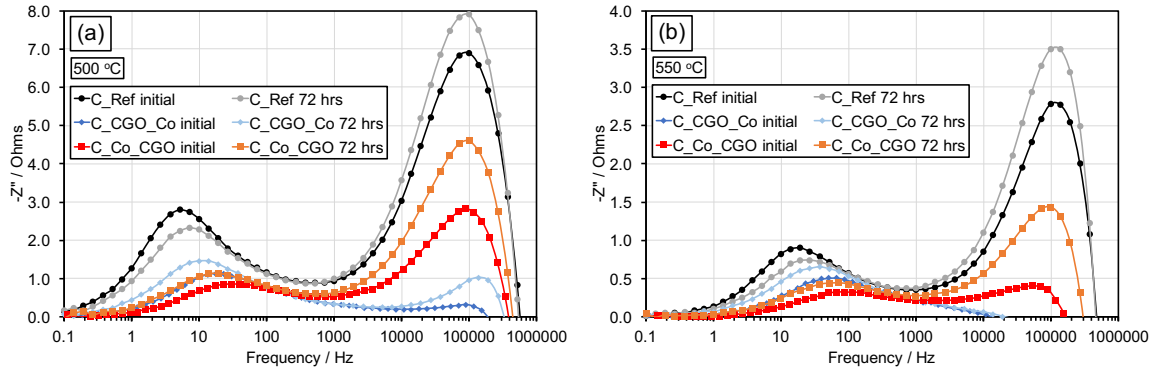
Figure 119. Frequency response for the imaginary component of the impedance for the symmetric cells at (a) 500 °C and (b) 550 °C. All samples show a low frequency peak between 5 Hz and 30 Hz. Most samples also show a high frequency peak near 100 kHz, except for the infiltrated C_CGO_Co sample at 550 °C.

The total polarisation resistance, R_p, was estimated using the difference in real axis intercepts and normalised to the electrode area (1.05 cm^2) and divided by 2 to reflect the contribution from both electrodes to give the area specific resistance, ASR. These are given in Table 18 for each of the symmetric cell samples.

Table 18. Area specific resistances for symmetric cathode cells before and after aging

| | | Area specific resistance (ASR) / $\Omega \cdot cm^2$ | |
	Sample	500 °C	550 °C
	C_Ref	15.1	5.7
Initial	C_CGO_Co	2.3	0.8
	C_Co_CGO	5.9	1.3
	C_Ref	15.8	6.6
72 hours	C_CGO_Co	4.1	1.0
	C_Co_CGO	9.1	3.1

The high-frequency arc in the complex impedance of the symmetric cells was attributed to charge transfer processes occurring between the LSCF and the CGO [271,311]. The low-frequency arc was thought to be due to oxygen exchange at the surface of the LSCF [300,312–315]. The presence of doped ceria on the surface of LSCF has been demonstrated to enhance the surface exchange reaction and was attributed by Hong et al. [316] to the doped ceria providing additional free oxygen vacancies. A similar mechanism has been proposed by

Gao et al. [309] for the enhancement when cobalt oxide nanoparticles decorate the surface of LSCF cathodes.

For the dual infiltrated cells the boundary where surface exchange was enhanced will be greater due to CoO and CGO nanoparticles decorating the surface of the LSCF. This can explain the reduced low-frequency polarisation losses in the infiltrated samples. The high-frequency losses are also lower in the infiltrated samples, primarily due to the higher density of boundaries between ionically and electrically conducting phases. At the measurement temperatures presented LSCF has a much lower ionic conductivity than CGO [317] and so transfer between the 2 phases is critical in terms of percolation paths in the CGO phase. Hence, the charge transfer processes (high frequency) are dominant at these temperatures. Therefore, increasing the boundary length between the two types of conductor, ionic and electronic, is expected to reduce the total resistance associated with the charge transfer processes.

All cells showed an increase in polarisation resistance after aging at 650 °C. Different mechanisms have been suggested for the degradation of LSCF/CGO composite cathodes including strontium segregation and microstructure coarsening [301,302]. Endler-Schuck et al. [318] found no significant microstructure coarsening over the course of 1000 hours aging at 600, 750 and 900 °C. This agrees with the results from Kiebach et al. [319] who found that the microstructure did not substantially change during 2000 hours of aging and the majority of strontium segregation occurred during the high temperature (1250 °C) cathode sintering phase. They found that chromium poisoning from the metal interconnects was the most likely cause of degradation. In our work on LSCF/CGO cathode enhancement via CGO solution infiltration the scale of the microstructure also appeared unaffected [296]. This lead us to conclude that the likely degradation mechanism was associated with strontium surface segregation. CGO has a lower CTE than LSCF and therefore might provide a localised surface micro-compression effectively suppressing the strontium segregation, as proposed by Ding et al. [301].

A study by Liu et al. [317] into the degradation of LSCF/CGO cathodes prepared by the infiltration of LSCF into a CGO porous scaffold found that coarsening of the nanosized LSCF was the primary cause for performance degradation with time. However, the X-ray photoelectron spectroscopy (XPS) results they presented suggested that cobalt surface segregation occurs. This may help explain the observed small reduction in low-frequency losses observed for the reference sample, Figure 119. The segregated cobalt oxide at the

surface may enhance the surface exchange reaction but the effect is outweighed by the increase in high-frequency losses. Liu et al. do not report the frequency dependence of the polarisation losses for their cells so it is not clear whether the cobalt oxide they detected could have had any positive effect.

The reason for the difference in performance between the infiltrated cells is not entirely clear. The frequency response of the two samples show opposite trends; as-infiltrated C_CGO_Co has dominant low-frequency losses whilst C_Co_CGO has dominant high-frequency losses. At 500 and 550 °C the total ASR is dominated by high-frequency losses and therefore the infiltration sequence of CGO before CoO results in a lower ASR. Assuming, simply, that the first ink infiltrated into the structure results in that material being more closely connected to the LSCF backbone then the difference might be partly explained by considering the expected effects of each nanoparticle. If the reduction in high-frequency polarisation loss is primarily due to an improved TPB between LSCF and CGO then one would expect the C_CGO_Co sample to show a significantly lower high-frequency loss, which in turn increase again due to nanoparticle agglomeration during aging. The infiltration sequence used in sample C_Co_CGO may prevent as large a TPB extension due to purely geometrical reasons; if the cobalt oxide nanoparticles coat the scaffold surface before the introduction of the CGO, therefore reduce the extent of the contact between LSCF and CGO nanoparticles. Hence, the high-frequency losses are larger in C_Co_CGO than in C_CGO_Co and the total polarisation loss is greater. Other effects such as the dissolution of segregated Sr and/or other phases by the infiltrated inks could also take place. Such effects could not be quantified without further high resolution TEM analyses, which are beyond the tasks of this thesis but are an aim for future work.

7.3.2.2 Microstructure

The fractured cross sections for the infiltrated samples are shown in Figure 120. The samples were imaged after aging and did not show signs of significant coarsening with scaffold grain sizes of the order of ~200–700 nm and nanoparticles ~20–50 nm. The difference in electrochemical performance between the two infiltrated samples did not have an obvious cause in the microstructure, at least at these length scales. Energy dispersive X-ray spectroscopy (EDX) was attempted to determine if different nanoparticles could be identified, but due to the non-planar cross section of the samples and interaction volume extending beyond the particle sizes the results were inconclusive.
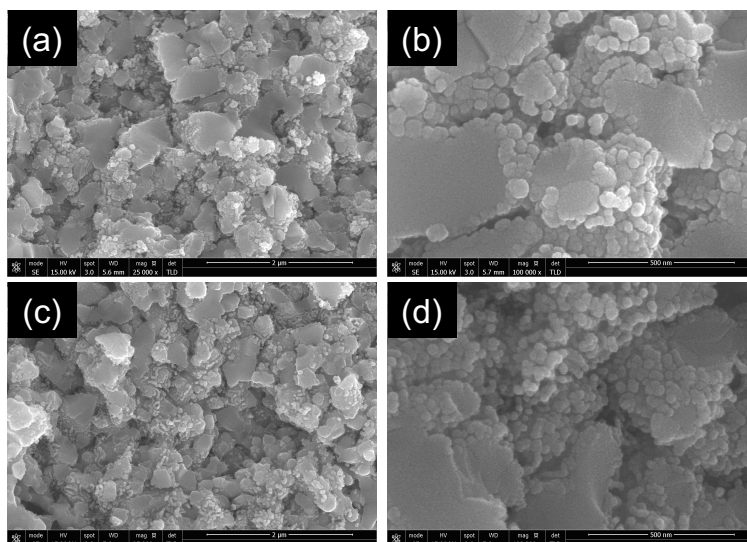
Figure 120. Secondary electron micrographs showing the fractured surface of the LSCF/CGO infiltrated cathodes. (a), (b) Sample C_CGO_Co and (c), (d) sample C_Co_CGO appear to have similar distributions and sizes of nanoparticle decorating the cathode scaffold surface.

7.3.2.3 XRD

XRD patterns of the three cells plus the starting LSCF powder are shown in Figure 121. There also does not appear to be a significant detectable difference between the infiltrated cells. If doping of the LSCF lattice by cobalt occurred then a shift in lattice parameter and therefore peak position would be expected; this was not observed indicating that infiltrated cobalt did not substantially alter the LSCF lattice.
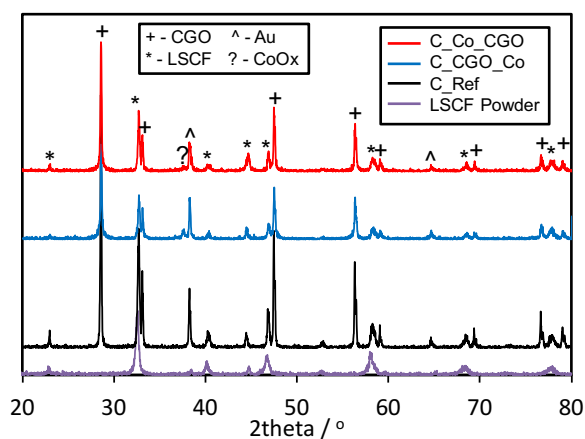
Figure 121. XRD patterns for the symmetric cells and the starting LSCF powder. No change in lattice parameters suggestive of doping were observed.

7.4 Summary and outlook

In this chapter symmetric, composite cathode cells, LSCF/CGO|CGO|LSCF/CGO were infiltrated with CGO and cobalt oxide precursor solutions using DoD inkjet printing. Different sequences of infiltration, CGO then cobalt oxide and vice versa, were tried. Both infiltrated samples showed significant improvements in the total polarisation resistance compared to a non-infiltrated reference. However, the sequence of infiltration was also found to be important, with the sample that had CGO infiltrated first displaying a lower polarisation resistance at low temperatures (500 and 550 °C). Impedance spectroscopy indicated a difference in dominant loss mechanism between the infiltrated samples. The CGO first sample had lower charge-transfer process resistance, whilst the cobalt oxide first sample had a slightly lower surface-exchange resistance. From the point of view of total polarisation loss reduction the preferred infiltration sequence was found to be CGO followed by cobalt oxide.

SEM and XRD analysis did not provide a conclusive reason for the difference in measured performance. Both infiltrated samples had a similar distribution and size of nanoparticle decorating the electrode surface and XRD did not detect doping of the electrode scaffold. Further characterisation will be carried out in collaboration with colleagues at Imperial College London using X-ray photoelectron spectroscopy (XPS) and high-temperature Raman spectroscopy to determine if there is a difference in surface chemistry between the samples that can explain the difference in performance. Also, nanoscale characterisation using TEM should provide information about differences in the nanoparticles in both infiltrated samples. Additionally, samples with simultaneously infiltrated CGO and cobalt oxide and separate CGO and cobalt infiltrated cells will be produced to determine the separate contribution to cell performance.

Finally, testing of large-area (25 cm^2), commercially available, anode supported fuel cells with infiltrated cathodes is underway. This will demonstrate that sequential inkjet infiltration of CGO and cobalt oxide enhances intermediate temperature performance and improves long-term stability.

8 CONCLUSIONS AND FUTURE WORK

This thesis presented work on low-cost methods to tailor the structures of HTS wires and SOFCs to reduce energy losses. Section I focussed on filamentary HTS coated conductors for AC power applications. Section II investigated nanostructuring SOFC electrodes to reduce polarisation losses. The main conclusions and future work recommendations are summarised for each chapter below.

8.1 Roebel cable offcuts & uniform fields

8.1.1 Main conclusions

Roebel cables are an effective cable design to reduce AC losses, however, the material wasted as part of the punching process substantially increases their cost. Stacks of the offcut tape can be magnetised to produce trapped field magnets. Different stacking arrangements can be used to achieve more spatially uniform trapped field profiles. A new 'angled stack' arrangement produces the most uniform profile.

Field magnitude and uniformity can be improved further by using wider tape pieces and self-supporting stacks can be produced from solder coated tape. Layering several stacks and including a bottom layer of a soft ferromagnetic material further improve magnitude and uniformity. FEM modelling indicates that the maximum trapped fields expected with optimal stacking and lower temperatures far exceeds that achievable from permanent magnets.

8.1.2 Future work

Future work should investigate pulse magnetisation of angled stacks, which is a more practical method for magnetising trapped field magnets. Additionally, field magnitudes and uniformity at lower temperatures should be studied to verify model predictions. Future Roebel cable designs may also lead to wider offcut pieces, which may only be feasible if the waste material can be successfully utilised.

8.2 Spark-discharge striation

8.2.1 Main conclusions

The spark-discharge that occurs during the dielectric breakdown of air between electrodes can be used to selectively degrade REBCO coated conductors and striate them to form filamentary tapes. The sparking process results in a resistive barrier between superconducting filaments and striated samples display lower AC losses than unstriated. The striation process does not substantially damage the conductor away from the impact zone and the process is effective for both silver stabilised tapes and un-coated samples.

Partially striated conductors, with multiple small bridges continuously connecting filaments, were proposed as a robust design to enable current sharing in the case of current blocking defects. However, the design was ineffective at reducing AC losses. Superconducting bridges between filaments can only be accommodated if their location with respect to the twist pitch length is carefully controlled.

8.2.2 Future work

Improvements to the spark-discharge spatial precision should be investigated through a more complete survey of the adjustable parameters including relative electrode speed, spark gap, voltage and electrode radius of curvature. Additionally, preliminary experiments with alternative atmospheres (reduced pressure or argon) suggest that a more controlled discharge is possible.

8.3 Printed structures

8.3.1 Main conclusions

Inkjet printing can be used as a deposition method to produce filamentary coated conductors with no subtractive post-processing. Direct printing of filaments and patterning of substrates using inert barrier materials are both possible routes, with the 'inverse' printing method displaying some practical advantages. Namely that filament resolution and filament thickness are decoupled with the inverse process, theoretically enabling thicker, narrower filaments than direct deposition.

Thin film textured PrBCO and PrYBCO can be produced using solution deposition and thermal treatment methods. This is promising as an enabling step for producing more

complex filamentary structures based on the Rutherford cable architecture. PrYBCO is a non-superconducting but isostructural REBCO material, which could allow multi-stage deposition of multi-layered superconductors with transposed filaments.

Solution deposition and growth of REBCO is a complex process and the conversion from wet film to textured oxide requires careful control of temperature and atmosphere. Solution precursors can degrade with time without visible changes, which leads to films with lower transitions temperatures. The specific growth conditions need to be carefully optimised for the specific experimental or production facility to enable reliable formation of superconducting layers.

8.3.2 Future work

Once reliable solution deposition and growth of superconducting layers is achieved then the following stages for producing the Rutherford architecture can be investigated. These stages are: demonstrating the growth of superconducting YBCO over the top of a layer of PrYBCO, growing a superconducting filament across a thin region of textured ceria, simultaneous deposition of PrYBCO and YBCO to form the first layer. After these steps are demonstrated then the final combination to produce a fully printed structure with transposed filaments should be possible. The greatest challenges are anticipated to be the growth of superconducting filaments over the ceria barrier, particularly in the step region, and the possibility of cation diffusion between regions during the high temperature thermal processing.

8.4 Anode infiltration

8.4.1 Main conclusions

The 0.5 mm thick anode of commercially available anode supported fuel cells can be infiltrated with ~1 wt% CGO nanoparticles using simple, scalable inkjet printing to deposit the solution precursors. Inkjet printing results in minimal wastage of rare-earth precursors and drop impact velocity is thought to improve penetration into the porous structure. Despite results on symmetric anode cells indicating a reduction in polarisation losses after infiltration there was no significant improvement measured for the complete fuel cells. This was due to limited nanoparticle loading and other losses dominating (cathode polarisation, diffusion losses).

Greater open porosity enables higher CGO loading and can be achieved by chemically reducing NiO to Ni metal in the anode or by lowering the pre-sintering temperature of anode pellets. If reduction is carried out following cell fabrication the cathode can become damaged and delaminate, however, if a composite cathode is used this can be mitigated. Lower pre-sintering temperatures combined with additional infiltration before electrolyte sintering results in retention of higher open porosity in Ni-Fe anodes. Secondary infiltration of CGO nanoparticles following electrolyte sintering results in a bimodal size distribution of infiltrated nanoparticles, which may be beneficial for lower polarisation losses.

8.4.2 Future work

The rheological and deposition parameters that affect the infiltration of precursor inks in the porous anode structure will be studied. An empirical model of the dominant factors influencing solution penetration into porous anodes will be constructed. This will confirm whether drop impingement velocity improves solution penetration. Additionally, the dominant factors that enable higher particle loadings in a single step e.g. ink concentration, surface tension, porosity and deposition temperature will be identified.

8.5 Cathode infiltration

8.5.1 Main conclusions

Dual infiltration of CGO and cobalt oxide precursors into LSCF/CGO composite cathodes reduces cathode polarisation resistance at intermediate temperatures. Infiltrated cathodes continue to display better properties after aging at 650 °C for more than 72 hours. The nanoparticles reduce both high frequency and low frequency polarisation losses by improving the charge transfer between different cathode phases and catalysing the oxygen reduction reaction respectively. The sequence when infiltrating the two precursor inks is important; samples that are infiltrated with CGO before cobalt oxide precursors demonstrate better performance that those produced using the opposite sequence. However, the effect does not appear to have an obvious microstructural cause.

8.5.2 Future work

Scale-up to demonstrate the benefit of dual infiltration in larger area ($25 \, \text{cm}^2$), commercially available cells is in progress. Furthermore, XPS and high temperature Raman spectroscopy will be performed to elucidate the difference between dual infiltrated cells.

Similarly, transmission electron microscopy (TEM) should provide important information about the structure and composition of nanoparticles that decorate the cathode surface. Also, separately infiltrated samples will be produced and compared to determine the relative effect of each type of oxide nanoparticle.

9 REFERENCES

[1] D. King, J. Browne, R. Layard, G.O. Donnell, M. Rees, N. Stern, A. Turner, A Global Apollo Programme to Combat Climate Change, 2015. http://cep.lse.ac.uk/pubs/download/special/ Global_Apollo_Programme_Report.pdf.

[2] V. Matias, R.H. Hammond, Perspectives on IBAD Coated Conductors: Cost and Future, in: Coat. Conduct. Appl., Aspen, CO, 2016. https://nationalmaglab.org/images/magnet_development/asc/searchable_docs/asc_reso urces/coated_conductors/2016/co_22_matias.pdf.

[3] D.W. Hazelton, 2G HTS Applications Developments, Symposium on Superconducting Devices for Wind Energy, Barcelona, 2011.

[4] C. Cobb, P. Barnes, T. Haugan, J. Tolliver, L. Eungkuk, M. Sumption, E. Collings, C. Oberly, Hysteretic loss reduction in striated YBCO, Phys. C Supercond. Its Appl. 382 (2002) 52–56. doi:10.1016/S0921-4534(02)01196-6.

[5] M.P. Oomen, AC Losses in Superconducting Tapes and Cables, University of Twente, Enschende, 2000.

[6] European Commission, http://ec.europa.eu/research/energy/eu/index_en.cfm?pg=research-fch-background, (2017).

[7] US Department of Energy, Fuel Cell Technologies Office Multi-year Research, Development, and Demonstration Plan, Https://energy.gov/eere/fuelcells/downloads/fuel-Cell-Technologies-Office-Multi-Year-Research-Development-and-22. (2016).

[8] H.K. Onnes, Further experiments with liquid helium. C. On the change of electric resistance of pure metals at very low temperatures etc. IV. The resistance of pure mercury at helium temperatures, Commun. from Phys. Lab. Leiden. (1911) 1274–1276.

[9] J. Eisenstein, Superconducting elements, Rev. Mod. Phys. 26 (1954) 277–291. doi:10.1103/RevModPhys.26.277.

[10]   B.T. Matthias, T.H. Geballe, V.B. Compton, Superconductivity, Rev. Mod. Phys. 35 (1963) 1–22. doi:10.1103/RevModPhys.35.1.

[11]   B. Matthias, T. Geballe, S. Geller, E. Corenzwit, Superconductivity of Nb3Sn, Phys. Rev. 95 (1954) 1435–1435. doi:10.1103/PhysRev.95.1435.

[12]   J.G. Bednorz, K.A. Müller, Possible High Tc Superconductivity in the Ba-La-Cu-O System, Zeitshcrift Fur Phys. B. 64 (1986) 189–193. doi:10.1007/BF01303701.

[13]   M.K. Wu, J.R. Ashburn, C.J. Torng, P.H. Hor, L. Meng, L. Gao, Z.J. Huang, Y.Q. Wang, C.W. Chu, Superconductivity at 93 K in a new mixed phase Y-Ba-Cu-O compound system at ambient pressure, Phys. Rev. Lett. 58 (1987) 908–910. doi:10.1103/PhysRevLett.58.908.

[14]   H. Maeda, Y. Tanaka, M. Fukutomi, T. Asano, A New High- T c Oxide Superconductor without a Rare Earth Element, Jpn. J. Appl. Phys. 27 (1988) 209–210. doi:10.1143/JJAP.27.L209.

[15]   A. Schilling, M. Cantoni, J.D. Guo, H.R. Ott, Superconductivity above 130 K in the Hg–Ba–Ca–Cu–O system, Nature. 363 (1993) 56–58. doi:10.1038/363056a0.

[16]   J. Nagamatsu, N. Nakagawa, T. Muranaka, Y. Zenitani, J. Akimitsu, Superconductivity at 39 K in magnesium diboride, 410 (2001) 63–64. doi:10.1038/35065039.

[17]   Y. Kamihara, T. Watanabe, M. Hirano, H. Hosono, Iron-based layered superconductor La[O(1-x)F(x)]FeAs (x = 0.05-0.12) with Tc = 26 K., J. Am. Chem. Soc. 130 (2008) 3296–7. doi:10.1021/ja800073m.

[18]   X.H. Chen, T. Wu, G. Wu, R.H. Liu, H. Chen, D.F. Fang, Superconductivity at 43 K in SmFeAsO1-xFx, Nature. 453 (2008) 761–762. doi:10.1038/nature07045.

[19]   C. Wang, L. Li, S. Chi, Z. Zhu, Z. Ren, Y. Li, Y. Wang, X. Lin, Y. Luo, S. Jiang, X. Xu, G. Cao, Z. Xu, Thorium-doping-induced superconductivity up to 56 K in Gd1-xThxFeAsO, Europhys. Lett. 83 (2008) 67006. doi:10.1209/0295-5075/83/67006.

[20]   A.P. Drozdov, M.I. Eremets, I.A. Troyan, V. Ksenofontov, S.I. Shylin, Conventional superconductivity at 203 kelvin at high pressures in the sulfur hydride system, Nature. 525 (2015) 73–76. doi:10.1038/nature14964.

[21]   B. Seeber, Handbook of Applied Superconductivity, Volume 2, CRC Press, 1998.

[22]   D.A. Cardwell, D.S. Ginley, Handbook of Superconducting Materials, Volume 1, IOP Publishing, 2003.

[23]   G. Krabbes, G. Fuchs, W.-R. Canders, H. May, R. Palka, High Temperature Superconductor Bulk Materials, Wiley-VCH Verlag GmbH & Co. KGaA, Weinheim, FRG, 2006. doi:10.1002/3527608044.

[24]   B.A. Glowacki, S.C. Hopkins, https://ascg.msm.cam.ac.uk/lectures/, Lect. Supercond. (2005).

[25]   J. Bardeen, L.N. Cooper, J.R. Schrieffer, Theory of Superconductivity, Phys. Rev. 108 (1957) 1175–1204. doi:10.1103/PhysRev.108.1175.

[26]   F. London, H. London, The Electromagnetic Equations of the Supraconductor, Proc. R. Soc. A Math. Phys. Eng. Sci. 149 (1935) 71–88. doi:10.1098/rspa.1935.0048.

[27]   V. Ginzburg, L. Landau, Toward the superconductivity theory, Zhurnal Eksp. Yheoret. Phys. 29 (1950) 1064.

[28]   L.P. Gor'kov, Microscopic derivation of the Ginzburg-Landau equations in the theory of superconductivity, J. Exp. Theor. Phys. 36 (1959) 1364–1366.

[29]   M. Mosiadz, Inkjet Printing of Buffer and Superconducting Layers for YBa2Cu3O7-x Coated Conductors, University of Cambridge, 2011.

[30]   A.A. Abrikosov, On the magnetic properties of superconductors of the second group, J. Exp. Theor. Phys. 5 (1957) 1174.

[31]   U. Essmann, H. Träuble, The direct observation of individual flux lines in type II superconductors, Phys. Lett. A. 24 (1967) 526–527. doi:10.1016/0375-9601(67)90819-5.

[32]   D. Larbalestier, A. Gurevich, D.M. Feldmann, A. Polyanskii, High-Tc superconducting materials for electric power applications., Nature. 414 (2001) 368–77. doi:10.1038/35104654.

[33]   J. Clem, Two-dimensional vortices in a stack of thin superconducting films: A model for high-temperature superconducting multilayers, Phys. Rev. B. 43 (1991) 7837–7846. doi:10.1103/PhysRevB.43.7837.

[34]   M. Chudy, Z. Zhong, M. Eisterer, T. Coombs, *n* -Values of commercial YBCO tapes before and after irradiation by fast neutrons, Supercond. Sci. Technol. 28 (2015) 35008. doi:10.1088/0953-2048/28/3/035008.

[35]   A. Zhukov, H. Küpfer, G. Perkins, L. Cohen, A. Caplin, S. Klestov, H. Claus, V. Voronkova, T. Wolf, H. Wühl, Influence of oxygen stoichiometry on the irreversible magnetization and flux creep in RBa2Cu3O7-δ (R=Y,Tm) single crystals, Phys. Rev. B. 51 (1995) 12704–12714. doi:10.1103/PhysRevB.51.12704.

[36]   R.J. Cava, B. Batlogg, C.H. Chen, E.A. Rietman, S.M. Zahurak, D. Werder, Oxygen stoichiometry, superconductivity and normal-state properties of YBa2Cu3O7–δ, Nature. 329 (1987) 423–425. doi:10.1038/329423a0.

[37]   A. Xu, J.J. Jaroszynski, F. Kametani, Z. Chen, D.C. Larbalestier, Y.L. Viouchkov, Y. Chen, Y. Xie, V. Selvamanickam, Angular dependence of Jc for YBCO coated conductors at low temperature and very high magnetic fields, Supercond. Sci. Technol. 23 (2010) 14003. doi:10.1088/0953-2048/23/1/014003.

[38]   T. Boutboul, S. Le Naour, D. Leroy, L. Oberli, V. Previtali, Critical Current Density in Superconducting Nb-Ti Strands in the 100 mT to 11 T Applied Field Range, IEEE Trans. Appl. Supercond. 16 (2006) 1184–1187. doi:10.1109/TASC.2006.870777.

[39]   J.A. Parrell, Nb3Sn Conductor Development for Fusion and Particle Accelerator Applications, in: AIP Conf. Proc., AIP, 2004: pp. 369–375. doi:10.1063/1.1774590.

[40]   G.Z. Li, M.D. Sumption, J.B. Zwayer, M.A. Susner, M.A. Rindfleisch, C.J. Thong, M.J. Tomsic, E.W. Collings, Effects of carbon concentration and filament number on advanced internal Mg infiltration-processed MgB2 strands, Supercond. Sci. Technol. 26 (2013) 95007. doi:10.1088/0953-2048/26/9/095007.

[41]   D.C. Larbalestier, J. Jiang, U.P. Trociewitz, F. Kametani, C. Scheuerlein, M. Dalban-Canassy, M. Matras, P. Chen, N.C. Craig, P.J. Lee, E.E. Hellstrom, Isotropic round-wire multifilament cuprate superconductor for generation of magnetic fields above 30 T., Nat. Mater. 13 (2014) 375–81. doi:10.1038/nmat3887.

[42]   S. Wimbush, N. Strickland, A high-temperature superconducting (HTS) wire critical current database, https://doi.org/10.6084/m9.figshare.c.2861821.v4. (n.d.).

[43]   S.C. Wimbush, N.M. Strickland, A Public Database of High-Temperature Superconductor Critical Current Data, IEEE Trans. Appl. Supercond. 27 (2017). doi:10.1109/TASC.2016.2628700.

[44]   P.J. Lee, http://fs.magnet.fsu.edu/~lee/plot/plot.htm, (2017).

[45]   G. Blatter, M. V Feigel'man, V.B. Geshkenbein, A.I. Larkin, V.M. Vinokur, Vortices in high-temperature superconductors, Rev. Mod. Phys. 66 (1994) 1125–1380. doi:10.1103/RevModPhys.66.1125.

[46]   E.M. Gyorgy, R.B. van Dover, K.A. Jackson, L.F. Schneemeyer, J. V. Waszczak, Anisotropic critical currents in Ba2YCu3O7 analyzed using an extended Bean model, Appl. Phys. Lett. 55 (1989) 283. doi:10.1063/1.102387.

[47]   T.R. Dinger, T.K. Worthington, W.J. Gallagher, R.L. Sandstrom, Direct obeservation of electronic anisotropy in single-crystal YBCO, Phys. Rev. Lett. 58 (1987) 2687–2691. doi:10.1103/PhysRevLett.58.2687.

[48]   Y. Jia, J. Hua, G.W. Crabtree, W.K. Kwok, U. Welp, A.P. Malozemoff, M. Rupich, S. Fleshler, C-axis critical current density of second-generation YBCO tapes, Supercond. Sci. Technol. 23 (2010) 115017. doi:10.1088/0953-2048/23/11/115017.

[49]   Y. Jia, U. Welp, G.W. Crabtree, W.K. Kwok, A.P. Malozemoff, M.W. Rupich, S. Fleshler, J.R. Clem, Microstructure dependence of the c-axis critical current density in second-generation YBCO tapes, J. Appl. Phys. 110 (2011) 83923. doi:10.1063/1.3653292.

[50]   M. Tachiki, S. Takahashi, Anisotropy of Critical Current in Layered Oxide Superconductors, Solid State Commun. 72 (1989) 1083–1086. doi:10.1016/0038-1098(89)90251-2.

[51]   J.R. Clem, M. Weigand, J.H. Durrell, A.M. Campbell, Theory and experiment testing flux-line cutting physics, Supercond. Sci. Technol. 24 (2011) 62002. doi:10.1088/0953-2048/24/6/062002.

[52]   J.H. Durrell, G. Burnell, V.N. Tsaneva, Z.H. Barber, M.G. Blamire, J.E. Evetts, Critical currents in vicinal YBa2Cu3O7−d films, Phys. Rev. B. 70 (2004) 214508. doi:10.1103/PhysRevB.70.214508.

[53]   A.M. Campbell, J.E. Evetts, Flux vortices and transport currents in type II superconductors, Adv. Phys. 21 (1972) 199–428. doi:10.1080/00018737200101288.

[54]   E.H. Brandt, The flux-line lattice in superconductors, Reports Prog. Phys. 58 (1995) 1465–1594. doi:10.1088/0034-4885/58/11/003.

[55]   D. Dew-Hughes, Flux pinning mechanisms in type II superconductors, Philos. Mag. 30 (1974) 293–305. doi:10.1080/14786439808206556.

[56]   S.R. Foltyn, L. Civale, J.L. MacManus-Driscoll, Q.X. Jia, B. Maiorov, H. Wang, M. Maley, Materials science challenges for high-temperature superconducting wire, Nat. Mater. 6 (2007) 631–642.

[57]   J.H. Durrell, N.A. Rutter, Importance of Low-Angle Grain Boundaries in YBa2Cu3O7-δ Coated Conductors, Supercond. Sci. Technol. 22 (2009) 13001. doi:10.1088/0953-2048/22/1/013001.

[58]   H. Hilgenkamp, J. Mannhart, Grain boundaries in high-Tc superconductors, Rev. Mod. Phys. 74 (2002) 485–549. doi:10.1103/RevModPhys.74.485.

[59]   Z.G. Ivanov, P.A. Nilsson, D. Winkler, J.A. Alarco, G. Brorsson, T. Claeson, E.A. Stepantsov, A.Y. Tzalenchuk, Properties of artificial grain boundary weak links grown on Y-ZrO 2 bicrystals, Supercond. Sci. Technol. 4 (1991) 439–441. doi:10.1088/0953-2048/4/9/016.

[60]   D.C. van der Laan, T.J. Haugan, P.N. Barnes, Effect of a compressive uniaxial strain on the critical current density of grain boundaries in superconducting YBa2Cu3O7-d films, Phys. Rev. Lett. 103 (2009) 1–4. doi:10.1103/PhysRevLett.103.027005.

[61]   A. Schmehl, B. Goetz, R.R. Schulz, C.W. Schneider, H. Bielefeldt, H. Hilgenkamp, J. Mannhart, Doping-induced enhancement of the critical currents of grain boundaries in YBa2Cu3O7−δ, Europhys. Lett. 47 (1999) 110–115. doi:10.1209/epl/i1999-00359-2.

[62]   Y. Iijima, N. Tanabe, O. Kohno, Y. Ikeno, In-plane aligned YBa2Cu3O7−x thin films deposited on polycrystalline metallic substrates, Appl. Phys. Lett. 60 (1992) 769. doi:10.1063/1.106514.

[63]   R.P. Reade, P. Berdahl, R.E. Russo, S.M. Garrison, Laser deposition of biaxially textured yttria-stabilized zirconia buffer layers on polycrystalline metallic alloys for high critical current Y-Ba-Cu-O thin films, Appl. Phys. Lett. 61 (1992) 2231. doi:10.1063/1.108277.

[64]   X.D. Wu, S.R. Foltyn, P.N. Arendt, W.R. Blumenthal, I.H. Campbell, J.D. Cotton, J.Y. Coulter, W.L. Hults, M.P. Maley, H.F. Safar, J.L. Smith, Properties of YBa2Cu3O7−δ thick films on flexible buffered metallic substrates, Appl. Phys. Lett. 67 (1995) 2397. doi:10.1063/1.114559.

[65]   A. Goyal, D.P. Norton, J.D. Budai, M. Paranthaman, E.D. Specht, D.M. Kroeger, D.K. Christen, Q. He, B. Saffian, F.A. List, D.F. Lee, P.M. Martin, C.E. Klabunde, E. Hartfield, V.K. Sikka, High critical current density superconducting tapes by epitaxial deposition of YBa2Cu3Ox thick films on biaxially textured metals, Appl. Phys. Lett. 69 (1996) 1795. doi:10.1063/1.117489.

[66]   M. Erbe, J. Hänisch, T. Freudenberg, A. Kirchner, I. Mönch, S. Kaskel, L. Schultz, B. Holzapfel, Improved REBa2Cu3O7−x (RE = Y, Gd) structure and superconducting properties by addition of acetylacetone in TFA-MOD precursor solutions, J. Mater. Chem. A. 2 (2014) 4932. doi:10.1039/c3ta15243j.

[67]   V.F. Solovyov, H.J. Wiesmann, L. Wu, Q. Li, L.D. Cooley, M. Suenaga, B. Maiorov, L. Civale, High critical currents by isotropic magnetic-flux-pinning centres in a 3 μm-thick YBa 2 Cu 3 O 7 superconducting coated conductor, Supercond. Sci. Technol. 20 (2007) L20–L23. doi:10.1088/0953-2048/20/4/L04.

[68]   Haynes International, http://www.haynesintl.com/alloys/specifications-codes/specifications-for-corrosion-restitant-alloys, (2017).

[69]   C. Sheehan, Y. Jung, T. Holesinger, D.M. Feldmann, C. Edney, J.F. Ihlefeld, P.G. Clem, V. Matias, Solution deposition planarization of long-length flexible substrates, Appl. Phys. Lett. 98 (2011) 71907. doi:10.1063/1.3554754.

[70]   D.P. Norton, Synthesis and properties of epitaxial electronic oxide thin-film materials, Mater. Sci. Eng. R Reports. 43 (2004) 139–247. doi:10.1016/j.mser.2003.12.002.

[71] J.L. MacManus-Driscoll, S.R. Foltyn, Q.X. Jia, H. Wang, A. Serquis, L. Civale, B. Maiorov, M.E. Hawley, M.P. Maley, D.E. Peterson, Strongly enhanced current densities in superconducting coated conductors of YBa2Cu3O7-x + BaZrO3., Nat. Mater. 3 (2004) 439–43. doi:10.1038/nmat1156.

[72] T. Shimizu, H. Nonaka, S. Hosokawa, S. Ichimura, K. Arai, Preparation of oxide superconducting films in MBE using NO2 and O3 gases, Phys. C Supercond. 185–189 (1991) 2003–2004. doi:10.1016/0921-4534(91)91126-O.

[73] N. Kashima, T. Niwa, M. Mori, S. Nagaya, T. Muroga, S. Miyata, T. Watanabe, Y. Yamada, T. Izumi, Y. Shiohara, Fabrication of Coated Conductors by Multiple-Stage CVD, IEEE Trans. Appl. Supercond. 15 (2005) 2763–2766. doi:10.1109/TASC.2005.847773.

[74] M. Mori, T. Watanabe, N. Kashima, S. Nagaya, T. Muroga, S. Miyata, Y. Yamada, T. Izumi, Y. Shiohara, Development of long YBCO coated conductors by multiple-stage CVD, Phys. C Supercond. 445–448 (2006) 515–520. doi:10.1016/j.physc.2006.04.046.

[75] W. V Hassenzahl, Superconductivity, An Enabling Technology for 21st Century Power Systems?, IEEE Trans. Appl. Supercond. 11 (2001) 1447–1453. doi:10.1109/77.920045.

[76] H. Yumura, Y. Ashibe, H. Itoh, M. Ohya, M. Watanabe, T. Masuda, C.S. Weber, Phase II of the albany HTS cable project, IEEE Trans. Appl. Supercond. 19 (2009) 1698–1701. doi:10.1109/TASC.2009.2017865.

[77] Y. Xin, B. Hou, Y. Bi, H. Xi, Y. Zhang, A. Ren, X. Yang, Z. Han, S. Wu, H. Ding, Introduction of China's first live grid installed HTS power cable system, IEEE Trans. Appl. Supercond. 15 (2005) 1814–1817. doi:10.1109/TASC.2005.849299.

[78] S.T. Dai, L.Z. Lin, Y.B. Lin, Z.Y. Gao, Y.F. Fang, L.H. Gong, Y.P. Teng, F.Y. Zhang, X. Xu, G. Li, L.F. Li, L.Y. Xiao, The three-phase 75m long HTS power cable, Cryogenics (Guildf). 47 (2007) 402–405. doi:10.1016/j.cryogenics.2007.04.020.

[79] J.F. Maguire, F. Schmidt, S. Bratt, T.E. Welsh, J. Yuan, Installation and testing results of long island transmission level HTS cable, IEEE Trans. Appl. Supercond. 19 (2009) 1692–1697. doi:10.1109/TASC.2009.2018221.

[80]   M. Stemmle, F. Merschel, M. Noe, A. Hobl, AmpaCity - Installation of advanced superconducting 10 kV system in city center replaces conventional 110 kV cables, 2013 IEEE Int. Conf. Appl. Supercond. Electromagn. Devices, ASEMD 2013. (2013) 323–326. doi:10.1109/ASEMD.2013.6780785.

[81]   J.F. Maguire, J. Yuan, W. Romanosky, F. Schmidt, R. Soika, S. Bratt, F. Durand, C. King, J. McNamara, T.E. Welsh, Progress and status of a 2G HTS power cable to be installed in the Long Island Power Authority (LIPA) grid, IEEE Trans. Appl. Supercond. 21 (2011) 961–966. doi:10.1109/TASC.2010.2093108.

[82]   S. Mukoyama, M. Yagi, N. Hirano, N. Amemiya, N. Kashima, S. Nagaya, T. Izumi, Y. Shiohara, Study of an YBCO HTS transmission cable system, Phys. C Supercond. 463–465 (2007) 1150–1153. doi:10.1016/j.physc.2007.03.452.

[83]   G. Venkataramanan, B.K. Johnson, A superconducting DC transmission system based on VSC transmission technologies, IEEE Trans. Appl. Supercond. 13 (2003) 1922–1925. doi:10.1109/TASC.2003.812947.

[84]   J.X. Jin, High efficient DC power transmission using high-temperature superconductors, Phys. C Supercond. 460–462 (2007) 1443–1444. doi:10.1016/j.physc.2007.04.181.

[85]   A. Morandi, State of the art of superconducting fault current limiters and their application to the electric power system, Phys. C Supercond. Its Appl. 484 (2013) 242–247. doi:10.1016/j.physc.2012.03.004.

[86]   M. Noe, M. Steurer, High-temperature superconductor fault current limiters: concepts, applications, and development status, Supercond. Sci. Technol. 20 (2007) R15–R29. doi:10.1088/0953-2048/20/3/R01.

[87]   B.W. McConnell, S.P. Mehta, M.S. Walker, HTS Transformers, IEEE Power Eng. Rev. 20 (2000) 7–11. doi:10.1109/39.846102.

[88]   M. Iwakuma, K. Funaki, K. Kajikawa, H. Tanaka, T. Bohno, A. Tomioka, H. Yamada, S. Nose, M. Konno, Y. Yagi, H. Maruyama, T. Ogata, S. Yoshida, K. Ohashi, K. Tsutsumi, K. Honda, AC loss properties of a 1 MVA single-phase HTS power transformer, IEEE Trans. Appl. Supercond. 11 (2001) 1482–1485. doi:10.1109/77.920054.

[89]   N. Glasson, M. Staines, N. Allpress, M. Pannu, J. Tanchon, E. Pardo, R. Badcock, R. Buckley, Test Results and Conclusions From a 1 MVA Superconducting Transformer Featuring 2G HTS Roebel Cable, IEEE Trans. Appl. Supercond. 27 (2017) 5500205. doi:10.1109/TASC.2016.2639032.

[90]   D.A. Cardwell, D.S. Ginley, Handbook of Superconducting Materials, Volume 2, IOP Publishing, 2003.

[91]   F. Berg, J. Palmer, P. Miller, M. Husband, G. Dodds, HTS electrical system for a distributed propulsion aircraft, IEEE Trans. Appl. Supercond. 25 (2015). doi:10.1109/TASC.2014.2384731.

[92]   P.N. Barnes, M.D. Sumption, G.L. Rhoads, Review of high power density superconducting generators: Present state and prospects for incorporating YBCO windings, Cryogenics (Guildf). 45 (2005) 670–686. doi:10.1016/j.cryogenics.2005.09.001.

[93]   D. Zhou, M. Izumi, M. Miki, B. Felder, T. Ida, M. Kitano, An overview of rotating machine systems with high-temperature bulk superconductors, Supercond. Sci. Technol. 25 (2012) 103001. doi:10.1088/0953-2048/25/10/103001.

[94]   K. Tamura, M. Iwakuma, T. Ueno, K. Yun, S. Sato, K. Yoshida, A. Tomioka, M. Konno, T. Izumi, Study on the Optimum Arrangement of the Field Winding for a 20-kW Fully Superconducting Motor, IEEE Trans. Appl. Supercond. 26 (2016) 1–5. doi:10.1109/TASC.2016.2544351.

[95]   D. Sekiguchi, T. Nakamura, S. Misawa, H. Kitano, T. Matsuo, N. Amemiya, Y. Ito, M. Yoshikawa, T. Terazawa, K. Osamura, Y. Ohashi, N. Okumura, Trial test of fully HTS induction/synchronous machine for next generation electric vehicle, IEEE Trans. Appl. Supercond. 22 (2012) 3–6. doi:10.1109/TASC.2011.2176094.

[96]   F. Grilli, A. Kario, How filaments can reduce AC losses in HTS coated conductors, Supercond. Sci. Technol. 29 (2016) 83002. doi:10.1088/0953-2048/29/8/083002.

[97]   C.P. Bean, Magnetization of High-Field Superconductors, Rev. Mod. Phys. 36 (1964) 31–39. doi:10.1103/RevModPhys.36.31.

[98]   E.H. Brandt, M. Indenbom, Type-II-superconducting strip with current in a perpendicular magnetic field, Phys. Rev. B. 48 (1993) 12894–12906. doi:10.1103/PhysRevB.48.12893.

[99]   N. Amemiya, S. Kasai, K. Yoda, Z. Jiang, G.A. Levin, P.N. Barnes, C.E. Oberly, AC loss reduction of YBCO coated conductors by multifilamentary structure, Supercond. Sci. Technol. 17 (2004) 1464–1471. doi:10.1088/0953-2048/17/12/018.

[100] W.J. Carr, C.E. Oberly, Filamentary YBCO Conductors For AC Applications, IEEE Trans. Appl. Supercond. 9 (1999) 1475–1478. doi:10.1109/77.784671.

[101] I. Kesgin, G. Majkic, V. Selvamanickam, Fully filamentized HTS coated conductor via striation and selective electroplating, Phys. C Supercond. Its Appl. 486 (2013) 43–50. doi:10.1016/j.physc.2013.01.016.

[102] G. Majkic, I. Kesgin, Y. Zhang, Y. Qiao, R. Schmidt, V. Selvamanickam, AC Loss Filamentization of 2G HTS Tapes by Buffer Stack Removal, IEEE Trans. Appl. Supercond. 21 (2011) 3297–3300. doi:10.1109/TASC.2010.2089416.

[103] S.P. Ashworth, F. Grilli, A strategy for the reduction of ac losses in YBCO coated conductors, Supercond. Sci. Technol. 19 (2006) 227–232. doi:10.1088/0953-2048/19/2/013.

[104] W. Goldacker, R. Nast, G. Kotzyba, S.I. Schlachter, A. Frank, B. Ringsdorf, C. Schmidt, P. Komarek, High current DyBCO-ROEBEL Assembled Coated Conductor (RACC), J. Phys. Conf. Ser. 43 (2006) 901–904. doi:10.1088/1742-6596/43/1/220.

[105] W. Goldacker, F. Grilli, E. Pardo, A. Kario, S.I. Schlachter, M. Vojenčiak, Roebel cables from REBCO coated conductors: a one-century-old concept for the superconductivity of the future, Supercond. Sci. Technol. 27 (2014) 93001. doi:10.1088/0953-2048/27/9/093001.

[106] M. Marchevsky, E. Zhang, Y. Xie, V. Selvamanickam, P.G. Ganesan, AC Losses and magnetic coupling in multifilamentary 2G HTS conductors and tape arrays, IEEE Trans. Appl. Supercond. 19 (2009) 3094–3097. doi:10.1109/TASC.2009.2017724.

[107] O. Tsukamoto, M. Ciszek, AC magnetization losses in striated YBCO-123/Hastelloy coated conductors, Supercond. Sci. Technol. 20 (2007) 974–979. doi:10.1088/0953-2048/20/10/014.

[108] A.C. Wulff, M. Solovyov, F. Gömöry, A.B. Abrahamsen, O. V Mishin, A. Usoskin, A. Rutt, J.H. Lundeman, K. Thydén, J.B. Hansen, J.-C. Grivel, Two level undercut-profile substrate for filamentary YBa2Cu3O7 coated conductors, Supercond. Sci. Technol. 28 (2015) 72001. doi:10.1088/0953-2048/28/7/072001.

[109] R. Nast, M. Vojenčiak, E. Demencik, A. Kario, B. Ringsdorf, A. Jung, B. Runtsch, F. Grilli, W. Goldacker, Influence of laser striations on the properties of coated conductors, J. Phys. Conf. Ser. 507 (2014) 22023. doi:10.1088/1742-6596/507/2/022023.

[110] M.D. Sumption, E.W. Collings, P.N. Barnes, AC loss in striped (filamentary) YBCO coated conductors leading to designs for high frequencies and field-sweep, Supercond. Sci. Technol. 18 (2004) 122–134. doi:10.1088/0953-2048/18/1/020.

[111] E. Demencik, F. Grilli, A. Kario, R. Nast, A. Jung, M. Vojenciak, J. Scheiter, W. Goldacker, AC magnetization loss and transverse resistivity of striated YBCO coated conductors, IEEE Trans. Appl. Supercond. 25 (2015) 3–7. doi:10.1109/TASC.2014.2381561.

[112] G.A. Levin, P.N. Barnes, J.W. Kell, N. Amemiya, Z. Jiang, K. Yoda, F. Kimura, Multifilament YBa2Cu3O6+x-coated conductors with minimized coupling losses, Appl. Phys. Lett. 89 (2006) 12506. doi:10.1063/1.2219393.

[113] K. Suzuki, M. Yoshizumi, T. Izumi, Y. Shiohara, M. Iwakuma, A. Ibi, S. Miyata, Y. Yamada, Development of scribing process of coated conductors for reduction of AC losses, Supercond. Sci. Technol. 20 (2007) 822–826. doi:10.1088/0953-2048/20/8/017.

[114] K. Suzuki, M. Yoshizumi, T. Izumi, Y. Shiohara, M. Iwakuma, a. Ibi, S. Miyata, Y. Yamada, Development of scribing process of coated conductors for reduction of AC losses, Phys. C Supercond. 468 (2008) 1579–1582. doi:10.1016/j.physc.2008.05.076.

[115] X. Cai, I. Kesgin, V. Selvamanickam, Reel-to-reel selective electroplating of Cu stabilizer for multifilamentary coated conductors, IEEE Trans. Appl. Supercond. 25 (2015) 3–6. doi:10.1109/TASC.2014.2369964.

[116] S. Terzieva, M. Vojenčiak, F. Grilli, R. Nast, J. Šouc, W. Goldacker, A. Jung, A. Kudymow, A. Kling, Investigation of the effect of striated strands on the AC losses of 2G Roebel cables, Supercond. Sci. Technol. 24 (2011) 45001. doi:10.1088/0953-2048/24/4/045001.

[117] D.C. van der Laan, YBa2Cu3O7−δ coated conductor cabling for low ac-loss and high-field magnet applications, Supercond. Sci. Technol. 22 (2009) 65013. doi:10.1088/0953-2048/22/6/065013.

[118] J. Šouc, F. Gömöry, J. Kováč, R. Nast, A. Jung, M. Vojenčiak, F. Grilli, W. Goldacker, Low AC loss cable produced from transposed striated CC tapes, Supercond. Sci. Technol. 26 (2013) 75020. doi:10.1088/0953-2048/26/7/075020.

[119] M. Vojenčiak, A. Kario, B. Ringsdorf, R. Nast, D.C. van der Laan, J. Scheiter, A. Jung, B. Runtsch, F. Gömöry, W. Goldacker, Magnetization ac loss reduction in HTS CORC® cables made of striated coated conductors, Supercond. Sci. Technol. 28 (2015) 104006. doi:10.1088/0953-2048/28/10/104006.

[120] F.A. List, T. Kodenkandath, M.W. Rupich, Fabrication of Filamentary YBCO Coated Conductor by Inkjet Printing, IEEE Trans. Appl. Supercond. 17 (2007) 3355–3358. doi:10.1109/TASC.2007.899991.

[121] R.C. Duckworth, M.P. Paranthaman, M.S. Bhuiyan, F.A. List, M.J. Gouge, AC Losses in YBCO Coated Conductor With Inkjet Filaments, IEEE Trans. Appl. Supercond. 17 (2007) 3159–3162. doi:10.1109/TASC.2007.897989.

[122] O. Tsukamoto, AC losses in a type II superconductor strip with inhomogeneous critical current distribution, Supercond. Sci. Technol. 18 (2005) 596–605. doi:10.1088/0953-2048/18/5/004.

[123] M. Solovyov, E. Pardo, J. Šouc, F. Gömöry, M. Skarba, P. Konopka, M. Pekarčíková, J. Janovec, Non-uniformity of coated conductor tapes, Supercond. Sci. Technol. 26 (2013) 115013. doi:10.1088/0953-2048/26/11/115013.

[124] R.C. Duckworth, M. Rupich, Low AC Loss YBCO Coated Conductor Geometry by Direct Inkjet Printing, 2009.

[125] M. Bäcker, B.A. Glowacki, M. Falter, J. Engell, Negativstrukturierung von Dünnschicht Hochtemperatur-Supraleitern, DE 10 2006 030 787 A1, 2008.

[126] S.C. Hopkins, D. Joseph, T.B. Mitchell-Williams, A. Calleja, V.R. Vlad, M. Vilardell, S. Ricart, X. Granados, T. Puig, X. Obradors, A. Usoskin, M. Falter, M. Bäcker, B.A. Glowacki, Inkjet printing of multifilamentary YBCO for low AC loss coated conductors, J. Phys. Conf. Ser. 507 (2014) 22010. doi:10.1088/1742-6596/507/2/022010.

[127] X. Cai, I. Kesgin, R. Schmidt, Y. Chen, V. Selvamanickam, Completely Etch-free Fabrication of Multifilamentary Coated Conductor Using Inkjet Printing and Electrodeposition, IEEE Trans. Appl. Supercond. 23 (2013) 6603005–6603005. doi:10.1109/TASC.2013.2244638.

[128] T.B. Mitchell-Williams, A. Patel, A. Baskys, S.C. Hopkins, A. Kario, W. Goldacker, B.A. Glowacki, Toward Uniform Trapped Field Magnets Using a Stack of Roebel Cable Offcuts, IEEE Trans. Appl. Supercond. 26 (2016) 6800404. doi:10.1109/TASC.2016.2518994.

[129] T.B. Mitchell-Williams, A. Baskys, S.C. Hopkins, V. Kalitka, A. Molodyk, B.A. Glowacki, A. Patel, Uniform trapped fields produced by stacks of HTS coated conductor tape, Supercond. Sci. Technol. 29 (2016) 85008. doi:10.1088/0953-2048/29/8/085008.

[130] V. Hussennether, M. Oomen, M. Leghissa, H.W. Neumüller, DC and AC properties of Bi-2223 cabled conductors designed for high-current applications, Phys. C Supercond. Its Appl. 401 (2004) 135–139. doi:10.1016/j.physc.2003.09.024.

[131] M.P. Philippe, M.D. Ainslie, L. Wéra, J.-F. Fagnard, A.R. Dennis, Y.-H. Shi, D.A. Cardwell, B. Vanderheyden, P. Vanderbemden, Influence of soft ferromagnetic sections on the magnetic flux density profile of a large grain, bulk Y–Ba–Cu–O superconductor, Supercond. Sci. Technol. 28 (2015) 95008. doi:10.1088/0953-2048/28/9/095008.

[132] S. Hahn, S.B. Kim, M.C. Ahn, J. Voccio, J. Bascunan, Y. Iwasa, Trapped field characteristics of stacked YBCO thin plates for compact NMR magnets: Spatial field distribution and temporal stability, IEEE Trans. Appl. Supercond. 20 (2010) 1037–1040. doi:10.1109/TASC.2010.2043832.

[133] S. Hahn, Y. Kim, J.P. Voccio, J. Song, J. Bascuñán, M. Tomita, Y. Iwasa, Temporal Enhancement of Trapped Field in a Compact NMR Magnet Comprising YBCO Annuli, IEEE Trans. Appl. Supercond. 24 (2014) 3–7.

[134] S. Kim, T. Nakano, R. Takano, S.Y. Hahn, Study on trapped field characteristics of HTS bulk annuli with iron rings for ferromagnetic shimming of a compact NMR magnet, IEEE Trans. Appl. Supercond. 19 (2009) 2273–2276. doi:10.1109/TASC.2009.2019083.

[135] T. Nakamura, D. Tamada, Y. Yanagi, Y. Itoh, T. Nemoto, H. Utumi, K. Kose, Development of a superconducting bulk magnet for NMR and MRI, J. Magn. Reson. 259 (2015) 68–75. doi:10.1016/j.jmr.2015.07.012.

[136] K. Selva, G. Majkic, Trapped magnetic field profiles of arrays of (Gd, Y)Ba2Cu3Ox superconductor tape in different stacking configurations, Supercond. Sci. Technol. 26 (2013) 115006. doi:10.1088/0953-2048/26/11/115006.

[137] A. Baskys, K. Filar, A. Patel, B.A. Glowacki, Trapped field of 13.4 T in an stack of HTS tapes with 30 μm substrate, Supercond. Sci. Technol. (2017) In preparation.

[138] A.G. Page, A. Patel, A. Baskys, S.C. Hopkins, V. Kalitka, A. Molodyk, B.A. Glowacki, The effect of stabilizer on the trapped field of stacks of superconducting tape magnetized by a pulsed field, Supercond. Sci. Technol. 28 (2015) 85009. doi:10.1088/0953-2048/28/8/085009.

[139] A. Patel, S.C. Hopkins, B.A. Glowacki, Trapped fields up to 2 T in a 12 mm square stack of commercial superconducting tape using pulsed field magnetization, Supercond. Sci. Technol. 26 (2013) 32001. doi:10.1088/0953-2048/26/3/032001.

[140] A. Patel, A. Baskys, S.C. Hopkins, V. Kalitka, A. Molodyk, B.A. Glowacki, Pulsed-Field Magnetization of Superconducting Tape Stacks for Motor Applications, IEEE Trans. Appl. Supercond. 25 (2015) 5203405. doi:10.1109/TASC.2015.2389142.

[141] A. Patel, A. Usoskin, A. Baskys, S.C. Hopkins, B.A. Glowacki, Trapped Field Profiles for 40-mm Wide Superconducting Tape Pieces, J. Supercond. Nov. Magn. 28 (2014) 397–401. doi:10.1007/s10948-014-2665-2.

[142] S. Samoilenkov, A. Molodyk, S. Lee, V. Petrykin, V. Kalitka, I. Martynova, A. Makarevich, A. Markelov, M. Moyzykh, A. Blednov, Customised 2G HTS wire for applications, Supercond. Sci. Technol. 29 (2016) 24001. doi:10.1088/0953-2048/29/2/024001.

[143] A. Baskys, A. Patel, S.C. Hopkins, V. Kalitka, A. Molodyk, B.A. Glowacki, Self-Supporting Stacks of Commercial Superconducting Tape Trapping Fields up to 1.6 T Using Pulsed Field Magnetization, IEEE Trans. Appl. Supercond. 25 (2015) 6600304. doi:10.1109/TASC.2014.2360871.

[144] K. Selva, X.F. Li, G. Majkic, Trapped Field and Flux Creep in Stacked (Gd,Y)Ba2Cu3Ox Superconductor Tape Arrays, IEEE Trans. Appl. Supercond. 25 (2015) 3–7. doi:10.1109/TASC.2014.2367159.

[145] A. Patel, S. Hopkins, A. Baskys, V. Kalitka, A. Molodyk, B.A. Glowacki, Magnetic levitation using high temperature superconducting pancake coils as composite bulk cylinders, Supercond. Sci. Technol. 28 (2015) 115007. doi:10.1088/0953-2048/28/11/115007.

[146] Y.B. Kim, C.F. Hempstead, A.R. Strnad, Magnetization and critical supercurrents, Phys. Rev. 129 (1963) 528–535. doi:10.1103/PhysRev.129.528.

[147] V.M.R. Zermeno, A.B. Abrahamsen, N. Mijatovic, B.B. Jensen, M.P. Sørensen, Calculation of alternating current losses in stacks and coils made of second generation high temperature superconducting tapes for large scale applications, J. Appl. Phys. 114 (2013). doi:10.1063/1.4827375.

[148] A. Baskys, A. Patel, S. Hopkins, B.A. Glowacki, Modeling of trapped fields by stacked (RE)BCO tape using angular transversal field dependency, IEEE Trans. Appl. Supercond. 26 (2016) 6601004. doi:10.1109/TASC.2016.2528992.

[149] E. Dennison, https://tiggerntatie.github.io/emagnet/solenoids/solenoidonaxis.htm, Magn. Formulas Web Site. (2017).

[150] W. Goldacker, A. Kario, R. Nast, F. Grilli, New double-core Roebel Assembled Coated Conductor (DOCO-RACC) cable for enhanced transport currents in large-scale applications, (2016). doi:https://publikationen.bibliothek.kit.edu/1000058309.

[151] T.B. Mitchell-Williams, A. Baskys, Y. Guo, S.C. Hopkins, U. Bangert, A. Molodyk, V. Petrykin, F. Gomory, L. Frolek, B.A. Glowacki, Spark-Discharge Plasma as a Method to Produce Low AC Loss Multifilamentary (RE)Ba2Cu3O7 Coated Conductors, IEEE Trans. Appl. Supercond. 27 (2017) 5900405. doi:10.1109/TASC.2017.2651584.

[152] J. Šouc, F. Gömöry, M. Vojenčiak, Calibration free method for measurement of the AC magnetization loss, Supercond. Sci. Technol. 18 (2005) 592–595. doi:10.1088/0953-2048/18/5/003.

[153] K.P. Brand, Dielectric Strength, Boiling Point and Toxicity of Gases - Different Aspects of the Same Basic Molecular Properties, IEEE Trans. Electr. Insul. EI-17 (1982) 451–456. doi:10.1109/TEI.1982.298489.

[154] A. Beroual, I. Fofana, Discharge in Long Air Gaps, IOP Publishing Ltd, 2016. doi:10.1088/978-0-7503-1236-3.

[155] R. Gyuráki, A. Godfrin, A. Jung, A. Kario, R. Nast, E. Demenčík, W. Goldacker, F. Grilli, Inter-filament Resistance at 77 K in Striated HTS Coated Conductors, IEEE Trans. Appl. Supercond. 26 (2016) 6603606. doi:10.1109/TASC.2016.2623222.

[156] J. Lu, E.S. Choi, H.D. Zhou, Physical properties of Hastelloy C-276 at cryogenic temperatures, J. Appl. Phys. 103 (2008) 64908. doi:10.1063/1.2899058.

[157] T. Machi, K. Nakao, T. Kato, T. Hirayama, K. Tanabe, Reliable fabrication process for long-length multi-filamentary coated conductors by a laser scribing method for reduction of AC loss, Supercond. Sci. Technol. 26 (2013) 105016 (15pp). doi:10.1088/0953-2048/26/10/105016.

[158] F. Grilli, R. Brambilla, L. Martini, Modeling high-temperature superconducting tapes by means of edge finite elements, IEEE Trans. Appl. Supercond. 17 (2007) 3155–3158. doi:10.1109/TASC.2007.902144.

[159] G.A. Levin, P.N. Barnes, Concept of Multiply Connected Superconducting Tapes, IEEE Trans. Appl. Supercond. 15 (2005) 2158–2161. doi:10.1109/TASC.2005.849601.

[160] G.A. Levin, P.N. Barnes, N. Amemiya, S. Kasai, K. Yoda, Z. Jiang, A. Polyanskii, Magnetization losses in multiply connected YBa2Cu3O6+x-coated conductors, J. Appl. Phys. 98 (2005) 113909. doi:10.1063/1.2139832.

[161] M. Majoros, B.A. Glowacki, A.M. Campbell, G.A. Levin, P.N. Barnes, M. Polak, AC Losses in Striated YBCO Coated Conductors, IEEE Trans. Appl. Supercond. 15 (2005) 2819–2822. doi:10.1109/TASC.2005.848234.

[162] W.J. Carr, Loss in a striated coated conductor, Supercond. Sci. Technol. 20 (2007) 168–175. doi:10.1088/0953-2048/20/3/010.

[163] S.C. Hopkins, T.B. Mitchell-Williams, D.R. Vanden Bussche, A. Calleja, V.R. Vlad, M. Vilardell, X. Granados, T. Puig, X. Obradors, A. Usoskin, M. Soloviov, M. Vojenciak, F. Gomory, I. Van Driessche, M. Backer, B.A. Glowacki, Low AC Loss Inkjet-Printed Multifilamentary YBCO Coated Conductors, IEEE Trans. Appl. Supercond. 26 (2016). doi:10.1109/TASC.2016.2542001.

[164] B.A. Glowacki, Preparation of Bi2Sr2CaCu2O8-x tracks and thick films by jet printing, Supercond. Sci. Technol. 13 (2000) 584–591. doi:10.1088/0953-2048/13/5/330.

[165] K. Vandaele, M. Mosiadz, S.C. Hopkins, A. Patel, I. Van Driessche, B.A. Glowacki, The influence of heat treatment parameters on pyrolysed TFA-derived YBCO films deposited by inkjet printing, Mater. Res. Bull. 47 (2012) 2032–2039. doi:10.1016/j.materresbull.2012.04.002.

[166] B.A. Glowacki, M. Mosiadz, The role of sol gel processing in the development of high-temperature superconductors for AC applications, J. Sol-Gel Sci. Technol. 51 (2009) 335–347. doi:10.1007/s10971-009-1980-8.

[167] M. Vilardell, X. Granados, S. Ricart, I. Van Driessche, A. Palau, T. Puig, X. Obradors, Flexible manufacturing of functional ceramic coatings by inkjet printing, Thin Solid Films. 548 (2013) 489–497. doi:10.1016/j.tsf.2013.09.012.

[168] P. Calvert, Inkjet Printing for Materials and Devices, Chem. Mater. 13 (2001) 3299–3305. doi:10.1021/cm0101632.

[169] B. Derby, Inkjet Printing of Functional and Structural Materials: Fluid Property Requirements, Feature Stability, and Resolution, Annu. Rev. Mater. Res. 40 (2010) 395–414. doi:10.1146/annurev-matsci-070909-104502.

[170] L. Li, M. Saedan, W. Feng, J.Y.H. Fuh, Y.S. Wong, H.T. Loh, S.C.H. Thian, S.T. Thoroddsen, L. Lu, Development of a multi-nozzle drop-on-demand system for multi-material dispensing, J. Mater. Process. Technol. 209 (2009) 4444–4448. doi:10.1016/j.jmatprotec.2008.10.040.

[171] FUJIFILM Holdings America Corporation, http://www.fujifilmusa.com/products/industrial_inkjet_printheads/index.html, (2017).

[172] I. Van Driessche, J. Feys, S.C. Hopkins, P. Lommens, X. Granados, B.A. Glowacki, S. Ricart, B. Holzapfel, M. Vilardell, A. Kirchner, M. Bäcker, Chemical solution deposition using ink-jet printing for YBCO coated conductors, Supercond. Sci. Technol. 25 (2012) 65017. doi:10.1088/0953-2048/25/6/065017.

[173] B.A. Glowacki, (RE)Ba2Cu3O7 Coated Conductors for AC and DC Applications, in: A. Narlikar (Ed.), YBCO Coat. Conduct., Springer Verlag, 2005: p. 765.

[174] K. De Keukeleere, I. Van Driessche, Nanoparticles and colloidal solutions, Intern. Rep. EUROTAPES Proj. Meet. (2014).

[175] N. Reis, B. Derby, Ink jet deposition of ceramic suspensions: modelling and experiments of droplet formation, MRS Symp. Proc. 625 (2000) 117–122. doi:dx.doi.org/10.1557/PROC-624-65.

[176] D. Jang, D. Kim, J. Moon, Influence of fluid physical properties on ink-jet printability, Langmuir. 25 (2009) 2629–2635. doi:10.1021/la900059m.

[177] M.W. Rupich, D.T. Verebelyi, W. Zhang, T. Kodenkandath, X. Li, Metalorganic Deposition of YBCO Films for Second-Generation-High-Temperature Superconductor Wires, MRS Bull. 29 (2004) 572–578.

[178] A. Gupta, R. Jagannathan, E.I. Cooper, E.A. Giess, J.I. Landman, B.W. Hussey, Superconducting oxide films with high transition temperature prepared from metal trifluoroacetate precursors, Appl. Phys. Lett. 52 (1988) 2077. doi:10.1063/1.99752.

[179] A. Gupta, E.I. Cooper, R. Jagannathan, E.A. Giess, Preparation of superconducting oxide films from metal trifluoroacetate solution precursors, in: Chem. High-Temperature Supercond. II, ACS, 1988: pp. 265–279. doi:10.1021/bk-1988-0377.ch020.

[180] X. Obradors, T. Puig, S. Ricart, M. Coll, J. Gazquez, A. Palau, X. Granados, Thin Films Based on Trifluoroacetate Solutions, Supercond. Sci. Technol. 25 (2012) 123001. doi:10.1088/0953-2048/25/12/123001.

[181] P.C. Mcintyre, R.C. Chiu, M.J. Cima, W.E. Rhine, Metal-Organic Decomposition and Microstructure Development in Ba2YCu3O7-x Films from Metal Trifluoroacetate Precursors, MRS Proc. 169 (1989) 743. doi:10.1557/PROC-169-743.

[182] J.T. Dawley, P.G. Clem, T.J. Boyle, L.M. Ottley, D.L. Overmyer, M.P. Siegal, Rapid processing method for solution deposited YBa2Cu3O7−δ thin films, Phys. C Supercond. 402 (2004) 143–151. doi:10.1016/j.physc.2003.09.072.

[183] W. Wu, F. Feng, Y. Zhao, X. Tang, Y. Xue, K. Shi, R. Huang, T. Qu, X. Wang, Z. Han, J.-C. Grivel, A low-fluorine solution with a 2:1 F/Ba mole ratio for the fabrication of YBCO films, Supercond. Sci. Technol. 27 (2014) 55006. doi:10.1088/0953-2048/27/5/055006.

[184] J. Feys, P. Vermeir, P. Lommens, S.C. Hopkins, X. Granados, B.A. Glowacki, M. Baecker, E. Reich, S. Ricard, B. Holzapfel, P. Van Der Voort, I. Van Driessche, Ink-jet printing of YBa2Cu3O7 superconducting coatings and patterns from aqueous solutions, J. Mater. Chem. 22 (2012) 3717. doi:10.1039/c1jm14899k.

[185] P.C. Duineveld, The stability of ink-jet printed lines of liquid with zero receding contact angle on a homogeneous substrate, J. Fluid Mech. 477 (2003) 175–200. doi:10.1017/S0022112002003117.

[186] S.R. Foltyn, Q.X. Jia, P.N. Arendt, L. Kinder, Y. Fan, J.F. Smith, Relationship between film thickness and the critical current of YBa2Cu3O7−δ-coated conductors, Appl. Phys. Lett. 75 (1999) 3692. doi:10.1063/1.125431.

[187] H. Wang, S.R. Foltyn, P.N. Arendt, Q.X. Jia, X. Zhang, Identification of the misfit dislocations at YBa2Cu3O7−δ/SrTiO3 interface using moiré fringe contrast, Phys. C Supercond. 444 (2006) 1–4. doi:10.1016/j.physc.2006.05.078.

[188] S.R. Foltyn, H. Wang, L. Civale, Q.X. Jia, P.N. Arendt, B. Maiorov, Y. Li, M.P. Maley, J.L. MacManus-Driscoll, Overcoming the barrier to 1000 A/cm width superconducting coatings, Appl. Phys. Lett. 87 (2005) 162505. doi:10.1063/1.2106021.

[189] T.G. Holesinger, L. Civale, B. Maiorov, D.M. Feldmann, J.Y. Coulter, D.J. Miller, V.A. Maroni, Z. Chen, D.C. Larbalestier, R. Feenstra, X. Li, Y. Huang, T. Kodenkandath, W. Zhang, M.W. Rupich, A.P. Malozemoff, Progress in nanoengineered microstructures for tunable high-current, high-temperature superconducting wires, Adv. Mater. 20 (2008) 391–407. doi:10.1002/adma.200700919.

[190] V.F. Solovyov, H.J. Wiesmann, Q. Li, D.O. Welch, M. Suenaga, Three- and four-μm-thick YBa2Cu3O7 layers with high critical-current densities on flexible metallic substrates by the BaF2 process, J. Appl. Phys. 99 (2006) 13902. doi:10.1063/1.2150590.

[191] C.E. Oberly, B. Razidlo, F. Rodriguez, Conceptual Approach to the Ultimate Low AC Loss YBCO Superconductor, IEEE Trans. Appl. Supercond. 15 (2005) 1643–1646. doi:10.1109/TASC.2005.849219.

[192] D. Abraimov, A. Gurevich, A. Polyanskii, X.Y. Cai, A. Xu, S. Pamidi, D. Larbalestier, C.L.H. Thieme, Significant reduction of AC losses in YBCO patterned coated conductors with transposed filaments, Supercond. Sci. Technol. 21 (2008) 82004. doi:10.1088/0953-2048/21/8/082004.

[193] A. Ben Yahia, X.-F. Li, M. Majoros, M. Sumption, V. Selvamanickam, AC loss reduction in multifilamentary coated conductors with transposed filaments, IEEE Trans. Appl. Supercond. 27 (2016) 5600105. doi:10.1109/TASC.2016.2637318.

[194] M.A.A.M. Van Wijck, M.A.J. Verhoeven, E.M.C.M. Reuvekamp, G.J. Gerritsma, D.H.A. Blank, H. Rogalla, CeO2 as insulation layer in high Tc superconducting multilayer and crossover structures CeO2 as insulation layer in high Tc superconducting multilayer and crossover structures, Appl. Phys. Lett. 68 (1996) 553–555. doi:10.1063/1.116397.

[195] H.B. Radousky, A review of the superconducting and normal state properties of Y(1-x)PrxBa2Cu3O7, J. Mater. Res. 7 (1992) 1917–1955. doi:10.1557/JMR.1992.1917.

[196] H.A. Blackstead, D.B. Chrisey, J.D. Dow, J.S. Horwitz, A.E. Klunzinger, D.B. Pulling, Superconductivity in PrBa2Cu3O7, Phys. Lett. A. 207 (1995) 109–112. doi:10.1016/0375-9601(95)00653-K.

[197] S. Favre, P. Romero, C. Stari, D. Ariosa, R. Faccio, Highly textured PrxY1−xBa2Cu3O7−δ polycrystalline ceramics sintered in Ar atmosphere, Mater. Chem. Phys. 155 (2015) 122–128. doi:10.1016/j.matchemphys.2015.02.008.

[198] K. Oka, Z. Zou, J. Ye, Crystal growth of superconductive PrBa2Cu3O7–y, Phys. C Supercond. 300 (1998) 200–206. doi:10.1016/S0921-4534(98)00130-0.

[199] C. Stari, L. Cichetto, C.H.M.A. Peres, V.A.G. Rivera, S. Sergeenkov, C.A. Cardoso, E. Marega, F.M. Araújo-Moreira, Comparative study on structure and magnetic properties of polycrystalline PrxY1-xBa2Cu3O7–δ prepared in oxygen and argon atmosphere, J. Alloys Compd. 528 (2012) 135–140. doi:10.1016/j.jallcom.2012.03.048.

[200] B. Holzapfel, G. Kreiselmeyer, M. Kraus, S. Bouffard, S. Klaumunzer, L. Schultz, G. Saemann-Ischenko, Effect of columnar defects on the critical current anisotropy of epitaxial YBCO thin films and YBCO/PrBCO multilayers, J. Alloys Compd. 195 (1993) 411–414. doi:10.1016/0925-8388(93)90767-H.

[201] J. Gao, J.L. Sun, The stationary properties of YBCO / PrBCO / YBCO ramp junctions with a graded barrier layer, Phys. C. 355 (2001) 238–244. doi:10.1016/S0921-4534(01)00126-5.

[202] H. Wang, S.R. Foltyn, L. Civale, B. Maiorov, Q.X. Jia, Attenuation of interfacial pinning enhancement in YBCO using a PrBCO buffer layer, Phys. C Supercond. 469 (2009) 2033–2036. doi:10.1016/j.physc.2009.08.014.

[203] H. Eloussifi, J. Farjas, P. Roura, S. Ricart, T. Puig, X. Obradors, M. Dammak, Thermoanalytical study of the decomposition of yttrium trifluoroacetate thin films, Thin Solid Films. 545 (2013) 200–204. doi:10.1016/j.tsf.2013.07.082.

[204] X. Palmer, C. Pop, H. Eloussifi, B. Villarejo, P. Roura, J. Farjas, A. Calleja, A. Palau, X. Obradors, T. Puig, S. Ricart, Solution design for low-fluorine trifluoroacetate route to YBa2Cu3O7 films, Supercond. Sci. Technol. 29 (2016) 24002. doi:10.1088/0953-2048/29/2/024002.

[205] M. Mosiadz, K.L. Juda, S.C. Hopkins, J. Soloducho, B.A. Glowacki, An in-depth in situ IR study of the thermal decomposition of yttrium trifluoroacetate hydrate, J. Therm. Anal. Calorim. 107 (2012) 681–691. doi:10.1007/s10973-011-1772-6.

[206] M. Mosiadz, K.L. Juda, S.C. Hopkins, J. Soloducho, B.A. Glowacki, An in-depth in situ IR study of the thermal decomposition of copper trifluoroacetate hydrate, J. Fluor. Chem. 135 (2012) 59–67. doi:10.1016/j.jfluchem.2011.08.010.

[207] M. Mosiadz, K.L. Juda, S.C. Hopkins, J. Soloducho, B.A. Glowacki, An in-depth in situ IR study of the thermal decomposition of barium trifluoroacetate hydrate, Thermochim. Acta. 513 (2011) 33–37. doi:10.1016/j.tca.2010.11.004.

[208] Y. Chen, C. Wu, G. Zhao, C. You, An advanced low-fluorine solution route for fabrication of high-performance YBCO superconducting films, Supercond. Sci. Technol. 25 (2012) 69501. doi:10.1088/0953-2048/25/6/069501.

[209] F.A. List, E.D. Specht, L. Heatherly, K.J. Leonard, S. Sathyamurthy, D.M. Kroeger, Crystalline phase development during vacuum conversion of thin barium fluoride precursor films on metallic substrates, Phys. C Supercond. Its Appl. 391 (2003) 350–362. doi:10.1016/S0921-4534(03)00965-1.

[210] V. Pinto, A. Angrisani Armenio, L. Piperno, A. Mancini, F. Rizzo, A. Vannozzi, A. Rufoloni, A. Augieri, V. Galluzzi, A. Frolova, G. Sotgiu, E. Silva, F. Fabbri, R. Lamanna, G. Celentano, Aging of precursor solutions used for YBCO films chemical solution deposition: Study of mechanisms and effects on film properties, IEEE Trans. Appl. Supercond. 26 (2016) 7500405. doi:10.1109/TASC.2016.2542587.

[211] L. Carrette, K.A. Friedrich, U. Stimming, Fuel Cells - Fundamentals and Applications, Fuel Cells. 1 (2001) 5–39. doi:10.1002/1615-6854(200105)1:1<5::AID-FUCE5>3.0.CO;2-G.

[212] S.P.S. Badwal, S. Giddey, C. Munnings, A. Kulkarni, Review of progress in high temperature solid oxide fuel cells, J. Aust. Ceram. Soc. 50 (2014) 23–37. doi:10.1002/chin.201531316.

[213] Z. Li, M. Toshiyuki, G.J. Auchterlonie, J. Zou, D. John, Mutual Diffusion Occurring at the Interface between during IT-SOFC Cell Preparation, Appl. Mater. Interfaces. (2011) 2772–2778. doi:10.1021/am2005543.

[214] S.P.S. Badwal, K. Foger, Solid oxide electrolyte fuel cell review, Ceram. Int. 22 (1996) 257–265. doi:10.1016/0272-8842(95)00101-8.

[215] K. Huang, S.C. Singhal, Cathode-supported tubular solid oxide fuel cell technology: A critical review, J. Power Sources. 237 (2013) 84–97. doi:10.1016/j.jpowsour.2013.03.001.

[216] A. Atkinson, S. Barnett, R.J. Gorte, J.T.S. Irvine, A.J. McEvoy, M. Mogensen, S.C. Singhal, J. Vohs, Advanced anodes for high-temperature fuel cells., Nat. Mater. 3 (2004) 17–27. doi:10.1038/nmat1040.

[217] R.J. Gorte, J.M. Vohs, Nanostructured anodes for solid oxide fuel cells, Curr. Opin. Colloid Interface Sci. 14 (2009) 236–244. doi:10.1016/j.cocis.2009.04.006.

[218] Hexis, http://www.hexis.com/en/home, (2017).

[219] Fuelcellmaterials, https://fuelcellmaterials.com, (2017).

[220] CEREL, http://www.cerel.eu/2.html, (2017).

[221] M.C. Tucker, Progress in metal-supported solid oxide fuel cells: A review, J. Power Sources. 195 (2010) 4570–4582. doi:10.1016/j.jpowsour.2010.02.035.

[222] S.P.S. Badwal, F.T. Ciacchi, Oxygen-ion conducting electrolyte materials for solid oxide fuel cells, Ionics (Kiel). 6 (2000) 1–21. doi:10.1007/BF02375543.

[223] J.B. Goodenough, Oxide-Ion Electrolytes, Annu. Rev. Mater. Res. 33 (2003) 91–128. doi:10.1146/annurev.matsci.33.022802.091651.

[224] E.D. Wachsman, K. Taek Lee, Lowering the Temperature of Solid Oxide Fuel Cells, Science (80-.). 334 (2011) 935–939. doi:10.1126/science.1204090.

[225] A.J. Jacobson, Materials for solid oxide fuel cells, Chem. Mater. 22 (2010) 660–674. doi:10.1021/cm902640j.

[226] B.C.H. Steele, Appraisal of Ce1−yGdyO2−y/2 electrolytes for IT-SOFC operation at 500°C, Solid State Ionics. 129 (2000) 95–110. doi:10.1016/S0167-2738(99)00319-7.

[227] N. Mahato, A. Banerjee, A. Gupta, S. Omar, K. Balani, Progress in material selection for solid oxide fuel cell technology: A review, Prog. Mater. Sci. 72 (2015) 141–337. doi:10.1016/j.pmatsci.2015.01.001.

[228] H.S. Spacil, Electrical device including nickel-containing stabilized zirconia electrode, US3503809, 1970.

[229] Y. Matsuzaki, I. Yasuda, The poisoning effect of sulfur-containing impurity gas on a SOFC anode: Part I. Dependence on temperature, time, and impurity concentration, Solid State Ionics. 132 (2000) 261–269. doi:10.1016/S0167-2738(00)00653-6.

[230] M.L. Toebes, J.H. Bitter, A.J. van Dillen, K.P. de Jong, Impact of the Structure and Reactivity of Nickel Particles on the Catalytic Growth of Carbon Nanofibers, Catal. Today. 76 (2002) 33–42. doi:10.1016/S0920-5861(02)00209-2.

[231] M.S. Khan, S.B. Lee, R.H. Song, J.W. Lee, T.H. Lim, S.J. Park, Fundamental mechanisms involved in the degradation of nickel-yttria stabilized zirconia (Ni-YSZ) anode during solid oxide fuel cells operation: A review, Ceram. Int. 42 (2015) 35–48. doi:10.1016/j.ceramint.2015.09.006.

[232] S. McIntosh, R.J. Gorte, Direct hydrocarbon solid oxide fuel cells, Chem. Rev. 104 (2004) 4845–4865. doi:10.1021/cr020725g.

[233] S. Tao, J.T.S. Irvine, A redox-stable efficient anode for solid-oxide fuel cells., Nat. Mater. 2 (2003) 320–323. doi:10.1038/nmat871.

[234] R. Mukundan, E.L. Brosha, F.H. Garzon, Sulfur Tolerant Anodes for SOFCs, Electrochem. Solid-State Lett. 7 (2004) A5–A7. doi:10.1149/1.1627452.

[235] S. Park, J.M. Vohs, R.J. Gorte, Direct oxidation of hydrocarbons in a solid-oxide fuel cell, Nature. 404 (2000) 265–267. doi:10.1038/35005040.

[236] N. Kiratzis, P. Holtappels, C.E. Hatchwell, M. Mogensen, J.T.S. Irvine, Preparation and Characterization of Copper/Yttria Titania Zirconia Cermets for Use as Possible Solid Oxide Fuel Cell Anodes, Fuel Cells. 1 (2001) 211–218. doi:10.1002/1615-6854(200112)1:3/4<211::AID-FUCE211>3.0.CO;2-H.

[237] R. Barfod, A. Hagen, S. Ramousse, P. V. Hendriksen, M. Mogensen, Break down of losses in thin electrolyte SOFCs, Fuel Cells. 6 (2006) 141–145. doi:10.1002/fuce.200500113.

[238] S.P. Jiang, Issues on development of (La,Sr)MnO3 cathode for solid oxide fuel cells, J. Power Sources. 124 (2003) 390–402. doi:10.1016/S0378-7753(03)00814-0.

[239] S.P. Jiang, Development of lanthanum strontium manganite perovskite cathode materials of solid oxide fuel cells: A review, 2008. doi:10.1007/s10853-008-2966-6.

[240] Y. Sakaki, Y. Takeda, A. Kato, N. Imanishi, O. Yamamoto, M. Hattori, M. Iio, Y. Esaki, Ln1−xSrxMnO3 (Ln=Pr, Nd, Sm and Gd) as the cathode material for solid oxide fuel cells, Solid State Ionics. 118 (1999) 187–194. doi:http://dx.doi.org/10.1016/S0167-2738(98)00440-8.

[241] S. Carter, A. Selcuk, R.J. Chater, J. Kajda, J.A. Kilner, B.C.H. Steele, Oxygen transport in selected nonstoichiometric perovskite-structure oxides, Solid State Ionics. 53–56 (1992) 597–605. doi:10.1016/0167-2738(92)90435-R.

[242] S.P. Jiang, A comparison of O2 reduction reactions on porous (La,Sr)MnO3 and (La,Sr)(Co,Fe)O3 electrodes, Solid State Ionics. 146 (2002) 1–22. doi:10.1016/S0167-2738(01)00997-3.

[243] E.P. Murray, T. Tsai, S.A. Barnett, Oxygen transfer processes in (La,Sr)MnO3/Y2O3-stabilized ZrO2 cathodes: an impedance spectroscopy study, Solid State Ionics. 110 (1998) 235–243. doi:10.1016/S0167-2738(98)00142-8.

[244] S.P. Jiang, Nanoscale and nano-structured electrodes of solid oxide fuel cells by infiltration: Advances and challenges, Int. J. Hydrogen Energy. 37 (2012) 449–470. doi:10.1016/j.ijhydene.2011.09.067.

[245] A. Esquirol, N.P. Brandon, J.A. Kilner, M. Mogensen, Electrochemical characterization of La0.6Sr0.4Co0.2Fe0.8O3 cathodes for intermediate-temperature SOFCs, J. Electrochem. Soc. 151 (2004) A1847–A1855. doi:10.1149/1.1799391.

[246] A. Martinez-Amesti, A. Larranaga, L.M. Rodriguez-Martinez, A.T. Aguayo, J.L. Pizarro, M.L. No, A. Laresgoiti, M.I. Arriortua, Reactivity between La(Sr)FeO3 cathode, doped CeO2 interlayer and yttria-stabilized zirconia electrolyte for solid oxide fuel cell applications, J. Power Sources. 185 (2008) 401–410. doi:10.1016/j.jpowsour.2008.06.049.

[247] M.D. Anderson, J.W. Stevenson, S.P. Simner, Reactivity of lanthanide ferrite SOFC cathodes with YSZ electrolyte, J. Power Sources. 129 (2004) 188–192. doi:10.1016/j.jpowsour.2003.11.039.

[248] H.Y. Tu, Y. Takeda, N. Imanishi, O. Yamamoto, Ln0.4Sr0.6Co0.8Fe0.2O3−δ (Ln=La, Pr, Nd, Sm, Gd) for the electrode in solid oxide fuel cells, Solid State Ionics. 117 (1999) 277–281. doi:http://dx.doi.org/10.1016/S0167-2738(98)00428-7.

[249] S. Bebelis, N. Kotsionopoulos, A. Mai, D. Rutenbeck, F. Tietz, Electrochemical characterization of mixed conducting and composite SOFC cathodes, Solid State Ionics. 177 (2006) 1843–1848. doi:10.1016/j.ssi.2006.05.041.

[250] L. Adijanto, R. Küngas, F. Bidrawn, R.J. Gorte, J.M. Vohs, Stability and performance of infiltrated La0.8Sr 0.2CoxFe1-xO3 electrodes with and without Sm0.2Ce0.8O1.9 interlayers, J. Power Sources. 196 (2011) 5797–5802. doi:10.1016/j.jpowsour.2011.03.022.

[251] J.W. Fergus, Lanthanum chromite-based materials for solid oxide fuel cell interconnects, Solid State Ionics. 171 (2004) 1–15. doi:10.1016/j.ssi.2004.04.010.

[252] K.J. Yoon, C.N. Cramer, J.W. Stevenson, O.A. Marina, Advanced ceramic interconnect material for solid oxide fuel cells: Electrical and thermal properties of calcium- and nickel-doped yttrium chromites, J. Power Sources. 195 (2010) 7587–7593. doi:10.1016/j.jpowsour.2010.06.040.

[253] Z. Yang, Recent advances in metallic interconnects for solid oxide fuel cells, Int. Mater. Rev. 53 (2008) 39–54. doi:10.1179/174328007X212526.

[254] N. Shaigan, W. Qu, D.G. Ivey, W. Chen, A review of recent progress in coatings, surface modifications and alloy developments for solid oxide fuel cell ferritic stainless steel interconnects, J. Power Sources. 195 (2010) 1529–1542. doi:10.1016/j.jpowsour.2009.09.069.

[255] S.P.S. Badwal, R. Deller, K. Foger, Y. Ramprakash, J. Zhang, Interaction between chromia forming alloy interconnects and air electrode of solid oxide fuel cells, Solid State Ionics. 99 (1997) 297–310. doi:10.1016/S0167-2738(97)00247-6.

[256] J. Wu, X. Liu, Recent development of SOFC metallic interconnect, J. Mater. Sci. Technol. 26 (2010) 293–305. doi:10.1016/S1005-0302(10)60049-7.

[257] K.S. Weil, The state-of-the-art in sealing technology for solid oxide fuel cells, JOM. 58 (2006) 37–44. doi:10.1007/s11837-006-0052-6.

[258] A. V Virkar, SOFC Materials and Processing Issues Presented at the SECA Core Technology Program Workshop SOFC Stack Materials and Processing Issues, 2001.

[259] W. Zhu, D. Ding, C. Xia, Enhancement in Three-Phase Boundary of SOFC Electrodes by an Ion Impregnation Method: A Modeling Comparison, Electrochem. Solid-State Lett. 11 (2008) B83. doi:10.1149/1.2895009.

[260] C. Wang, Triple phase boundary engineering of electrodes for solid oxide fuel cells by inkjet printing, University of Cambridge, 2013.

[261] K. Yamahara, C.P. Jacobson, S.J. Visco, X.F. Zhang, L.C. De Jonghe, Thin film SOFCs with cobalt-infiltrated cathodes, Solid State Ionics. 176 (2005) 275–279. doi:10.1016/j.ssi.2004.08.017.

[262] M. Dudek, R.I. Tomov, C. Wang, B.A. Glowacki, P. Tomczyk, R.P. Socha, M. Mosialek, Feasibility of direct carbon solid oxide fuels cell (DC-SOFC) fabrication by inkjet printing technology, Electrochim. Acta. 105 (2013) 412–418. doi:10.1016/j.electacta.2013.04.139.

[263] R.I. Tomov, M. Krauz, A. Tluczek, R. Kluczowski, V. V. Krishnan, K. Balasubramanian, R. V. Kumar, B.A. Glowacki, Vacuum-sintered stainless steel porous supports for inkjet printing of functional SOFC coatings, Mater. Renew. Sustain. Energy. 4 (2015) 14. doi:10.1007/s40243-015-0056-7.

[264] C. Wang, R.I. Tomov, R.V. Kumar, B.A. Glowacki, Inkjet printing of gadolinium-doped ceria electrolyte on NiO-YSZ substrates for solid oxide fuel cell applications, J. Mater. Sci. 46 (2011) 6889–6896. doi:10.1007/s10853-011-5653-y.

[265] C. Wang, S.C. Hopkins, R.I. Tomov, R.V. Kumar, B.A. Glowacki, Optimisation of CGO suspensions for inkjet-printed SOFC electrolytes, J. Eur. Ceram. Soc. 32 (2012) 2317–2324. doi:10.1016/j.jeurceramsoc.2012.03.001.

[266] R.I. Tomov, R. Duncan, M. Krauz, R.V. Kumar, B.A. Glowacki, Inkjet printing and inkjet infiltration of functional coatings for SOFCs fabrication, in: E3S Web Conf. SEED 2016, 2016: p. 98. doi:10.1051/e3sconf/20161000098.

[267] R.I. Tomov, A. Fakeeh, V.V. Krishnan, K. Balasubramanian, V.R. Kumar, B.A. Glowacki, Direct Ceramic Inkjet Printing and Infiltration of Functional Coatings for Metal Supported SOFC, ECS Trans. . 68 (2015) 2491–2501. doi:10.1149/06801.2491ecst.

[268] A. Fakeeh, R.I. Tomov, V.R. Kumar, B.A. Glowacki, Fabrication of Bimetallic (NiFe) Anode-Supported SOFCs with Direct Ceramic Inkjet Printing, ECS Trans. 68 (2015) 1531–1539. doi:10.1149/06801.1531ecst.

[269] E. Barsoukov, J.R. Macdonald, Impedance Spectroscopy, Wiley-Interscience, 2005. doi:10.1002/0471716243.

[270] T.B. Mitchell-Williams, R.I. Tomov, S.A. Saadabadi, M. Krauz, P. V. Aravind, B.A. Glowacki, R.V. Kumar, Infiltration of commercially available, anode supported SOFC's via inkjet printing, Mater. Renew. Sustain. Energy. 6 (2017) 12. doi:10.1007/s40243-017-0096-2.

[271] T.E. Burye, J.D. Nicholas, Nano-ceria pre-infiltration improves La0.6Sr0.4Co0.8Fe0.2O3-x infiltrated Solid Oxide Fuel Cell cathode performance, J. Power Sources. 300 (2015) 402–412. doi:10.1016/j.jpowsour.2015.09.080.

[272] R. Fernández-González, J.C. Ruiz-Morales, J. Canales-Vázquez, J.R. Jurado, A. Makradi, P. Núñez, Decreasing the polarisation resistance of a Ni-YSZ solid oxide fuel cell anode by infiltration of a ceria-based solution, Int. J. Hydrogen Energy. (2016) 1–6. doi:10.1016/j.ijhydene.2016.03.092.

[273] H. Kurokawa, T.Z. Sholklapper, C.P. Jacobson, L.C. De Jonghe, S.J. Visco, Ceria Nanocoating for Sulfur Tolerant Ni-Based Anodes of Solid Oxide Fuel Cells, Electrochem. Solid-State Lett. 10 (2007) B135-138. doi:10.1149/1.2748630.

[274] M.C. Tucker, G.Y. Lau, C.P. Jacobson, L.C. DeJonghe, S.J. Visco, Performance of metal-supported SOFCs with infiltrated electrodes, J. Power Sources. 171 (2007) 477–482. doi:10.1016/j.jpowsour.2007.06.076.

[275] Z. Jiang, C. Xia, F. Chen, Nano-structured composite cathodes for intermediate-temperature solid oxide fuel cells via an infiltration/impregnation technique, Electrochim. Acta. 55 (2010) 3595–3605. doi:10.1016/j.electacta.2010.02.019.

[276] Z. Liu, D. Ding, B. Liu, W. Guo, W. Wang, C. Xia, Effect of impregnation phases on the performance of Ni-based anodes for low temperature solid oxide fuel cells, J. Power Sources. 196 (2011) 8561–8567. doi:10.1016/j.jpowsour.2011.05.076.

[277] B. Timurkutluk, C. Timurkutluk, M.D. Mat, Y. Kaplan, Anode-supported solid oxide fuel cells with ion conductor infiltration, Int. J. Energy Res. 35 (2011) 1048–1055. doi:10.1002/er.1832.

[278] T.Z. Sholklapper, H. Kurokawa, C.P. Jacobson, S.J. Visco, L.C. De Jonghe, Nanostructured solid oxide fuel cell electrodes, Nano Lett. 7 (2007) 2136–2141. doi:10.1021/nl071007i.

[279] R.P. Dowd, S. Lee, Y. Fan, K. Gerdes, Engineering the solid oxide fuel cell electrocatalyst infiltration technique for industrial use, Int. J. Hydrogen Energy. 41 (2016) 14971–14981. doi:10.1016/j.ijhydene.2016.06.015.

[280] I. Clancy, G. Amarandei, C. Nash, B.A. Glowacki, Metal particle compaction during drop-substrate impact for inkjet printing and drop-casting processes, J. Appl. Phys. 119 (2016) 54903. doi:10.1063/1.4941344.

[281] M. Mosiadz, R.I. Tomov, S.C. Hopkins, G. Martin, B. Holzapfel, B.A. Glowacki, Inkjet printing of multiple Ce0.8 Gd0.2O2 buffer layers on a Ni-5%W substrate, J. Phys. Conf. Ser. 234 (2010) 22024. doi:10.1088/1742-6596/234/2/022024.

[282] C.A. Schneider, W.S. Rasband, K.W. Eliceiri, NIH Image to ImageJ: 25 years of image analysis, Nat. Methods. 9 (2012) 671–675. doi:10.1038/nmeth.2089.

[283] N.C. Reis, R.F. Griffiths, J.M. Santos, Parametric study of liquid droplets impinging on porous surfaces, Appl. Math. Model. 32 (2008) 341–361. doi:10.1016/j.apm.2006.12.006.

[284] J. Li, Z. Bai, E. Croiset, A two-dimensional modeling of solid oxide fuel cell button cells with detailed electrochemistry mechanism, J. Power Sources. 333 (2016) 164–172. doi:10.1016/j.jpowsour.2016.08.125.

[285] R. Kiebach, P. Zielke, J.V.T. Høgh, K. Thydén, H.J. Wang, R. Barford, P. V. Hendriksen, Infiltration of SOFC Stacks: Evaluation of the Electrochemical Performance Enhancement and the Underlying Changes in the Microstructure, Fuel Cells. 16 (2016) 80–88. doi:10.1002/fuce.201500107.

[286] T. Klemensø, K. Thydén, M. Chen, H.J. Wang, Stability of Ni-yttria stabilized zirconia anodes based on Ni-impregnation, J. Power Sources. 195 (2010) 7295–7301. doi:10.1016/j.jpowsour.2010.05.047.

[287] M.S. Khan, W. Wahyudi, S.B. Lee, R.H. Song, J.W. Lee, T.H. Lim, S.J. Park, Effect of various sintering inhibitors on the long term performance of Ni-YSZ anodes used for SOFCs, Int. J. Hydrogen Energy. 40 (2015) 11968–11975. doi:10.1016/j.ijhydene.2015.04.145.

[288] N.M. Sammes, Z. Cai, Ionic conductivity of ceria/yttria stabilized zirconia electrolyte materials, Solid State Ionics. 100 (1997) 39–44. doi:10.1016/S0167-2738(97)00306-8.

[289] T. Ishihara, J. Yan, M. Shinagawa, H. Matsumoto, Ni-Fe bimetallic anode as an active anode for intermediate temperature SOFC using LaGaO3 based electrolyte film, Electrochim. Acta. 52 (2006) 1645–1650. doi:10.1016/j.electacta.2006.03.103.

[290] J. Yan, M. Enoki, H. Matsumoto, T. Ishihara, Nanoporous Ni–Fe Bimetallic Plates for Nonfragile, Reliable SOFCs, Electrochem. Solid-State Lett. 10 (2007) B139-141. doi:10.1149/1.2751839.

[291] Y.W. Ju, H. Eto, T. Inagaki, S. Ida, T. Ishihara, Preparation of Ni-Fe bimetallic porous anode support for solid oxide fuel cells using LaGaO3 based electrolyte film with high power density, J. Power Sources. 195 (2010) 6294–6300. doi:10.1016/j.jpowsour.2010.04.068.

[292] T. Ishihara, J. Yan, M. Enoki, S. Okada, H. Matsumoto, Ni–Fe Alloy-Supported Intermediate Temperature SOFCs Using LaGaO Electrolyte Film for Quick Startup, J. Fuel Cell Sci. Technol. 5 (2008) 31205. doi:10.1115/1.2930763.

[293] H.C. Park, A. V. Virkar, Bimetallic (Ni-Fe) anode-supported solid oxide fuel cells with gadolinia-doped ceria electrolyte, J. Power Sources. 186 (2009) 133–137. doi:10.1016/j.jpowsour.2008.09.080.

[294] R. Knibbe, H.J. Wang, P. Blennow, K. Thydén, Å.H. Persson, L. Mikkelsen, T. Klemensø, Oxidation in ceria infiltrated metal supported SOFCs-A TEM investigation, J. Power Sources. 228 (2013) 75–82. doi:10.1016/j.jpowsour.2012.11.051.

[295] K. Taek Lee, H.S. Yoon, J.S. Ahn, E.D. Wachsman, Bimodally integrated anode functional layer for lower temperature solid oxide fuel cells, J. Mater. Chem. 22 (2012) 17113. doi:10.1039/c2jm34465c.

[296] R.I. Tomov, T.B. Mitchell-Williams, C. Gao, R. V. Kumar, B.A. Glowacki, Performance optimization of LSCF/Gd:CeO2 composite cathodes via single-step inkjet printing infiltration, J. Appl. Electrochem. 47 (2017) 641–651. doi:10.1007/s10800-017-1066-1.

[297] A.N. Petrov, V.A. Cherepanov, A.Y. Zuev, Thermodynamics, defect structure, and charge transfer in doped lanthanum cobaltites: An overview, J. Solid State Electrochem. 10 (2006) 517–537. doi:10.1007/s10008-006-0124-0.

[298] L.W. Tai, M.M. Nasrallah, H.U. Anderson, D.M. Sparlin, S.R. Sehlin, Structure and electrical properties of La1-xSrxCo1-yFeyO3. Part 2. The system La1-xSrxCo0.2Fe0.8O3, Solid State Ionics. 76 (1995) 273–283. doi:10.1016/0167-2738(94)00245-N.

[299] Y. Teraoka, H.M. Zhang, K. Okamoto, N. Yamazoe, Mixed ionic-electronic conductivity of La1-xSrxCo1-yFeyO3-d perovskite-type oxides, Mater. Res. Bull. 23 (1988) 51–58. doi:10.1016/0025-5408(88)90224-3.

[300] A. Esquirol, J. Kilner, N. Brandon, Oxygen transport in La0.6Sr0.4Co0.2Fe0.8O3-d/Ce0.8Ge0.2O2-x composite cathode for IT-SOFCs, Solid State Ionics. 175 (2004) 63–67. doi:10.1016/j.ssi.2004.09.013.

[301] H. Ding, A. V Virkar, M. Liu, F. Liu, Suppression of Sr surface segregation in La(1-x)Sr(x)Co(1-y)Fe(y)O(3-d): a first principles study, Phys Chem Chem Phys. 15 (2013) 489–496. doi:10.1039/c2cp43148c.

[302] E. Bucher, W. Sitte, Long-term stability of the oxygen exchange properties of (La,Sr)1−z(Co,Fe)O3−d in dry and wet atmospheres, Solid State Ionics. 192 (2011) 480–482. doi:10.1016/j.ssi.2010.01.006.

[303] D. Ding, X. Li, S.Y. Lai, K. Gerdes, M. Liu, Enhancing SOFC cathode performance by surface modification through infiltration, Energy Environ. Sci. 7 (2014) 552. doi:10.1039/c3ee42926a.

[304] L. Nie, M. Liu, Y. Zhang, M. Liu, La0.6Sr0.4Co0.2Fe0.8O3-d cathodes infiltrated with samarium-doped cerium oxide for solid oxide fuel cells, J. Power Sources. 195 (2010) 4704–4708. doi:10.1016/j.jpowsour.2010.02.049.

[305] J.W. Yun, J. Han, S.P. Yoon, S. Park, H.S. Kim, S.W. Nam, Ce0.8Gd0.2O2 modification on La0.6Sr0.4Co0.2Fe0.8O3 cathode for improving a cell performance in intermediate temperature solid oxide fuel cells, J. Ind. Eng. Chem. 17 (2011) 439–444. doi:10.1016/j.jiec.2010.10.016.

[306] M. Liu, D. Ding, K. Blinn, X. Li, L. Nie, M. Liu, Enhanced performance of LSCF cathode through surface modification, Int. J. Hydrogen Energy. 37 (2012) 8613–8620. doi:10.1016/j.ijhydene.2012.02.139.

[307] D. Chen, C. Huang, R. Ran, H.J. Park, C. Kwak, Z. Shao, New Ba0.5Sr0.5Co0.8Fe0.2O3−δ + Co3O4 composite electrode for IT-SOFCs with improved electrical conductivity and catalytic activity, Electrochem. Commun. 13 (2011) 197–199. doi:10.1016/j.elecom.2010.12.012.

[308] A.J. Samson, M. Sogaard, N. Bonanos, Electrodes for Solid Oxide Fuel Cells Based on Infiltration of Co-Based Materials, Electrochem. Solid-State Lett. 15 (2012) B54. doi:10.1149/2.020204esl.

[309] C. Gao, Y. Liu, T. Zhao, G. Kerherve, D.J. Payne, R. Maher, L.F. Cohen, R.I. Tomov, R.V. Kumar, Co3O4 infiltration—a simple way to enhance and stabilize the performance of LSCF/CGO cathode in SOFC, Prep. (2017).

[310] N. Imanishi, R. Ohno, K. Murata, A. Hirano, Y. Takeda, O. Yamamoto, K. Yamahara, LSM-YSZ cathode with infiltrated cobalt oxide and cerium oxide nanoparticles, Fuel Cells. 9 (2009) 215–221. doi:10.1002/fuce.200800090.

[311] V. Dusastre, J.A. Kilner, Optimisation of composite cathodes for intermediate temperature SOFC applications, Solid State Ionics. 126 (1999) 163–174. doi:10.1016/S0167-2738(99)00108-3.

[312] F.S. Baumann, J. Fleig, H.U. Habermeier, J. Maier, Impedance spectroscopic study on well-defined (La,Sr)(Co,Fe)O3-x model electrodes, Solid State Ionics. 177 (2006) 1071–1081. doi:10.1016/j.ssi.2006.02.045.

[313] N.J. Simrick, A. Bieberle-Hütter, T.M. Ryll, J.A. Kilner, A. Atkinson, J.L.M. Rupp, An investigation of the oxygen reduction reaction mechanism of La0.6Sr0.4Co0.2Fe0.8O3 using patterned thin films, Solid State Ionics. 206 (2012) 7–16. doi:10.1016/j.ssi.2011.10.029.

[314] M. Prestat, J.F. Koenig, L.J. Gauckler, Oxygen reduction at thin dense La0.52Sr0.48Co 0.18Fe0.82O3-δ electrodes: Part I: Reaction model and faradaic impedance, J. Electroceramics. 18 (2007) 87–101. doi:10.1007/s10832-007-9012-y.

[315] L.J. Miara, S.N. Basu, U.B. Pal, S. Gopalan, 2D Numerical Model for Identification of Oxygen Reduction Reaction Mechanisms in Patterned Cathodes of La0.6Sr0.4Co0.2Fe0.8O3-δ, J. Electrochem. Soc. 159 (2012) F419–F425. doi:10.1149/2.021208jes.

[316] T. Hong, L. Zhang, F.L. Chen, C.R. Xia, Oxygen surface exchange properties of La0.6Sr0.4Co0.8Fe0.2O3-d coated with SmxCe1-xO2-d, J. Power Sources. 218 (2012) 254–260. doi:10.1016/j.jpowsour.2012.07.004.

[317] Y. Liu, F. Wang, B. Chi, J. Pu, L. Jian, S.P. Jiang, A stability study of impregnated LSCF-GDC composite cathodes of solid oxide fuel cells, J. Alloys Compd. 578 (2013) 37–43. doi:10.1016/j.jallcom.2013.05.021.

[318] C. Endler-Schuck, J. Joos, C. Niedrig, A. Weber, E. Ivers-Tiffee, The chemical oxygen surface exchange and bulk diffusion coefficient determined by impedance spectroscopy of porous La0.58Sr0.4Co0.2Fe0.8O3-d (LSCF) cathodes, Solid State Ionics. 269 (2015) 67–79. doi:10.1016/j.ssi.2014.11.018.

[319] R. Kiebach, W. Zhang, M. Chen, K. Norrman, H.J. Wang, J.R. Bowen, R. Barfod, P.V. Hendriksen, W. Zhang, Stability of La0.6Sr0.4Co0.2Fe0.8O3/Ce0.9Gd0.1O2 cathodes during sintering and solid oxide fuel cell operation, J. Power Sources. 283 (2015) 151–161. doi:10.1016/j.jpowsour.2015.02.064.